Strategies for the Formation of Covalently Bonded Nano-Networks on Metal Surfaces through Amine Reactions.

A thesis for the degree of

PHILOSOPHIAE DOCTOR

Presented to

DUBLIN CITY UNIVERSITY

Ollscoil Chathair Bhaile Átha Cliath

by

Hooi Ling Lee,

M.Sc., B. App. Sci.(Hons)

School of Physical Sciences

Dublin City University

Research Supervisor:

Dr. A. A. Cafolla

External Examiner: Prof. Andrew Evans

Internal Examiner: Prof. Greg Hughes

May 2012

Declaration

I hereby certify that this material, which I now submit for assessment on the programme of study leading to the award of Doctor of Philosophy is entirely my own work, that I have exercised reasonable care to ensure that the work is original, and does not to the best of my knowledge breach any law of copyright, and has not been taken from the work of others save and to the extent that such work has been cited and acknowledged within the text of my work.

Hooi Ling Lee

ID No: 58125361

April, 2012.

Acknowledgements

First of all, I wish to convey my heartfelt gratitude to my Ph.D supervisor, Dr. Tony Cafolla for his patience and guidance throughout my doctorate study. I am thankful to my colleagues in my laboratory particularly Dr. John P. Cuniffe, Mr. John P. Beggan, Ms. Catherine Doyle, Ms. Nina Berner and Mr. Thomas Carpy. It has been a wonderful experience working with all of you. I also wish to thank academicians and staff support in Dublin City University especially School of Physical Sciences for their assistance.

My deepest appreciation is also dedicated to all my collaborators who have contributed enormously in my research work. I am truly honoured to have had the opportunity to work with the following collaborators who are specialised in their own field:

1. Prof. Louis Porte, Dr. Luca Giovanelli, Dr. Mathieu Abel, Dr. Mathieu Koudia, Dr. Sylvain Clair from IM2NP-CNRS, Aix-Marseille Université, Marseille, France.
2. Dr. Corinne Dufaure from ENSIACET/CIRIMAT, Toulouse, France.
3. Dr. Zheshen Li from The Institute for Storage Rings Facilities (ISA), Aarhus, Denmark.
4. Dr. Alexei B. Preobrajenski from MAX Lab, University of Lund, Sweden.

To all my friends who know me, thank you for your friendships and care.

Last but not least, thank you to my family especially my parents in Malaysia. Without their continuous faith, I would never make it until this stage. In short, it has been a very humbling journey.

This Ph.D work was funded by Science Foundation Ireland (SFI) under grant number 08/RFP/PHY1366. My synchrotron trip to ISA laboratory was supported by the EU grant. The travelling grant to IM2NP was awarded by Ulysses Grant 2011 from Irish Research Council for Sciences, Engineering and Technology, IRCSET-Embark Initiative. Their financial supports are gratefully acknowledged.

Thank you.

Terima kasih.

Go raibh maith agat.

For my parents

Table of Contents

List of Poster Presentations

BOC POSTER COMPETITION

The formation of surface supported covalently bonded 5,10,15,20-tetrakis(4-aminophenyl)-porphyrin (TAPP) networks.

School of Physical Sciences, Dublin City University, 13th April, 2012.

ECOSS28

The formation of surface supported covalently bonded 5,10,15,20-tetrakis(4-aminophenyl)-porphyrin (TAPP) networks.

Wroclaw, Poland, 28th August, 2011 – 2nd September, 2011.

BOC POSTER COMPETITION

The formation of surface supported covalently bonded porphyrin networks through polyimidisation.

School of Physical Sciences, Dublin City University, 24th September, 2010.

-won 3rd prize in the poster competition.

ECOSS27

The formation of surface supported covalently bonded porphyrin networks through polyimidisation.

Groningen, The Netherlands, 29th August, 2009 – 3th September, 2009.

List of Acronym.

E_p	Pass energy
BE	Binding energy
EBD	Electron beam deposition
EDC	Energy distribution curve
ESCA	Electron Spectroscopy for Chemical Analysis
FWHM	Full width half maximum
GI	Grazing incidence
HOMO	Highest occupied molecular orbital
hv	Photon energy
KE	Kinetic energy
LEED	Low energy electron diffraction
LUMO	Lowest occupied molecular orbital
MFP	Mean free path
ML	Monolayer
MO	Molecular orbital
NE	Normal emission
NI	Normal incidence
PES	Photoelectron spectroscopy
PTCDA	3, 4, 9, 10-perylene tetracarboxylic dianhydride
RT	Room temperature
SECO	Secondary electrons cut-off
STM	Scanning tunnelling microscopy
STS	Scanning tunnelling spectroscopy
TAPB	1,3,6-tris(4-aminophenel)benzene
TAPP	5,10, 15,20-tetrakis(4-aminophenyl)porphyrin
TPP	Tetra(4-aminophenyl)porphyrin
UHV	Ultra high vacuum
UPS	Ultraviolet photoelectron spectroscopy
VB	Valence band
WF	Workfunction
XAS	X-ray absorption spectroscopy
XPS	X-ray photoelectron spectroscopy

Abstract

Recently, there has been increasing interest in the development of covalent surface supported polymeric networks. This is attributed to the fact that they are thermally, mechanically and chemically more stable than those based on hydrogen bonded or metal-organic frameworks. The formation and characterization of organic nano-networks on metal surfaces is important for applications such as gas sensors, catalysis and molecular templates. In this thesis, strategies for the formation of covalent networks of 5,10,15,20-tetrakis(4-aminophenyl)-porphyrin (TAPP) and 1,3,5-tris(4aminophenyl)benzene (TAPB), both of which have amine groups that are attached to phenyl rings, were extensively investigated on Au(111), Ag(111) and Cu(111) surfaces. The strategies employed to form covalently bonded networks are based on reactions between the amine groups on the TAPP or TAPB molecules. An investigation of the self-assembly of these molecules, deposited at room temperature, on different metal surfaces was carried out to investigate the effect of intermolecular and molecule-surface interactions. The surface elevated at different temperature was employed to investigate the formation of networks through the polymerization of these molecules at various substrate temperatures. Polymerisation of the TAPP molecules is expected to form networks with a four-fold symmetry networks whereas the reaction among TAPB molecules would gave three-fold symmetry networks. Further investigations were carried out on a polyimidisation reaction between the amine molecules and the anhydride groups present on 3,4,9,10-perylenetetracarboxylic dianhydride (PTCDA). All samples were studied in detail using scanning tunneling microcopy (STM) and X-ray photoelectron spectroscopy (XPS) measurements to investigate the structural and chemical properties of the networks. In addition, ultraviolet photoelectron spectroscopy (UPS) and synchrotron based techniques were utilized in some of these studies. The ordering observed in the resulting structure is largely determined by the initial molecular coverage, substrate temperature, type of single crystal used and the deposition rate.

Keywords: Covalently bonded, amine reactions, STM, XPS, UPS.

Chapter 1:
Introduction and Literature Review.

1.0 Introduction.

The objective of this chapter is to discuss the motivation for this research project and to provide an outline of the thesis. A general literature review which includes a short explanation of self-assembly on surfaces and a discussion of different strategies to form covalent bonding of organic molecules on noble metal surfaces is presented. Finally, a brief description of porphyrin and porphyrin derivatives together with their electronic properties is presented.

1.1. Literature Review.

1.1.1. Supramolecular Chemistry and Self-Assembly.

Supramolecular chemistry has evolved in the past forty years as 'chemistry beyond the molecule'. Since then, supramolecular chemistry has progressed from the chemistry focusing on intermolecular non-covalent to covalent bonding interactions. Following the success of supramolecular chemistry, the molecular self-assembly concept achieved substantial attention as a key method for the 'bottom-up' fabrication of nano-scale functional structures [1,2]. For example, self-assembled porphyrin and graphitic nanotubes are interesting materials for surface patterning [3] and molecular electronics [4].

Molecular networks on surfaces are usually formed via different non-covalent bonding mechanisms such as hydrogen bonding [5-7], π-π stacking [3], van der Waals [8], metal-ligand [9] or dipole-dipole interactions [10]. Nonetheless, the physical and chemical properties of such networks for nanotechnology applications are deficient due to the weak bonding in these non-covalent chemical structures [11,12]. In order to circumvent this challenge, many strategies for the formation of covalently bonded structures have been reported and they are discussed in more detail below. Examples of these covalent bonding strategies are; bonding through thermal dissociation of halogen-carbon bonds [13-18]; bonding through dehydration of borate functionalised porphyrins [19-21] and imide formation by polycondensation reactions [22-24]. These covalently

bonded systems would display higher stability although the coordination is more difficult to control.

a) Covalent bonding through thermal dissociation of halogen-carbon bonds.

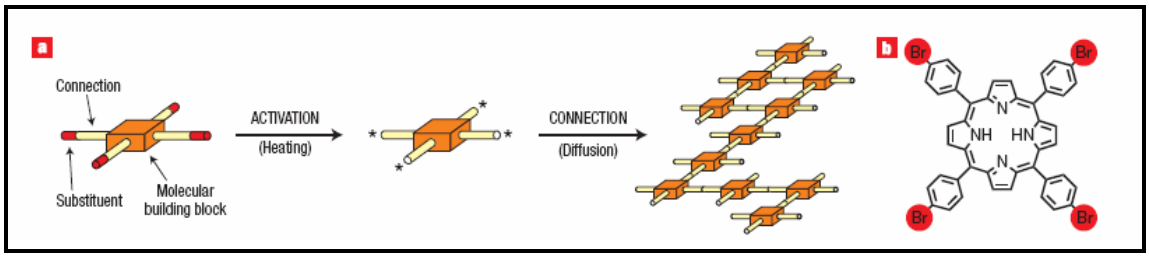

Fig. 1.1 Nano-architectures of covalently bound Br_4TPP molecular networks. (a) Concept of the formation of covalently bound networks by connecting activated molecular building blocks (b) Chemical structure of the Br_4TPP molecule (substituent Br atoms are highlighted in red) [13].

Grill *et al.* and other groups [13-15] have reported that covalently bound molecular nanostructures can be produced on noble metals upon thermal activation of porphyrin building blocks. Grill *et al.* have developed macromolecular structures with controlled shape and size that are based on small molecular building blocks with reactive side groups (legs) that form permanent chemical bonds at pre-defined connection points. According to this report, these covalent bonds could facilitate efficient charge transport [25] and have high stability [26]. In their case study tetra(4-bromophenyl) porphyrin (Br_4TPP), Figure 1.1(b) was selected as the carbon–halogen bonds exhibit much smaller binding energies compared with the central framework. Also, this molecule is chemically stable and mobile [12,27] on metal surfaces which is crucial for efficient intermolecular bond formation. Bromine was employed at each leg as the labile substituent atom to be detached in a controlled manner. This mechanism is depicted in Fig. 1.1. In the initial step the halogen atoms are dissociated by heating, and subsequently, the monomer building blocks are attached to each other via the activated legs by thermal diffusion directly on the surface. There are a number of groups who have studied 1,3,5-tris(4-bromophenyl)benzene (Fig. 1.2) on the noble metals [16-18]. They successfully formed extended two-dimensional covalently bonded networks. At this stage, the networks formed are disordered, containing various pore sizes due to different polygon sizes.

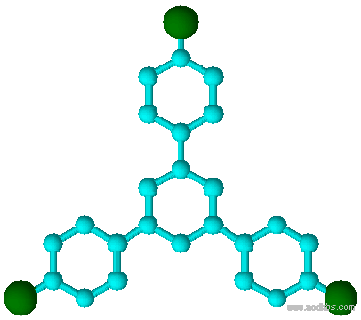

Fig. 1.2 The chemical structure of 1,3,5-tris(4-bromophenyl)benzene(TBB). In the molecular representation, light blue balls are carbon atoms and green balls are bromine.

b) Covalent bonding through dehydration of boronate functionalised molecules.

Zwaneveld *et al.* and other research groups [19-21] have employed a boronate-based chemistry that has formerly been revealed to be efficient for the synthesis of highly ordered three-dimensional covalent organic frameworks (COFs) and applied it in two-dimensional network formation on metallic surfaces. They have presented the first example of surface covalent organic frameworks (SCOFs) extended to near-complete monolayer coverage. One of the SCOF examples presented by Zwaneveld *et. al.* is through the molecular dehydration of 1,4-benzenediboronic acid (BDBA) with three boronic acid molecules reacting to form a six-membered B_3O_3 (boroxine) ring on Ag(111) with water elimination (see Fig. 1.3) [15]. In this work, they demonstrated the feasibility of forming surface covalent organic frameworks of varying pore sizes and a network displaying an extended array on a large area and the high temperature stability to conduct further functionalisation. These properties are necessary for advanced application in the patterning of nanoscopic arrays of magnetic, catalytic or electronic devices. One of the recent examples of functionalisation work has been reported by Clair *et al.* [28]. They have created a surface pattern of Fe islands through a sequential construction of self-assembled molecular systems by following the principles of nano-lithography. The positive mask was initially formed from the island growth mode of NaCl on Ag(100). BDBA molecules were deposited and they formed 2D-polymerized networks which were used as a negative mask. The NaCl mask was then removed by thermal evaporation. After that, Fe was deposited on the exposed area on Ag(100). Various configurations Fe/polymer including polymer nano-ribbons were produced in this work.

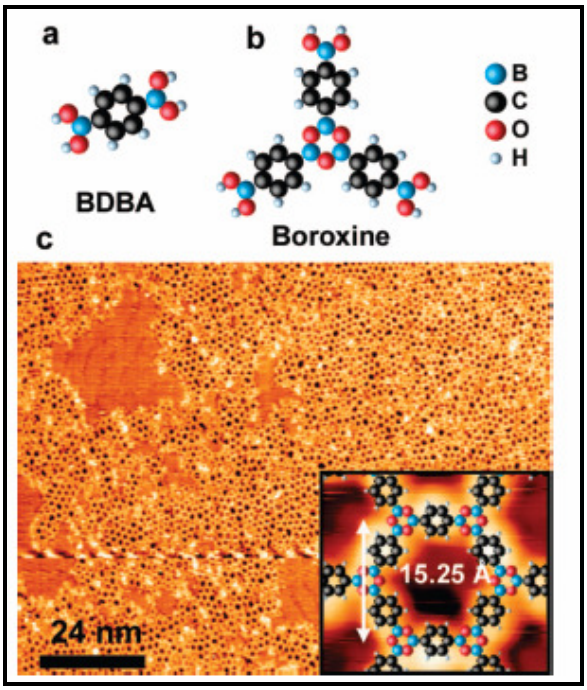

Fig. 1.3 SCOF-1 formed from BDBA deposition on Ag(111): (a) the chemical structure of BDBA; (b) the chemical structure of the boroxine repeat unit formed from dehydration of 3 BDBA monomers; (c) STM image (120 nm × 90 nm) of near-complete monolayer SCOF-1 film. The tunnelling conditions were I = 0.4 nA, V= -2.1 V. The inset shows the overlaid chemical structure obtained by DFT calculation [19].

c) Imide formation by polyimidisation reactions.

Polyimides (PIs) are a group of high-performance polymers possessing the cyclic imide and aromatic groups in the main polymer chains [29]. Currently, they are used in microelectronics, photonics, optics, and aerospace industries for their excellent thermal stability, good mechanical properties, low dielectric constant, low coefficient of thermal expansion, and high radiation resistance [29]. The basic reaction takes place when dianhydrides are reacted with amines under a dehydration process to form imides or iso-imides. This process is called an imidisation process. The amine initially attacks the anhydride to produce amic acid as an intermediate product. Subsequent removal of water results in the formation of an imide or iso-imide (see Fig. 1.4).

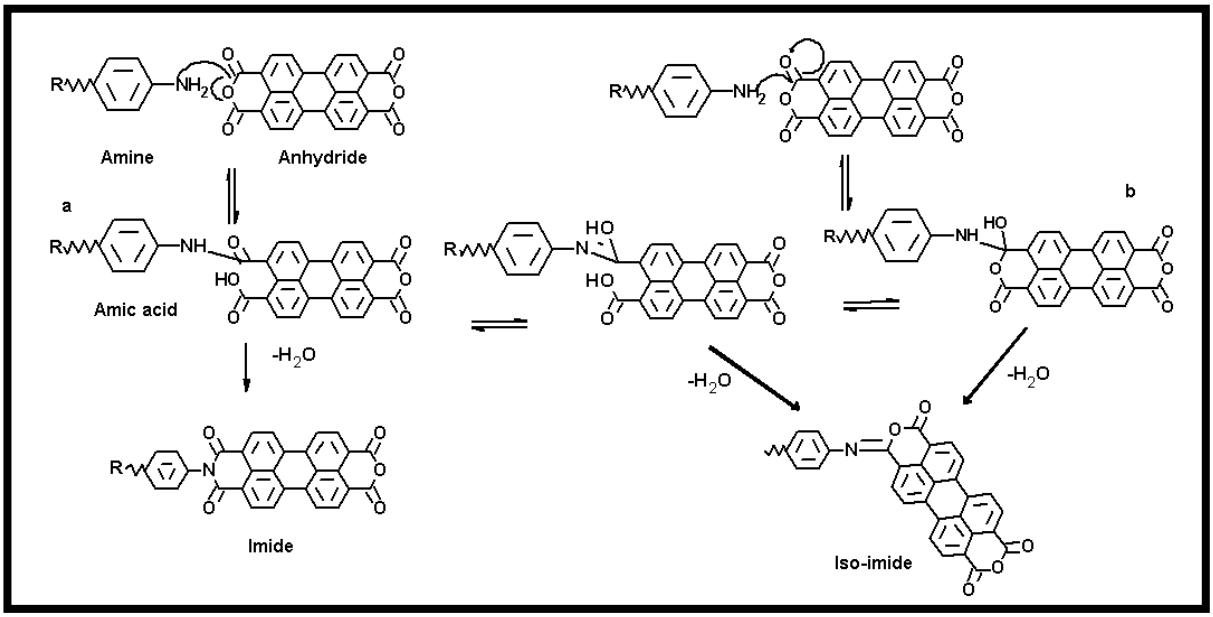

Fig. 1.4 Basic reaction of amine and anhydride to form an imide and an iso-imide.

The reaction described above is therefore a good prospective candidate for covalent surface-supported networks. This approach was first reported by Treier *et al.* [22,24] and Weigelt *et al.* [30]. Treier *et al.* used 4,4′-diamino-*p*-terphenyl (DATP) or 2,4,6-tris(4-aminophenyl)-1,3,5-triazine (TAPT) molecules to react with 3,4,9,10-perylene tetracarboxylic-dianhydride (PTCDA). They have shown that the condensation reaction between diamines and dianhydrides resulted in the formation of polyimides on Au(111). Weigelt *et. al.* used a similar approach with either octylamine or trioctylamine reacting with 1, 6-diaminohexane to form a covalently interlinked aldehyde and an amine when they were co-adsorbed on a Au(111) surface under UHV conditions. In this project, imide condensation reactions between a 3,4,9,10 perylenetetracarboxylic dianhydride (PTCDA) precursor and a porphyrin molecule functionalized with an amine group are investigated. This study is then extended to an investigation of the reaction of 1,3,5-tris(4-aminophenyl)benzene (TAPB) with PTCDA on different noble metal surfaces.

1.2. Porphyrin and Porphyrin Derivatives.

Porphyrins and metallo-porphyrins are very robust, polyfunctional and readily available with a range of different electronic and steric properties [31]. The name ‘porphyrin’ originates from the Greek word for purple. These molecules are deeply coloured due to the highly conjugated macrocycle. The general chemical structure of tetraphenyl porphyrin (TPP) molecules is shown in Fig. 1.5. Tetraphenyl porphyrin is a heterocyclic macromolecule which has four modified pyrrole subunits interconnected at the *meso*, α

carbon atoms, via =CH- linkages, which allow rotation of the C-H bond and this can result in a reduction of symmetry [31]. The macrocycle is an aromatic molecule which follows the Huckel's Rule, that is, the number of π electrons is equals to $4n+2$, where n is zero or positive integer, that are delocalized over the macrocycle. In the case of the porphyrin macrocycle there are 26 π electrons, including the four π electrons due to the lone pair electrons on the pyrrolic nitrogen atoms. The centre of the macrocycle can host two hydrogen atoms bonded to opposite nitrogen atoms (a free-base porphyrin) or a metallic ion (metallo-porphyrin).

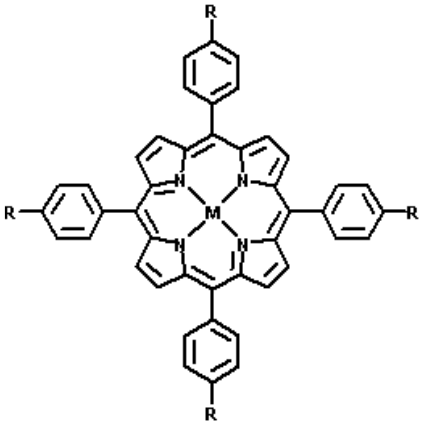

Fig. 1.5 Chemical structure of TPP. The molecules have an inner porphyrin core which hosts a metallic centre (M) or two hydrogen atoms. Attached to the core are phenyl rings, which are terminated by H or by an additional substituent R (R =amino group, NH_2 in this project).

Metallo-porphyrins are porphyrin molecules that bind with metal ions such as Fe, Zn, Cu, Ni and Co. Many porphyrin derivatives including metallo-porphyrins, are found in nature. Over the last two decades, metallo-porphyrins have been effectively used as models for the cytochrome P-450 enzyme, with respect to the oxidation of organic compounds such as hydrocarbons [32]. Examples of Fe-porphyrin include hemoproteins, haemoglobins in blood and the cytochrome enzymes that exist in small quantities in most cells and play a vital role in the oxidative process. Hemoproteins have many biological functions such as oxygen transport and electron transfer. Some other examples are photosynthetic chlorophylls of higher plants and vitamin B-12 which have magnesium and cobalt ions respectively in the porphyrin macrocycle. Chlorophyll is important for photosynthesis that allows plants to obtain energy from light and vitamin B-12 is crucial in the metabolism of the cell in our body. Taking into account the capabilities and role of porphyrin in the photosynthetic systems, it could be employed to mediate visible photon–electron energy transfer processes [33]. With this basis, the

metallo-porphyrin has great potential in the function of opto-electronics, data storage, solar cells and gas sensors [34].

1.2.1. Electronic Properties of Porphyrins and Porphyrin Derivatives.

The electronic properties of porphyrin molecules can be broadly explained through Gouterman's theory, also known as the four-orbital model. This theory originates from the simple Hűckel theory and only accounts for the two highest occupied (with electrons) molecular orbitals (HOMOs) of a porphyrin molecule and the two lowest unoccupied molecular orbitals (LUMOs) [35]. The model of Gouterman's Theory in the zinc octaethylporphyrin investigation by Anderson is illustrated in Fig.1.6 [33]. This diagram (Fig. 1.6) shows two π orbitals (a_{1u} and a_{2u}) and a degenerate pair of π^* orbitals (e_{gx} and e_{gy}). In this zinc octaethylporphyrin example, the two highest occupied π orbitals have almost the same energy. The transitions from a_{1u} to e_g and a_{2u} to e_g would result in two bands with very different intensities and wavelengths which are labelled as the Soret (B) and Q bands. This is discussed in detail in Ref. [40]. Therefore, the HOMO-LUMO gap can be tuned by varying the metal ions that bind in the centre of the macrocycle or by adding substituents such as phenyl rings functionalised with, for example, Br or -NH_2 attached to the *meso* site of the porphyrin. Some example studies on metallo-prophyrins such as 5,10,15,20-tetrakis-(4-bromophenyl)-porphyrin-Co (TBrPP-Co) on Ag/Si(111) [36], 3,5-di(*tert*-butyl)phenyl and the 3-cyanophenyl substituents on Ag(111)[27] or tertiary butyl-phenyl substituted Pt-porphyrin (-Pt-TBPP)on Ag(110) [37] are reported for various applications.

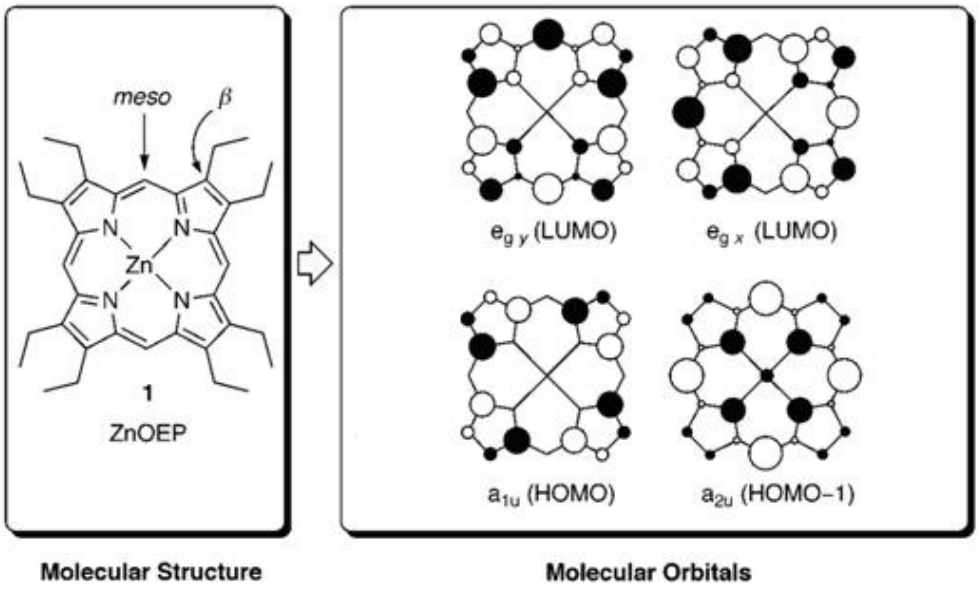

Fig. 1.6 The four Gouterman molecular orbitals explain the absorption spectra of simple porphyrins, such as zinc octaethylporphyrin [33].

1.3. Motivation.

The motivation for this project is to form covalently bonded nano-networks because they are chemically and mechanically more stable than those based on hydrogen bonded [5,6,38] or metal-organic frameworks [39-41]. Non-covalent organic networks have low binding energies and these self-assembled networks are often unstable at high temperatures. In recent years, covalent organic networks based on a variety of thermally induced chemical reactions on noble metals (Au(111), Ag(111), Cu(111)) have been investigated extensively [13-17,19-21]. In addition to understanding and gaining fundamental knowledge of these self-assembly and polymerization processes, this work also has potential applications especially in the areas of sensor [42] and photovoltaic cell research [43,44]. To date, device miniaturization has been based primarily on 'top-down' approaches using lithographic techniques. However, these techniques are limited by the wavelength of light used and thus, it is vital to search for new paths to create functional nano devices on surfaces. One possible method is to investigate 'bottom-up' approaches and this 'bottom-up' approach is employed in the current research project with the intention to form covalently bonded nano-networks. The ability to tackle this challenge will open up another level of research in the surface and nanoscience fields.

1.4. Outline of the Thesis.

This thesis focuses on investigations of the growth and ordering of 5,10,15,20-tetrakis(4-aminophenyl) porphyrin (TAPP) and 1,3,5-tris(4aminophenyl)benzene (TAPB) molecules on noble metals under UHV conditions to form covalently bonded nano-networks. These investigations were further extended to include bi-molecular films containing 3,4,9,10-perylene tetracarboxylic dianhydride (PTCDA) for polyimidisation reactions to form covalently bonded networks. A number of experimental techniques are used in the course of this research to characterize the molecular films. Scanning tunnelling microscopy (STM) is used to image the adsorbed molecules, providing information about their orientation and conformation on the surface. X-ray photoelectron spectroscopy (XPS) is used to investigate the core levels of the investigated materials. Ultraviolet photoelectron spectroscopy (UPS) is utilised to examine the valence bands and the work function of the studied systems. Additional measurements such as low energy electron diffraction (LEED) and synchrotron based techniques such as X-ray absorption spectroscopy (XAS) and soft XPS measurements are also employed to complement the STM results.

In Chapter 2, the experimental methods employed and the basic principles of scanning tunnelling microscopy (STM), X-ray photoelectron spectroscopy (XPS), ultraviolet photoelectron spectroscopy (UPS), synchrotron techniques, X-ray absorption (XAS) and low energy electron diffraction (LEED) are presented. In Chapter 3, a detailed investigation of the self–assembly and polymerisation of 5, 10, 15, 20-tetrakis(4-aminophenyl)porphyrin (TAPP) molecules on the Au(111), Ag(111) and Cu(111) surfaces are described. Two experimental approaches pursued in this work are described: (i) molecular deposition on substrates held at room temperature and subsequent annealing; and (ii) molecular deposition on substrates held at elevated temperatures. An ultraviolet photoelectron spectroscopy (UPS) study of TAPP growth and polymerisation on Au(111) and Cu(111) surfaces is presented in Chapter 4. In Chapter 5, the growth and ordering of 3, 4, 9, 10-perylene tetracarboxylic dianhydride (PTCDA) films, and the polyimidisation reaction to form covalently bonded networks between TAPP and PTCDA on Au(111) are described. In Chapter 6, a detailed study of 1,3,5-tris(4aminophenyl)benzene (TAPB) molecules deposited on Au(111) and Ag(111) surfaces is described. This investigation was extended to include bi-molecular films containing TAPB and PTCDA in an attempt to form covalently bonded networks of these compounds on Ag(111). Finally, conclusions and future research directions are described and proposed in Chapter 7.

References:

[1] J. Lehn. *Toward Self-Organization and Complex Matter,* Science. **295** (2002) 2400.

[2] J.M. Lehn. *From supramolecular chemistry towards constitutional dynamic chemistry and adaptive chemistry,* Chem. Soc. Rev. **36** (2007) 151.

[3] R. van Hameren, P. Schon, A.M. van Buul, J. Hoogboom, S.V. Lazarenko, J.W. Gerritsen, H. Engelkamp, P.C.M. Christianen, H.A. Heus, J.C. Maan. *Macroscopic hierarchical surface patterning of porphyrin trimers via self-assembly and dewetting,* Science. **314** (2006) 1433.

[4] J.P. Hill, W. Jin, A. Kosaka, T. Fukushima, H. Ichihara, T. Shimomura, K. Ito, T. Hashizume, N. Ishii, T. Aida. *Self-Assembled hexa-peri-hexabenzocoronene graphitic nanotube,* Science. **304** (2004) 1481.

[5] J.A. Theobald, N.S. Oxtoby, M.A. Phillips, N.R. Champness, P.H. Beton. *Controlling molecular deposition and layer structure with supramolecular surface assemblies,* Nat. **424** (2003) 1031.

[6] M. Stöhr, M. Wahl, C.H. Galka, T. Riehm, T.A. Jung, L.H. Gade. *Controlling Molecular sssembly in two dimensions: The concentration dependence of thermally induced 2D aggregation of molecules on a metal surface,* Angew. Chem. Int. Ed. **44** (2005) 7394.

[7] D.L. Keeling, N.S. Oxtoby, C. Wilson, M.J. Humphry, N.R. Champness, P.H. Beton. *Assembly and processing of hydrogen bond induced supramolecular nanostructures,* Nano Lett. **3** (2003) 12.

[8] M. Schunack, L. Petersen, A. Kühnle, E. Lægsgaard, I. Stensgaard, I. Johannsen, F. Besenbacher. *Anchoring of organic molecules to a metal surface: HtBDC on Cu (110),* Phys. Rev. Lett. **86** (2001) 456.

[9] N. Lin, A. Dmitriev, J. Weckesser, J.V. Barth, K. Kern. *Real-time single-molecule imaging of the formation and dynamics of coordination compounds,* Angew. Chem. Int. Ed. **41** (2002) 4779.

[10] K. Morgenstern, E. Laegsgaard, I. Stensgaard, F. Besenbacher, M. Böhringer, W.D. Schneider, R. Berndt, F. Mauri, A. De Vita, R. Car. *Stability of two-dimensional nanostructures,* Appl. Phys. A. **69** (1999) 559.

[11] G.M. Whitesides, B. Grzybowski. *Self-assembly at all scales,* Science. **295** (2002) 2418.

[12] T. Yokoyama, S. Yokoyama, T. Kamikado, Y. Okuno, S. Mashiko. *Selective assembly on a surface of supramolecular aggregates with controlled size and shape,* Nat. **413** (2001) 619.

[13] L. Grill, M. Dyer, L. Lafferentz, M. Persson, M.V. Peters, S. Hecht. *Nano-architectures by covalent assembly of molecular building blocks,* Nat. **2** (2007) 687.

[14] C.M. Doyle, S.A. Krasnikov, N.N. Sergeeva, A.B. Preobrajenski, N.A. Vinogradov, Y.N. Sergeeva, M.O. Senge, A.A. Cafolla. *Evidence for the formation of an intermediate complex in the direct metalation of tetra (4-bromophenyl)-porphyrin on the Cu (111) surface,* Chem. Commun. **47** (2011) 12134.

[15] S.A. Krasnikov, C.M. Doyle, N.N. Sergeeva, A.B. Preobrajenski, N.A. Vinogradov, Y.N. Sergeeva, A.A. Zakharov, M.O. Senge, A.A. Cafolla. *Formation of extended covalently bonded Ni porphyrin networks on the Au (111) surface,* Nano Res. (2011) 1.

[16] J.C. Russell, M.O. Blunt, J.M. Garfitt, D.J. Scurr, M. Alexander, N.R. Champness, P.H. Beton. *Dimerization of tri (4-bromophenyl) benzene by aryl− aryl coupling from solution on a gold surface,* J. Am. Chem. Soc. (2011).

[17] M.O. Blunt, J.C. Russell, N.R. Champness, P.H. Beton. *Templating molecular adsorption using a covalent organic framework,* Chem. Commun. **46** (2010) 7157.

[18] R. Gutzler, H. Walch, G. Eder, S. Kloft, W.M. Heckl, M. Lackinger. *Surface mediated synthesis of 2D covalent organic frameworks: 1,3,5-tris(4-bromophenyl)benzene on graphite(001), Cu(111), and Ag(110),* Chem. Commun. (2009) 4456.

[19] N. Zwaneveld, R. Pawlak, M. Abel, D. Catalin, D. Gigmes, D. Bertin, L. Porte. *Organized formation of 2D extended covalent organic frameworks at surfaces.* J. Am. Chem. Soc. **130** (2008) 6678.

[20] R. Coratger, B. Calmettes, M. Abel, L. Porte. *STM observations of the first polymerization steps between hexahydroxy-tri-phenylene and benzene-di-boronic acid molecules,* Surf. Sci. **605** (2011) 831.

[21] O. Ourdjini, R. Pawlak, M. Abel, S. Clair, L. Chen, N. Bergeon, M. Sassi, V. Oison, J.M. Debierre, R. Coratger. *Substrate-mediated ordering and defect analysis of a surface covalent organic framework,* Phys. Revi. B. **84** (2011) 125421.

[22] M. Treier, R. Fasel, N.R. Champness, S. Argent, N.V. Richardson. *Molecular imaging of polyimide formation,* Phys. Chem. Chem. Phys. **11** (2009) 1209.

[23] M. Treier, M.T. Nguyen, N.V. Richardson, C. Pignedoli, D. Passerone, R. Fasel. *Tailoring low dimensional organic semiconductor nanostructures,* Nano Lett. **9** (2009) 126.

[24] M. Treier, N.V. Richardson, R. Fasel. *Fabrication of surface-supported low-dimensional polyimide networks,* J. Am. Chem. Soc. **130** (2008) 14054.

[25] A. Nitzan, M.A. Ratner. *Electron transport in molecular wire junctions,* Science. **300** (2003) 1384.

[26] A.P. Cote, A.I. Benin, N.W. Ockwig, M. O'Keeffe, A.J. Matzger, O.M. Yaghi. *Porous, crystalline, covalent organic frameworks,* Science. **310** (2005) 1166.

[27] H. Spillmann, A. Kiebele, M. Stohr, T.A. Jung, D. Bonifazi, F. Cheng, F. Diederich. *A two-dimensional porphyrin-based porous network featuring communicating cavities for the templated complexation of fullerenes,* Adv. Mater. **18** (2006) 275.

[28] S. Clair, O. Ourdjini, M. Abel, L. Porte. *Two‐dimensional polymer as a mask for surface nanopatterning,* Adv. Mater. (2012).

[29] M. Hasegawa, K. Horie. *Photophysics, photochemistry, and optical properties of polyimides,* Prog. Polym. Sci. **26** (2001) 259.

[30] S. Weigelt, C. Busse, C. Bombis, M.M. Knudsen, K.V. Gothelf, T. Strunskus, C. Woll, M. Dahlbom, B. Hammer, E. Laegsgaard, F. Besenbacher, T.R. Linderoth. *Covalent interlinking of*

an aldehyde and an amine on a Au(111) surface in ultrahigh vacuum, Angew. Chem. Int. Ed. Engl. **46** (2007) 9227.

[31] J. Brede, M. Linares, S. Kuck, J. Schwobel, A. Scarfato, S. Chang, G. Hoffmann, R. Wiesendanger, R. Lensen, P.H.J. Kouwer, J. Hoogboom, Rowan,A.E., Broring,M., M. Funk, S. Stafstrom, F. Zerbetto, R. Lazzaroni. *Dynamics of molecular self-ordering in tetraphenyl porphyrin monolayers on metallic substrates,* Nanotechnol. **20** (2009) 275602.

[32] M.A. Schiavon, Y. Iamamoto, O.R. Nascimento, M.d.D. Assis. *Catalytic activity of nitro- and carboxy-substituted iron porphyrins in hydrocarbon oxidation: Homogeneous solution and supported systems,* J. Mol. Catal. A: Chem. **174** (2001) 213.

[33] H.L. Anderson. *Building molecular wires from the colours of life: conjugated porphyrin oligomers,* Chem. Commun. **23** (1999) 2323-2330.

[34] A. Tsuda, A. Osuka. *Fully Conjugated Porphyrin Tapes with Electronic Absorption Bands That Reach into Infrared,* Science. **293** (2001) 79.

[35] LR Milgrom, **The Colours of Life**, An Introduction to the Chemistry of Porphyrins and Related Compounds, Oxford University Press, Oxford, 1997.

[36] Q. Li, S. Yamazaki, T. Eguchi, Y. Hasegawa, H. Kim, S. Kahng, J.F. Jia, Q.K. Xue. *Adsorption, manipulation and self-assembling of TBrPP-Co molecules on a Ag,* Nanotechnol. **19** (2008) 465707.

[37] T. Yokoyama, Y. Tomita. *Temperature dependence of conformation and self-assembly of Pt-TBPP on Ag(110),* J.Chem.Phys. **129** (2008) 164704.

[38] D. Keeling, N. Oxtoby, C. Wilson, M. Humphry, N. Champness, P. Beton. *Assembly and processing of hydrogen bond induced supramolecular nanostructures,* Nano Lett. **3** (2003) 9.

[39] R. Decker, U. Schlickum, F. Klappenberger, G. Zoppellaro, S. Klyatskaya, M. Ruben, J. Barth, H. Brune. *Using metal-organic templates to steer the growth of Fe and Co nanoclusters,* Appl. Phys. Lett. **93** (2008) 243102.

[40] A. Dmitriev, H. Spillmann, N. Lin, J.V. Barth, K. Kern. *Modular assembly of two-dimensional metal-organic coordination networks at a metal surface,* Angew. Chem. Int. Ed. **42** (2003) 2670.

[41] L. Bartels. *Tailoring molecular layers at metal surfaces,* Nat. Chem. **2** (2010) 87.

[42] F. Davis, S.P.J. Higson. *Structured thin films as functional components within biosensors,* Biosens. Bioelectron. **21** (2005) 1.

[43] P. Margaron, M.J. Grégoire, V. Ŝĉasnár, H. Ali, J.E. Lier. *Structure‐photodynamic activity relationships of a series of 4‐substituted zinc phthalocyanines,* Photochem. Photobiol. **63** (1996) 217.

[44] K.A. Hahn, M. Panjehpour, X. Lu. *Fluence‐Dependent induction of micronuclei by aluminum phthalocyanine tetrasulfonate‐Mediated photodynamic therapy,* Photochem. Photobiol. **63** (1996) 117.

Chapter 2:
Methodologies.

2.0 Experimental Methods.

This chapter describes the experimental apparatus, sample preparation procedures and the theoretical background for the techniques employed in this research project. The emphasis is mainly focused on scanning tunnelling microscopy (STM), together with a description of low-energy electron diffraction (LEED), X-ray photoelectron spectroscopy (XPS), ultraviolet photoelectron spectroscopy (UPS) and synchrotron techniques. The synchrotron techniques include photoelectron spectroscopy (PES) and X-ray absorption spectroscopy (XAS).

2.1 The Ultra High Vacuum (UHV) System.

The UHV system employed is an Omicron (Omicron Nanotechnology GmBH, Germany) vacuum system as depicted in Fig. 2.1. It comprises three different chambers: an analysis chamber (1)* a sample preparation chamber (2) and an STM chamber (3). The analysis chamber is equipped with a Vacuum Generators sample manipulator and heater (11) and houses the STM, LEED and XPS instruments. The preparation chamber is equipped with a VG sample manipulator (11) with a heating stage, an Argon Ion Gun (Omicron ISE5) which is used for cleaning the single crystal samples and several home-made evaporators for molecular deposition. The preparation and analysis chambers are pumped by ion pumps (9) equipped with titanium sublimation pumps (TSP) (10). The analysis chamber is separated from the preparation chamber by a manual gate valve (7). Both chambers have a base pressure below 1×10^{-10} mbar**.** A turbo molecular pump is used to pump down both the analysis and preparation chambers. In addition samples and STM tips can be transferred into the vacuum system from atmosphere through a fast entry load-lock (FEL) (4). Sample transfer between the FEL, preparation chamber and analysis chamber is performed using two linear magnetic transfer drives (13). Transfer from the analysis manipulator to the STM sample stage is performed using a wobble stick (12) in the STM chamber.

* number in the bracket refer to the items in Fig. 2.1.

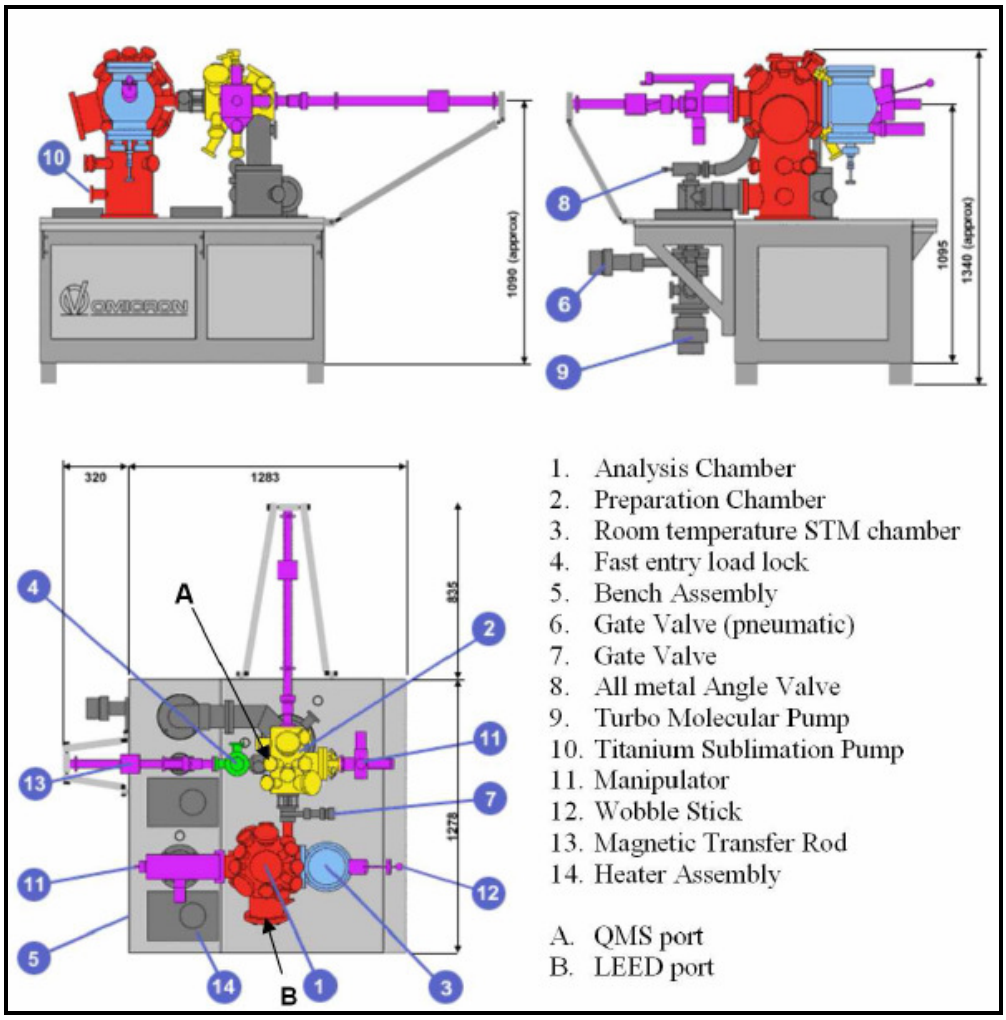

Fig. 2.1 The Omicron UHV system shown in plane and elevation [1,2]*: the preparation chamber (yellow), the analysis chamber (red), the fast entry load lock (green) and the STM chamber (light blue).*

2.2 Scanning Tunnelling Microscopy (STM).

The scanning tunnelling microscope (STM) developed by Binnig, Rohrer, Gerber and Weibel at the IBM Rüschlikon laboratory in the 1980s [3], has proven to be one of the most widely used techniques in surface science over the past three decades. [4].The birth of STM was officially recorded on the 16th of March 1981 when the first recorded log[I(*I*-s)] spectra showed an exponential dependence of the tunnel current *I* on the tip-surface separation using a tungsten tip and a platinum sample [5]. The real breakthrough for STM however was achieved when the same group obtained the first atomic resolution image of the Si (111) 7×7 surface [3,5]. Since then, STM has expanded into an imaging and spectroscopic method with diverse potential for real spacing imaging on scales that extend to atomic resolution [6].

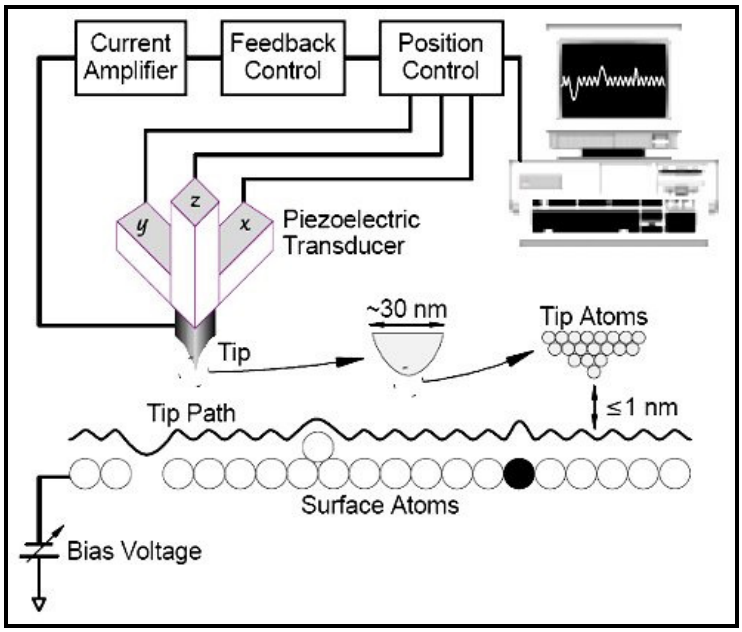

Fig. 2.2 Basic STM set up [7].

The basis of operation of the STM is the exponential dependence of the quantum mechanical tunnelling current on the width of the barrier between the STM tip and the sample. The tunnelling current is confined to a filament between the apex of the tip and the surface under investigation [6] (see Fig. 2.2). The tunnelling current reduces by approximately an order of magnitude for every increase of 0.1 nm in the tip-sample distance and the effective diameter of the filament, L_{eff}, can become extremely small for a pointed tip. However, in the case of a single atom at the apex, L_{eff} decreases to atomic dimensions. STM can thus obtain lateral and height resolutions of 0.1 nm and 0.01 nm respectively. The basic principles of STM operation and a description of the STM unit that was employed in the current work, including the tip preparation procedures, are discussed in the following sub-sections.

2.2.1 Basic Operational Principles.

This report is primarily concerned with imaging molecules on surfaces. To this end, the STM is a powerful technique as it permits the characterisation and imaging of individual molecules with sub molecular resolution and can also be used to obtain information about the electronic and, in low temperature STM, the vibrational structure of the molecule [8]. The basic physical process can be described using a one-dimensional tunnelling model is as shown in Fig. 2.3.

In classical mechanics, the energy of an electron in a potential U(z) is described by

$$E = \frac{p^2}{2m} + U(z) \qquad \textit{Eqn. 2.1}$$

where m is the electron mass and E is the energy. In regions where $E>U(z)$,the electron has a non-zero momentum $p = [2m(E-U)]^{1/2}$. On the other hand, the electron cannot penetrate into the potential barrier region if $E < U(z)$.

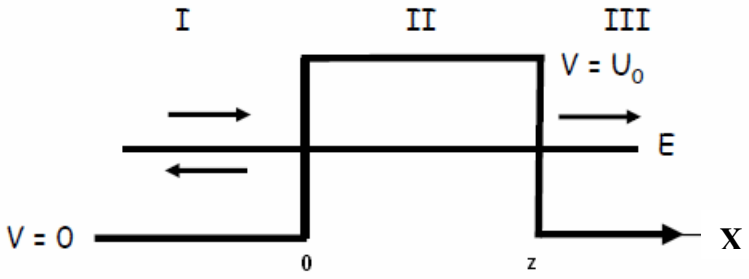

Fig. 2.3 1-D Tunnelling model.

However, in quantum mechanics, the energy levels $\psi_n(z)$ of the electrons are described by solutions of the Schrödinger equation,

$$-\frac{\hbar^2}{2m}\frac{\partial^2\psi_n(z)}{\partial z^2} + U(z)\psi_n(z) = E\psi_n(z) \qquad \textit{Eqn. 2.2}$$

where $\hbar$ is the reduced Planck's constant, z is the electron position, *d is* the barrier width and m is the electron mass.

In the classically allowed region where $E > U(z)$, the solution of Equation 2.2 is

$$\psi_n(z) = \psi_n(0)e^{\pm ikz},$$

where

$$k = \frac{\sqrt{2m(E-U(z))}}{\hbar} \qquad \textit{Eqn. 2.3}$$

is the wave vector. The electron moves (in either a positive or negative direction) with a constant momentum $p = \hbar k$. However, in the classically forbidden region where $E < U(z)$, Equation. 2.2 has a solution

$$\psi_n(z) = \psi_n(0)e^{\pm \kappa z},$$

where

$$\kappa = \frac{\sqrt{2m(U-E)}}{\hbar} \qquad \textit{Eqn. 2.4}$$

is the wave vector inside the barrier region. This describes an electron penetrating through the barrier in the $+z$ direction. The probability density, $|\psi(z)|^2$ of observing an electron near a point z is proportional to $e^{-2\kappa z}$, which has a non-zero value inside the potential barrier. The other solution, $\psi(z) = \psi(0)e^{\kappa z}$, describes an electron state decaying in the $-z$ direction, suggesting that the tunnelling is bidirectional [9].

With this model, the basic features of metal-vacuum-metal tunnelling (Fig. 2.4) are introduced. The work function, ϕ, of a metal is defined as the minimum energy required to remove an electron from the bulk to the vacuum level. Generally, the work function depends on the material and the crystallographic orientation of the surface. The Fermi level is the highest occupied states in a metal. By taking the vacuum as the reference point of the energy, we have $E_F = -\phi$.

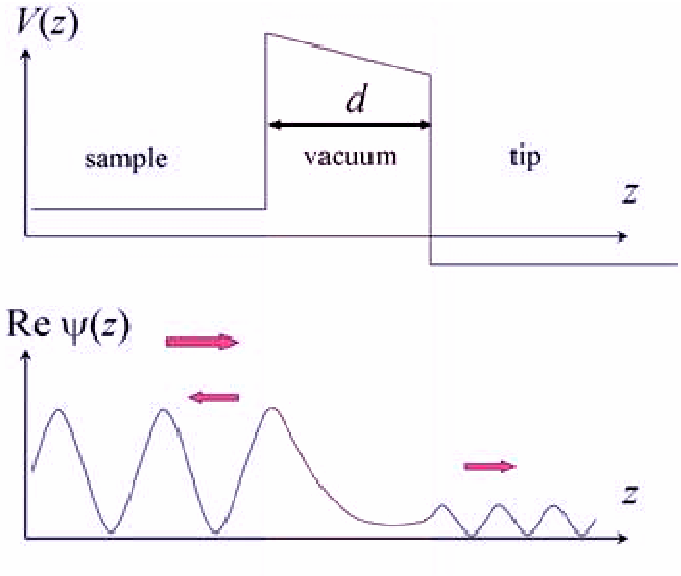

Fig. 2.4 Schematic of the potential energy of an electron incident on the sample. The electrons are free to move in either electrode and the wave function is an oscillatory function. In the barrier region, the wave function is exponentially decaying and explains the similar dependence of the tunnelling current on barrier width [10].*d is the distance between the sample and the tip.*

A net tunnelling current occurs when a bias voltage is applied. A sample state ψ with energy level E lying between $(E_F\text{-}eV)$ and E_F has a finite probability of tunnelling into

the tip with the assumption that the bias is much smaller than the value of the work function, $eV<<\phi$. The energy levels of all the states of interest are very close to the Fermi level, $E \approx -\phi$. Hence, the ratio of the tunnelling current at the tip surface z to the impinging current at z = 0 is defined as a transmission coefficient, T.

$$T \equiv \frac{I(z)}{I(0)} = e^{-2\kappa z} \qquad \textit{Eqn. 2.5}$$

where $\kappa = \frac{\sqrt{2m\phi}}{\hbar}$ is the decay constant of a sample state near the Fermi level in the barrier region [9].

In 1961, J. Bardeen discussed the tunnelling process through the vacuum region between two metal plates as depicted in Fig. 2.5. He divided it into two independent subsystems instead of solving the Schrődinger equation for the whole system. In this one-dimensional theory the specific geometry of the gap is ignored. Fermi's golden rule explains the transition rate between two quantum states, and gives the probability of an electron to elastically tunnel between a sample state at the surface and a tip state. The tunnelling current I is directly proportional to the number of sample states at the surface within the energy interval eU. Using Bardeen's approach, the tunnel current can be approximated as (with the Fermi energy $E_F = 0$)

$$I \propto \int_0^{eU} dE \rho_t(E - eU)\rho_s(E)T(E, eU, d) \qquad \textit{Eqn. 2.6}$$

where U is the small applied bias voltage (with respect to the tip), ρ_t and ρ_s are the electronic densities of states for the tip and the sample, respectively, and T(E, eU, d) is the transmission coefficient.

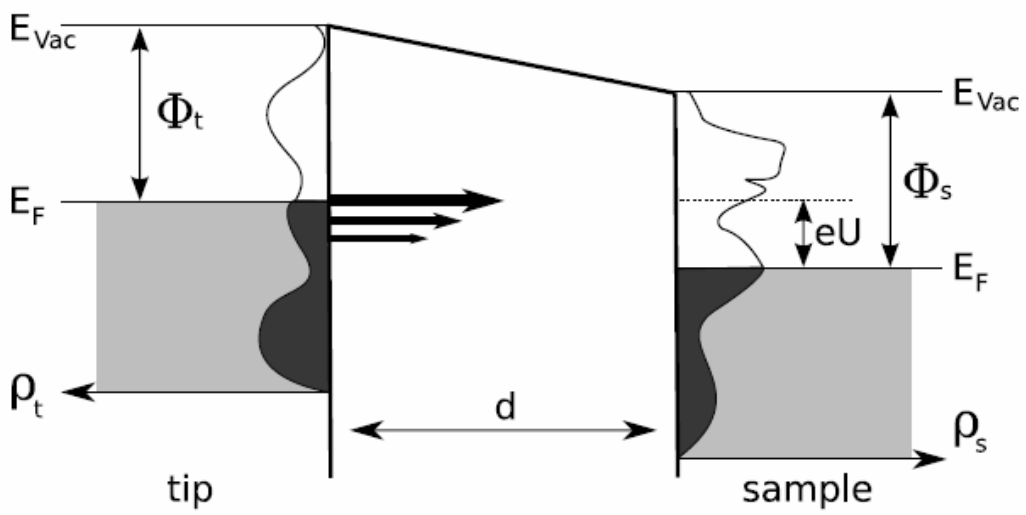

Fig. 2.5 One-dimensional schematic energy diagram for tunnelling from tip (grounded) to sample (positive bias voltage U applied). ρ_a, ρ_s *indicates the density of states and* ϕ_t *and* ϕ_s *the work function for the tip and the sample respectively. The sizes of the arrows in the gap indicate that the probability for tunnelling has its maximum at* $E = eU$ [11].

2.2.2 Scanning Tunnelling Microscopy: Apparatus.

The STM used in this work comprises an atomically sharp tip, a piezoelectric tube scanner, a vibration isolation system, and a tunnelling current feedback controller. It is placed in a UHV environment in order to keep the sample atomically clean. The tip is an electrochemically etched wire, usually tungsten (W) or platinum iridium alloy (Pt/Ir).

The STM has a coarse approach mechanism which brings the tip into tunnelling range of the surface as illustrated in Fig 2.6. Once in range, a cylindrical piezoelectric transducer permits the controlled vertical and lateral positioning of the tip and rastering of the tip over the sample surface. The tip is positioned in a magnetic holder at the top of this piezoelectric transducer tube. The outer surface of the tube is separated into four electrodes, while the inner surface has a single electrode. Lateral motion of the tip (*x* or *y* direction) is achieved by providing equal and opposite voltages to two opposing vertical outer electrodes while keeping the other two outer electrodes grounded or at a constant voltage. Vertical motion (z direction) is achieved by providing the same voltage to the four outer electrodes while grounding the inner electrode, thus causing the tube to expand or contract.

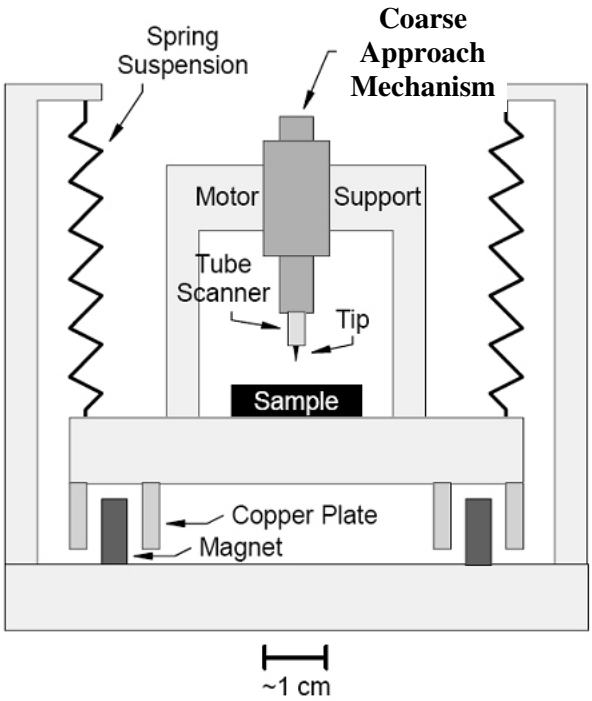

Fig. 2.6 Common elements of an STM, including a tip mounted on a piezoelectric tube scanner, a coarse approach mechanism and a damped vibration isolation system [7].

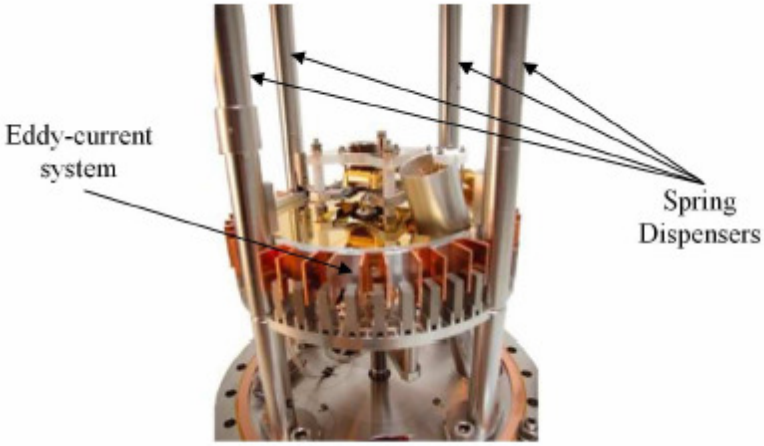

Fig. 2.7 Omicron damping system consisting of Eddy-current damping system combined with support four springs [1].

Vibrational noise is detrimental to the atomic resolution during the scanning process, since the typical corrugation amplitude on an atomic surface is in the order of an Angstrom or less. In the Omicron STM, passive damping is achieved by using adjustable viscoelectric blocks that are placed between the platform supporting the UHV system and the floor. Additionally, the STM is equipped with metal springs that support the STM table. In turn the table is equipped with an Eddy-current damping system comprising of copper elements and permanent magnets (see Fig. 2.7) which provides additional vibrational isolation.

There are two scanning modes that are commonly employed in STM; constant current mode and constant height mode. In constant current mode the feedback signal is used to adjust the height of the tip at each point in the x-y rastering in order to maintain a constant tunnel current. In the constant height mode, the tip is rastered over the surface at a fixed height. The measured tunnel current changes in response to changes in the tip-sample separation during the scanning process. These current changes are recorded and converted into a topographic surface image. The advantages of constant height mode are that it is much faster than constant current mode, since the height of the tip is not constantly changing to meet a pre-set current value; and it is less susceptible to low frequency noise because of the fast scanning. However, if the surface is rough the height differences can be large enough to cause the tip to crash into the surface. In this case, the constant current mode is more favourable and is the most commonly used scan mode.

2.2.3 Preparation of STM Tip.

The preparation of STM tips is an important step in STM work. There are many methods such as electrochemical-etching [12,13], ion milling, vapour deposition and electron beam deposition (EBD) [14] reported in the literature for tip preparation. The art of preparing a good tip still remains a great challenge for STM users. An STM tip should be free from oxides, extremely sharp and without mini-tips in order to achieve atomic resolution.

Tip preparation procedures are divided into two main methods: mechanical and physicochemical processes. Mechanical procedures include cutting, machining and fragmenting metal wires to form sharp tips. Mechanically prepared tips often suffer from poor reproducibility, lack of tip symmetry, large cone angle, and multiple tip formation [14]. Such tips will produce non representative images of the real surface and hence, mechanically produced tips can suffer from poor imaging capability. However, mechanical processes can be used on many different materials, including non oxidizing metals such as gold and platinum/iridium alloys, avoiding contamination issues which can arise with electrochemical methods.

Electrochemical etching can be used on a number of metals, and generally offers more reproducible results than mechanical methods. Tungsten tips have a high melting temperature, great mechanical strength, relatively low cost and simplicity of fabrication

using the electrochemical etching technique [12]. The drawback of using tungsten is its poor resistance to oxidation, as the tungsten tip is prone to surface contamination. Nonetheless, tungsten tips usually produce good images after an *in situ* cleaning process which involves pulsing the voltage on the tip while imaging a clean substrate. For this work, an Omicron electrochemical etching unit was used to prepare the tungsten tips. Tungsten tips were prepared by etching tungsten wire in high concentrations (2.5 M- 5.0 M) of sodium hydroxide (NaOH) or potassium hydroxide (KOH). They are then rinsed in deionised water and propanol before mounting in the STM. However, this step usually does not remove all of the contaminants which occur during the preparation process. Contaminants include water (H_2O), carbon monoxide (CO), hydrogen (H_2) , oxygen (O_2), hydrocarbons, etching residuals and tungsten oxide (WO_3) [13,15]. These oxides and contaminants can cause unstable tunnel currents. The tip looses some of its metallic behaviour, which could result in tip crashing during tip approaching processes in the STM and subsequently, it may also cause damage to the tip as well as to the surface under investigation. Many procedures to optimise the tip performance have been proposed. Some techniques are quite complex which use Ar^+ or Ne^+ ion bombardment [13], or controllable UHV annealing treatment [12]. Other simple methods include rinsing the tip with alcohol (ethanol, iso-propanol) or using low concentration of hydrofluoric acid (HF) [13] after rinsing with de-ionized water. This step can be repeated many times. The tip is then gently dried with clean compressed nitrogen gas. The objective for all of these procedures is to get a clean tip. Once the tip is confirmed clean and sharp by inspection in a microscope or camera, the tip is ready to be used in the STM.

2.3 X-ray Photoelectron Spectroscopy (XPS).

X-ray photoelectron spectroscopy (XPS), also known as Electron Spectroscopy for Chemical Analysis (ESCA), is a common and versatile technique used for the chemical characterisation of materials [16]. When a monochromatic beam of X-rays is incident upon a solid surface, it causes photoemission from the core levels and valence band of surface atoms into the vacuum. Core levels are defined as the inner energy levels that are not involved in chemical bonding whereas the valence levels are comprised of electrons in the more weakly bound and partially filled outer energy levels [16]. XPS provides qualitative and quantitative information on all elements present in a sample (except H and He). The XPS method is based on Einstein's explanation of the

photoelectric effect in which photons can produce electron emission from a solid provided the photon energy $(h\nu)$ is larger than the work function (ϕ) of the material [16]. The work function of a solid is defined as the minimum energy required to remove an electron from the highest occupied energy level in the solid to the 'vacuum level'. The binding energy (E_B) of an electron is element specific, and is also sensitive to the chemical state of the emitting atom. Thus, the kinetic energy of the emitted photoelectrons (E_k) can be estimated using Einstein's photoelectric equation:

$$E_k = h\nu - E_B - \phi \qquad \textit{Eqn. 2.7}$$

which can be written as $E_B = h\nu - E_k - \phi$ where $h\nu$ is the energy of the exciting photon from the X-ray source , E_B is the binding energy of the electron in the sample and ϕ is the work function of the electron energy analyser .

Based on the above equation, the binding energy of a core level (E_B) is calculated with respect to the highest occupied level in the solid which is the Fermi level. This Fermi level is the same as the Fermi level of the spectrometer, as the sample and the spectrometer share an electrical ground. The total energy accessible to elevate a core electron is the energy of the photon generated by the X-ray source $(h\nu)$. The emitted photoelectron therefore has a kinetic energy of $E_k = h\nu - E_B - \phi$. This is illustrated in Fig. 2.8.

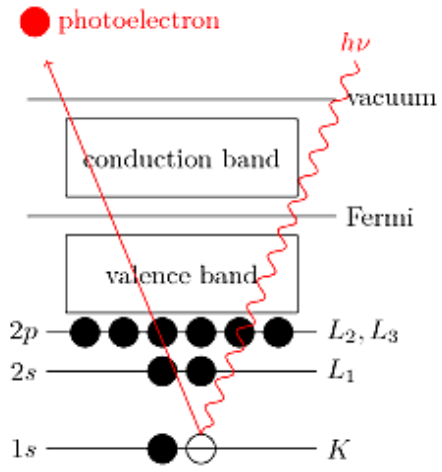

Fig. 2.8 X-ray excitation of a 1s core level [17].

The configuration of a typical XPS system is illustrated in Fig. 2.9. The surface to be analysed is placed in a vacuum environment and subsequently irradiated with X-ray

photons. After a direct transfer of energy from the photon to the core-level electron the atoms in the material emit photoelectrons [18]. The emitted electrons are then analysed according to their kinetic energy using an electron energy analyser. The energy of the photoelectron is related to the atomic and molecular environment from which they are emitted. The number of emitted electrons is dependant on the concentration of the emitting atom in the sample [18].

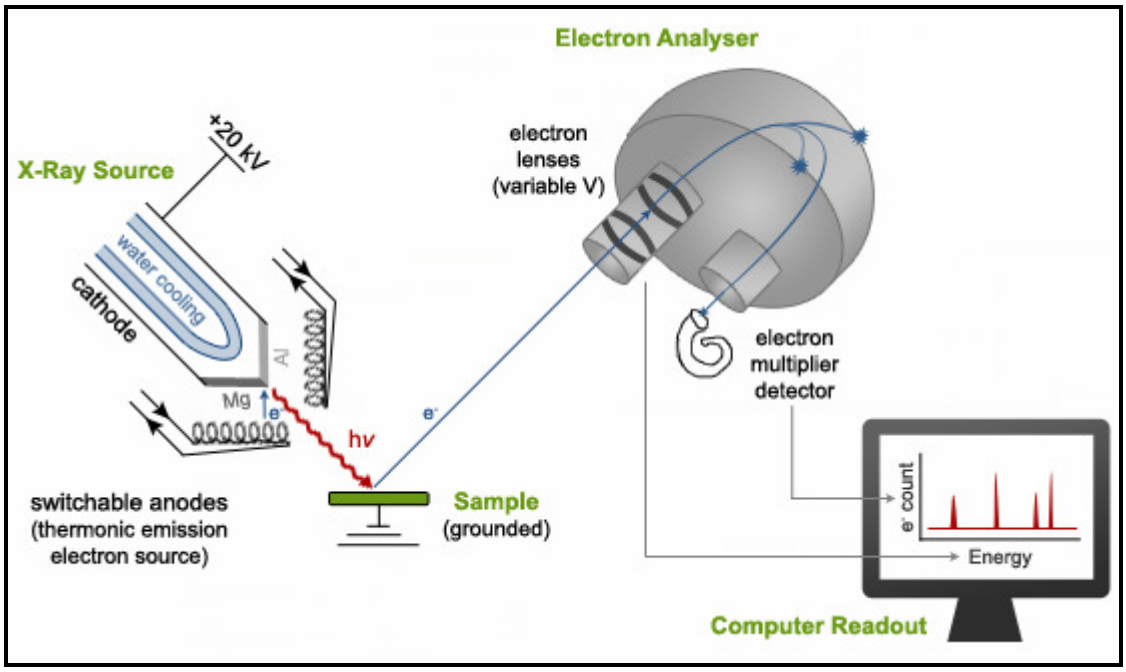

Fig. 2.9 Basic components of XPS system [19].

The XPS measurements were performed using an Omicron EA 125 electron energy analyser and an Omicron DAR 400 twin anode (Al, Mg) X-ray source installed on the UHV analysis chamber. Core level spectra were obtained using the Al K_α line of an X-ray source (hv = 1486.7 eV). The average film thickness was estimated from the attenuation of the substrate core level (eg. Au 4*d*) signal by using a mean free path for the photoelectrons of approximately 2.0 nm which is obtained from Universal Curve for Mean Fee Path (MFP) [18] as depicted in Fig. 2.10. The pass energy of the analyser was fixed at 50 eV with an entrance aperture of 6 mm diameter and exit slit dimensions of 3 x 10 mm. Pass energy, E_p is a constant energy applied to retard all the photoelectrons entering the analyser. Lower pass energy would give better peak resolution in the spectra. However, this higher resolution comes at the cost of the count rate, and hence, influences the signal to noise ratio. The tuning of pass energy and slit dimensions in XPS are essential to optimise the experimental conditions. The process of tuning the

analyser slits and pass energies in order to optimise the signal to noise ratio must be carried out for each experiment.

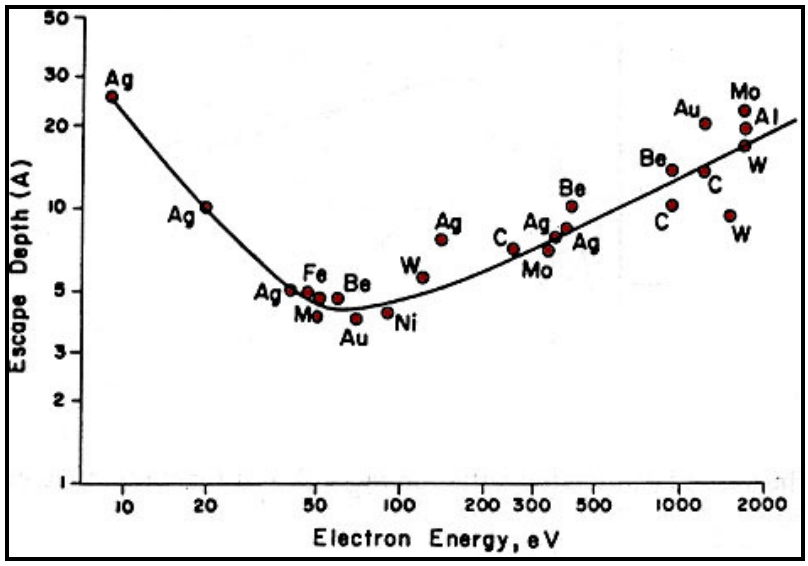

Fig. 2.10 The inelastic electron mean free path (escape depth) is plotted versus initial kinetic energy [20].

The resolution of the XPS measurements is controlled by the analyser which can be calculated using the following equation:

$$\text{Resolution} = \Delta E = \mathrm{E_p} \times \frac{S}{2R_0} \qquad \textit{Eqn. 2.8}$$

where R_o is the mean radius of the analyser hemisphere (0.125 m for EA125 analyser), S is the exit slit width in mm (3 mm), and E_p is a pass energy in eV.

For example, an analyser with a pass energy of 50 eV will have a resolution of 0.6 eV as shown in the example below:

$$\textit{Resolution} \quad \Delta E = 50 \times \frac{3 \times 10^{-3}}{2 \times 0.125} = 0.6eV$$

Thus, the total resolution is obtained by convolving the above value with the resolution of the Al X-ray source (0.85 eV):

$$\Delta E = \sqrt{\Delta E^2_{analyser} + \Delta E^2_{source}} = \sqrt{0.6^2 + 0.85^2} = 1.04eV \qquad \textit{Eqn. 2.9}$$

2.4 Ultraviolet Photoelectron Spectroscopy (UPS).

Ultraviolet photoelectron spectroscopy (UPS) is an extremely sensitive technique whereby a monolayer (ML) coverage of an adsorbate or contaminant is sufficient to grossly change the signal from a given surface. UPS derives its surface sensitivity from the small penetration depth of UV light in most solids. UPS relies on the photoelectric effect whereby monochromatic photons are used to eject electrons from the valence/conduction band region of a material. Its main strength lies in its ability to explore the electronic structure of a wide variety of solids. The objective of the UPS experiments is to gain information about the distribution of electrons in the outermost valence or conduction band region of the material. The minimum requirements for performing a simple UPS experiment are (a) a resonance radiation lamp, (b) an electron energy analyser capable of operation in the range 0 – 25.0 eV with an energy resolution of approximately 0.1 eV and finally (c) an atomically clean crystalline or polycrystalline sample in a UHV environment. The analyser need not be capable of angular resolution but the energy resolution requirement implies the need for magnetic shielding. Sample surface cleanliness must be maintained on an atomic scale since electrons of approximately 20 eV kinetic energy have an inelastic scattering mean free-path of approximately 0.5 nm which is the requirement that leads to the need for a UHV environment (typically in the 10^{-10} mbar range).

The photon source is a hallow cathode discharge lamp running in an inert gas which is usually helium (He I line at 21.21 eV) or neon, (Ne II line at 16.86 eV). Since the bandwidth of the conduction/valence band of the materials is in the range of 5 - 10 eV, these photon energies are sufficient to probe the entire band structure region of most materials. The photo emitted electrons are divided into two groups as illustrated in Fig. 2.11. They are as follows:

(a) The first group of electrons are the electrons that have been excited within the uppermost few atomic layers and escape into vacuum having suffered no inelastic collisions. The binding energy, E_b of each such electron is simply related to the observed kinetic energy E_k via the Einstein formula $E_k + E_b = h\nu + \varphi$ as a first approximation

(b) The second group of electrons observed comprises those electrons which have either suffered one and more inelastic collisions, most probably with the other bound valence electrons, or are secondary electrons which have gained sufficient energy to escape from the material from such a collision. This group of electron constitutes a largely featureless low energy peak in all UPS spectra with a shape that resembles a Maxwellian distribution.

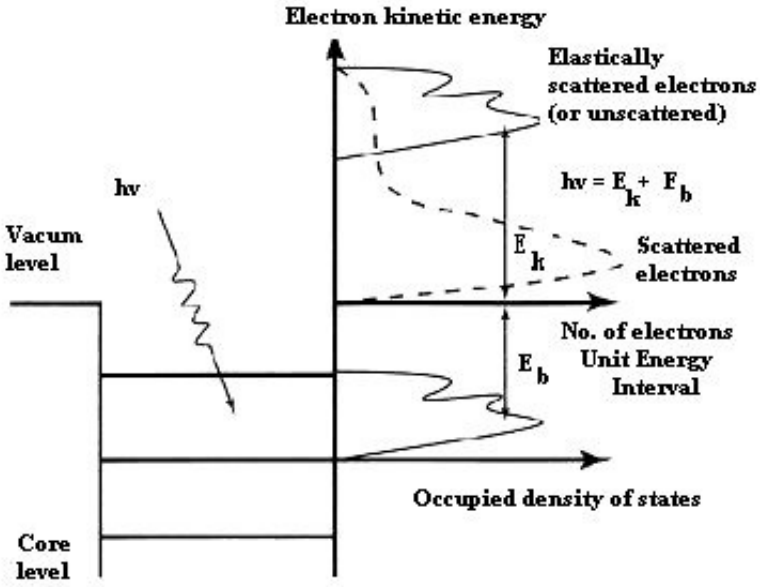

Fig. 2.11 Illustrating the photoexcitation of electrons from a valence band due to monochromatic photons of energy hv. An idealised energy distribution is also shown with primary emission distinguished from secondary electrons [21] .

The UPS measurements in the current work were performed at the Institut Matériaux Microélectronique Nanosciences de Provence (IM2NP) in Marseille, France, using a He discharge lamp (hv = 21.22 eV) and an Omicron EA125 electron energy analyser under UHV conditions. The VB spectra were recorded at normal emission (θ = 0°) and at an emission angle of 45°, with an energy resolution of about 0.1 eV and an analyser acceptance angle of 7°. All of the VB spectra were recorded with the sample biased at −5 V in order to detect the low kinetic energy cut-off from which the work function (WF) value was measured. The contributions from the He I satellite lines were subtracted from the spectra which were then referenced to the Fermi level (E_F) of a tantalum (Ta) foil in contact with the sample. The work function (φ) value can be calculated from the following equation.

$$\varphi_{sample} = hv - (KE_{FL} - KE_{cutoff}) \qquad \textit{Eqn. 2.10}$$

2.5 Synchrotron Radiation Techniques.

The use of synchrotron radiation for the excitation of photoelectrons has become an increasingly popular and important surface science research technique because it permits measurements that cannot be carried out with conventional, laboratory based XPS sources. The most striking feature offered by this technique is the tunability of the photon energy using an appropriate monochromator, thus providing photon energies extending from the infra red region up to hard X-rays [22]. Other important benefits of synchrotron light are its high intensity and brightness, variable polarisation, small spot size and the possibility of time-resolved measurements in a very short timeframe in the nanoseconds range or lower [22]. The basic synchrotron radiation source usually comprises an electron gun, linear accelerator, a booster ring, undulators, bending magnets, beamlines containing appropriate monochromators and experimental end-stations.

In order to generate synchrotron radiation, charged particles (electrons or positrons) from a linear accelerator with a speed close to that of light are injected into a storage ring under high vacuum. Some synchrotrons are equipped with booster rings. Electrons from the booster ring are accelerated into the storage ring periodically to maintain the current in the storage ring. The storage ring comprises curved sections joined by straight sections. Magnetic fields from bending magnets placed around the curved sections force the accelerated electrons to follow the ring in the curved sections. Some of the energy of the high-energy particles is lost and emitted as synchrotron radiation, tangential to these curved sections. A radio frequency cavity in the ring intermittently “kicks” the particles to restore the energy lost in the bending magnets. In addition, wigglers or undulators consisting of an array of dipole magnets can provide a continuous energy range from infrared to hard X-rays. Wigglers and undulators boost the brilliance (intensity) of the light by several orders of magnitude.

A beamline generally consists of a monochromator, curved mirrors, a set of slits or filters and the end station. Focusing is achieved with curved mirrors and the radiation is monocromatised either with reflection gratings or with a back-diffracting crystal. The analyser and monochromator are fitted with a set of slits controlled by a single rotary drive that allows both resolution and intensity control. A lower value of slit size would offer a higher resolution of the spectra and *vice versa.* The resolution of the

measurements can be calculated using Eqn. 2.12 . Finally, the end station allows the researchers to control the experiments and collect data.

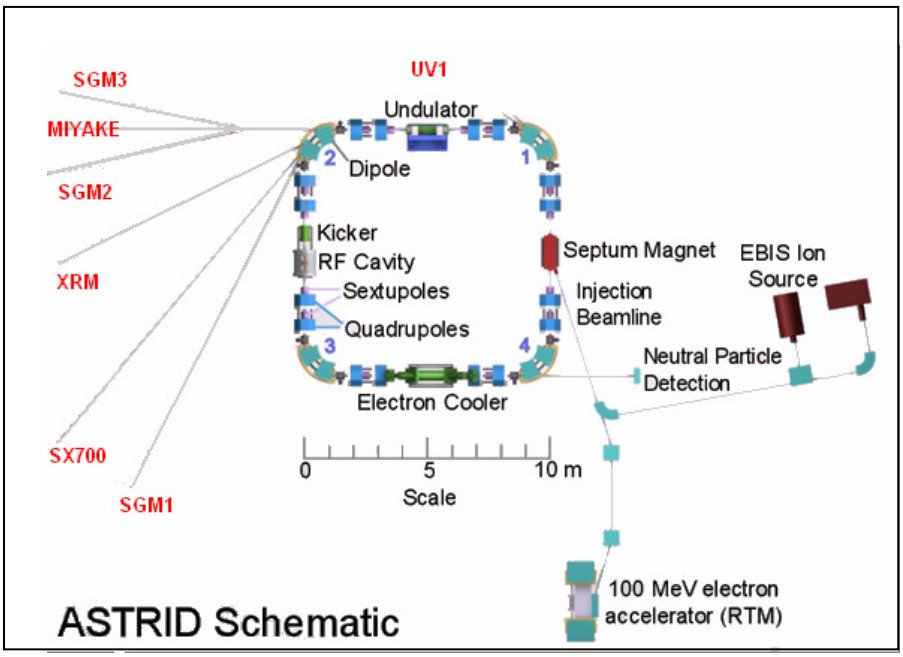

Fig. 2.12 Schematic of synchrotron radiation in ISA laboratory [23].

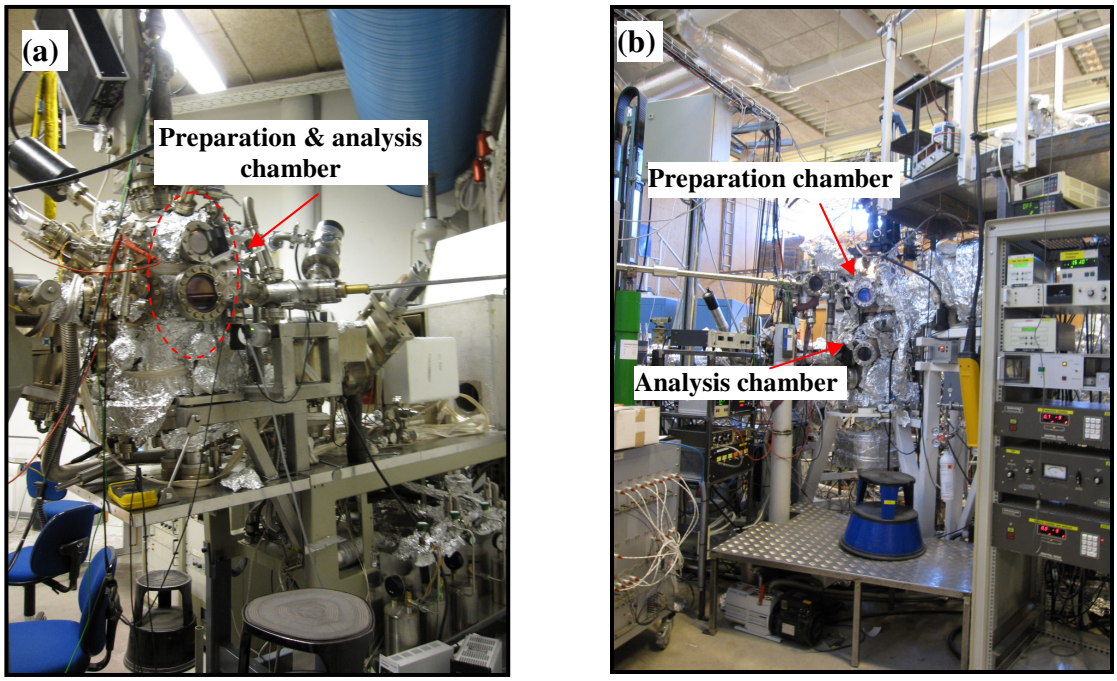

Fig. 2.13(a) The chamber is ISA laboratory in Aarhus, Denmark; (b) Two UHV chamber (preparation and analysis chambers) in MAX Laboratory, Lund, Sweden.

The XPS and X-ray absorption spectroscopy (XAS) experiments presented in this thesis were obtained at the SX700 beamline at the Institute of Storage Facilities (ISA) in University of Aarhus, Denmark [24] and the D1011 beamine at Max Lab in University of Lund, Sweden [25]. The ISA beamline has a single chamber whereas the beamline in MAX Lab consists of a two-chamber ultra high vacuum (UHV) system as shown in Fig. 2.13.

2.5.1 X-ray Absorption Spectroscopy (XAS).

XAS offers element specific information about the density of states, local atomic structure, molecular orientation, as well as the chemical state of the sample. When X-rays interact with a sample, the oscillating electric field of the electromagnetic radiation interacts with the electrons bound in an atom. The radiation will either be scattered by these electrons or absorbed in order to excite the electrons as depicted in Fig. 2.14.

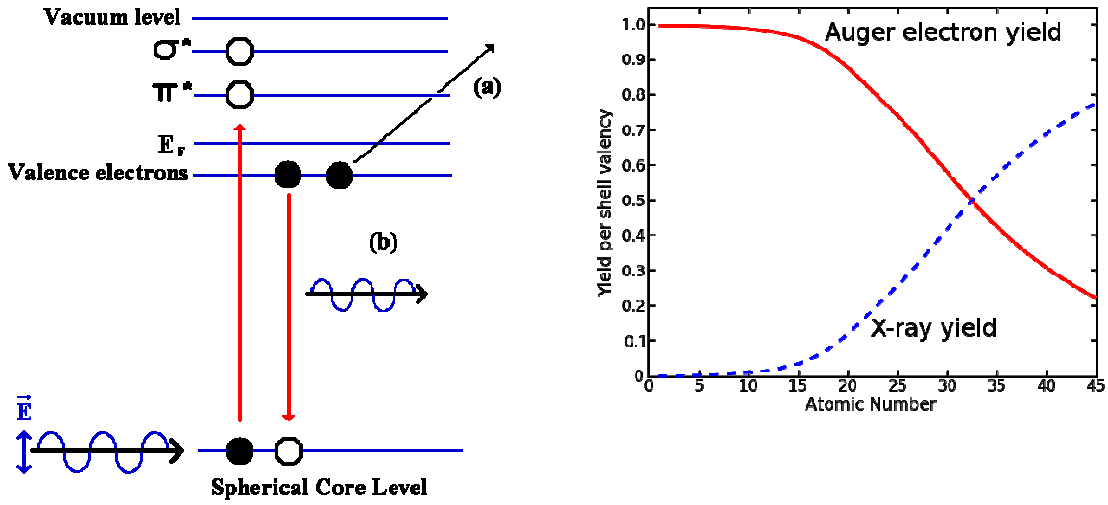

(a) (b)

Fig. 2.14 Two-step process that forms the basis for XAS studies. The first step involves excitation of core level electrons into π and σ* unoccupied levels. The core hole left by the excitation process is then filled by a valence electron with the surplus energy resulting in either the emission of (a) an Auger electron or (b) a fluorescent photon* [26]*; (b) Fluorescence and Auger electron yields as a function of atomic number for K shell vacancies. Auger transitions (red curve) are more probable for lighter elements, while X-ray yield (dotted blue curve) becomes dominant at higher atomic numbers* [27].

In XAS, a core electron is excited into an unoccupied atomic/molecular orbital above the Fermi level. XAS is categorised into two regions namely Near Edge X-ray Absorption Fine Structure (NEXAFS) for bound states as well as low energy resonances in the continuum and Extended X-ray Absorption Fine Structure (EXAFS) where the outgoing electron is well above the ionisation continuum. These transitions are caused by the absorption of an X-ray photon with energy tuned by means of a monochromator

to the ionisation energy of the bound state and hence, lead to a pronounced fine structure in the XAS spectrum. The XAS spectrum records the absorption intensity as a function of the incoming photon energy.

There are several detection methods which are commonly used in XAS including florescence yield detector (diodes), partial yield detector (channel plates) and total yield detector (drain current measured from sample). A clear transition from electron to photon emission is clearly depicted in Fig. 2.14(b) for increasing atomic number. The Auger electron yield is sensitive to the lighter elements and hence, Auger peaks can be detected for elements as light as lithium ($Z = 3$). Conversely, for heavier elements, the X-ray florescence yield becomes greater than the Auger yield, indicating an increased difficulty in measuring the Auger peaks for large Z-values. Therefore, a partial yield detector with a retarding voltage of 200 V is used to acquire C and O K-edge spectra in the current studies. Spectra were recorded with the angle of incidence of the linearly polarised synchrotron light at normal incidence (NI), normal emission (NE) and grazing incidence (70°). The raw XAS spectra were normalised to the incident photon flux by dividing the acquired sample spectra by a corresponding background spectra recorded from the clean substrate.

2.6 Low Energy Electron Diffraction (LEED).

Low energy electron diffraction (LEED) is a standard method used to determine the structure of a crystal surface. LEED uses electrons with energies of between 20 - 200 eV which have a penetration depth in most materials of the order of 1 nm and is therefore a highly surface sensitive technique [6]. The challenge of doing LEED studies of molecules on substrate is to use low a primary beam energy which is required because of the large unit cell of the molecular overlayer as compared to substrate unit cell. If high beam energy is applied, desorption of molecules from the substrate usually occurs, destroying the possibly well-ordered self-assembled layers on the substrate.

The diffraction of electrons at a surface can be demonstrated by taking into account the scattering of electrons from a two-dimensional array of scattering sites and by treating the electrons as waves. The electron wave incident on the surface can be represented by a wave-vector, k_o which is determined from the de Broglie equation:

$$k_0 = \frac{2\pi}{\lambda} = 2\pi\left(\frac{2m_e V}{h^2}\right)^{1/2} \approx 2\pi\left(\frac{V(eV)}{150}\right)^{1/2} \qquad \textit{Eqn. 2.11}$$

where λ is wavelength, h is Planck's constant, m_e is the mass of the electron, and V is the accelerating potential .

The interaction between the electron wave and the two dimensional lattice is best represented in reciprocal space. In three dimensions, the primitive reciprocal space vectors are related to the real space lattice vectors {**a, b, c**} by defining reciprocal lattice vectors relative to the real space lattice vectors as shown below:

$$\mathbf{a}^* = \frac{2\pi\,\mathbf{b}\times\mathbf{c}}{\mathbf{a}\bullet(\mathbf{b}\times\mathbf{c})}; \qquad \mathbf{b}^* = \frac{2\pi\,\mathbf{c}\times\mathbf{a}}{\mathbf{a}\bullet(\mathbf{b}\times\mathbf{c})}; \qquad \mathbf{c}^* = \frac{2\pi\,\mathbf{a}\times\mathbf{b}}{\mathbf{a}\bullet(\mathbf{b}\times\mathbf{c})} \qquad \textit{Eqn. 2.12}$$

In this case, the condition for constructive interference for an incident electron with wave vector, $k_0 = \frac{2\pi}{\lambda_o}$ and scattered vector, $k' = \frac{2\pi}{\lambda}$, is given by the Laue condition:

$$(\boldsymbol{k}' - \boldsymbol{k}_0) = \boldsymbol{g}_{hkl} = h\boldsymbol{a}^* + k\boldsymbol{b}^* + l\boldsymbol{c}^* \qquad \textit{Eqn. 2.13}$$

where (h,k,l = 0, 1, 2…)

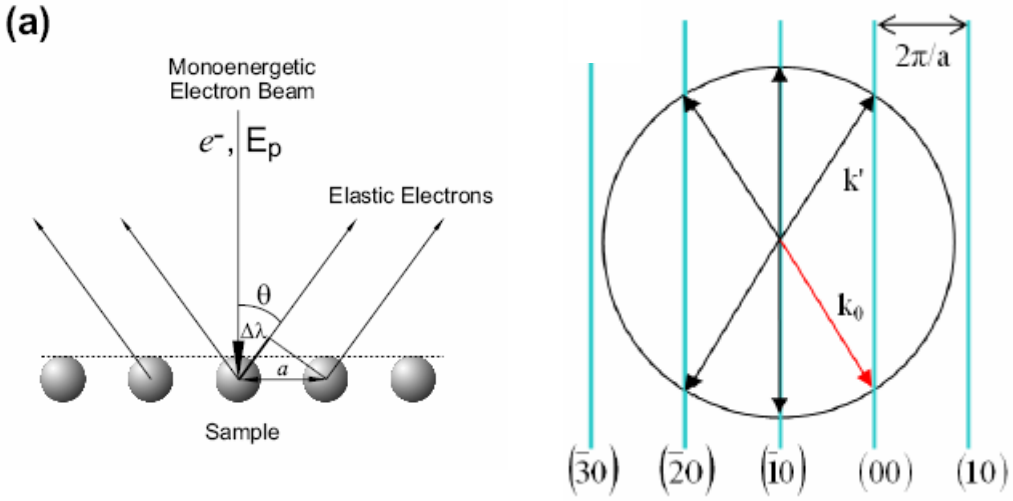

Fig. 2.15(a) Low energy electron diffraction from atomic structures in Bragg formalism [28] *(b) Ewald geometric constructions 2D* [2].

As depicted in Fig. 2.14(a),

$$sin\,\theta = \frac{|\boldsymbol{g}|/2}{|\boldsymbol{k}_0|} \qquad \textit{Eqn. 2.14}$$

where $|\boldsymbol{g}| = \frac{2\pi\sqrt{h_2 + k_2 + l_2}}{|\boldsymbol{a}|}$.

Substitution and re-arrangement of Eqn. 2.14 gives the Bragg equation

$$\mathrm{n}\,\lambda = 2\mathbf{a}\sin\theta \qquad \textit{Eqn. 2.15}$$

where the order of diffraction n, is given by ,

$$\mathrm{n} = \sqrt{h_2 + k_2 + l_2} \qquad \textit{Eqn. 2.16}$$

When a monoenergetic electron plane wave undergoes scattering from a periodic atomic structure as shown in Fig. 2.15(a), the condition for constructive interference is described by the Bragg equation. The magnitude of the wave vectors remains unchanged ($|\boldsymbol{k}_0| = |\boldsymbol{k'}|$) even though the direction of the elastically scattered wave is changed as shown in Fig 2.15(b). There are no diffraction conditions in the direction perpendicular to the sample surface and hence this will lead to $\mathbf{c}^* \rightarrow 0$. As a result, the reciprocal lattice of a surface is a 2D lattice with rods which extend perpendicular from each lattice point. The rod is shown as areas where the reciprocal lattices are infinitely dense. Thus, Eqn. 2.13 is translated into 2D form in the case of diffraction from the surface as shown in Eqn. 2.17.

$$(\mathrm{k}^{\parallel} - \mathrm{k_o}^{\parallel}) = \mathrm{g}_{hk} = h\mathbf{a}^* + k\mathbf{b}^* \qquad \textit{Eqn. 2.17}$$

where $\mathrm{k}^{\parallel}$, $\mathrm{k_o}^{\parallel}$ are the components of the incident and reflected wave vector parallel to the sample surface respectively; $\mathbf{a}^*$ and $\mathbf{b}^*$ are the primitive translation vectors of the 2D reciprocal lattice of the surface with

$$\mathbf{a}^* = \frac{2\pi\mathbf{b}\times\hat{\mathbf{n}}}{(\mathbf{a}\times\mathbf{b})} \qquad\qquad \mathbf{b}^* = \frac{2\pi\mathbf{c}\times\hat{\mathbf{n}}}{(\mathbf{a}\times\mathbf{b})} \qquad \textit{Eqn. 2.18}$$

The basic configuration of a LEED apparatus is shown in Fig. 2.16. The system consists of an electron gun used to produce the primary electron beam, which is

generally about 1 mm in diameter. The sample is usually mounted perpendicular to the electron beam and must have an electrical connection to earth to avoid charging. The sample sits at the centre of a series of high transparency hemispherical grids and a phosphor screen that is held at a high positive potential [29]. Diffracted electrons are backscattered from the periodic surface towards the hemispherical grids. The outer grid, (nearest to the sample), is earthed to ensure that the electrons move in a 'field free' region. The inner pair of grids acts as a cut-off filter and are held at a negative potential ($-E_p + \Delta V$), where E_p is the energy of the primary beam and ΔV is in the range of 0 - 10 V. This is to ensure that only elastically scattered electrons reach the screen. The screen is biased at a high positive voltage (~6 keV) to accelerate the transmitted electrons to a sufficient kinetic energy to cause light emission from the phosphor coated glass screen. The diffracted electrons give rise to a pattern comprising bright spots on a dark background, which indicate the symmetry and crystalline order of the surface. The LEED pattern can be viewed via a video camera that is attached to a computer.

This instrument is used to verify the crystallographic orientation and level of crystallinity of a single crystal sample. It can also be used to determine the symmetry and orientation of an ordered molecular adlayer. Further details can be found in van Hove [30].

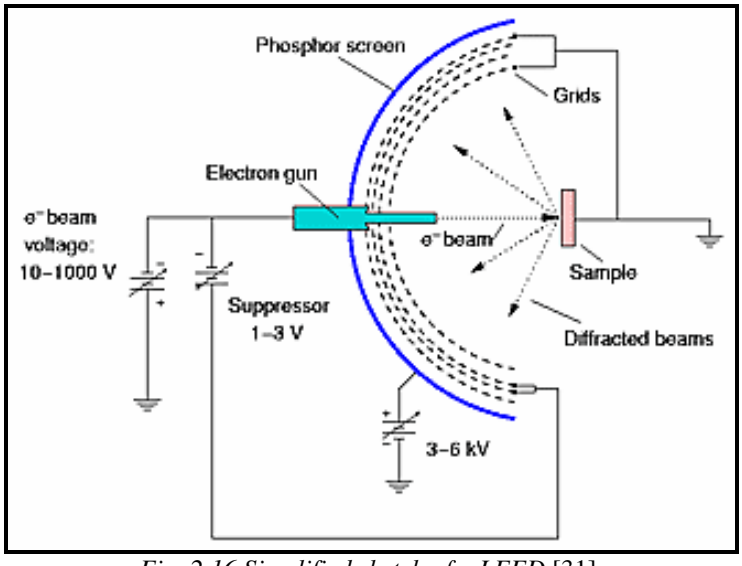

Fig. 2.16 Simplified sketch of a LEED [31].

2.7 Metal Surfaces

2.7.1 The ($22 \times \sqrt{3}$) on Au(111) Reconstruction.

Gold is a suitable substrate for STM investigations because it is generally inert and the gold crystal surfaces exhibit large (> 100nm) atomically flat terraces [32]. The Au(111) surface displays a reconstruction which is characterized by alternating domains of fcc and hcp stacking of Au atoms. It was first observed and reported by van Hove and his co-researchers in 1981 [33]. They suggested a uniaxial, homogenous contraction of the Au top layer in the $[\bar{1}10]$ direction, with 23 surface atoms per 22 bulk atoms and three 120° rotational domains. The transition between fcc and hcp stacking domains lead to two parallel corrugation lines in the $[11\bar{2}]$ direction per unit cell [34] (see Fig. 2.17a). These features are the most prominent to identify Au(111) in the STM images [35,36]. A correlated bending of the corrugation lines by 120° leads to the reconstruction in which domains are arranged in parallel stripes of about 25 nm width. These zig-zag patterns could be observed easily when analysed with STM (Fig. 2.17b). The inter-atomic distance of Au(111) is 0.289 nm.

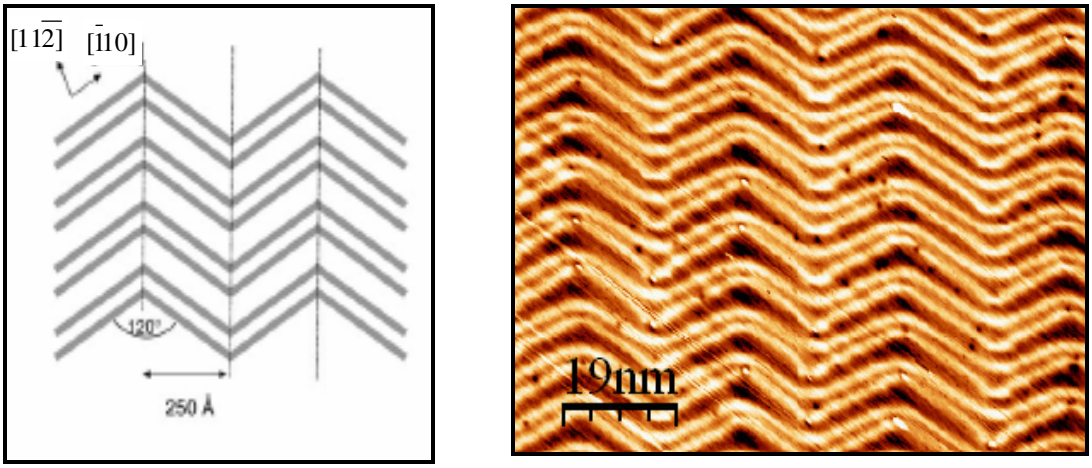

(a) **(b)**

Fig. 2.17(a) Schematic illustration of the Au(111)- ($22 \times \sqrt{3}$) surface. The zig-zag arrangement of the corrugation lines leads to a stripped arrangement of the ($22 \times \sqrt{3}$) reconstructed domains [34]. (b) STM image of the Au(111) ($22 \times \sqrt{3}$) (120 nm x 120 nm, Vs = -0.95 V, I = 0.14 nA).

2.7.2 Cu(111) and Ag(111) Surfaces.

Cu and Ag have face centred cubic (fcc) crystalline structure. As a result, the (111) surfaces are hexagonal with an inter-atomic distance of the lattice constant divided by $\sqrt{2}$, as depicted in Fig. 2.18(a) for Cu(111) and Fig. 2.18(b) for Ag(111). The inter-

atomic distance for Cu(111) is 0.255 nm and 0.289 nm for Ag(111). In general, Cu is the most reactive among the three noble metals. Therefore, Cu is expected to have a stronger interaction with any adsorbate. Conversely, Au is the least reactive.

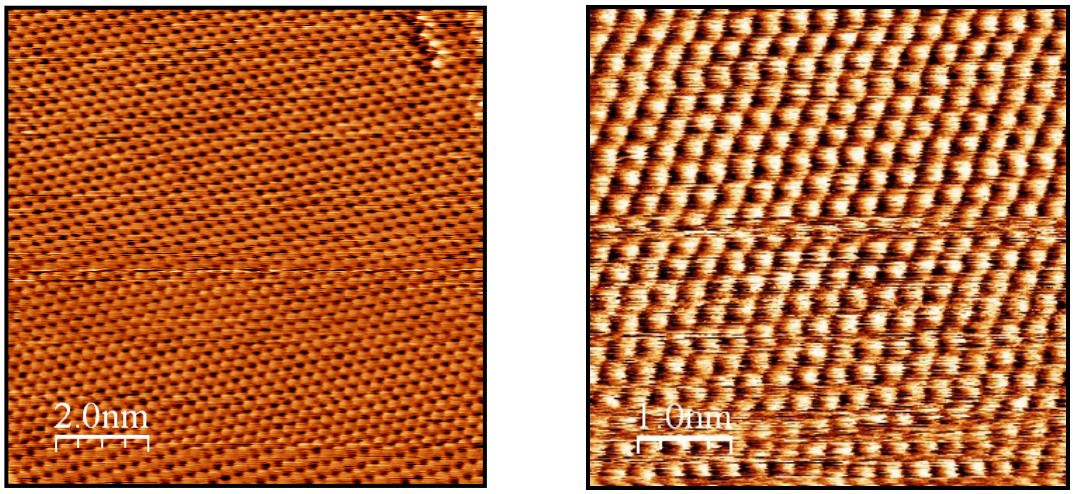

Fig. 2.18(a) STM image (10 nm ✕10 nm, Vs = -0.37 V, I =1.0 nA) of clean Cu(111) surface; (b) STM image (5 nm ✕5 nm, Vs = -2.0 V, I =2.3 nA) of clean Ag(111) surface.

2.8 Sample Preparation.

Metal single crystals (Au(111), Ag(111) or Cu(111)) were cleaned in the preparation chamber by sputtering with 1 keV Ar^+ ions and annealing by direct heating temperature from a filament mounted on the sample manipulator. Repeated cycles of Ar^+ ion bombardment and annealing were performed with the final annealing done in the analysis chamber. The crystal is initially analysed with LEED and/or STM to verify the crystallographic orientation and the absence of contamination before the organic deposition process.

All of the organic materials used in this project exist in powder form at room temperature (RT). A number of degassing cycles are performed on the organic molecular powders at slightly above deposition temperature prior to the deposition process in order to fully degas the materials. Deposition of the organic molecules is carried out in the preparation chamber by heating a tantalum or molybdenum crucible surrounded by a tungsten heating wire. The deposition temperature is set by applying a current (power supply running in current control mode) appropriate for the respective molecule. The temperature of the crucible is measured by a thermocouple spot welded to the base of the crucible.

References:

[1] Omicron NanoTechnology GmbH. *Users manual Multiprobe® Surface Science Systems USer's Guide Version 1.5* ,2002 (2002).

[2] G. Sheerin. *Ordering of organic molecules on templated surfaces,*Ph.D Thesis (2006).

[3] R. Wiesendanger, **Scanning probe microscopy and spectroscopy methods and applications**, Cambridge University Press, Cambridge, 1994.

[4] G. J. Leggett, Scanning tunnelling microcopy and atomic force microscopy, in: Vickerman J.C. (Ed.), **Surface analysis the principal technique**s, John Wiley & Sons, West Sussex, England, 1997, pp. 393.

[5] G. Binnig, H. Rohrer, C. Gerber, E. Weibel. *Surface studies by scanning tunnelling microscopy,* Phys. Rev. Lett. **49** (1982) 57.

[6] G. Binnig, H. Rohrer. *Scanning Tunneling Microscopy,* IBM J. Res. Develop. **44** (2000) 279.

[7] http://research.ncku.edu.tw/re/articles/e/20080606/5.html.

[8] L. Grill. *Functionalized molecules studied by STM: motion, switching and reactivity,* J. Phys.: Condens. Matter. **20** (2008) 53001.

[9] C.J. Chen, **Introduction to scanning tunnelling microscopy**, 2nd ed., Oxford University Press, USA, New York, 1993.

[10] http://ln-www.insp.upmc.fr/axe1/Dispositifs%20quantiques/AxeI2_more/PRINCIPLE/STSprin.HTM.

[11] N. Wintjes. *Tailoring supramolecular assemblies on a metal surface by specifically functionalized porphyrins,* Ph.D Thesis (2007).

[12] Z. Yu, C.M. Wang, Y. Du, S. Thevuthasan, I. Lyubinetsky. *Reproducible tip fabrication and cleaning for UHV STM,* Ultramicroscopy. **108** (2008) 873.

[13] I. Ekvall, E. Wahlström, D. Claesson, H. Olin, E. Olsson. *Preparation and characterization of electrochemically etched W tips for STM,* Meas.Sci. Technol.**10** (1999) 11.

[14] R. Zhang, D. Ivey. *Preparation of sharp polycrystalline tungsten tips for scanning tunneling microscopy imaging,* J. Vac. Sci. Technol.; B. **14** (1996) 1.

[15] Y. Akama, E. Nishimura, A. Sakai, H. Murakami. *New scanning tunneling microscopy tip for measuring surface topography,* J J. Vac. Sci. Technol.; A. **8** (1990) 429.

[16] G. Attard, C. Barnes, **Surfaces**, Oxford University Press, Oxford, 1998.

[17] http://www.texample.net/tikz/examples/ principle-of-x-ray-photoelectron-spectroscopy-xps/.

[18] B.D. Ratner, D.G. Castner, Electron spectroscopy for chemical analysis, in: Vickerman JC (Ed.), **Surface analysis - The principal analysis**, John Wiley & Sons, West Sussex, England, 1997, pp. 43.

[19] http://www.chem.queensu.ca/people/faculty/horton/research.html.

[20] http://www.globalsino.com/micro/TEM/TEM9923.html.

[21] S. Hüfner, **Photoelectron spectroscopy: principles and applications**, Springer Verlag, New York, 1996.

[22] F. Reinert, S. Hüfner. *Photoemission spectroscopy—from early days to recent applications,* New J. Phys. **7** (2005) 97.

[23] http://www.isa.au.dk/facilities/astrid/astridfig.html.

[24] www.isa.au.dk.

[25] www.maxlab.lu.se.

[26] O. McDonald. *Growth and characterisation of pentacene thin films on clean and modified metal surfaces,* Ph.D Thesis (2006).

[27] http://en.wikipedia.org/wiki/Auger_electron_spectroscopy.

[28] A. Varykhalov. *Quantum-size effects in the electronic structure of novel self-organized systems with reduced dimensionality,* Ph.D Thesis (2005).

[29] J.B. Hudson, Atomic Structure and Surfaces, in: Hudson JB (Ed.), **Surface science An introduction**, John Wiley and Sons, New York, 1998, pp. 6.

[30] M.A. Van Hove, W.H. Weinberg, C. Chan, **low-energy electron diffraction: Experiment, theory and surface structure determination**, Springer-Verlag, Berlin, 1986.

[31] http://www.fmc.uam.es/lasuam/glossary.php.

[32] T. Schmitz-Hübsch, T. Fritz, F. Sellam, R. Staub, K. Leo. *Epitaxial growth of 3, 4, 9, 10-perylene-tetracarboxylic-dianhydride on Au (111): A STM and RHEED study,* Phys. Rev. B: Condens. Matter. **55** (1997) 7972.

[33] M.A. Van Hove, R.J. Koestner, P.C. Stair, J.P. Biberian, L.L. Kesmodel, I. Bartoš, G.A. Somorjai. *The surface reconstructions of the (100) crystal faces of iridium, platinum and gold I. Experimental observations and possible structural models,* Surf. Sci. **103** (1981) 189.

[34] L. Kilian, E. Umbach, M. Sokolowski. *A refined structural analysis of the PTCDA monolayer on the reconstructed Au (111) surface—"Rigid or distorted carpet?",* Surf.Sci. **600** (2006) 2633.

[35] J.V. Barth, H. Brune, G. Ertl, R.J. Behm. *Scanning tunnelling microscopy observations on the reconstructed Au (111) surface: Atomic structure, long-range superstructure, rotational domains, and surface defects,* Phys. Rev. B. **42** (1990) 9307.

[36] C. Wöll, S. Chiang, R.J. Wilson, P.H. Lippel. *Determination of atom positions at stacking-fault dislocations on Au (111) by scanning tunnelling microscopy,* Phys. Rev. B. **39** (1989) 7988.

Chapter 3:

The Formation of Surface Supported Covalently Bonded 5,10,15,20-tetrakis(4-aminophenyl) porphyrin (TAPP) Networks on Au(111), Ag(111) and Cu(111) Surfaces.

3.0 Introduction.

In the past, the self-assembly of two dimensional organic nano-networks was achieved via the formation of metal complexes [1], hydrogen bonding [2] and van der Waal forces [3]. Furthermore, various approaches for the formation of covalently bonded structures on metal surfaces have been investigated by other scientists [4,5]. These strategies involve bonding through thermal dissociation of halogen carbon bonds [4,4,6]; bonding through dehydration of borate functionalised molecules [7] and imide formation by polycondensation reactions [8,9]. The covalent bonded nano-networks are known to be chemically, thermally and mechanically more stable than those based on hydrogen bonding, even though the organization of the molecules into periodic networks is more complicated to control.

As described in the Chapter 1, porphyrins belong to an interesting group of molecules with a large variety of electronic, magnetic and structural characteristics [10]. Their applications range from biological functions in enzymes and oxygen transport to industrial processes [10] such as photovoltaic cells and sensors. Due to their extensively *pi* bonded nature, the macrocycle is planar and they show relatively high thermal stability up to 440 ^{o}C. 5,10,15,20-tetrakis(4-aminophenyl)porphyrin (TAPP) is a porphyrin which has four amino (NH_2) groups attached to the phenyl rings (see Fig. 3.1) in the *para* position. In this work the formation of covalently bonded networks of TAPP through either annealing of thin films or deposition onto a substrate held at different elevated temperatures. TAPP (Tokyo Chemical Industry, TCI), is studied using scanning tunnelling microscopy (STM), X-ray photoelectron spectroscopy (XPS) and synchrotron based techniques.

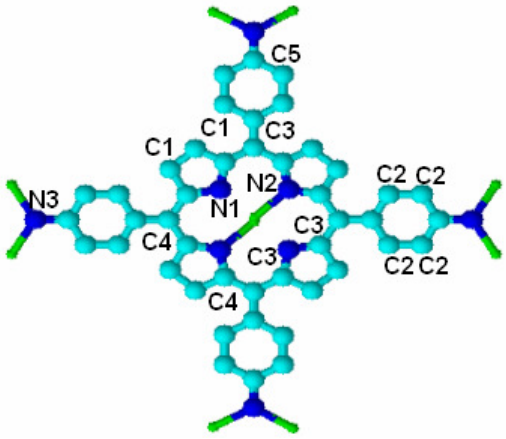

Fig. 3.1 The chemical structure of 5,10,15,20-tetrakis(4-aminophenyl)porphyrin (TAPP) The assignment/numbering of C and N atoms is discussed below for XPS curve fitting. In the molecular representation, light blue balls are carbon atoms, green balls are hydrogen atoms and dark blue balls are nitrogen atoms.

3.1 Experimental.

All measurements were carried out in the ultra-high vacuum (UHV) system described in Chapter 2. Au(111), Ag(111) and Cu(111) crystals were cleaned in the preparation chamber by repeated cycles of Ar^+ ion sputtering at 1kV and annealing to 450 ^oC by resistive heating using a tungsten filament. The cleaned crystal is initially analysed with XPS and STM to verify the absence of contaminations before the organic deposition process. TAPP molecules were purified using a sublimation method which was developed by the surface science group in Institut Matériaux Microélectronique Nanosciences de Provence (IM2NP), in Marseilles, France. The molecules were thoroughly degassed for 12 hours in the preparation chamber and then deposited onto Au(111), Ag(111) and Cu(111) crystals. A thermocouple, spot-welded to the crucible, was used to monitor the deposition temperature. The substrate temperature was controlled during deposition via a tungsten filament on the sample holder. The base pressure in the preparation chamber was less than 9×10^{-11} mbar prior to deposition. The TAPP coverage was estimated by XPS measurements with an Al K_α ($h\nu$ = 1486.7 eV) source. All STM images were recorded at room temperature. The coverage was determined by calculating the C 1s to metal ratio and comparing with the coverage determined from the corresponding STM images.

3.2 Results and Discussion.

3.2.1. Scanning Tunnelling Microscopy (STM) of TAPP on the Au(111) Surface at Room Temperature (RT).

TAPP was deposited at 390 ^{o}C evaporator temperature for approximately 90 minutes (1 ML) on the clean Au(111) surface held at room temperature and subsequently annealed at (a) 150 ^{o}C for 15 minutes to improve the ordering of the molecules. The sample was then annealed to (b) 350 ^{o}C, (c) 400 ^{o}C and (d) 450 ^{o}C. Figure 3.2 shows a series of the STM images recorded at room temperature after each stage of the experiment.

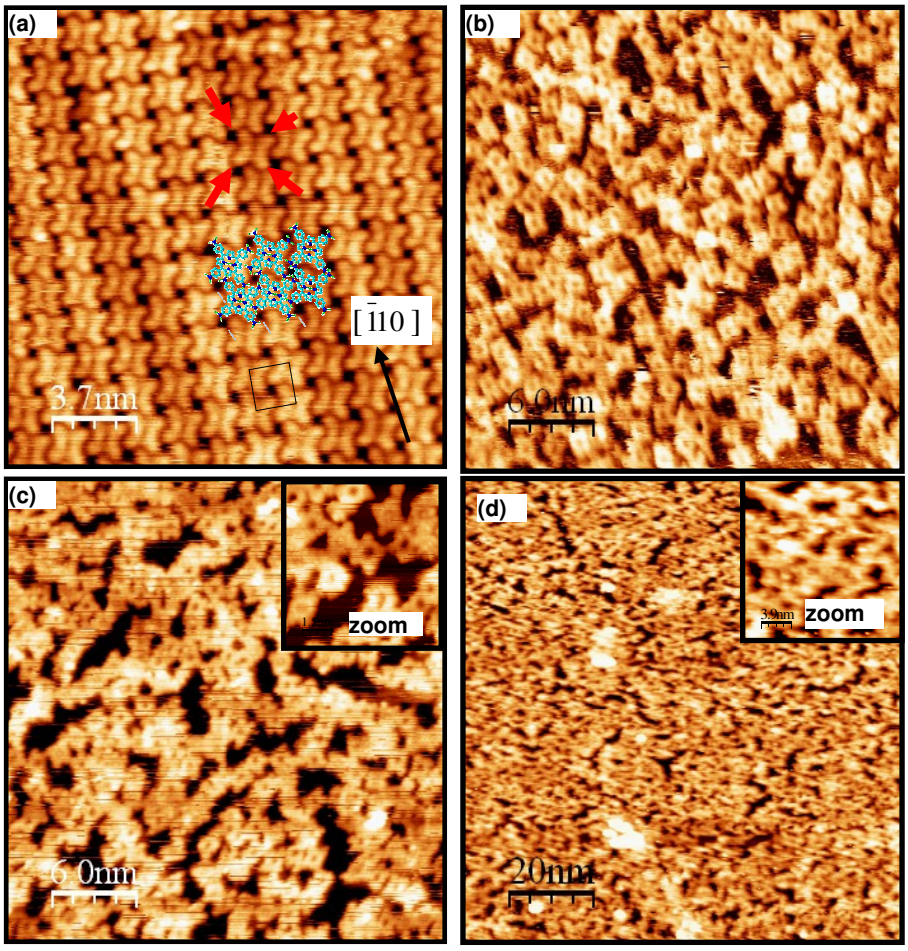

Fig. 3.2 (a) STM image (18.4 nm × 18.4 nm, Vs = -1.0 V, I =0.2 nA) of 1 ML of TAPP; (b) STM image (30 nm × 30 nm, Vs = +1.6 V, I =0.3 nA) at 350 ^{o}C annealing; (c) STM image (30 nm × 30 nm, Vs = +1.4 V, I =0.3 nA) at 400 ^{o}C annealing; (d) STM image (100 nm × 100 nm, Vs = +1.4 V, I =0.2 nA) at 450 ^{o}C annealing.

The square unit cell measured from the STM images are $\boldsymbol{a}$ = (1.57 ± 0.05) nm and $\boldsymbol{b}$ = (1.57 ± 0.05) nm. At room temperature, four lobes corresponding to the phenyl groups are distinguished clearly in the STM images (as indicated by the arrows in Fig. 3.2a). Three domains are observed which are rotated by 120 ^{o} with respect to each other. This

observation indicates a well defined registry of the domain relative to the Au(111) substrate [$\bar{1}10$] direction which exhibits a three-fold symmetry. This alignment along the substrate high symmetry directions suggests that the orientation of the domains is induced by adsorbate-substrate interactions.

The covalently bonded TAPP networks were observed at 350 ^{o}C (Fig. 3.2b) as confirmed by XPS measurements discussed below. However, the networks formed were disordered and consisted of mainly oligomers. This could be attributed to the fact that the molecules arrange randomly during the polymerisation process in order to achieve equilibrium of energy and thus produce the disordered nanostructures [11]. Further annealing was performed to test the stability of the networks. The covalently bonded networks were stable and intact at 400 ^{o}C (Fig. 3.2c). However, partial decomposition has taken place after 400 ^{o}C. This phenomena was further confirmed when the sample was annealed at 450 ^{o}C where the STM image (Fig. 3.2d) showed that the macrocycle rings of TAPP networks have decomposed. This result is also in agreement with a thermal gravimetric analysis (TGA) analysis that was performed on the TAPP molecules (Appendix A) which showed that the TAPP molecules begin to decompose at 450 - 460 ^{o}C.

According to Buchner *et al.*[12], there are two observed types of attractive interactions between the phenyl legs of adjacent tetraphenyl porphyrins (TPPs), described as π-π stacking and T-stacking, respectively. To differentiate between the two proposed interactions, space filling models of the π-π and T-type molecular arrangements of the peripheral phenyl groups are illustrated in Fig. 3.3(a and b, after Buchner *et al.* [12]). The resulting arrangements can be distinguished by the different azimuthal angles of the individual porphyrins with respect to the lattice vector of the unit cell. Fig. 3.3(a) and (b) show an azimuthal angles of ~15 ^{o} and ~30 ^{o}, respectively, for the π-π stacking T-type arrangement, for tetraphenyl porphyrin on Ag(111).

Fig. 3.3(c) shows an enlarged image of Fig. 3.2(a) for self-assembled TAPP molecules on Au(111). The STM image in Fig. 3.3(c) was an average of the individual unit cells using the WSxM [13] software to calculate the azimuthal angle. The measured azimuthal angle is (26 ± 2)^{o} suggesting that a T-type interaction is most likely involved in the formation of the self assembled monolayer. The T-type intermolecular lateral

interactions are responsible for stabilising the square packing and dominate over the adsorbate-substrate interactions based on the Buchner *et al*. system on tetraphenyl porphyrin on Ag(111).

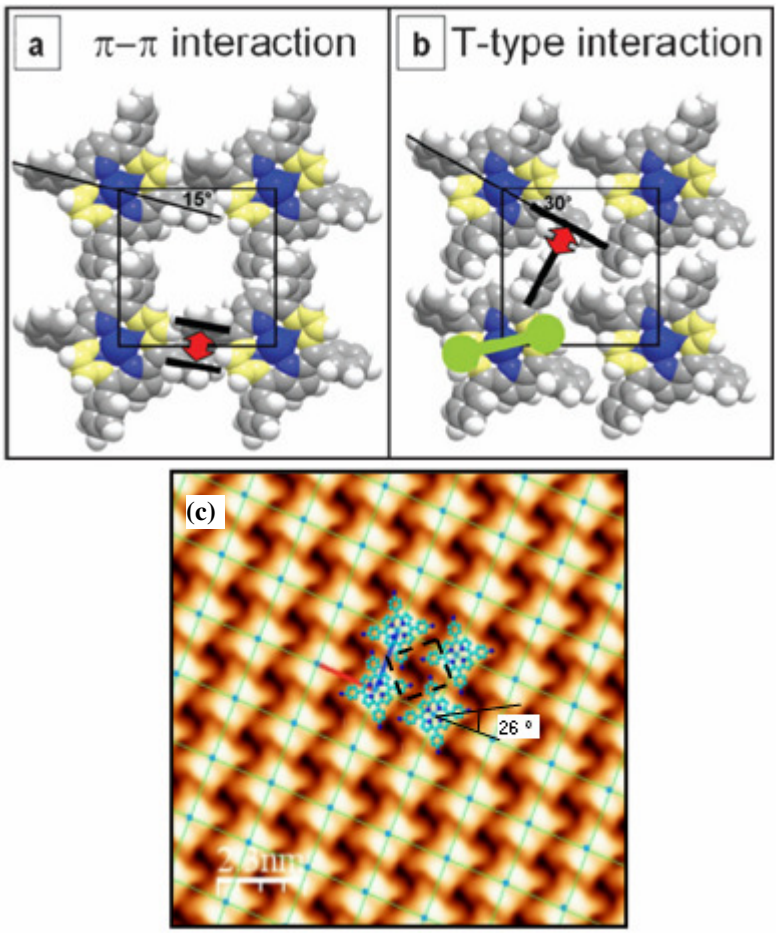

Fig. 3.3 Space-filling models of two-possible arrangements of tetraphenyl porphyrin on Ag(111) from Buchner et. al [12] .(a) π-π stacking yielding a rotation of the molecular axis relative to the unit cell by 15 ^{o} and resulting in a parallel alignment of adjacent phenyl legs; (b) T-stacking, yielding a rotation by 30 ^{o} and resulting in a perpendicular motif of neighbouring phenyl rings [12]*; (c) Enlarged image of Fig.3.2(a) above, which was superimposed with corresponding TAPP structures. The proximate substituents show a 'T'-shaped arrangement on Au(111).*

There are four possible reaction mechanisms proposed for the polymerisation reaction as illustrated in Scheme 3.1. Generally, when the two amino groups react, oxidation takes place involving the loss of hydrogen. The first three reactions (Scheme 3.1a-c) are continuous or two-step coupling oxidation reactions accompanied by the elimination of N_2. Reactions (a) and (b) are highly probable. The final mechanism for polymerisation is assumed to proceed in a manner analogous to that observed in aniline polymerisation and involves an oxidative coupling as illustrated in Scheme 3.1(d) [13]. The *ortho* connections is where the linkages involving diphenylamine, dihydrophenazine or phenazine are proposed since the *para* positions of TAPP are already occupied [14].

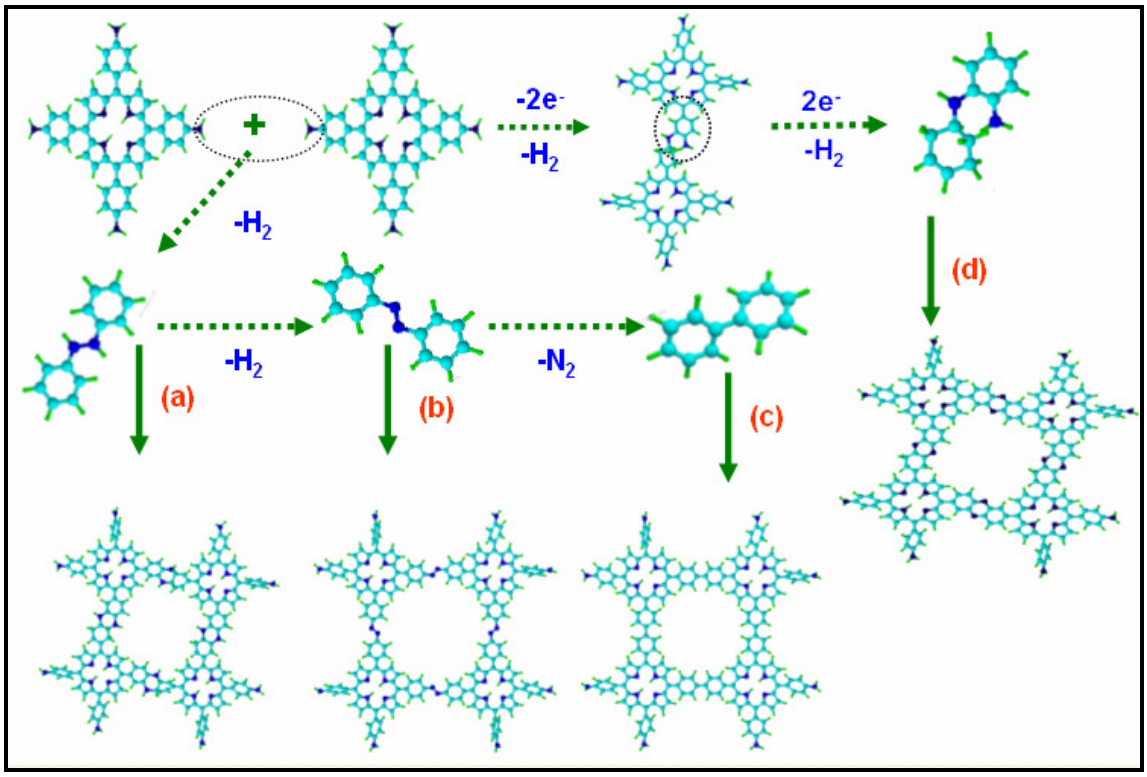

Scheme 3.1 Four possible routes to form covalently bonded TAPP nano-networks. Bonding on (a) is HN-NH and (b) is –N=N-.

3.2.2. Synchrotron Based X-ray Photoemission Spectroscopy (XPS) of TAPP on Au(111) Surface at Room Temperature (RT).

The XPS analysis of TAPP on Au(111) is performed in MAX Lab, University of Lund, Sweden. The photon energy used to measure C 1s and N 1s was at 380 eV and 500 eV respectively. The total resolution for C 1s is 0.2 eV and for N 1s is 0.3 eV. All binding energies are determined to an accuracy of $\pm$ 50 meV.

From the results obtained, five different carbon chemical environments can be identified in the TAPP molecule: (i) sixteen carbons atoms in the macrocycle ring; (ii) twenty phenyl carbon atoms (excluding C-NH_2); (iii) four *meso* carbons and two carbons attached to the azanitrogen atoms (iminic, -C=N); (iv) the two carbons attached to the pyrrolic nitrogen (-C-NH) and (v) four carbon atoms attached to the amino (NH_2) group.

Table 3.1 Binding energy positions and relative intensities of C 1s and N 1s peaks of the TAPP molecules. The percentage is the fraction of the component area relative to the total core level area. ΔE is the distance of the component energy with respect to the main peak.

Experimental analysis				
Core level	**Component**	**eV**	**ΔE**	**%**
C 1s	**C1** Macrocycle carbon atoms	284.09	-0.38	18.4
	C2 Phenyl carbon atoms	284.47	0	45.5
	C3 *Meso* carbons and on azanitrogen atoms	284.97	+0.50	21.5
	C4 Carbon attached to pyrrolic nitrogen	285.41	+0.94	7.7
	C5 Carbon attached to amino group	285.78	+1.31	6.9
N 1s	**N1** Azanitrogen atoms (C=N)	398.20	0	27.6
	N2 Pyrrolic group (R-NH) + **N3** Amino group ($R\text{-}NH_2$)	400.10	+1.90	72.4

The carbon 1s core level XPS spectrum of TAPP on Au(111) is shown in Fig. 3.4 (a) The lineshape is dominated by two structures which are identified as the main peak at 284.09 eV, associated with a typical free base porphyrin and a second peak at 284.47 eV, associated with the amino functionalised phenyl groups. However, the asymmetric broadening of the main peak indicated the presence of more than one component particularly on the higher binding energy side. The fitting and assignment of the C1, C2, C3 and C4 peaks (see Fig. 3.1) is based on the work of Nardi *et. al*.[15] for tetra(phenyl) porphyrin. The spectrum can be decomposed into five peaks with Voigt lineshapes with parameters summarised in Table. 3.1. The main peak which is associated with the phenyl carbon atoms (C2) is at a binding energy of 284.47 eV. The macrocycle carbon peak (C1) is at 284.09 eV; the *meso* carbons and carbon attached to azanitrogen atoms (C3) are at 284.97 eV; the carbons attached to pyrrolic nitrogen (C4) are at 285.41 eV, while the carbons attached to the amino group (C5) are observed at 285.78 eV. The carbon stoichiometry of C1:C2:C3:C4:C5 is 3:7:3:1:1 which is in approximate agreement with the stoichiometry of a TAPP molecule.

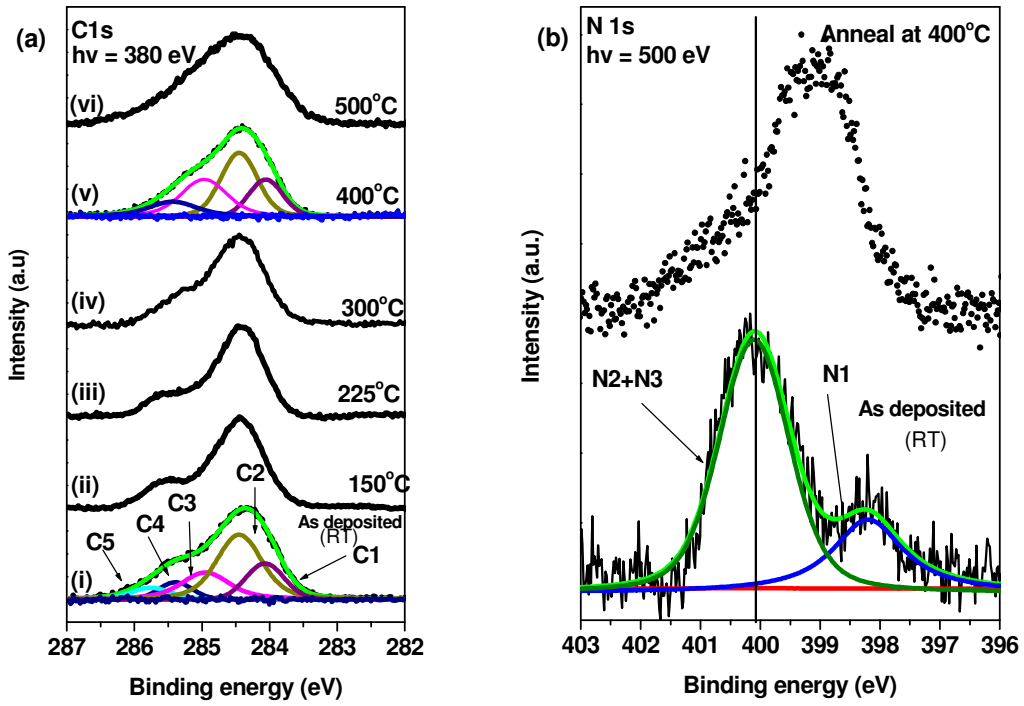

Fig. 3.4 Results of the peak fitting analysis of (a) the C 1s and (b) the N 1s core level photoemission spectra. Experimental data is displayed as black lines and fitted peaks as solid coloured lines.

Fig. 3.4 (b) shows the N 1s core level XPS spectrum before and after polymerisation process. Two peaks are identified and are associated with azanitrogen atoms, -C=N (N1), the pyrrolic nitrogen atoms, -C-NH (N2) and the nitrogen atoms in the amino groups, $-NH_2$ (N3). The N1 photoemission peak is at a binding energy of 398.20 eV, while the N2+N3 peaks are at a binding energy of 400.10 eV. The individual N2 and N3 peaks cannot be resolved. The nitrogen spectrum is deconvolved into Voigt profiles with a fixed area ratio of N1:(N2+N3) of approximately 1:2.6 which is in agreement with the stoichiometric ratio of nitrogen atoms in the TAPP molecule which is 1:3. The energy difference between the azanitrogens (-C=N) and the pyrrolic nitrogens (R-NH) is 1.90 eV. This value is in agreement with the value of 2.0 eV reported by Krasnikov *et al.* for the N 1s splitting in free base porphine (H_2P) [16].

The sample was annealed for 30 minutes at different temperatures from 150 °C to 500 °C. Fig. 3.4(a) shows a decrease in the intensity of the peak associated with the C5 (C-NH_2) carbon atoms in the C 1s spectra as the annealing temperature is increased. Fig. 3.4(b) also shows that the N 1s peak associated with the N2 and N3 nitrogen atoms decreases after annealing at 400 °C when compared to the initial N 1s peak intensity. Furthermore, a new peak appears between the peaks associated with the N1 and N2 nitrogen atoms. This peak is assigned to a new chemical environment associated with a

new R–N bond formed during a covalent reaction between neighbouring TAPP molecules. This observation could also indicate the disassociation of the phenyl groups (decomposition) from the TAPP molecule which is confirmed by XAS measurements presented in the following section.

3.2.3. X-ray Absorption Spectroscopy (XAS) of TAPP on Au(111) Surface at Room Temperature (RT).

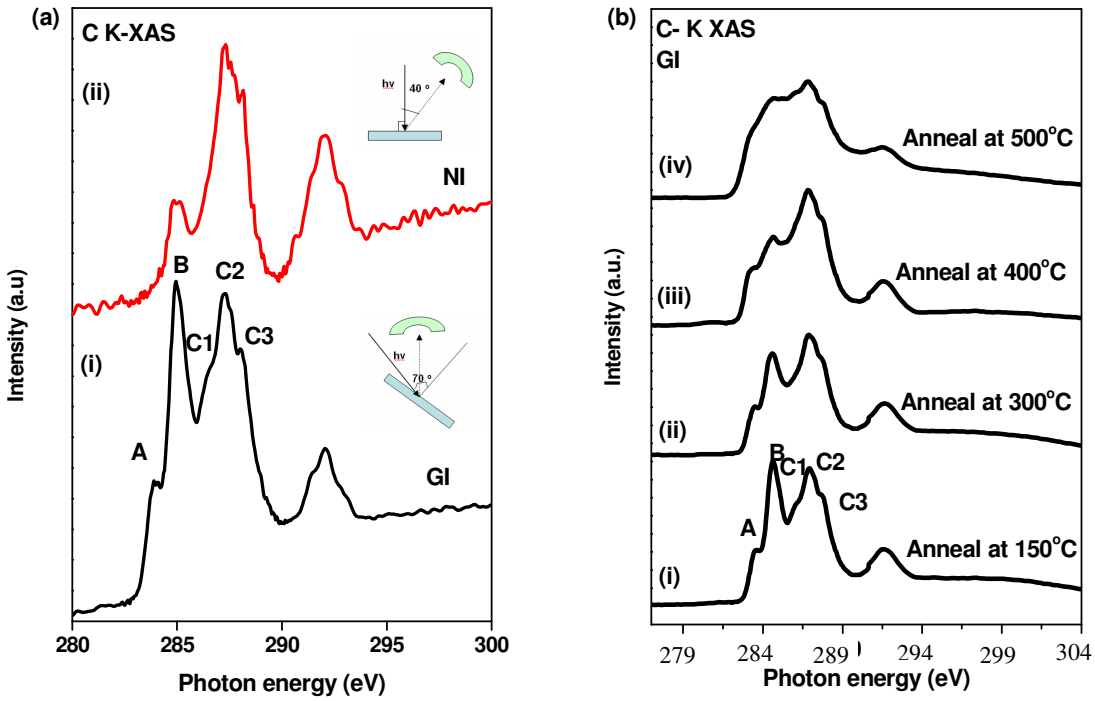

Fig. 3.5(a) XAS spectra of a monolayer of TAPP molecules on the Au(111)surface at the grazing incidence (GI,70°) and normal incidence (NI) ;(b) XAS recorded at GI, (ii)-(iv) X-ray beam at different annealed temperature (150 - 500 °C) for 30 minutes each cycle.

Fig. 3.5(a) shows the C- 1s XAS spectra acquired at grazing incidence (GI) and normal incidence (NI). Fig. 3.5(b) shows a series of XAS spectra recorded at grazing incidence after a series of anneals. All photon energies are determined to an accuracy of ± 50 meV. The observed structure in the XAS spectra is based on the assignments of Schmidt *et al.*[17] for free based tetraphenyl porphyrin (TPP). Peak A at 283.9 eV, is associated with the π* resonances from the carbon atoms in the macrocycle. Peak B at 284.9 eV contains contributions from transition into π* states on the peripheral phenyl rings. Peak C1 and C3 at 286.5 and 288.1 eV; respectively correspond to the π* resonances from macrocycle carbon atoms into empty states localised on the azanitrogen. Peak C2 at

287.3 eV is assigned to the π^* state from the macrocycle carbon atoms into empty states localised on the pyrollic nitrogen [17]. These results are tabulated in Table 3.2.

Peak B, associated with the carbon atoms in the phenyl ring that is attached to the amino group, is broadened and the peak B ratio intensity decreases when the sample is annealed to temperatures greater than 300 ^{o}C as shown in Fig. 3.5b(ii). This indicates that a reaction has taken place involving the amino groups and the charge distribution on the phenyl rings has changed. This depends on the number of amino groups that are involved in reactions between the TAPP molecules. The amino groups are expected to react, which then form a covalently bonded network of TAPP molecules as observed in the STM. A further increase in the annealing temperature to 400 ^{o}C increases the dissociation of the amino groups and the corresponding covalent reactions between the TAPP molecules. Therefore, the XAS peaks occurring in the energy range 284 - 288 eV are broadened and peak B decreased due to polymerisation process involving phenyl functionalised amino group. This broadening could also be intensity change associated with a delocalisation of the electrons on the macromolecule resulting from covalent bonding. When the temperature is increased to 500 ^{o}C, the peaks are further broadened. This finding suggests that decomposition of the TAPP molecule occurs at 500 ^{o}C.

The ratio of peaks A: B: C from the GI spectrum is 2:5:5. Figure 3.5 (a) shows intensities of peak A, produced by C atoms in the macrocycle, in the XAS spectra recorded at (i) GI and (ii) NI. The intensity of this peak is almost zero in the NI spectrum showing that the plane of the macrocycle lies parallel to the Au(111) surface. Furthermore, as peak B has reduced substantially in the NI spectrum, this shows that the plane of the phenyl rings is tilted relative to the plane of the surface.

Table 3.2 Assignments and energy positions of the C- K XAS resonances for TAPP.

TAPP	**Peak**	**Resonance Position (eV)**	**Assignments**
C- *K* XAS	**A**	283.9	π* macrocycle >NH
	B	284.9	1. π* C=C phenyl
	C1	286.5	1. π * C-H
	C2	287.3	2. π * C=C
	C3	288.1	3.π* macrocycle >NH

In this experiment, deposition of TAPP molecules on Au(111) was studied using STM, XPS and XAS. STM results at RT indicate that TAPP molecules self-assemble into a

structure with a square unit cell on the Au(111) surface. XPS results show reactions among the amino groups to form covalently bonded networks. Finally, XAS spectra suggest that the porphyrin macrocycle is orientated parallel to the surface with the phenyl rings slightly tilted relative to the surface.

3.2.4. Scanning Tunnelling Microscopy (STM) of TAPP on the Au(111) Surface at Elevated Temperature.

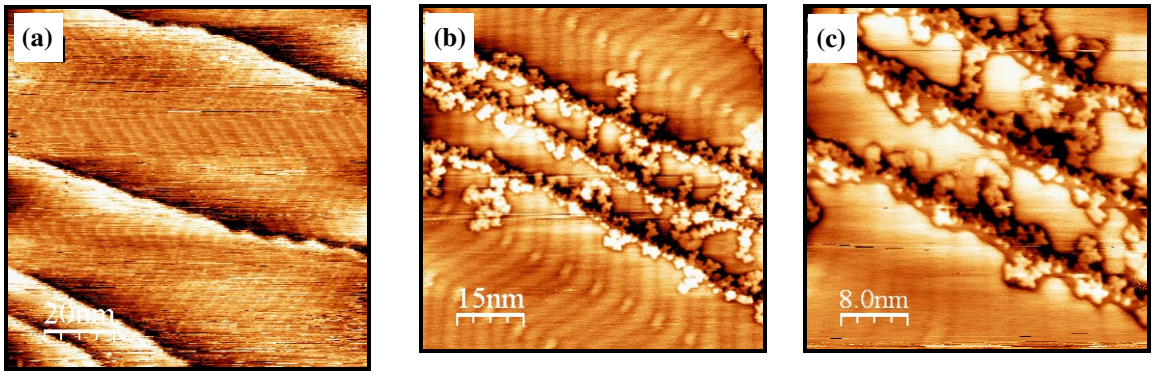

Fig.3.6 (a) STM image (100 nm × 100 nm, Vs = -0.3 V, I = 0.3 nA); (b) STM image (75 nm × 75 nm, Vs = -0.8 V, I =0.1 nA); (c) STM image (40 nm × 40 nm, Vs = -0.3 V, I =0.3 nA) on Au(111) when the substrate is held at 250 ^{o}C.

In this experiment, the TAPP molecules were deposited for two hours on an Au(111) substrate at 250 ^{o}C, 300 ^{o}C and 350 ^{o}C respectively. The STM images were recorded at room temperature. This approach was adopted with the intention of causing the amino groups to react on the substrate held at elevated temperature in an attempt to form better ordered networks. This method has been employed by several groups [6,18,19] where they looked at tetra(bromophenyl) porphyrin (TBB) [6], 1,4-benzenediboronic acid (BDBA) [18] and 1,3,5-tris(4-bromophenyl)benzene (TBPB) systems on different noble metal surfaces [19].

The STM images show that TAPP networks are formed mainly at the step-edges of the Au(111) when the substrate is held at 250 ^{o}C. They are mostly oligomers as observed with substrate held at room temperature. Most of the surface was bare, and the Au(111) reconstruction could be observed clearly in STM (Fig. 3.6, a-c). It appears that at 250 ^{o}C, most of the TAPP molecules do not remain on the Au(111) surface. Hence, the coverage is very small despite 120 minutes of deposition time (1 ML of TAPP on Au(111) at room temperature requires approximately 90 minutes).This result shows that a temperature of 250 ^{o}C is not hot enough to initiate the polymerisation reaction.

On the contrary, deposition for 120 minutes on a substrate at 300 ^{o}C resulted in approximately 0.6 ML coverage based on the STM observations as depicted in Fig. 3.7(a). The networks appeared to be denser (Fig. 3.7b) when compared to the deposition at 250 ^{o}C. However, the networks formed remained disordered.

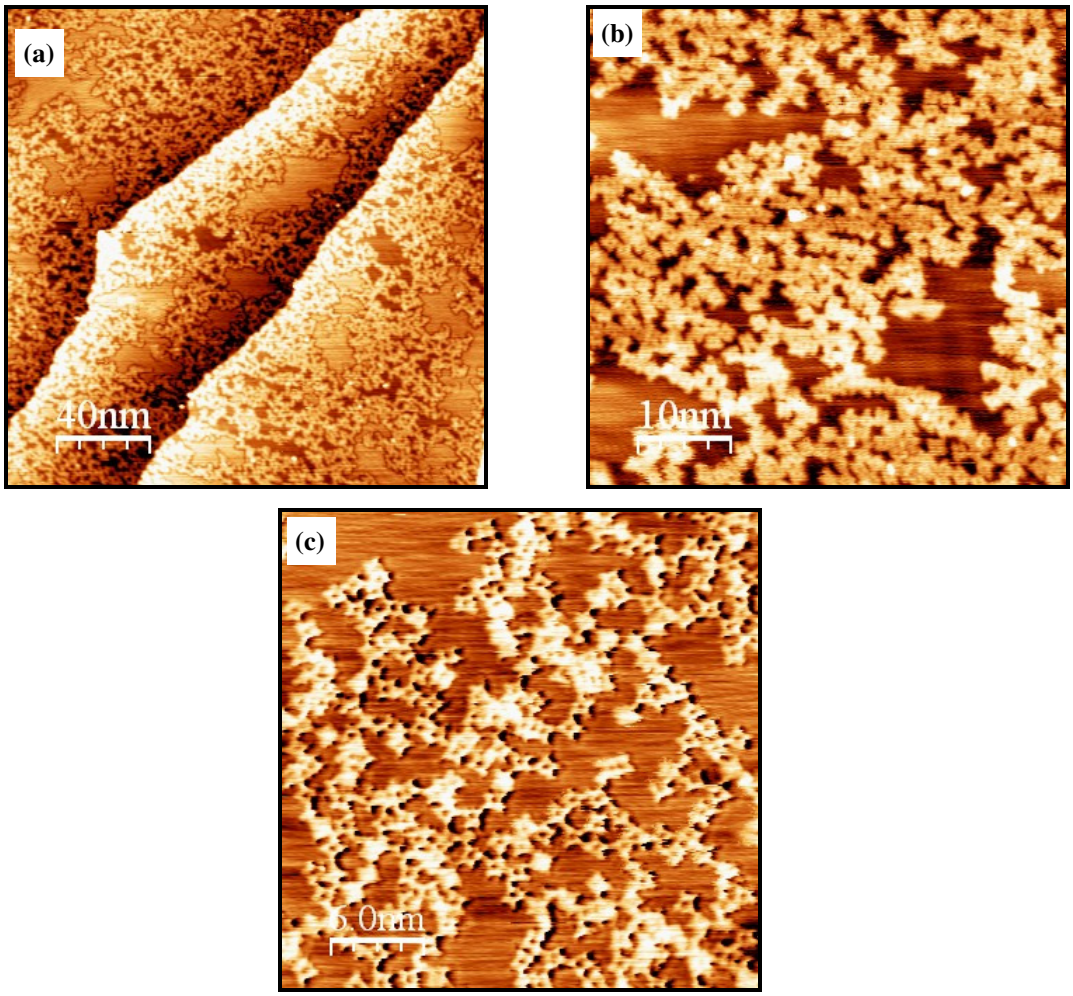

Fig. 3.7 (a) STM image (200 nm ×200 nm, Vs = +0.8 V, I = 0.2 nA); (b) STM image (50 nm ×50 nm, Vs = +2.5 V, I =0.3 nA); (c) STM image (30 nm ×30 nm, Vs = +0.1 V, I =0.3 nA) on Au(111) when the substrate is held at 300 ^{o}C.

When the molecule was deposited on a surface held at 350 ^{o}C, networks were formed at the step-edges as observed in Fig. 3.8 (a) and (b). However, the networks were observed to be partially decomposed with amorphous blobs appearing on the STM images and the macrocycles of some of the molecules are decomposed.

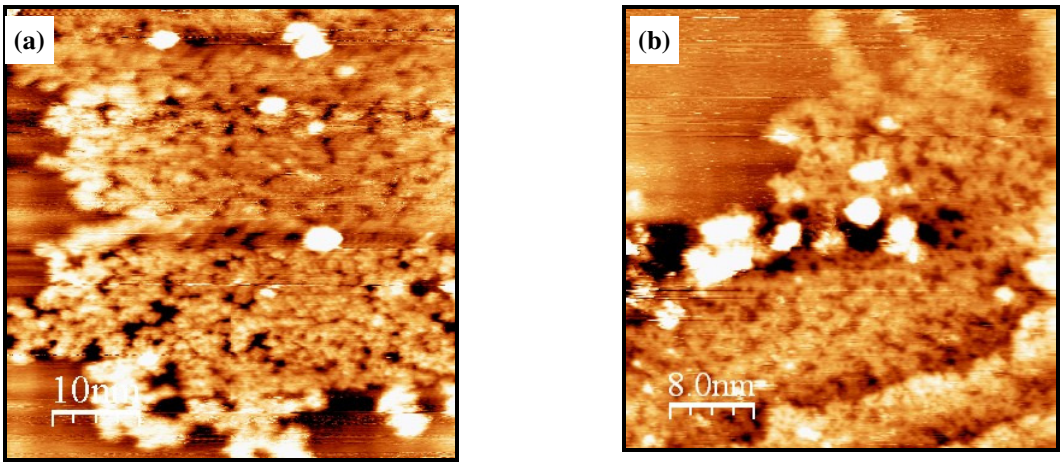

Fig. 3.8 (a) STM image (50 nm × 50 nm, Vs = -0.8V, I = 0.3 nA); (b) STM image (50 nm × 50 nm, Vs = -0.1 V, I =0.3 nA) on Au(111) when the substrate is held at 350 °C.

3.2.5. X-ray Photoemission Spectroscopy (XPS) of TAPP on Au(111) Surface at Elevated Temperature.

The XPS measurements reported in this section were recorded using an Al Kα X-ray source. Therefore, the resolution of the spectra is not directly comparable with the spectra obtained using the synchrotron radiation techniques presented above.

Fig. 3.9 shows a comparison of N 1s XPS spectra recorded before and after polymerisation via deposition on a room temperature substrate and a substrate held at 300 °C. A 1 eV shift in the binding energy is observed between the RT sample and the 300 °C sample. The main point to highlight is that the N 1s spectra from experiments at elevated substrate temperature are comparable with the N 1s spectrum performed on RT substrate (after annealing at 350 °C) for the polymerisation process. The intensity at higher binding energy in all N 1s spectra has decreased on heating and this is a signature that a reaction of the amino groups has occurred.

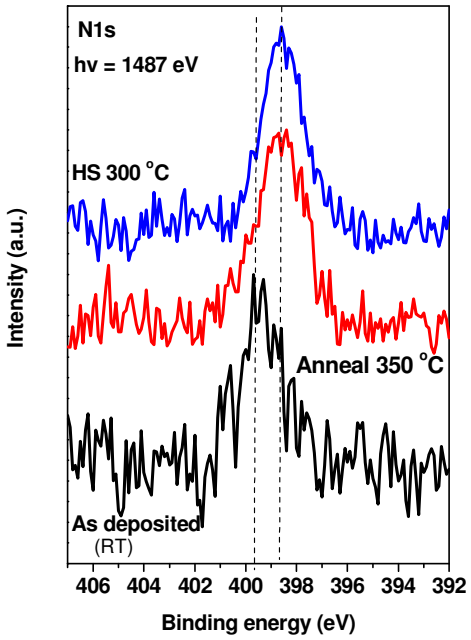

Fig. 3.9 Comparison of XPS N 1s spectra of as deposited of TAPP on Au(111), anneal at 350 °C and substrate temperature elevated to 300 °C.

Based on the three experiments at different substrate temperatures, the STM data shows that deposition on the 300 °C surface provides the best results as a better networks coverage is obtained. However, the data obtained by holding the substrate at elevated temperature are comparable with data from the room temperature experiments and therefore this procedure does not assist in the ordering of the network.

3.2.6. Scanning Tunnelling Microscopy (STM) of TAPP on Cu(111) Surface at Room Temperature (RT).

Self assembled monolayers of TAPP on Cu(111) showed significant differences from those prepared on Au(111). The deposition is carried out for approximately 120 minutes to get one ML on Cu(111). Fig. 3.10(a) shows a large area of TAPP molecules on the Cu(111) surface. There were a number of domains observed on the terrace but the orientation of the domains appears random, unlike on Au(111) where the domains were rotated at 120° relative to each other. The unit cell is square, with dimensions of (1.60 ± 0.05) nm × (1.60 ± 0.05) nm. When the sample was annealed to 110 °C, the molecules became mobile and in some areas developed into disordered patches as depicted in Fig. 3.10(b). Despite the disordered domains, there were still local patches of order which were not densely packed due to the presence of defects (insert of Fig. 3.10b). These regions have an oblique unit cell with dimensions of (1.81 ± 0.05) nm × (1.81 ± 0.05) nm that were aligned at (70 ± 2)° relative to the lattice vector of the unit cell.

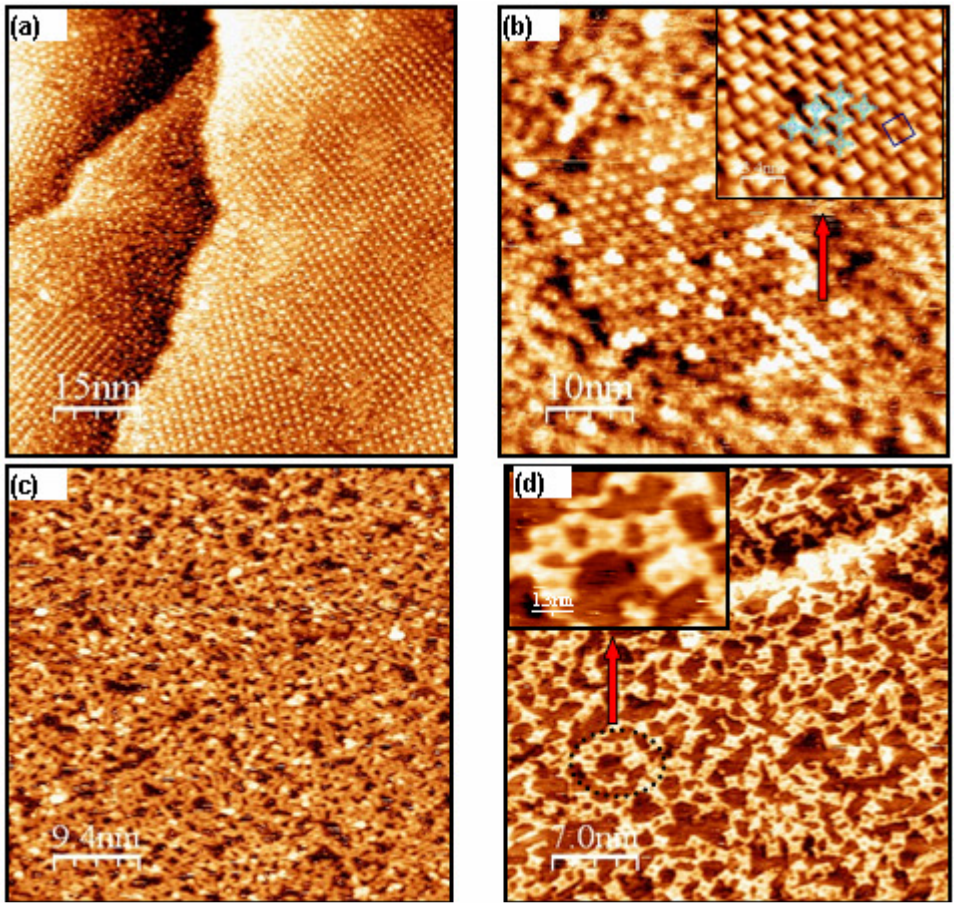

Fig. 3.10(a) STM image (75 nm × 75 nm, Vs = +1.3 V, I =0.4 nA); (b) STM image (50 nm × 50 nm, Vs =+ 0.3 V, I =0.3 nA) after annealing at 110 °C; Insert:(Vs = -0.1 V, I = 0.2 nA); (c) STM image (46 nm × 46 nm, Vs = +1.6 V, I =0.3 nA) at 240 °C annealing (polymerisation); (d) STM image (35 nm × 35 nm, Vs = -1.7 V, I =0.3 nA) after polymerisation.

The onset of polymerisation was observed at a temperature of 150 °C much lower that the corresponding temperature of 350 °C for the Au(111) system (Fig. 3.2). According to the XPS measurements which will be discussed in the following section, the polymerisation was fully completed at around 240 °C. The networks after polymerisation were comprised mostly of short oligomers as observed in Fig 3.10(c and d).

3.2.7. X-ray Photoemission Spectroscopy (XPS) of TAPP on the Cu(111) Surface at Room Temperature (RT).

The XPS spectrum of N 1s on Cu(111) has a large contribution at lower binding energy from the Cu Auger LMM peak (BE = 404.0 eV for Al K_α radiation). Hence, a baseline subtraction method was carried out before the spectrum was deconvolved by Voigt fitting. This nonlinear baseline was subtracted using Fityk [20] before the fitting of the desired peaks was performed.

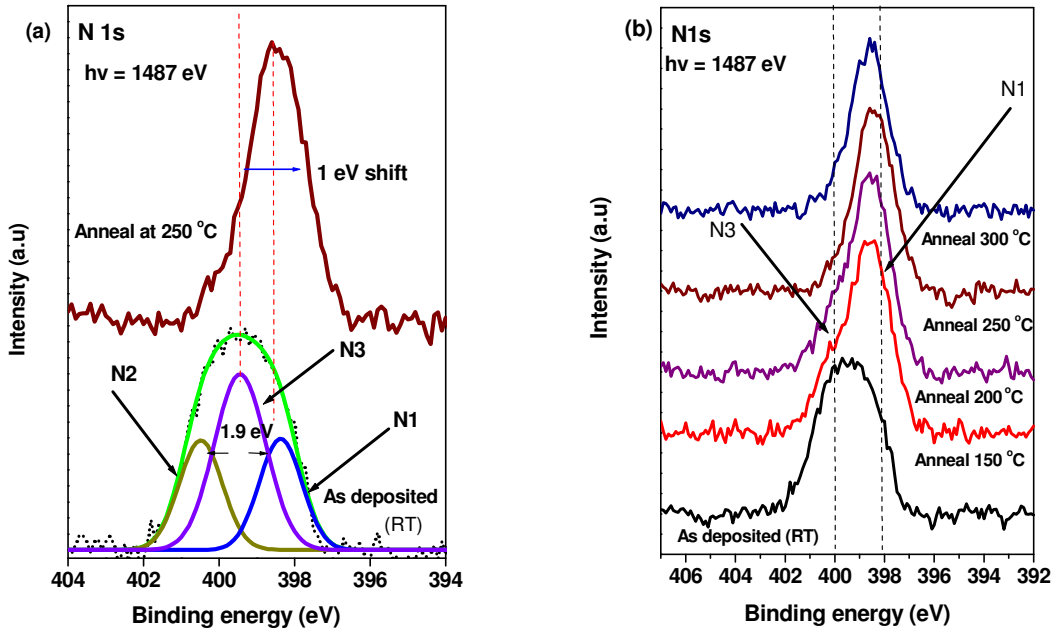

Fig. 3.11 XPS results of (a) the peak fitting analysis of the N 1s spectra for as deposited and after polymerisation 240 °C; (b) the evolution of different annealing temperature of TAPP on Cu(111) deposited at room temperature.

Fig. 3.11 shows the N 1s core level spectra of TAPP on Cu(111) as deposited at room temperature and after annealing at 250 °C for 10 minutes. The nitrogen spectrum is deconvolved into Voigt profiles with a fixed area ratio of N1:N2:N3 of 1:2:1which are assigned to azanitrogen atoms (N1), the pyrrolic nitrogen atoms (N2) and the nitrogen atoms in the amino groups (N3) as described in Section 3.2.1 under XPS analysis (refer to Fig. 3.1). The energy splitting between N1 and N2 is 1.9 eV which is in agreement with the reported value by Krasnikov *et al.* [16] for free base porphine (H_2P). Two processes are observed to take place as the sample is annealed: (i) the polymerisation process; and (ii) the metalation process of the N atoms in the macrocycle by Cu atoms either extracted from the Cu surface or Cu adatoms [21,22]. After annealing the N3 peak shows a decrease in intensity and single peak at a binding energy of 398.5 eV is observed in the 250 °C spectrum in agreement with the value reported by Doyle *et.al.* [21] for tetra(bromophenyl) porphyrin on Cu(111). The total intensity the N 1s peak for the as-deposited and the polymerised samples are almost 1:1. The intensity of the peak at 398.5 eV is larger after annealing due to the change in chemical environment produced by the polymerisation reaction, which has caused a shift of the N3 peak to lower binding energy [3].

A 1 eV shift towards lower binding energy was also observed in the polymerisation of TAPP on Au(111) (see Fig. 3.4) after polymerisation at 350 °C -N=N- bonding is more

likely to occur after polymerisation instead of –HN-NH- bonding, evidence for this is provided by the shift towards lower binding energy of the N2 peak which coincides with the binding energy of the azanitrogen (N1) in the macrocycle. The on-going DFT calculations by Dr. Corrine Dufaure from ENSIANET/CIRIMAT, Toulouse, France are performed to confirm the hypothesis proposed above.

The evolution of the N 1s XPS peak for different annealing temperatures for TAPP molecules on Cu(111) is shown in Fig. 3.11(b). From the STM images, polymerisation of TAPP has started to occur at 150 ^{o}C. As the annealing temperature is increased to 200 ^{o}C, a slight decrease in intensity on the higher BE side of the peak is observed. A further decrease in the intensity at higher BE is observed when the annealing temperature is 250 ^{o}C. The annealing at 250 ^{o}C shows the most obvious change in the spectrum and no significant change is observed when the temperature is increased to 300 ^{o}C showing that metalation of the macrocycle and the polymerisation processes are completed at this stage.

3.2.8. Scanning Tunnelling Microscopy (STM) of TAPP on the Cu(111) Surface Held at Elevated Temperatures.

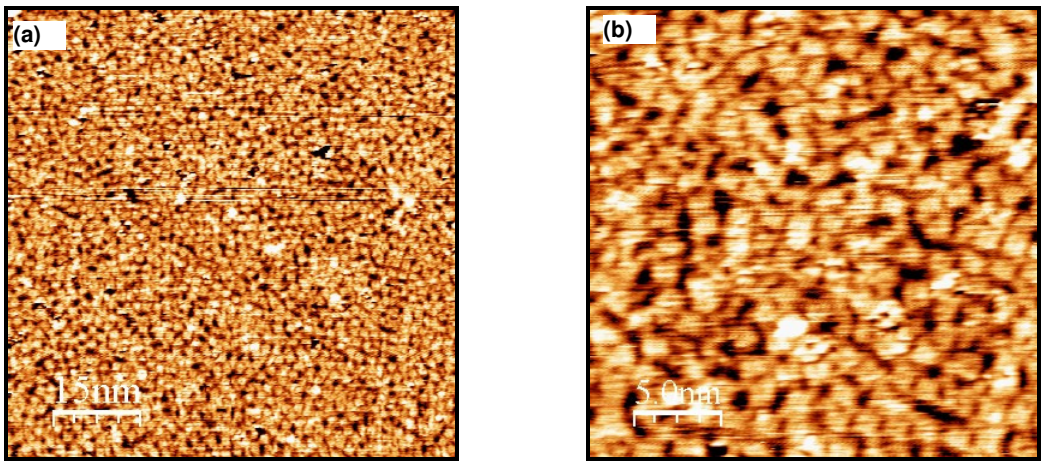

Fig. 3.12 (a) STM image (75 nm × 75 nm, Vs = +0.9 V, I = 0.2 nA); (b) STM image (25 nm × 25 nm, Vs = +1.0 V, I =0.2 nA) on Cu(111) when the substrate is held at 150 ^{o}C.

Fig. 3.12 shows STM images recorded at RT after deposition of TAPP onto a Cu(111) substrate held at 150 ^{o}C for 120 minutes. It is shown that increasing the substrate temperature from room temperature to 150 ^{o}C provides denser network coverage (approximately 0.9 ML) due to the increase in the diffusion of molecules on the surface [18]. The molecules form disordered oligomers with a variation in their lengths. A similar observation is also made for deposition on the 200 ^{o}C substrate for 60 minutes

where again oligomers are formed and consist of highly disordered covalently linked molecules as shown in Fig. 3.13.

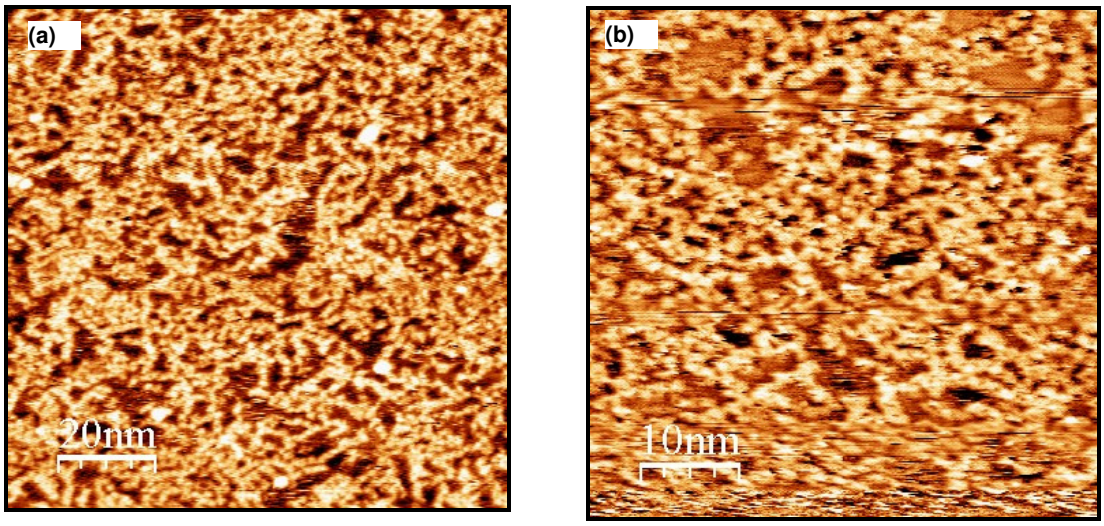

Fig. 3.13 (a) STM image (100 nm × 100 nm, Vs = -1.49 V, I = 0.1 nA); (b) STM image (50 nm × 50 nm, Vs = -1.0 V, I =0.1 nA) on Cu(111) when the substrate is held at 200 °C.

3.2.9. X-ray Photoemission Spectroscopy (XPS) of TAPP on the Cu(111) Surface Held at Elevated Temperature.

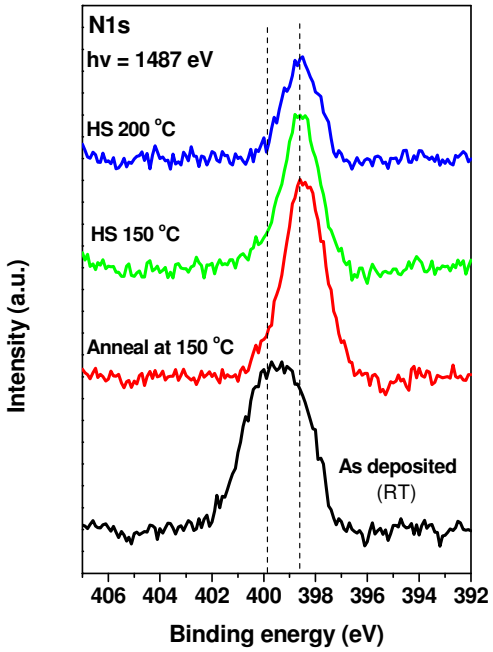

Fig. 3.14 Comparison of XPS N 1s spectra of as deposited (RT) of TAPP on Cu(111), anneal at 150 °C, hot surface experiments at 150 °C and 200 °C.

N 1s XPS spectra were recorded from TAPP molecules deposited on Cu(111) held at 150 ^{o}C and 200 ^{o}C. In Fig. 3.14, these spectra are compared with that recorded from room temperature substrate and subsequently annealed to 150 ^{o}C. A 1 eV shift in the binding energy is measured when compared with the sample deposited at room temperature and again metalation of the macrocycle with Cu atoms also occurred.

In summary, the self-assembled TAPP monolayer on Cu(111) has a square unit cell of dimension 1.60 nm x 1.60 nm. The networks formed by deposition on substrates at room temperature or at elevated temperatures produce disordered covalently bonded networks. Two phenomena occur when the sample is annealed: (i) the polymerisation of TAPP on Cu(111) starts at 150 ^{o}C and (ii) metalation with either Cu adatoms or Cu atoms from the surface occurs.

3.2.10. Scanning Tunnelling Microscopy (STM) of TAPP Self-assembled on the Ag(111) Surface at Room Temperature (RT).

Fig. 3.15(a) shows a 200 nm × 200 nm STM image of 1 ML of self-assembled TAPP molecules on Ag(111). The deposition is carried out for 30 minutes to get one ML on Ag(111). It is possible to identify individual TAPP molecules, which are resolved as square features (Fig. 3.15b). The TAPP molecule is imaged as two elevated parallel rods with a gap in between (see Fig.3.15c). This is attributed to a distortion of the macrocycle with two opposing pyrrole positions appearing elevated from the surface while the other two appear lowered towards the surface (Fig 3.3 and Fig. 3.15c). This configuration is also reported by Buchner *et. al* [12] for 2HTPP molecules on Ag(111). According to Buchner *et al.* [12], this is the lowest energy configuration for the molecule even in the gas phase. The STM image is dominated by the details of the electronic structure at low bias voltages, whereas the topography of the adsorbed molecule becomes important at high bias voltages [23]. Therefore, the appearance of the individual molecules in these STM images obtained at bias voltages of + 0.7 V in the current experiment should reflect the topography of the TAPP molecule. The azimuthal angle of the porphyrin relative to the unit cell vector was measured as (30 ± 2) ^{o} corresponding to T-type stacking similar to that observed by Buchner *et. al* [12].

The square unit cell has lattice vectors of $\boldsymbol{a}$ = (1.55 ± 0.1) nm, $\boldsymbol{b}$ = (1.55 ± 0.1) nm (Fig. 3.15d). The molecules on the Ag(111) surfaces are not densely packed. Hence, it is not possible to image molecules at room temperature due to their high mobility. In

addition, to induce the reaction between the amino groups requires an annealing temperature of at least 150 °C which was observed for Cu(111) and as high as 350 °C on Au(111). However, 75 % of the TAPP molecules desorb from the Ag surface at a temperature of 100 °C and no networks due to polymerisation were observed. The current scenario on Ag(111) has made the polymerisation unfeasible and therefore, deposition on substrate held at elevated temperature was pursued.

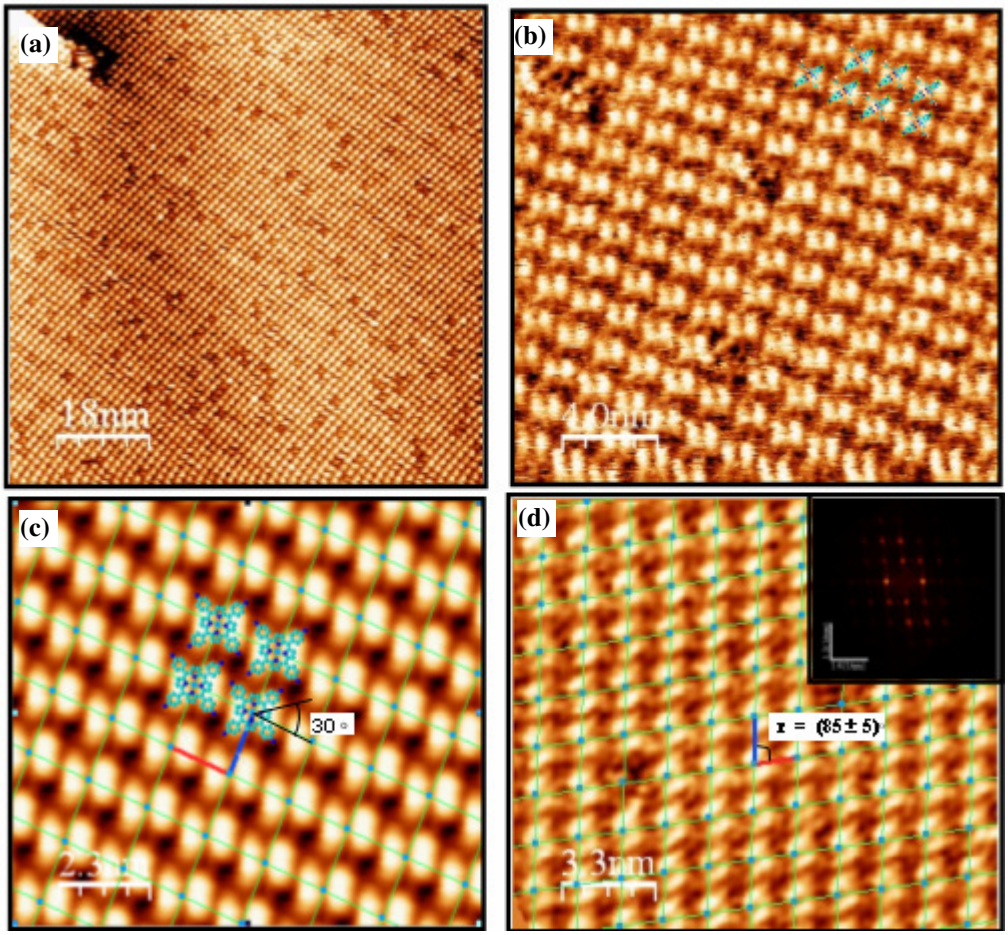

Fig. 3.15 Self-assembly of TAPP on Ag(111) (a) STM image (90 nm × 90 nm, Vs = +0.7 V, I =0.1 nA); (b) STM image (30 nm × 30 nm, Vs =+ 1.07 V, I =0.9 nA); (c)Enlarged Image of (b), which is superimposed with corresponding TAPP structures. The proximate substituents show a 'T'-shaped arrangement; (d) The WSxM analysis to determine the lattice constant Insert: FFT Image from STM (35 nm ×35 nm, Vs = -1.7 V, I =0.3 nA).

3.2.11. X-ray Photoemission Spectroscopy (XPS) of TAPP Self-assembled on the Ag(111) Surface at Room Temperature (RT).

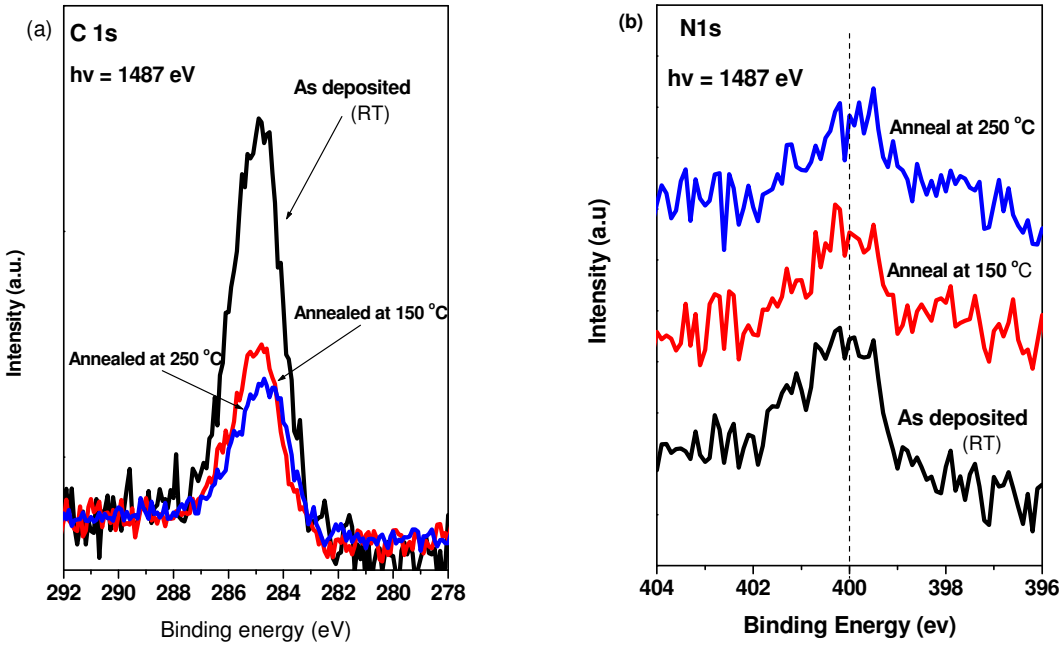

Fig. 3.16 Comparison of XPS (a) C 1s and (b) N 1s spectra of as deposited of TAPP on Ag(111), annealed at 150 °C and 250 ° C for polymerisation reactions.

Fig. 3.16(a) shows the evolution of C 1s after annealing at 150 °C and 250 °C. The C 1s intensity decreases as the annealing temperature is increased. The C 1s to Ag 3*d* ratio showed that the TAPP coverage has reduced to one third after annealing to 250 °C. The N 1s core level is at a binding energy close to a plasmon [24] energy loss line from the Ag $3d_{3/2}$ peak. The effect of this phenomenon could be reduced by using angular resolved XPS as reported by Schmitz *et al.*[24]. However this method could not be employed here as it was not possible to change the emission angle in the XPS system used for these experiments. Hence, the background was subtracted using the Origin® software [25]. The N 1s region of the clean Ag(111) surfaces was measured and scaled to match the background in the N 1s spectrum. The N 1s spectrum is then divided by the clean Ag(111) spectrum to obtain the background corrected spectra.

The N 1s spectra have poor signal to noise ratio and were unable to provide an accurate Gaussian fitting but they are still adequate to provide a qualitative comparison. The N 1s peak did not shift to lower BE (1 eV shift) after annealing at 150 °C and 250 °C as shown in Fig. 3.16(b). The intensity of the peaks after each anneals decreased indicating that fewer molecules remain on the surface as observed in the C 1s spectra.

3.2.12. Scanning Tunnelling Microscopy of TAPP on the Ag(111) Surface Held at Elevated Temperature.

Fig. 3.17 shows 0.25 ML of TAPP deposited on the Ag(111) surface held at 200 ^{o}C for 45 minutes. The STM images were recorded at RT. It is observed that small networks, made up of 30 to 40 molecules, are interconnected randomly on the Ag(111). It appears that the networks are all over the surface. The networks formed consist mainly of oligomers.

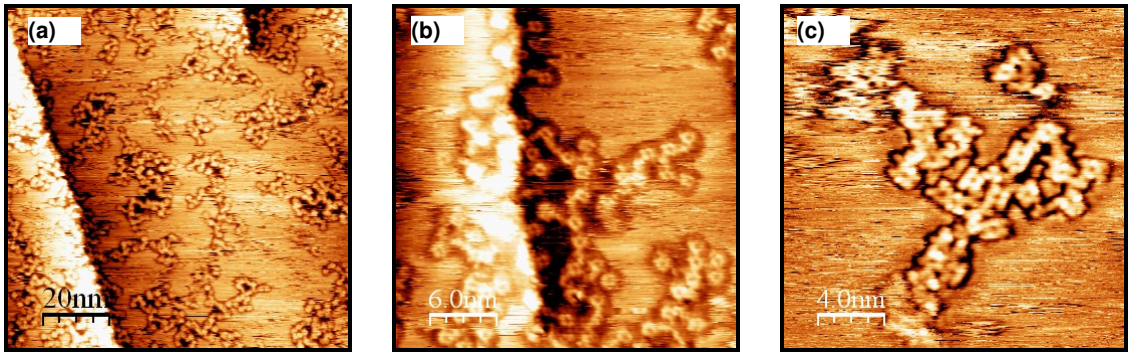

Fig. 3.17 (a) STM image (100 nm × 100 nm, Vs =+0.5 V, I = 0.1 nA); (b) STM image (30 nm × 30 nm, Vs = +0.5 V, I =0.1 nA); (c) STM image (20 nm × 20 nm, Vs = -1.49 V, I = 0.1 nA) on Ag(111) when the substrate is held at 200 ^{o}C .

The STM images show that the 250^{o} C substrate temperature experiments (see Fig. 3.18a-c) are similar to the experiments with substrate held at 200 ^{o}C. The coverage is less than 0.5 ML for the same deposition time as deposition carried out on the substrate held at 200 ^{o}C. Small patches of network are observed and consist of short oligomers.

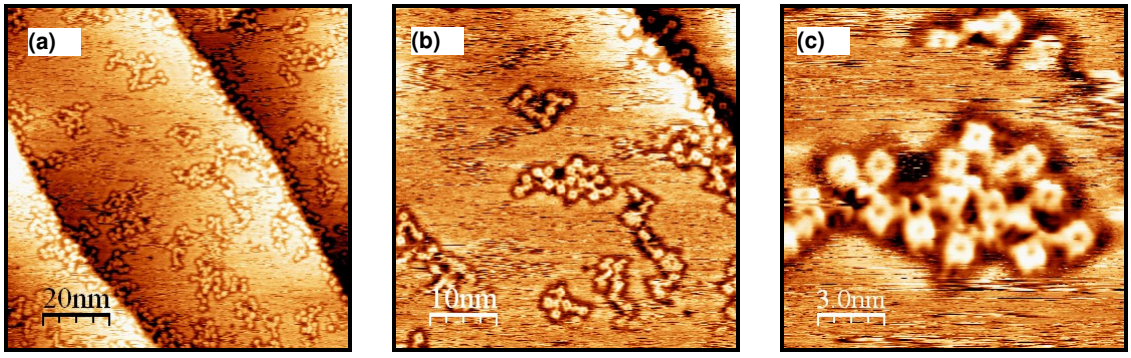

Fig. 3.18 (a) STM image (100 nm × 100 nm, Vs =+0.6 V, I = 0.2 nA); (b) STM image (50 nm × 50 nm, Vs = +0.6 V, I =0.2 nA); (c) STM image (15 nm × 15 nm, Vs = +0.6 V, I = 0.2 nA when the substrate is held at 250 ^{o}C.

A different growth pattern is observed with the substrate temperature at 300 ^{o}C during the deposition. The coverage of this sample is estimated at 0.3 ML for a deposition time of 45 minutes. The growth of TAPP networks is concentrated at the step-edges as

depicted in Fig. 3.19. The networks formed are interconnected randomly. From these three experiments, the hotter substrate temperature (300 ^{o}C) discourages the networks from locating on the terraces surface but promote the growth from the step-edges as shown in Fig. 3.19(a).

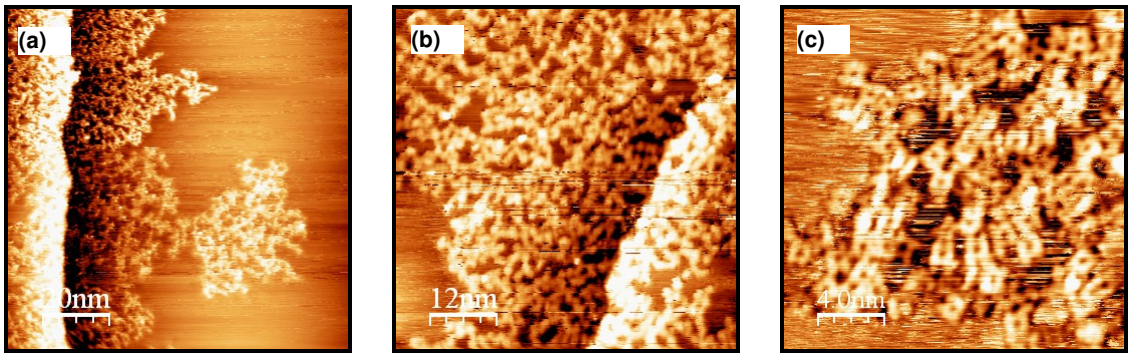

Fig. 3.19 (a) STM image (100 nm × 100 nm, Vs =+1.3 V, I = 0.1 nA); (b) STM image (60 nm × 60 nm, Vs = +0.2 V, I =0.4 nA); (c) STM image (20 nm × 20 nm, Vs = +0.8 V, I = 0.3 nA) on Ag(111) when the substrate is held at 300 ^{o}C.

3.2.13. X-ray Photoemission Spectroscopy (XPS) of TAPP on the Ag(111) Surface Held at Elevated Temperature.

Fig. 3.20(a and b) illustrates the comparison of C 1s and N 1s spectra for a substrate held at different elevated temperatures of (200 ^{o}C, 250 ^{o}C and 300 ^{o}C) during a 45 minute deposition of TAPP. The coverage in all three experiments is approximately 0.5 ML (as determined from the C 1s/Ag 3*d* ratio) as seen from the C 1s spectra in Fig. 3.20(a). The N 1s peak from the 300 ^{o}C experiment had a lower intensity as compared to substrate held at the 200 ^{o}C and 250 ^{o}C, respectively. This could suggest more dissociation of amino groups from TAPP to form covalently C-C bonded networks as illustrated in Scheme 3.1(c) compared to HN-NH or –N=N- bonding. However, this is highly speculative, due to the poor signal to noise ratio on the N 1s measurements.

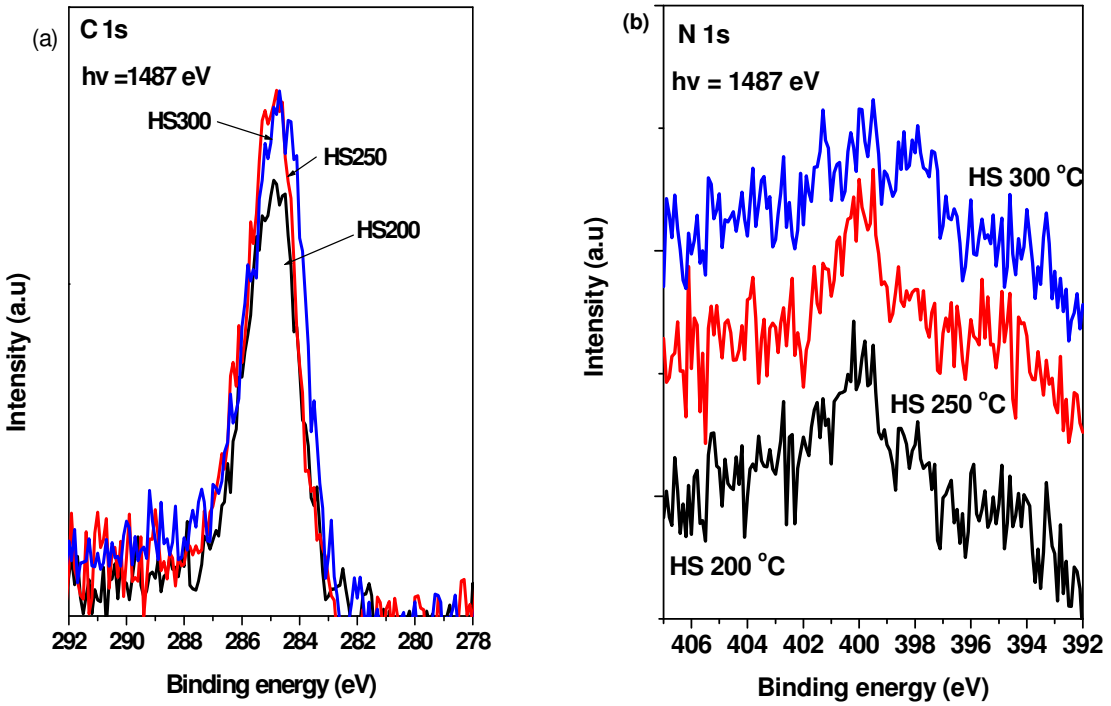

Fig. 3.20 Comparison of XPS (a) C 1s; (b)N 1s of TAPP on Ag(111) deposited when substrate is held at 300 °C, 250 °C and 200 °C.

The polymerisation of TAPP on an Ag(111) room temperature substrate was not successful. However, deposition on an Ag(111) substrate held at elevated temperature resulted in polymerised TAPP molecules. Nonetheless, the polymerised structures formed in these experiments are disordered oligomers.

3.3 Summary.

TAPP molecules self-assembled on the Au(111), Ag(111) and Cu(111) surfaces. The unit cell of the TAPP on Au(111) is square with measured cell constants of (1.57 ± 0.1) nm × (1.57 ± 0.1) nm. The T-stacking arrangement with the azimuthal angle of (26 ° ± 2)° relative to the lattice unit cell vectors was observed. The covalently bonded networks were successfully formed on the room temperature substrate and substrate held at 300 °C although they are not well-ordered.

TAPP molecules self-assembled on Cu(111) surfaces with a square unit cell measured as (1.60 ± 0.05) nm × (1.60 ± 0.05) nm. However, the domains are randomly ordered

relative to each other, and as such, the molecular overlayer was not commensurate with the underlying substrate. Nonetheless, polymerisation of TAPP molecules on Cu(111) occurs at 150 ^{o}C and annealing at this temperature also resulted in the metalation of the porphyrin macrocycle with Cu adatoms or Cu atoms from the surface. Full metalation occurred at 250 ^{o}C as illustrated by XPS measurements.

Among the three metal surfaces that have been investigated, it appears that Ag(111) has the weakest interaction with the TAPP molecules. Almost 75 % of the TAPP molecules would desorb from the Ag(111) after as low as 100 ^{o}C annealing. The measured unit cell of self-assembled TAPP molecules on Ag(111) is square at (1.55 ± 0.1) nm × (1.55 ± 0.1) nm. The T-stacking arrangement with the azimuthal angle of (30 ^{o}± 2)^{o} relative to the lattice unit cell vectors was also observed in this system. The molecules polymerised on this surface above a temperature of 200 ^{o}C to form covalently bonded networks.

The TAPP molecules on Au(111), Cu(111) and Ag(111) generally can be polymerised successfully by room temperature deposition and subsequent annealing and by deposition on a substrate held at elevated temperature. However, the networks formed are short-range, disconnected and consist of mainly oligomers. More creative and innovative approach such as the introduction of a second type of molecule (e.g. PTCDA) could be explored in order to achieve more connected and long ranged networks.

References:

[1] A. Dmitriev, H. Spillmann, N. Lin, J.V. Barth, K. Kern. *Modular assembly of two-dimensional metal-organic coordination networks at a metal surface,* Angew. Chem. Int. Ed. **42** (2003) 2670.

[2] J.A. Theobald, N.S. Oxtoby, M.A. Phillips, N.R. Champness, P.H. Beton. *Controlling molecular deposition and layer structure with supramolecular surface assemblies,* Nat. **424** (2003) 1031.

[3] D. Sun, F.S. Tham, C.A. Reed, L. Chaker, P.D.W. Boyd. *Supramolecular fullerene-porphyrin chemistry. Fullerene complexation by metalated "jaws porphyrin" hosts,* J. Am. Chem. Soc. **124** (2002) 6604.

[4] S.A. Krasnikov, C.M. Doyle, N.N. Sergeeva, A.B. Preobrajenski, N.A. Vinogradov, Y.N. Sergeeva, A.A. Zakharov, M.O. Senge, A.A. Cafolla. *Formation of extended covalently bonded Ni porphyrin networks on the Au (111) surface,* Nano Res. (2011) 1.

[5] M. Di Marino, F. Sedona, M. Sambi, T. Carofiglio, E. Lubian, M. Casarin, E. Tondello. *STM investigation of temperature-dependent two-dimensional supramolecular architectures of C60 and amino-tetraphenylporphyrin on Ag (110),* Langmuir. **26** (2010) 2081.

[6] L. Grill, M. Dyer, L. Lafferentz, M. Persson, M.V. Peters, S. Hecht. *Nano-architectures by covalent assembly of molecular building blocks,* Nat. **2** (2007) 687.

[7] N. Zwaneveld, R. Pawlak, M. Abel, D. Catalin, D. Gigmes, D. Bertin, L. Porte. *Organized formation of 2D extended covalent organic frameworks at surfaces.* J. Am. Chem. Soc. **130** (2008) 6678.

[8] M. Treier, R. Fasel, N.R. Champness, S. Argent, N.V. Richardson. *Molecular imaging of polyimide formation,* Phys. Chem. Chem. Phys. **11** (2009) 1209.

[9] M. Treier, N.V. Richardson, R. Fasel. *Fabrication of surface-supported low-dimensional polyimide networks,* J. Am. Chem. Soc. **130** (2008) 14054.

[10] J. Brede, M. Linares, R. Lensen, A.E. Rowan, M. Funk, M. Bröring, G. Hoffmann, R. Wiesendanger. *Adsorption and conformation of porphyrins on metallic surfaces,* J. Vac. Sci. Technol. B. **27** (2009) 799.

[11] M. Marschall, J. Reichert, A. Weber-Bargioni, K. Seufert, W. Auwärter, S. Klyatskaya, G. Zoppellaro, M. Ruben, J.V. Barth. *Random two-dimensional string networks based on divergent coordination assembly,* Nat. Chem. **2** (2010) 131.

[12] F. Buchner, I. Kellner, W. Hieringer, A. Görling, H.P. Steinrück, H. Marbach. *Ordering aspects and intramolecular conformation of tetraphenylporphyrins on Ag (111),* Phys. Chem. Chem. Phys. **12** (2010) 13082.

[13] I. Horcas, R. Fernández, J.M. Gómez-Rodríguez, J. Colchero, J. Gómez-Herrero, A.M. Baro. *WSXM: A software for scanning probe microscopy and a tool for nanotechnology,* Rev. Sci. Instrum. **78** (2007) 013705.

[14] M.G. Walter, C.C. Wamser. *Synthesis and characterization of electropolymerized nanostructured aminophenylporphyrin films,* J. Phys. Chem. **114** (2010) 7574.

[15] M. Nardi, R. Verucchi, C. Corradi, M. Pola, M. Casarin, A. Vittadini, S. Iannotta. *Tetraphenylporphyrin electronic properties: a combined theoretical and experimental study of thin films deposited by SuMBD,* Phys. Chem. Chem. Phys. **12** (2010) 871.

[16] S.A. Krasnikov, N.N. Sergeeva, M.M. Brzhezinskaya, A.B. Preobrajenski, Y.N. Sergeeva, N.A. Vinogradov, A.A. Cafolla, M.O. Senge, A.S. Vinogradov. *An x-ray absorption and photoemission study of the electronic structure of Ni porphyrins and Ni N-confused porphyrin,* J. Phys.B: Condens. Matter. **20** (2008) 235207.

[17] N. Schmidt, R. Fink, W. Hieringer. *Assignment of near-edge x-ray absorption fine structure spectra of metalloporphyrins by means of time-dependent density-functional calculations,* J. Chem. Phys. **133** (2010) 054703.

[18] O. Ourdjini, R. Pawlak, M. Abel, S. Clair, L. Chen, N. Bergeon, M. Sassi, V. Oison, J.M. Debierre, R. Coratger. *Substrate-mediated ordering and defect analysis of a surface covalent organic framework,* Phys. Rev. B. **84** (2011) 125421.

[19] M.O. Blunt, J.C. Russell, N.R. Champness, P.H. Beton. *Templating molecular adsorption using a covalent organic framework,* Chem. Commun. **46** (2010) 7157.

[20] M. Wojdyr. *Fityk: a general-purpose peak fitting program,* J. Appl. Cryst. **43** (2010) 1126.

[21] C.M. Doyle, S.A. Krasnikov, N.N. Sergeeva, A.B. Preobrajenski, N.A. Vinogradov, Y.N. Sergeeva, M.O. Senge, A.A. Cafolla. *Evidence for the formation of an intermediate complex in the direct metalation of tetra (4-bromophenyl)-porphyrin on the Cu (111) surface,* Chem. Commun. **47** (2011) 12134.

[22] K. Diller, F. Klappenberger, M. Marschall, K. Hermann, A. Nefedov, C. Woell, J.V. Barth. *Self-metalation of 2H-tetraphenylporphyrin on Cu(111): An x-ray spectroscopy study,* J. Chem. Phys. **136** (2012) 014705.

[23] F. Buchner, K.G. Warnick, T. Wo̲lfle, A. Go̲rling, H.P. Steinru̲ck, W. Hieringer, H. Marbach. *Chemical fingerprints of large organic molecules in scanning tunnelling microscopy: imaging adsorbate− substrate coupling of metalloporphyrins,* The J. Phys. Chem. C. **113** (2009) 16450.

[24] C.H. Schmitz, M. Schmid, S. Ga̲rtner, H.P. Steinru̲ck, J.M. Gottfried, M. Sokolowski. *Surface polymerization of poly (p-phenylene-terephthalamide) on Ag (111) investigated by X-ray photoelectron spectroscopy and scanning tunnelling microscopy,* The J. Phys. Chem. C. (2011).

[25] http://www.originlab.com/.

Chapter 4:

Ultraviolet Photoelectron Spectroscopy (UPS) Measurements of TAPP Molecules on Au(111) and Cu(111) Surfaces.

4.0 Introduction.

The properties of an interface between a π-conjugated organic semiconductor and a metal substrate are of great importance for the development of future organic-inorganic devices. The key features concern the interface energy level alignment [1], the conformation of the molecules [2] as well as the geometrical order of the interface superstructure [3]. The first two items are responsible for interface electronic and spin transport, the latter also influences the morphology of further layers in the thin organic film and in turn its electronic properties. Recently, it was shown that the molecular conformation can have a strong influence on the electronic properties of the first adsorbed layer [4]. Molecule-metal interaction can induce conformational changes including molecular distortion and metalation affecting the interface electronic structure [5,6]. Moreover it was recently found that such electronic properties may not only be different to those of the less interacting second and deeper layers but that even *within* the first monolayer (ML), the balance between molecule-substrate and molecule-molecule interaction can change as a function of sub-monolayer (sub-ML) coverage [3,4].

In the previous chapter, extensive STM studies were performed on TAPP deposition on noble metals. The main goal of this chapter is to study the evolution of the electronic structure of the π-conjugated organic molecule 5,10,15,20-tetrakis(4-aminophenyl)porphyrin (TAPP) on noble metal substrates, from the earliest stages of adsorption (sub-ML), to the completion of a ML and to a multilayer film of weakly interacting molecules. The effect of the polymerisation process on the electronic structure is also discussed.

UPS analysis was performed as a function of coverage from the sub-ML regime to a multilayer film. This technique probes the valence band (VB) electronic structure and is particularly adapted to study the evolution of molecular states upon adsorption. Moreover, by measuring the low energy secondary electrons cut-off (SECO), the surface work function (WF) can be probed, a crucial parameter to assess the interface energy level alignment. Since UPS is a sensitive technique, the interface electronic structure can be inferred by comparing the spectra of the sub-ML and ML to that of a multilayer film in which the molecules interact weakly among each other through van der Waals forces and in which the interface contribution to the spectrum is no longer visible. Studying the interface behaviour of a given molecule with two noble metal substrates of different reactivity such as Au(111) and Cu(111) is used as a further means to pin point the modifications of molecular orbital upon adsorption.

4.1. Experimental.

The experiments were performed on the STM/PES apparatus in the Nanostructure laboratory at the Institut Matériaux Microélectronique Nanosciences de Provence (IM2NP) in Marseille, France. All samples were prepared under ultra-high vacuum conditions. The experimental parameters for the STM and XPS measurements are described in more detail in Sections 2.2 and 2.3.

UPS measurements were performed with a He I discharge lamp ($h\nu$ = 21.22 eV). UPS spectra were collected at normal emission (NE) and 45º emission with an Omicron EA125 hemispherical analyzer in a high magnification mode (angular acceptance ± 7º). The overall energy resolution is limited by the sample temperature (room temperature), and is about 100 meV. The binding energy is referenced to the Fermi level of the substrate or sample holder according to the thickness of the molecular film. All spectra were recorded with the sample biased at -9 V in order to avoid the influence of the analyzer secondary electrons and to obtain a clear SECO. The -9 V potential was provided by a battery between the manipulator and ground.

4.2. Results and Discussion.

4.2.1. Valence Band Spectra as a Function of Coverage on Au(111).

In Fig. 4.1, the valence band spectra of TAPP on Au(111) are presented for increasing coverage. NE and 45º emission spectra are displayed in panels (a) and (b); respectively. Contributions from He I β-satellite have been subtracted from the original spectra. The spectra of the clean substrate and those at low-coverage were normalized in intensity to fully appreciate the spectroscopic evolution as a function of molecular film thickness. Spectral contributions from direct transitions are dominant in the UPS spectrum of clean Au(111). As a consequence changing the emission angle from normal to 45º strongly affects the spectral features from the π- states of adsorbates. At NE, a structured 5*d* band down to 2 eV binding energy is observed followed by the featureless *sp* plateau. In the vicinity of the Fermi level the Shockley surface state is observed as expected. At 45º, the *sp* band shows density of states and direct transition features down to the Fermi level. When performing UPS on clean Au(111), the energy and momentum (k vector) conservation rules are applied. The difference between initial (E_i) and final (E_f) states is equal to the photon energy: $E_f = hv - E_i$. Since the UV photon has a very small wave vector, the momentum conservation rule is $k_f = k_i + G$, where G is a reciprocal lattice vector. In other words, only vertical transitions between bands in the repeated zone scheme are allowed. By looking at different angles above the sample, a different value of k_f is observed. For instance, by looking at normal emission (NE), states which have negligible parallel k vector ($k_{//} = 0$) are observed. Hence, when there is a change in the sample angle with respect to the analyzer, the $k_{//}$ and k perpendicular will change and a different point in the reciprocal space is observed. Thus, the allowed transitions and spectrum observed are different.

When TAPP molecules are deposited, the direct transitions are attenuated and new substrate features appear. At about 0.8 - 1.0 ML coverage, the substrate contribution to the energy distribution curve (EDC) is the same as that of a polycrystalline Au sample (spectrum labelled with asterisk *) [7]. This is particularly clear for the 45º emission spectrum in which a peak at 4.40 eV increases at 0.25 ML and it is more intense than the direct transition peak at 2.70 eV for 0.5 ML. At NE, the 4.40 eV peak is more intense than the direct transition at 3.80 eV in the same coverage range. Such an effect is largely due to the scattering of the substrate photoelectrons by the adsorbate [8,9].

The correct assignment of the modification of the substrate contribution to the spectra is important to recognize real interface features.

*Both below and above the 5d spectral region, where the substrate dominates the spectrum, molecular orbitals can be detected at sub-ML coverages. At NE, the MOs are al*ready visible at 0.5 ML coverage as two broad features between 7 eV and 10.5 eV. At the same coverage, a peak can be detected at 0.77 eV in the 45º emission spectrum. The intensity of the molecular features increases with coverage and the sample contribution reduces accordingly due to the surface sensitivity of UPS. At 4.0 ML coverage, the substrate is no longer visible and the EDC is that of a thick film of weakly interacting molecules. Changing from NE to 45º emission does influence the shape of the spectrum, this anisotropic emission is well documented for organic molecules [10]. The fact that this anisotropy is observed in the thick film and that it is essentially the same as that in a ML is a sign that the molecules are lying in a flat orientation.

In the following, the behaviour of the low-lying molecular orbitals as a function of coverage is analyzed. Spectra taken at 45º emission angle are focused on, in which the emission of the π-states such as HOMO and HOMO-1 are favoured. In Fig.4.1(c) spectra of the low binding energy region recorded with higher resolution are shown. The peak at 0.77 eV, detected at 0.5 ML, gradually increases in intensity and shifts to higher binding energy for coverages of 0.7 ML and 0.8 ML. At the completion of the first ML a more important change occurs: two peaks are now present in the low binding energy region of the spectrum: positioned at 0.58 eV and 1.05 eV; respectively. Such a strong change in the EDC occurring from 0.8 to 1.0 ML can be understood by first examining the spectra recorded at higher coverages. The spectrum corresponding to 1.6 ML is the sum of the first and second layer molecules. First layer molecule peaks are strongly attenuated due to the short mean free path (MFP) for photoelectrons (about 1 ML) [11]. These features are still recognizable and visible at the lowest binding energy peak of the first layer at 0.58 eV. However, the second layer molecular features prevail in the 1.6 ML spectrum. In fact, the 1.6 ML spectrum has all the features in terms of binding energy and intensity as the 4.0 ML spectrum once it is shifted by 0.27 eV to higher binding energy (see Fig. 4.1). At 4.0 ML, the highest thickness explored, the interface is no longer visible: the HOMO and HOMO-1 are at binding energies of 1.47 eV and 1.89 eV respectively (labelled H and H-1 in Fig. 4.1c). Hence, in this case, the

screening effect, (an effect on the binding energy caused by the influence of the core hole on the excited states which is explained in Ertl and Küppers, 1985 [12]), of the substrate electrons is less effective and the whole spectrum is shifted to higher binding energy. For second layer molecules in the 1.6 ML spectrum, these peaks are positioned at 1.20 eV and 1.62 eV due to the shift of 0.27 eV mentioned above. The energy gap between the two lowest-lying features is 0.42 eV which is considered quite small in light of the fact that the energy difference between the HOMO and HOMO-1 of other metalated porphyrins or phthalocyanines is usually more than 0.9 eV [4]. However, the observation of two low-lying states close in energy is typical for free-based porphyrins or phthalocyanines [13-15]. Consequently, it is then natural to assign the two low-lying peaks of the 1.0 ML spectrum as the HOMO and HOMO-1 since a small value for the difference between these two low-lying features on 1 ML of TAPP/Au(111) is obtained. The question remains open as to why for sub-ML coverage, only one peak is present at low binding energy. A clear interpretation of this effect will not be complete without further investigations including ab-initio calculations. Nevertheless, a possible explanation for this scenario is proposed. The presence of a single peak could be due to different causes. As a matter of fact, completing the first monolayer could involve a non-negligible redistribution of the electronic charge, a fact which may seem at odds with an expectedly weak molecule-substrate interaction for an inert surface as Au(111). However, charge transfer from the molecule to the substrate has been observed in the past and emptied MOs have already been reported for organic molecules on Au(111) [5]. In general, charge transfer is accompanied by a significant change in the work function (up to 2 eV) and, as shown below, this is clearly not observed in this case. Moreover, in the case of charge transfer from the Au substrate to the molecules, a new HOMO located much closer to the Fermi level would be expected because the former LUMO would appear on the π-band. Therefore, an explanation for the observations in the present system, based on interface charge transfer, is excluded. Redistribution of the MOs at sub-ML coverage may also take place through a consistent change in the energy gap between HOMO and HOMO-1. By comparing the 0.8 ML and 1 ML spectra, the spectral weight of the single peak in the 0.8 ML spectrum is comparable to the combined intensities of the two peaks in the 1 ML spectrum.

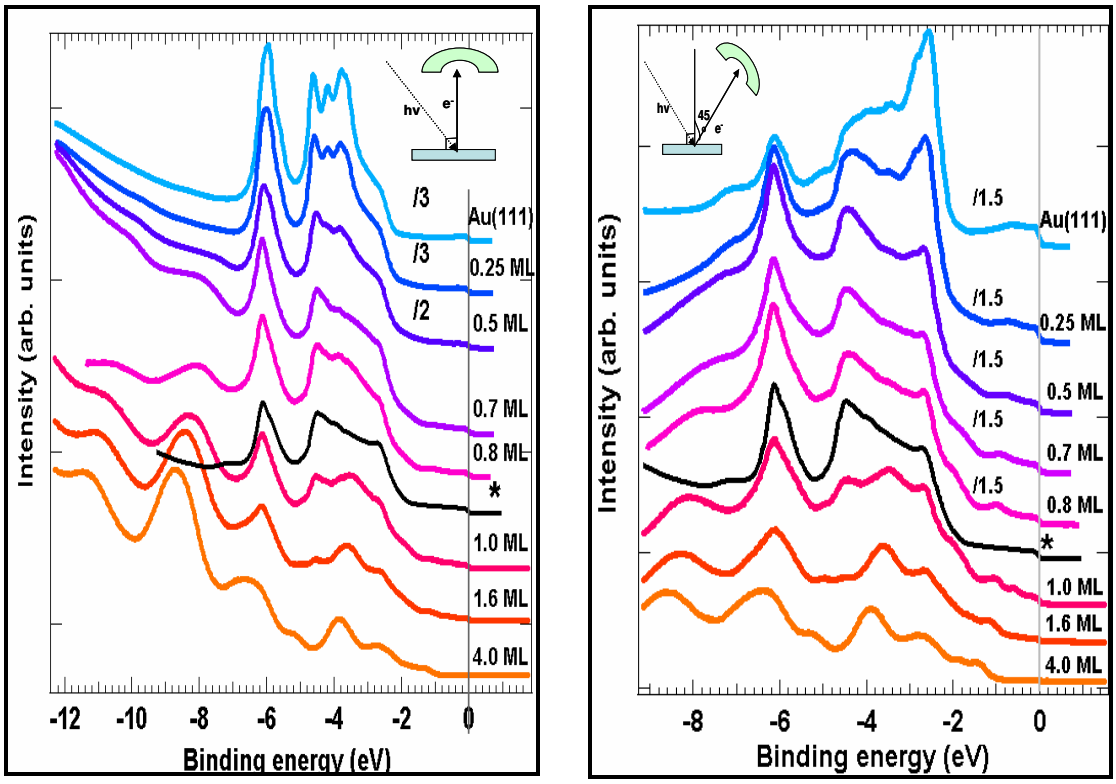

(a) (b)

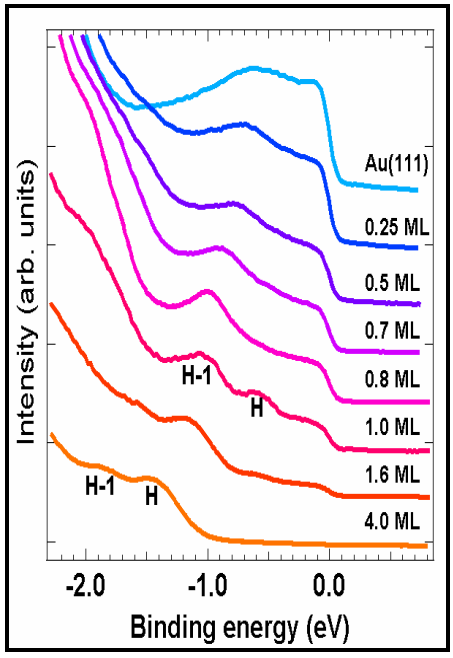

(c)

Fig. 4.1 The wide scan UPS spectra at (a) NE ; (b) 45^{o} of TAPP adsorbed on Au(111) as a function of the film thickness; (c) Valence band photoemission spectra at 45^{o} of a thin film of TAPP adsorbed on Au(111) as a function of the film thickness. is energy distribution curve (EDC) of Au polycrystalline.*

In Fig. 4.2, the calculated charge distribution of HOMO and HOMO-1 over the TAPP molecule is displayed [16]: the HOMO-1 is localized on the internal macrocycle whereas the HOMO extends to the phenyl rings and amino groups. If the molecule-

substrate interaction is stronger for sub-ML molecules, it would be likely to involve the phenyl rings. In fact, their orientation is perpendicular to the macrocycle plane in the gas phase but can distort at some energy cost to enhance the interaction with the substrate [17]. Such a distorted orientation is expected to induce a binding energy shift in any MO with significant weight on the phenyl rings, such as the HOMO. The HOMO-1 shift would be less important and the two peaks may then merge together. The fact that at the completion of the first ML, the HOMO and HOMO-1 are observed as two separate peaks; testifies to the fact that the molecule-substrate interaction is now reduced. The phenyl rings assume their relaxed orientation and the MOs are split reaching an energy separation similar to that found for the second or further layer of molecules. Although the above scenario may appear rather speculative, it is nevertheless supported by the XAS measurements performed in section 3.2.1 in Chapter 3. The XAS results show that the phenyl rings are distorted from their perpendicular orientation due to the molecule-substrate interaction. However, this could be explained if the coverage used in the XAS measurements was slightly lower, resulting in less densely packed layer.

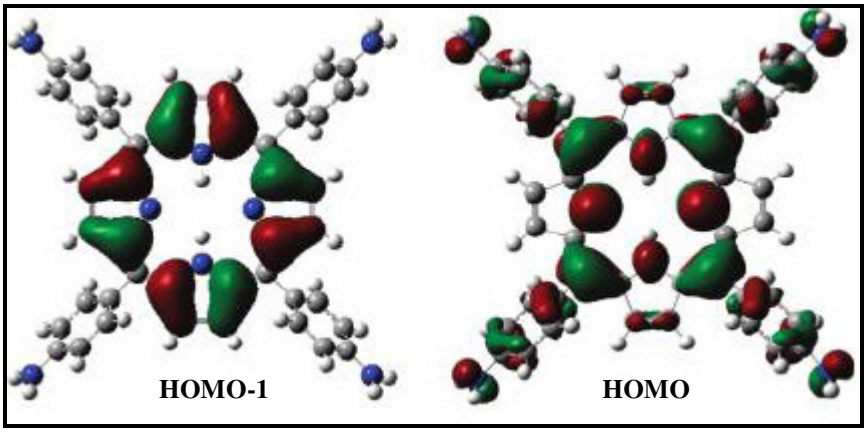

Fig. 4.2 The calculated charge distribution in the HOMO-1 and HOMO over the TAPP molecule [16].

As stated previously, a deeper investigation is needed to fully understand the spectral changes occurring between 0.8 ML and 1.0 ML. If the scenario outlined above is confirmed then it will be interesting to understand why the molecule-substrate interaction changes with coverage. Such a phenomenon was reported recently for CuPc deposited on Ag(111) [4]. By combining SPA-LEED, NIXSW, UPS and first principle calculations, it was shown that, within a rather rich phase diagram, increasing the coverage and consequently the density within the first ML, caused a weakening of the bonding to the substrate and a higher molecule-substrate distance [3,4].

When the coverage is increased from 0.5 to 0.8 ML, a shift of the peak at 0.77 eV to higher binding energy is observed (Fig. 4.1). Such a shift can be due to a decreasing interaction between the molecules and the substrate as the molecular density is increased. Reducing this interaction would decrease the final-state screening of the substrate metal electrons; thus resulting in a shift to higher binding energy. Recent studies of sub-ML growth of M-Pc on Ag(111) and Au(111) have shown similar behaviour [3,4,18]. For the CuPc/Ag(111) system [4], a shift to higher binding energy as a function of sub-ML coverage was found for some MOs participating in the molecule-substrate bond. Such a shift was interpreted as resulting from a weakening of the interface interaction. For CuPc/Au(111) [4], since the distance between the MOs and the vacuum level is constant, the shift is explained by the effect of the molecular overlayer on the work function which results in the MOs shifting with respect to the substrate features. Since the strength of interaction between the molecule and the substrate affects the WF, this can cause the apparent shift in the MOs.

4.2.2. UPS Study of the Polymerisation of TAPP on Au(111).

In the previous section, the evolution of the MOs with coverage was used to study the interface properties of the TAPP/Au(111) interface. The next step is to identify the spectroscopic changes caused by the polymerisation process. STM images of the TAPP/Au(111) interface before and after polymerisation are shown in Fig. 4.3.

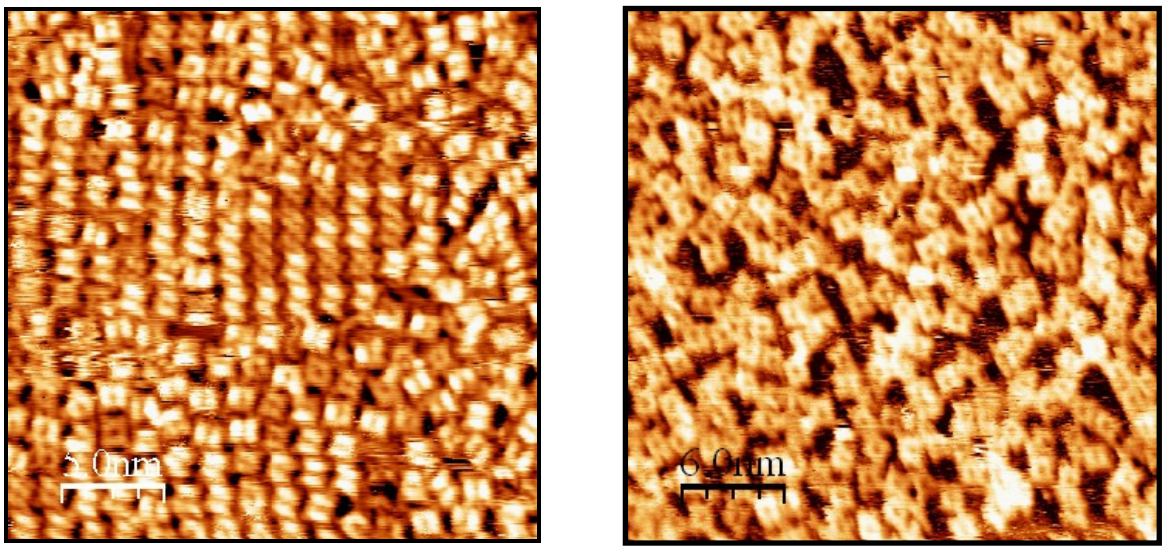

Fig. 4.3 (a) STM image (25 nm × 25 nm, Vs = +1.6 V, I =0.3 nA) before annealing and (b) STM image (30 nm × 30 nm, Vs = +1.6 V, I =0.3 nA) after 350 °C annealing.

The UPS spectra recorded after each of the STM images are displayed in Fig. 4.4 for NE (a) and (b) 45° emission. The spectra show an overall intensity increase after polymerisation due to the desorption of material during the annealing required to

activate the polymerisation process. Most of the spectrum is contributed by the substrate and the molecular features are barely visible in the wide scan spectra after polymerisation. In Figs. 4.4(c) and (d) samples of similar coverage, 0.5 ML, are compared with the polymerised film to monitor the evolution of the MOs. Regions in which the MOs are intense (high binding energy for NE and low binding energy for 45º) are focused on and discussed.

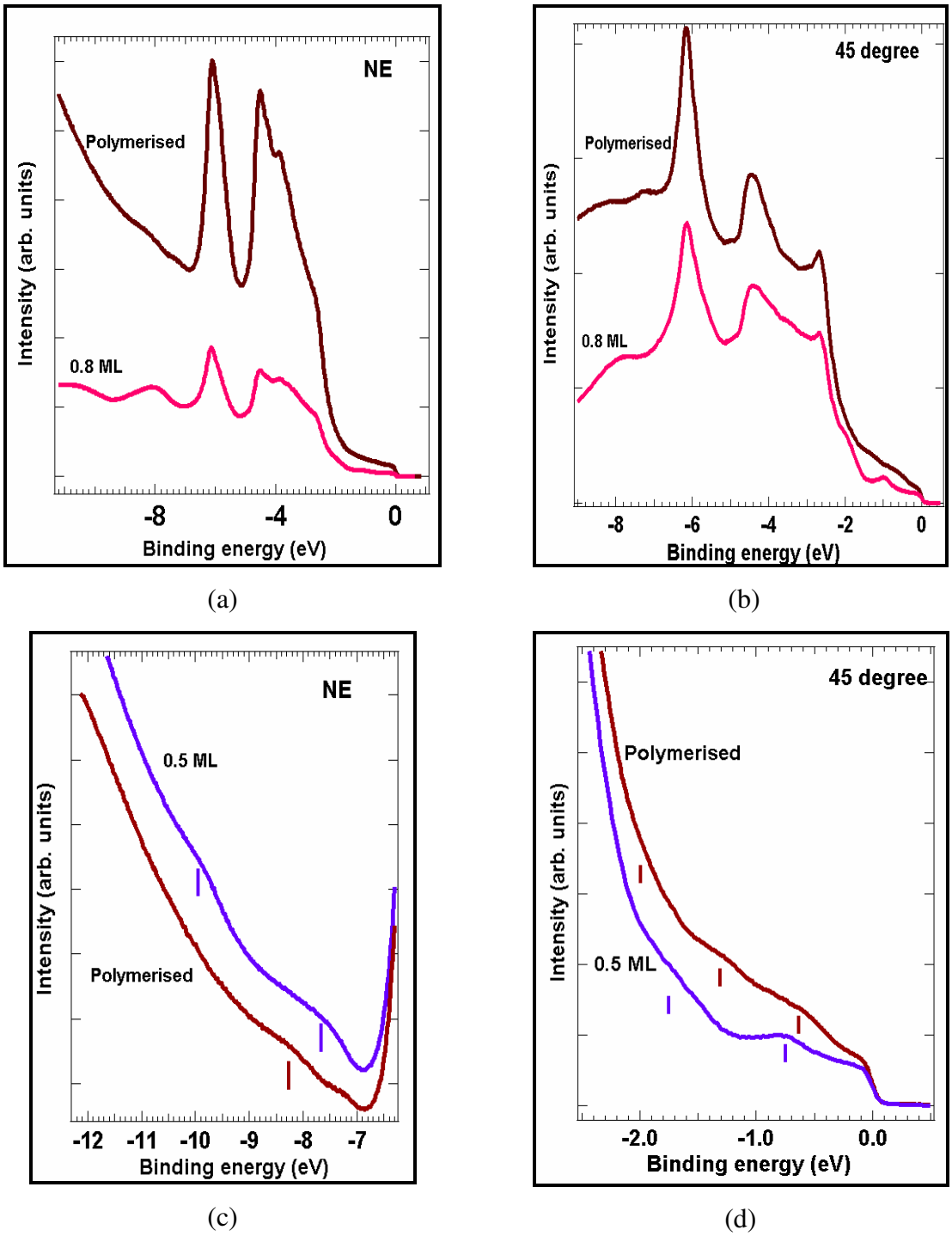

Fig. 4.4 The wide scan of UPS spectra at (a) NE ; (b) 45^o for TAPP film at 0.8 ML before and after polymerisation; Comparison of UPS spectra between 0.5 ML film and polymerised film at (c) NE for MO region ; (d) 45^o at low binding energy region.

Fig.4.4(c) shows the energy region above the Au 5*d* band in the NE spectra. Between the two MOs visible in the 0.5 ML spectrum, at 7.6 eV and 9.9 eV respectively , only one feature is visible at 8.2 eV after polymerisation. It is not clear whether the feature at 7.2 eV belongs to the overlayer or to the substrate since the polycrystalline Au has a feature at the same binding energy. Fig. 4.4(d) shows the low-binding energy region measured at 45° emission. The intensity near the Fermi level is similar for the two spectra as expected for samples with similar coverage. The 0.5 ML spectrum displays a single peak at low binding energy (see previous section) and a broader feature at 1.7eV. Three broad features are visible after polymerisation at 0.60 eV, 1.30 eV and 2.0 eV.

The presence of the higher energy feature in the two spectra is more evident after subtracting the contribution of the Au(111) substrate, as shown in Fig. 4.5(a) and 4.5(b).

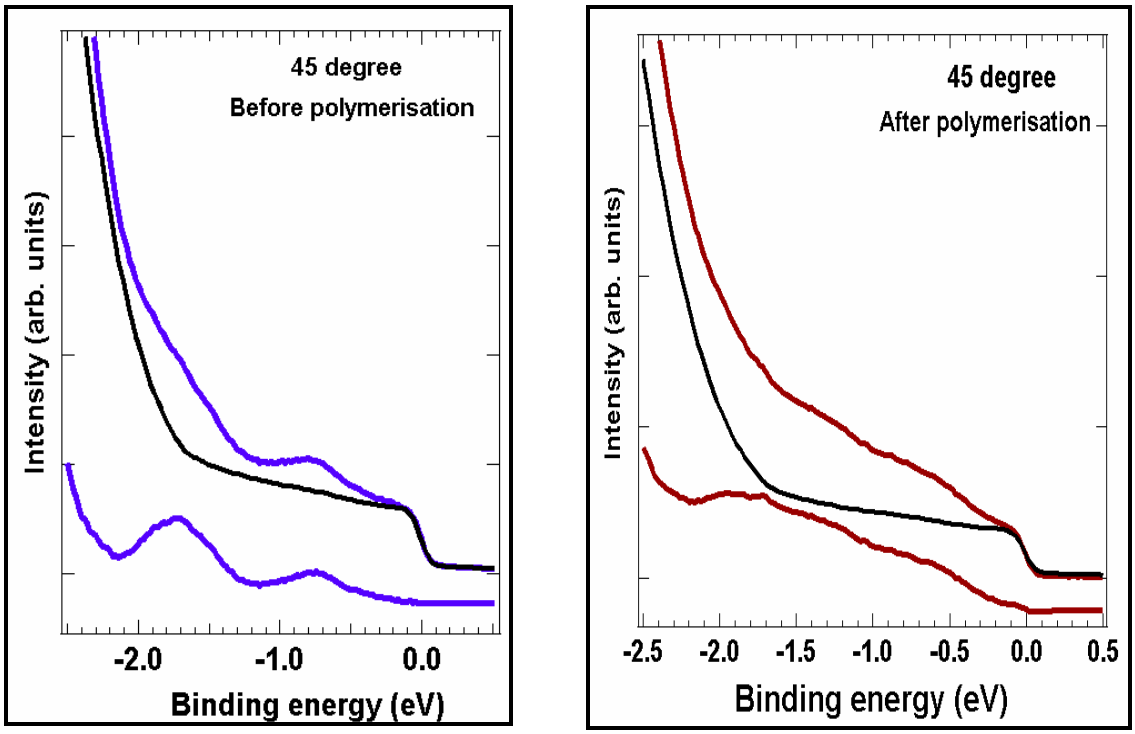

(a) (b)

Fig. 4.5 Subtraction of Au polycrystalline curve from (a) 0.8 ML of thin film before ;(b) after polymerisation.

To take into account the scattering of substrate photoelectrons at the interface, the substrate spectrum was modelled by that of a polycrystalline Au sample [7,9]. The difference spectra for four different coverages are displayed in Fig. 4.6. All spectra, except that for the 4.0 ML coverage, are aligned to the Fermi level. The 4.0 ML spectrum is aligned with the HOMO of the 1.0 ML spectrum. This step is to assist in

identifying the features above 1.5 eV of the non-polymerized samples such as HOMO-2 and HOMO-3 MOs.

In comparing the two uppermost spectra, we see that the TAPP MOs have broadened after polymerisation. The amino group contributes to the HOMO (see Fig. 4.2) and therefore it is expected to be involved in the polymerisation process. As a consequence, the lowest lying feature of the polymerised TAPP is broader than the HOMO in the 1 ML spectrum. A deeper analysis of the actual evolution of the other MOs will be performed based on comparison with *ab-initio* calculations.

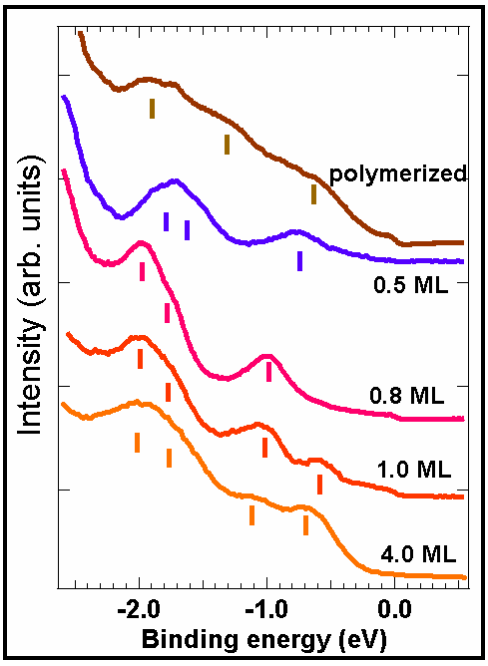

Fig. 4.6 Four samples at different thickness and a polymerised film after Au polycrystalline subtraction at 45^o emission angle.

4.2.3. Work Function Measurements of the TAPP/Au(111) Interface.

The work function is defined as the energy needed to bring a bulk electron from the Fermi level to the vacuum level outside the surface as illustrated in Fig. 4.8. In the UPS spectrum, the work function (φ_M) can be calculated using Eqn. 4.1, where KE_{cutoff} is the measured kinetic energy at the SECO, hv is the photon energy of He I and KE_{FL} is the measured kinetic energy of the Fermi level. For a clean metal surface, the work function is determined by surface electrons. The lack of nearest neighbours on the vacuum side makes the surface electrons to spill out and hence, creates an electric dipole on the surface.

$$\varphi_M = hv - (KE_{FL} - KE_{cutoff}) \qquad \textit{Eqn. 4.1}$$

The SECO and work function measurements are reported in Fig. 4.8 (a) and (b) for different coverages, and for the polymerised TAPP, (a nominal thickness of 0.5 ML has been assigned to the polymerised surface as found from the Valence Band UPS analysis above). For the clean Au(111), the measured work function is 5.51 eV, in agreement with previously reported values [19].

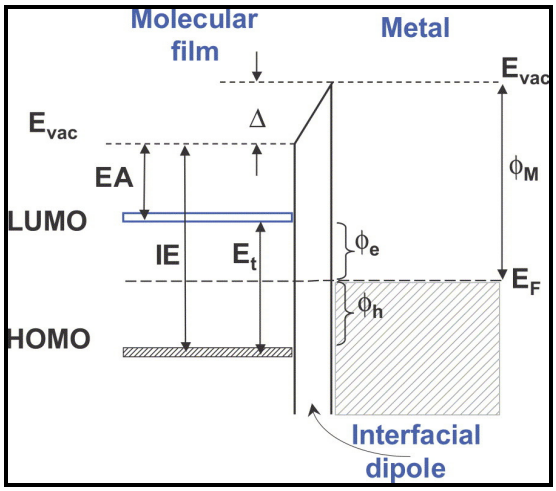

Fig. 4.7 Energy diagram of an interface between a molecular film and a metal surface. The effect of an interfacial layer with the energy offset Δ is shown [20].

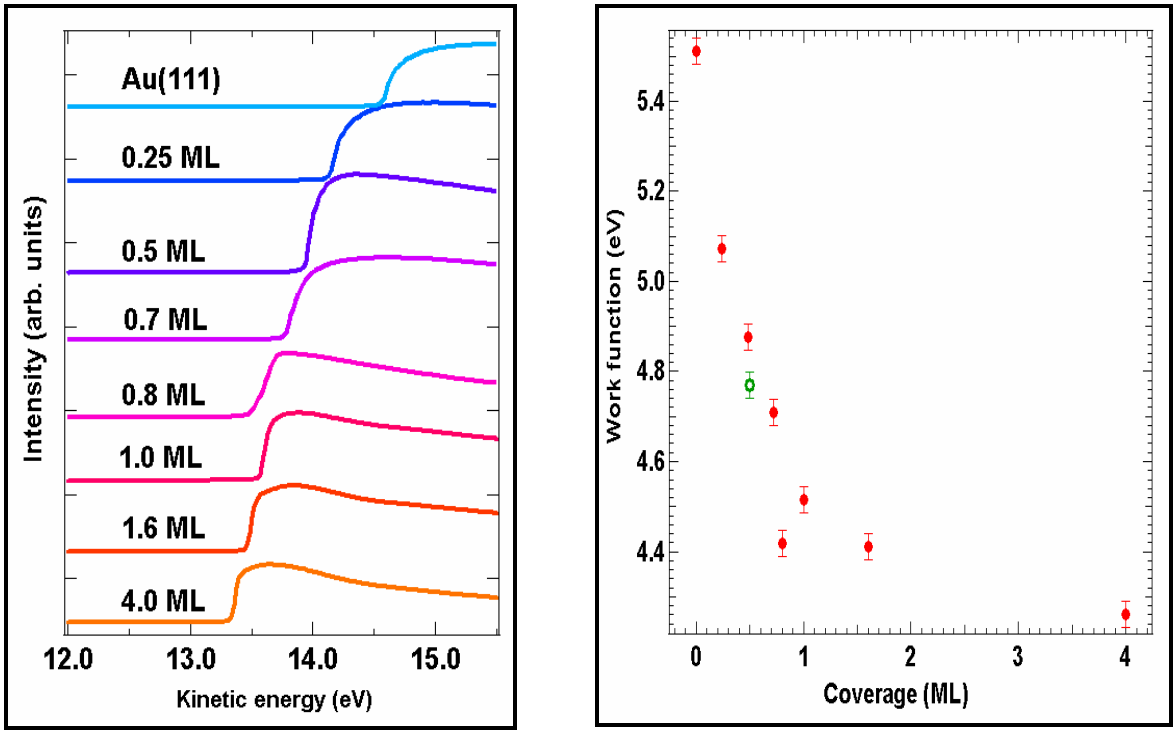

(a) (b)

Fig. 4.8(a) Work function (WF) at NE of TAPP incrementally deposited on Au(111) substrate as a function of film thickness; (b) WF value against coverage (ML) plot.

When a foreign species (atom or molecule) is deposited on a surface, the work function changes due to the modification of the surface dipole (Fig.4.7). Such a modification can be explained by two factors: (i) a reduction of the work function due to the pillow effect where the electrons in the molecule push-back the metal electrons because of the Pauli Exclusion Principle thus, reducing the surface dipole; (ii) the formation of a new dipole due to a redistribution of the charge at the interface. The second factor is typical of chemisorption which can give either a decrease or increase in the work function.

Fig. 4.8(b) shows a monotonic decrease of the work function as a function of coverage up to 0.8 ML. Such behaviour is expected due to the above mentioned pillow-effect [21] of the MOs on the substrate electrons. Interestingly, the work function shows an increase on completion of the first ML. This behaviour may be due to the relaxation of the molecule-substrate interaction observed in the UPS spectra: relaxing the interaction would increase the molecule-substrate distance and reduce the push back effect, thus influencing the work function value. This scenario is incomplete and needs to be supported by *ab initio* DFT calculations to take into account the modification of the interface dipole. Finally, the work function shows a decrease for the last two coverages. The work function of the polymerised film is 4.8 eV. It increases because some TAPP molecules desorbed from the Au surface after the polymerisation to a coverage that is equivalent to a nominal layer thickness of 0.5 ML.

4.2.4. Valence Band Spectra as a Function of Coverage on Cu(111).

The Cu(111) surface is more reactive than the Au(111) surface. Hence, it would be interesting to explore the evolution of molecular orbitals as a function of coverage and also, the effect of the polymerisation process on the MOs on the Cu(111) surface.

As in the case of Au(111), two major points are discussed in this section. The first concerns the evolution of the valence band spectra of the TAPP molecules from sub-ML; to a full ML and to a multilayer coverage. The second part of the discussion focuses on the spectral evolution of the valence band in the low binding energy region. The valence band spectra of TAPP/Cu(111) are plotted as a function of coverage at NE and 45º emission in Fig. 4.9(a) and (b) respectively. Contributions from He I β-satellite have been subtracted from the original spectra. Satellite peak subtraction is particularly difficult for Cu because the satellite emission from the 4*d* band occurs close to the Fermi level.

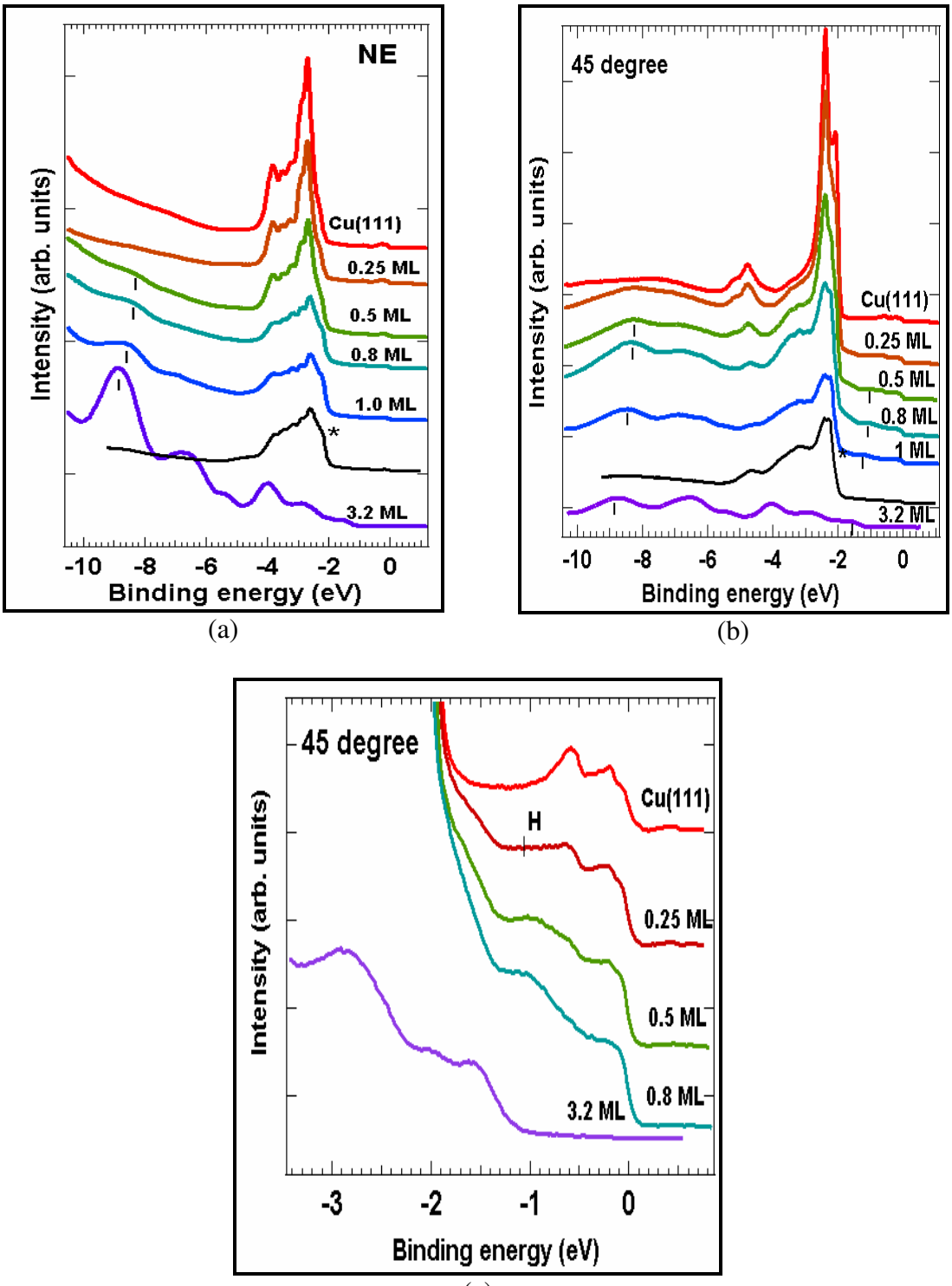

*Fig. 4.9 The wide scan of UPS spectra at (a) NE ; (b) 45^{o} of TAPP adsorbed on Cu(111) as a function of the film thickness; (c) Valence band photoemission spectra at 45^{o} of a thin film of TAPP adsorbed on Cu(111) as a function of the film thickness. * is energy distribution curve (EDC) of Cu polycrystalline.*

In Fig. 4.9, the top spectrum is that of the clean Cu(111). The intense density of states between binding energies of 2.7 and 3.9 eV is ascribed to the Cu 4*d* bands and to a lesser extent to the Cu *sp* contribution. The almost flat density of states between the Fermi level and 2 eV binding energy is attributed to electrons from the Cu *sp* band. As

in the case of Au, the spectrum is a combination of direct transitions and DOS contributions. The direct transition contributions are attenuated when molecules are deposited because of the scattering of substrate photoelectrons by the adsorbed molecules. At 1 ML, the 4*d* substrate contribution is very similar to that of polycrystalline Cu (see spectra marked with asterisk *)[unpublished data from IM2NP].

Molecular orbitals are detected at sub-ML coverage in both NE and 45^{o} emission. For coverages as low as 0.5 ML, a MO is observed at 8.30 eV at both NE and 45^{o}. The intensity of the molecular features increases as a function of thickness and the Cu(111) contribution is reduced accordingly due to the surface sensitivity of the UPS technique. The substrate contribution is no longer visible at 3.2 ML. At this stage, the EDC may be regarded as a thick film of weakly interacting molecules. Six features are observed at binding energies of 1.60 2.90, 4.00, 5.40, 6.70 and 8.90 eV respectively. At lower coverage, the MOs are still visible. A shift to higher binding energy with increasing coverage is observed for features both above and below the Cu 4*d* bands.

Fig. 4.9(c) shows the features of the low-lying MOs as a function of coverage. Spectra taken at 45 ° emission angle are displayed for this region since the π-states such as the HOMO are more intense at this angle. A peak (labelled as H) is observed after 0.5 ML of TAPP is deposited. Due the low work function of the Cu(111) surface charge transfer is expected, however, no charge transfer is observed. A single peak is observed at sub-ML coverage testifying to a strong molecule-substrate interaction. In contrast with the Au(111) interface, the peaks do not split into two components upon completion of the first ML. Importantly, the low binding energy peak is broader for first-layer TAPP/Cu(111) than it is at interface with Au(111) and in the thick film. A comparison of the full width at half maximum (FWHM) of the low-binding energy peaks is reported in Table 4.1 for the different systems studied here.

Table 4.1 A comparison of the full width half maximum (FWHM) of the low-binding energy peaks on Au(111) and Cu(111) systems.

System		**Position (± 0.1 eV)**	**FWHM (eV)**
Au(111)	0.8 ML	1.05	0.39
	1 ML	0.58	0.23 (HOMO)
	Thick layer	1.42	0.42 (HOMO)
Cu(111)	0.8 ML	1.02	0.68
	Thick layer	1.6	0.42 (HOMO)

The interface interaction could be too strong to relax when higher coverages are achieved at completion of the first monolayer. Consequently, the peaks do not split into doublets as observed in Au(111) system. Similar to that observed on Au(111), a shift of peak H to higher binding energy occurs as a function of coverage. This shift can be explained by a different final state screening for interface molecules and molecules in the thick film (the former being more efficient because of the substrate charges). Moreover, peaks from the multilayer also shift to align with the molecular vacuum level. This situation is more significant for coverages below a ML. As in the case of Au(111), a change in binding energy might be due to a decrease in the molecule-substrate interaction as the molecular density increases [4,18].

4.2.5. Valence Band Polymerisation of TAPP on Cu(111).

In this section, spectroscopic changes caused by the polymerisation process are identified and discussed. Fig. 4.10 (a) and (b) show the STM images of 0.8 ML TAPP on the Cu(111) surface before and after the polymerisation process which occurs after annealing at 240 ^{o}C for 5 minutes.

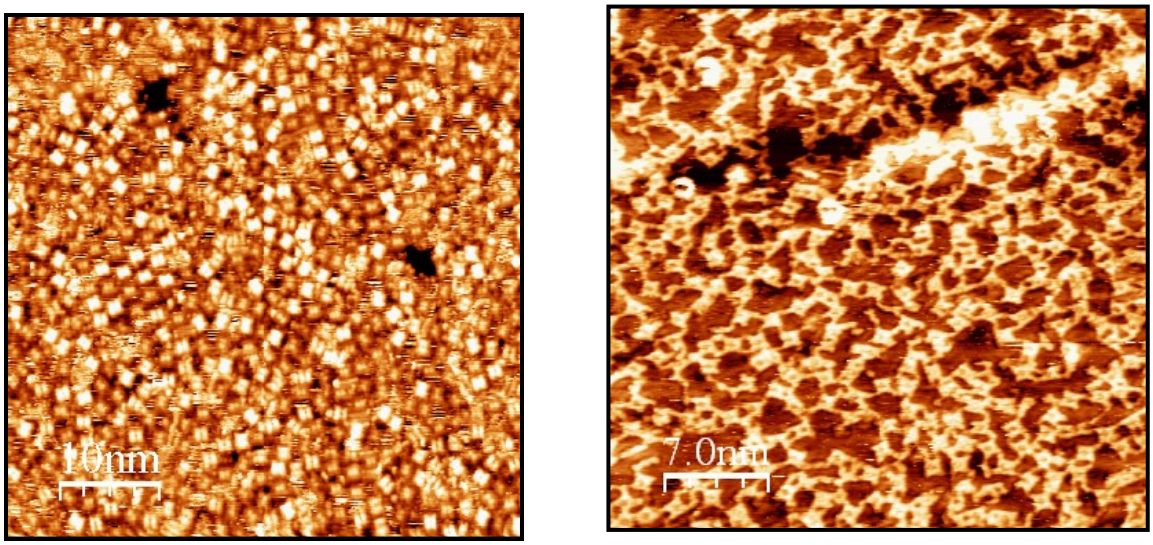

Fig. 4.10 (a) STM image (50 nm × 50 nm, Vs = +1.6 V, I =0.3 nA) before annealing and (b) STM Image (35nm ×35 nm, Vs = -1.7 V, I =0.3 nA) after annealing at 240 ^{o}C.

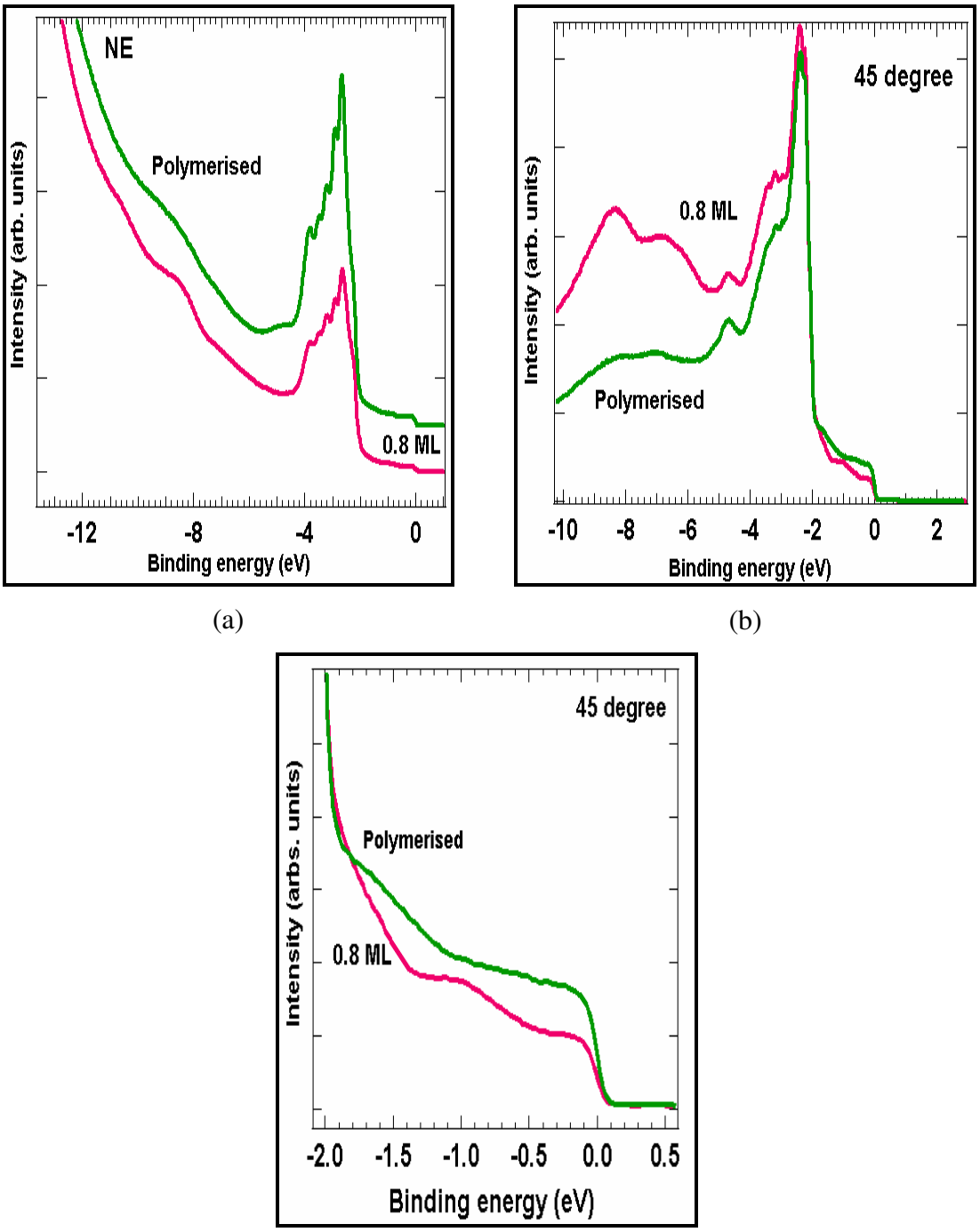

Fig. 4.11 The wide scan of UPS spectra at (a) NE ; (b) 45^o for TAPP film at 1 ML before and after polymerisation on Cu(111); (c) UPS spectra between a ML TAPP film before and after polymerisation at low binding energy region.

Fig 4.11(a) and (b) show the UPS spectra measured at NE (a) and (b) 45° emission before and after polymerisation. For the polymerised samples, the intensity depends on the contribution of the substrate which is more critical at NE (see Fig. 4.1(a and b) in which division was made at 1/3 in NE and 1/1.5 in 45^o emission spectra above). After polymerisation the contribution from the Cu(111) substrate is more intense. This is

attributed to the fact that more Cu surface is exposed after the polymerisation process. The actual coverage can be determined by comparing the NE spectrum to sub-ML spectra taken under the same conditions. After polymerisation; the coverage is estimated to be approximately 0.5 ML. At NE, the MOs at 8.60 eV and 10.70 eV are observed before the polymerisation. After polymerisation, a single broad peak is observed positioned at 9.00 eV. At 45 ^{o} emission, the modifications are stronger at the region between the Fermi edge and the *d* band.

Fig. 4.11(c) shows the low binding energy region at 45 ^{o} emission before and after polymerisation. Before polymerisation occurs a peak is observed at 1.0 eV. After polymerisation this peak is shifted towards higher binding energy to 1.6 eV. After the polymerisation process, the π-region has broadened and the intensity between the Fermi edge and 1.8 eV has increased which is unexplainable at this stage. The broadening of the peak could be due to the delocalisation of the electron from different chemical environments present after the polymerisation process.

4.2.6. Work function Measurements of TAPP/Cu(111) Interface.

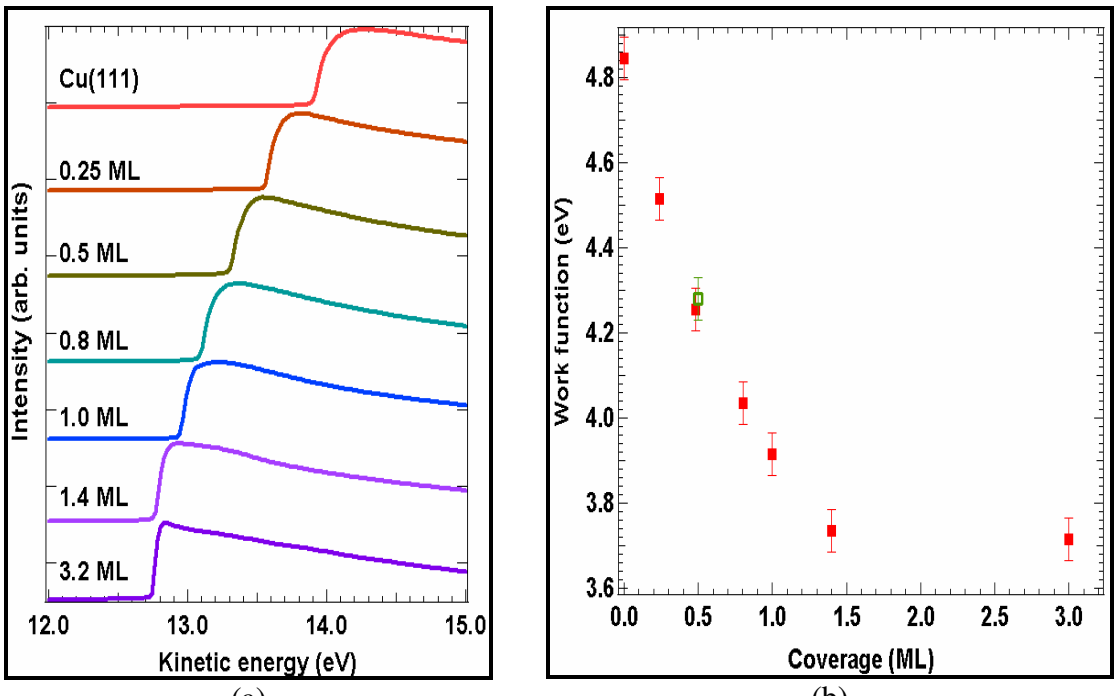

(a) (b)

Fig. 4.12 (a) Work function (WF) at NE of TAPP incrementally deposited on Cu(111) substrate as a function of film thickness ; (b) WF value against coverage (ML) plot.

The measurement of the SECO and the work function for the different coverages of TAPP on Cu(111) are presented in Fig. 4.12(a) and (b). The measured work function of the clean Cu(111) substrate is 4.98 eV, in agreement with the reported values of 4.9 eV in the literature [22]. Fig. 4.12(b) shows a monotonic decrease of the work function as a function of coverage up to 1.0 ML. This phenomenon is attributed to the pillow-effect [21] of the MOs on the substrate electrons as mentioned in Section 4.2.3 for Au(111) system. The value of the work function for the polymerised film is measured at 4.85 eV which is equivalent to a nominal thickness of 0.5 ML as estimated from the UPS spectra. This indicates that some TAPP molecules have desorbed from the surface during the polymerisation process.

4.3. Summary.

The electronic structure of TAPP molecules deposited on Au(111) from sub-ML to thick film was explored. The polymerisation process was followed and the resulting spectroscopic features were discussed and explained. The binding energy of the MOs evolve as a function of coverage and three types of interaction are found: (i) at sub-ML coverage a single peak is found at low binding energy due to the stronger molecule-substrate interaction, this is attributed to a conformational adaptation of the phenyl rings to optimize the molecule-substrate interaction; (ii) at one monolayer densely-packed coverage, two peaks are found at low-binding energy: the molecule-substrate interaction is relaxed and a MO distribution similar to that of the isolated molecule is found; (iii) for coverages of more than a monolayer, the molecules only interact with each other through van der Waals forces. The polymerisation reaction causes significant modifications to the electronic structure observed both above and below the substrate 5*d* bands. An overall broadening and shifting of the molecular orbitals were observed. The decrease of the work function as a function of coverage in the sub-ML regime was interpreted as mainly due to the pillow-effect [21]. Completion of the first monolayer results in a significant change in which the work function suddenly increases. This is interpreted as being due to the relaxation of the interface interaction .

Similar to the Au system, the electronic structure of TAPP molecules deposited on Cu(111) from sub-ML to thick film was studied. In the case of Cu(111) there was a stronger interaction between the TAPP molecules and Cu(111) as compared to the Au(111) system for measurements made in the sub-ML regime. A single peak (HOMO) is monitored throughout these coverages. The van der Waals interaction is the dominant

force when the coverage is more than a ML. Strong modifications were observed in the region below the *d* band and in the π-regions of the spectra on the Cu(111) system. The π-region broadened and the intensity between the Fermi edge and the *d* band increased. A broadened peak above the *d* band was observed after the polymerisation. These changes are still not fully understood at this stage. Finally, the work function decreased in the sub-ML to ML regime and again, this was attributed to the pillow-effect. All the observations mentioned in this chapter will be developed through comparison with *ab initio* calculations in a future study.

References:

[1] N. Koch. *Energy levels at interfaces between metals and conjugated organic molecules,* J.Phys.: Condens. Matter. **20** (2008) 184008.

[2] F. Klappenberger, A. Weber-Bargioni, W. Auwärter, M. Marschall, A. Schiffrin, J. Barth. *Temperature dependence of conformation, chemical state, and metal-directed assembly of tetrapyridyl-porphyrin on Cu (111),* J. Chem. Phys. **129** (2008) 214702.

[3] C. Stadler, S. Hansen, I. Kröger, C. Kumpf, E. Umbach. *Tuning intermolecular interaction in long-range-ordered submonolayer organic films,* Nat. Phys. **5** (2009) 153.

[4] I. Kröger, B. Stadtmüller, C. Stadler, J. Ziroff, M. Kochler, A. Stahl, F. Pollinger, T.L. Lee, J. Zegenhagen, F. Reinert. *Submonolayer growth of copper-phthalocyanine on Ag (111),* New J. Phys. **12** (2010) 083038.

[5] J. Fraxedas, S. García-Gil, S. Monturet, N. Lorente, I. Fernandez-Torrente, K.J. Franke, J.I. Pascual, A. Vollmer, R.-. Blum, N. Koch, P. Ordejon. *Modulation of surface charge transfer through competing long-range repulsive versus short-range attractive interactions,* J . Phys. Chem. C. **115** (2011) 18640.

[6] G. Di Santo, C. Castellarin-Cudia, M. Fanetti, B. Taleatu, P. Borghetti, L. Sangaletti, L. Floreano, E. Magnano, F. Bondino, A. Goldoni. *Conformational Adaptation and Electronic Structure of 2H-Tetraphenylporphyrin on Ag (111) during Fe Metalation,* The J. Phys. Chem. C. (2011).

[7] M. Helander, M. Greiner, Z. Wang, Z. Lu. *Angle-dependent ultraviolet photoelectron spectroscopy of sputter cleaned polycrystalline noble metals,* Appl. Surf. Sci. **255** (2009) 9553.

[8] F. Bocquet, L. Giovanelli, P. Amsalem, L. Petaccia, D. Topwal, S. Gorovikov, M. Abel, N. Koch, L. Porte, A. Goldoni. *Final-state diffraction effects in angle-resolved photoemission at an organic-metal interface,* Phys. Rev. B. **84** (2011) 241407.

[9] L. Giovanelli, P. Amsalem, T. Angot, L. Petaccia, S. Gorovikov, L. Porte, A. Goldoni, J.M. Themlin. *Valence band photoemission from the Zn-phthalocyanine/Ag (110) interface: Charge transfer and scattering of substrate photoelectrons,* Phys. Rev. B. **82** (2010) 125431.

[10] P. Puschnig, S. Berkebile, A.J. Fleming, G. Koller, K. Emtsev, T. Seyller, J.D. Riley, C. Ambrosch-Draxl, F.P. Netzer, M.G. Ramsey. *Reconstruction of molecular orbital densities from photoemission data,* Science. **326** (2009) 702.

[11] T. Graber, F. Forster, A. Scholl, F. Reinert. *Experimental determination of the attenuation length of electrons in organic molecular solids: The example of PTCDA,* Surf. Sci. (2011).

[12] Ertl,G., Kuppers,J., **Low energy electrons and surface chemistry** , 2nd ed., VCH, Weinheim, Federal Republic of Germany, Deerfield Beach, FL, USA , 1985.

[13] N.S. Venkataramanan, A. Suvitha, H. Nejo, H. Mizuseki, Y. Kawazoe. *Electronic structures and spectra of symmetric meso‐substituted porphyrin: DFT and TDDFT—PCM investigations,* Int.J. Quantum Chem. **111** (2011) 2340.

[14] P. Yao, S. Han, Y. Zhang, X. Zhang, J. Jiang. *Structures and spectroscopic properties of meso-tetrasubstituted porphyrin complexes: Meso-substitutional and central metallic effect study based on density functional theory calculations,* Vib. Spectrosc. **50** (2009) 169.

[15] M. Palummo, C. Hogan, F. Sottile, P. Bagalá, A. Rubio. *Ab initio electronic and optical spectra of free-base porphyrins: The role of electronic correlation,* J. Chem. Phys. **131** (2009) 084102.

[16] H. Wang, J. Xu, J. Wan, Y. Zhao, X. Zheng. *Excited state structural dynamics of tetra (4-aminophenyl) porphine in the condensed phase: resonance raman spectroscopy and density functional theory calculation study,* The J. Phys. Chem. B. **114** (2010) 3623.

[17] M. Fanetti, A. Calzolari, P. Vilmercati, C. Castellarin-Cudia, P. Borghetti, G. Di Santo, L. Floreano, A. Verdini, A. Cossaro, I. Vobornik. *Structure and molecule–substrate interaction in a co-octaethyl porphyrin monolayer on the Ag (110) surface,* The J. Phys. Chem. C. (2011).

[18] B. Stadtmüller, I. Kröger, F. Reinert, C. Kumpf. *Submonolayer growth of CuPc on noble metal surfaces,* Phys. Rev. B. **83** (2011) 085416.

[19] G.N. Kastanas, B.E. Koel. *Interaction of Cl2 with the Au(111) surface in the temperature range of 120 to 1000 K,* Appl. Surf. Sci. **64** (1993) 235.

[20] D. Cahen, A. Kahn, E. Umbach. *Energetics of molecular interfaces,* Mater. Today. **8** (2005) 32.

[21] G. Witte, S. Lukas, P.S. Bagus, C. Woll. *Vacuum level alignment at organic/metal junctions:"Cushion" effect and the interface dipole,* Appl. Phys. Lett. **87** (2005) 263502.

[22] S. Duhm, A. Gerlach, I. Salzmann, B. Bröker, R.L. Johnson, F. Schreiber, N. Koch. *PTCDA on Au (111), Ag (111) and Cu (111): Correlation of interface charge transfer to bonding distance,* Org. Electron. **9** (2008) 111.

Chapter 5:

Covalent Bonding of TAPP and PTCDA on Au(111) Surface.

5.0 Introduction.

In previous chapters, the reaction of TAPP between TAPP molecules has been studied. However, there are many strategies for the formation of covalently bonded networks on metal surfaces [1-4] including polyimidisation reaction involving two distinct molecules. Weigelt [5] has demonstrated polymerisation of molecules on the Au(111) surface based on imine formation in a reaction between vapour-deposited amines and aldehydes. The aim of the work presented in this chapter is to exploit imide reactions to generate covalent extended networks on the Au(111) surface as depicted in Scheme 5.1.

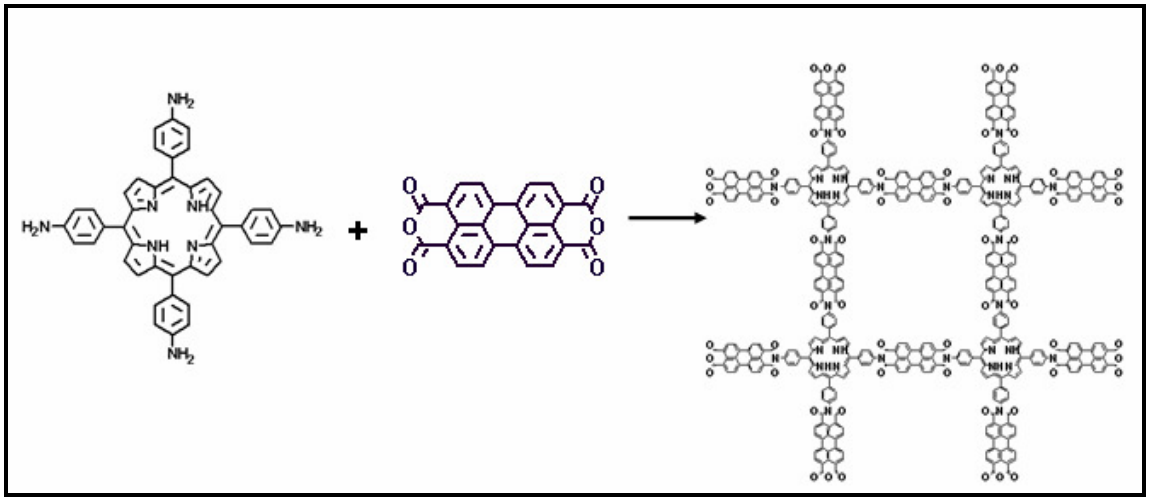

Scheme 5.1 Formation of porphyrin nanomesh molecules.

The focus of this chapter is on covalently bonded bimolecular networks between 5,10, 15,20-tetrakis(4-aminophenyl)porphyrin (TAPP) and 3,4,9, 10-perylene tetracarboxylic dianhydride (PTCDA) formed through a polyimidisation reaction on the Au(111) surface and subsequently, to obtain a comprehensive understanding of the stability, structural and electronic properties of these systems using scanning tunnelling microscopy (STM), X-ray photoelectron spectroscopy (XPS) and low energy electron diffraction (LEED). Initial studies of PTCDA on Au(111) were also conducted before the formation of covalent-bonded TAPP and PTCDA nano-network was explored.

5.1 Material and Experimental.

5.1.1. 3, 4, 9, 10-perylene tetracarboxylic dianhydride (PTCDA).

PTCDA (Fig. 5.1) is a small conjugated molecule belonging to the family of perylene derivatives. PTCDA layers show semiconducting behaviour and strong anisotropy in their electronic transport and optical properties [6]. A number of studies have been performed on the growth mode and structural properties of PTCDA on different metallic substrates such as silver [7-9], copper [7,10] and gold [10-12]. On the Au(111) surface, below one monolayer coverage, PTCDA adopts an orientation in which the undistorted molecular plane lies parallel to the substrate and forms two distinct and ordered phases. These phases are the square phase and the herringbone phase respectively, discussed in more detail below

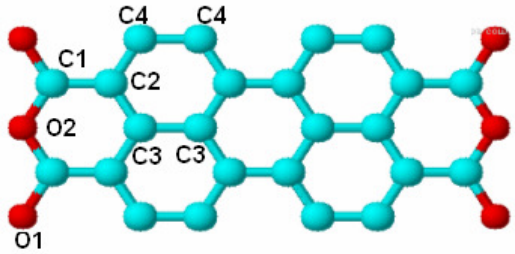

Fig. 5.1 The chemical structure of PTCDA. The assignment/numbering of C and O atoms for PTCDA XPS curve fitting. In the molecular representation, light blue balls are carbon atom and red balls are oxygen.

PTCDA was deposited at 420 °C on the room temperature Au(111) surface at a base pressure of 2.0×10^{-10} mbar. The chamber pressure was 2.1×10^{-9} mbar during the PTCDA deposition. The PTCDA deposition rate was estimated at approximately 0.1 ML per minute based on STM and XPS calibrations. After deposition the sample was annealed at 150 ^{o}C for 30 minutes to allow the PTCDA to diffuse and order on the surface.

5.1.2. Methodology.

All measurements were conducted at room temperature and carried out in an ultra-high vacuum (UHV) chamber. The PTCDA (Sigma Aldrich) and 5,10,15,20-tetrakis(4-aminophenyl) porphyrin (TAPP) (Tokyo Chemical Industry, (TCI)) molecules were deposited under UHV conditions from molybdenum crucibles thermocouples, spot-welded to the crucible was used to determine the deposition temperature. A thorough degassing process was performed for approximately 12 hours to remove water vapour and excess solvent from both the PTCDA and TAPP materials before deposition. A

careful estimation of the coverage of PTCDA and TAPP was performed by XPS measurements with Al K_α ($h\nu$ = 1486.7 eV) source and by comparison to STM images. The coverage was determined by calculating the C 1s to metal ratio and comparing with the coverage determined from the corresponding STM images.The kinetic energy of the ejected photoelectrons was analysed using a five channeltron hemispherical energy analyser (Omicron) operating at a pass-energy of 50 eV and with an energy increment of 0.1 eV.

XPS spectra were recorded at the SX700 beam-line at ASTRID, University of Aarhus, Denmark [13] and the D1011 beamline at MAX Lab, Lund University, Sweden [14]. XAS measurements were carried out at D1011 beamline at the MAX Lab using a partial electron yield detection mode. The parameters and procedures to perform these experiments have been described in detail in Section 2.5 in Chapter 2.

STM measurements were performed at room temperature (RT) to image the self-assembled layer of 3, 4, 9, 10-perylene tetracarboxylic dianhydride (PTCDA) and to observe the reacted networks that were formed through the imidisation reaction between the PTCDA and TAPP molecules on Au(111). The PTCDA/Au(111) interface was studied using LEED. The LEED images were captured with a CCD camera at low primary electron energy in order to minimise electron beam damage to the adsorbate layer.

5.2 Results and Discussion.

5.2.1. Scanning Tunnelling Microscopy (STM) of PTCDA on Au(111).

Deposition of PTCDA on Au(111) at room temperature leads to the formation of self assembled layers. A typical STM image of a submonolayer coverage of PTCDA on Au(111) is shown in Fig. 5.2 and consists of two differently arranged structures. Both domains can be observed in the image; the domain in the upper part of the image is the herringbone (HB) phase, while the lower part of the image shows the square (S) phase. The HB phase has been reported and discussed in detail in many publications [6,15,16] and the structure has been confirmed by X-ray diffraction (XRD) [17]. The square phase was first reported by Chizhov *et al*. [15]. Most STM images recorded at approximately one monolayer coverage predominantly show the HB-phase with a much smaller fraction of the S-phase. The S-phase is less dense than the HB-phase and is preferred

when the surface coverage of PTCDA is less than a full monolayer. The deposition of PTCDA does not lift the reconstruction observed on the clean Au(111) surface [6,15], the characteristic zigzag pattern of the ($22 \times \sqrt{3}$) reconstruction can still be observed in the STM images of the 1ML HB phase as indicated by the arrows in Fig. 5.2. The zigzag pattern is also visible on the surface covered by the S-phase, although it is harder to distinguish in Fig. 5.2 because of the higher apparent corrugation in the image due to the more open structure of S-phase. The fact that the Au(111) reconstruction is still observable beneath the PTCDA molecular is attributed to a weak interaction of the molecules with the Au substrate and also the fact that the molecule–molecule interaction dominates over the molecule–substrate interaction. The observation of the Au(111) reconstruction through the PTCDA layer provides a guide with which to resolve the orientation of the PTCDA molecules with respect to the Au substrate.

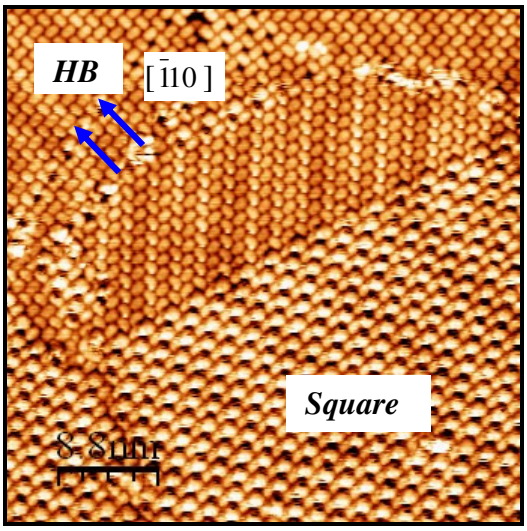

Fig. 5.2 STM image (44 nm ×44 nm, V_s = -1.0 V, I = 0.1 nA) of 1 ML of PTCDA on Au(111). Domains of two different structural phases ('herringbone'(HB) and 'square'(S)) are marked on the image.

Figs. 5.3(a) and (c) show high resolution images of the two phases. The HB-phase consists of PTCDA molecules arranged in rows alternatively tilted in the plane of the molecular layer. The HB-phase has a rectangular unit cell with dimensions (1.89 ± 0.1) nm × (1.37 ± 0.1) nm as measured from a series of STM images. This result is in reasonably good agreement with the reported STM values of (1.90 ± 0.10) nm × (1.20 ± 0.10) nm [15]. The dotted line in Fig. 5.3(a) lies along [$\bar{1}$10] of the Au reconstruction direction.

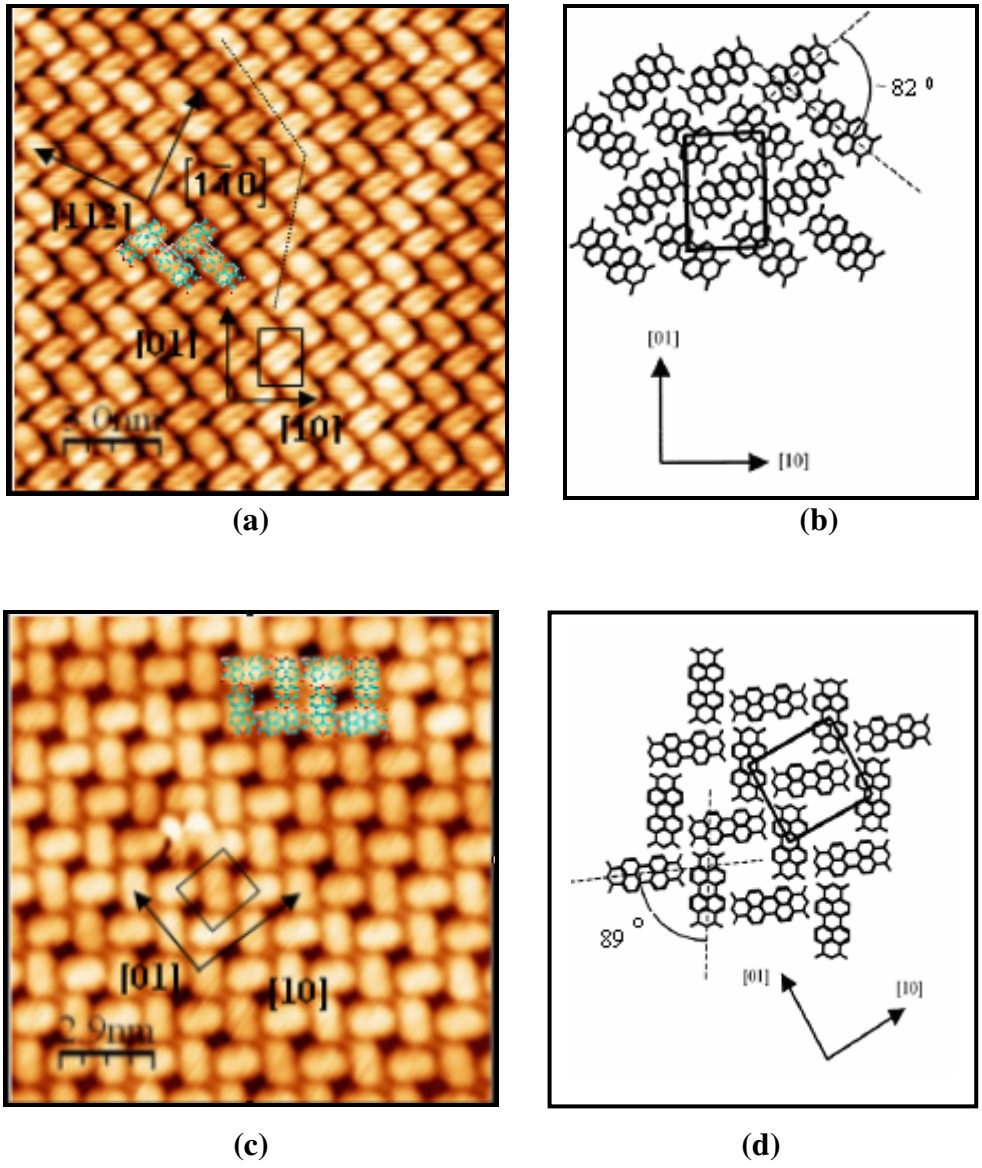

Fig. 5.3 (a) STM image (15 nm × 15 nm, V_s = -1.3 V, I = 0.9 nA) of the herringbone (HB) phase. The zigzag pattern of the Au(1 1 1)-(22×$\sqrt{3}$) reconstruction (marked with dashed lines) is visible through the PTCDA monolayer (c) STM image (20 nm × 20 nm, V_s = -1.0 V, I = 0.1 nA) of the square (S) phase. (b) and (d) schematic diagrams of the PTCDA molecular arrangement in the HB and S-phases, respectively. Unit cells, crystallographic directions of the Au(111)-(22×$\sqrt{3}$) surface ([1$\bar{1}$0] *and [112]) and two dimensional PTCDA layer ([1 0] and [0 1]) are indicated* [15].

The molecular orientation is measured in terms of the angle, α between the [112] direction of the Au(111) lattice and the [10] direction of the two-dimensional PTCDA layer as illustrated in Fig. 5.3(b). The [112] direction is perpendicular to the direction of the zigzag pattern and gives an angle of less than 90° with the [10] direction of the PTCDA layer (Fig. 5.3a). The [01] and [10] directions of the PTCDA layer are depicted in Fig. 5.3(b) and (d). The [10] and [01] directions are selected to be along the short and the long axis of the rectangular unit cell, respectively for the HB-phase and they correspond to the [010] and [201] directions of the monoclinic bulk PTCDA molecular

crystal, respectively [15]. The long axes of adjacent PTCDA molecules are not strictly perpendicular to each other and form an angle of approximately (82° $\pm$ 1°) for HB phase. The unit cell angle measured for the HB phase corresponds with the value of approximately 83° reported by Chizhov *et. al* [15].

The S-phase is comprised of PTCDA molecules aligned in a square pattern and has dimensions of (1.80 $\pm$ 0.1) nm × (1.80 $\pm$ 0.1) nm. This value is in good agreement with the reported STM value of (1.70 $\pm$ 0.10) nm × (1.70 $\pm$ 0.10) nm [15]. The long axes of adjacent PTCDA molecules are at a measured angle of (89° $\pm$ 1°) for S-phase. The S-phase value obtained from analysis is in good agreement with the STM determined value of (91° $\pm$ 2°) reported by Mannsfeld *et. al* [12].

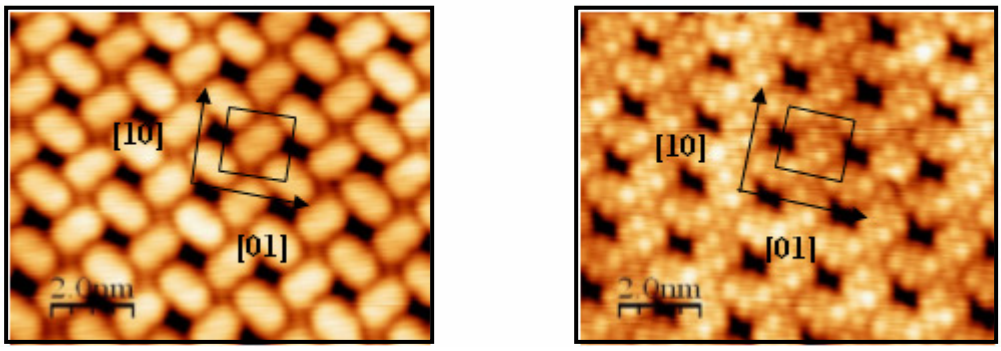

(a) **(b)**

Fig. 5.4 STM images of the S-phase taken under different current and voltage parameters (a) (10 nm × 10 nm, V_s = -1.25 V, I = 0.3 nA). (b) STM image (10 nm × 10 nm, V_s = +1.25 V, I = 0.3 nA).

STM images obtained at positive and negative polarities on the same region of the PTCDA molecules are depicted in Fig. 5.4(a) and (b). STM images of the S-phase reveal the occupied molecular states (V = 1.25 V) and distinct internal structures for unoccupied molecular states (V = +1.25V) at a constant current which is shown in Fig. 5.4(a) and (b) respectively.

5.2.2. Low Energy Electron Diffraction (LEED) of PTCDA on Reconstructed Au(111).

The geometric structure of a monolayer coverage of PTCDA on the Au(111) surface was observed with LEED. The LEED images were recorded at a low primary beam energy (10 - 21 eV), to avoid destroying the PTCDA layer. A series of LEED patterns

were also recorded for the clean Au(111) substrate at a range of energies from 60 to 210 eV.

The hexagonal diffraction pattern for the first-order spots of the clean Au(111)-(22 × $\sqrt{3}$) reconstruction, recorded with a primary beam energy of 80.7 V, is shown in Fig. 5.5(a). Fig. 5.5(b) shows the LEED image, recorded at a beam energy of 20.8 eV, from approximately 1-ML of PTCDA deposited on the reconstructed Au(111) surface. The observed diffraction pattern can be described by a superposition of six symmetry-equivalent domains of a rectangular adsorbate structure, i.e. the herringbone unit cell.

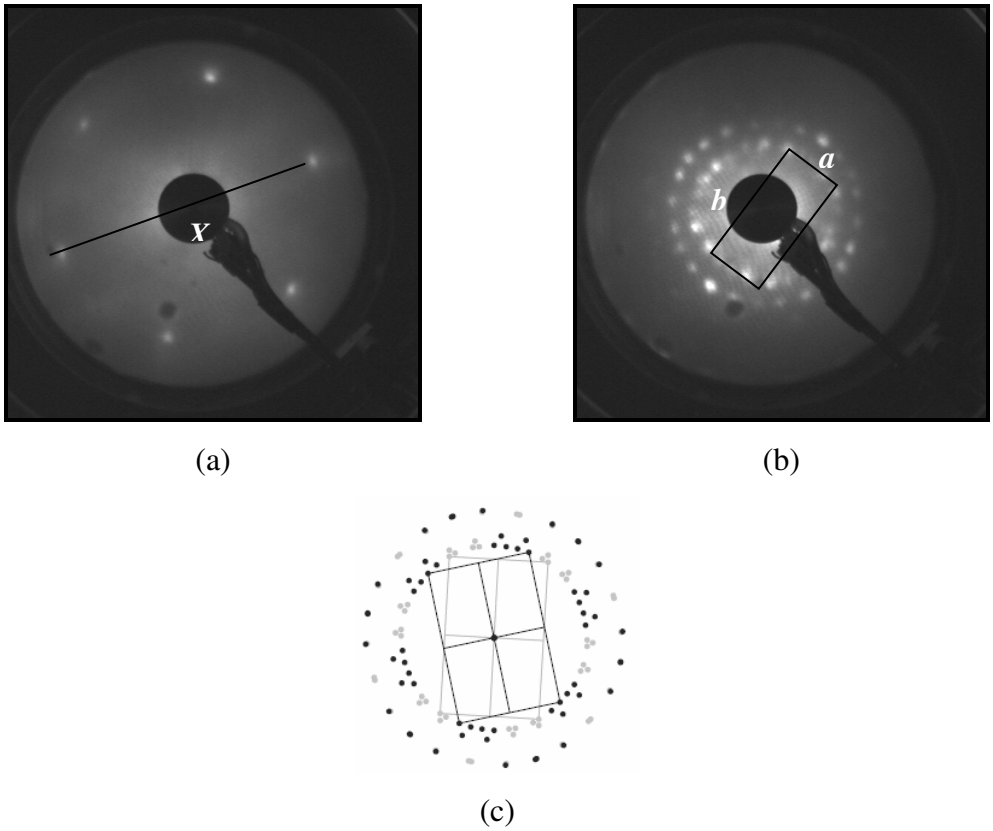

Fig. 5.5(a) LEED image of 1st order diffraction spots from Au(111) -(22 × $\sqrt{3}$) reconstruction recorded at E_o = 80.7 V; (b) LEED image from ~1ML of PTCDA on Au(111) at E_o = 20.8 V; (c) Schematic drawing of the LEED image shown in (b). The diffraction pattern can be explained by six symmetry equivalent domains of a rectangular adsorbate structure [12].

The distances between the first order diffraction spots are measured from the LEED patterns as shown in Fig. 5.5(a). To estimate the lattice parameters of the PTCDA herringbone phase, multiple measurements of the distances between the diffraction spots (see Fig. 5.5) of both the Au(111) -(22 × $\sqrt{3}$) reconstruction and the PTCDA overlayer were taken from the LEED patterns and the average distance was calculated. The measurements were repeated with LEED images recorded at different primary

beam energies. These average distances are then plotted as a function of $1/\sqrt{E}$, where E is the primary beam energy, and fitted with a straight line through the origin (Fig. 5.6). The unit cell parameters of the PTCDA can then be calculated from Equation 5.1 using a value of 0.289 nm for the inter-atom distance, $\mathbf{a}_{Au(111)}$ of Au.

$$\frac{a_{PTCDA}}{a_{Au(111)}} = \sqrt{\frac{E_{PTCDA}}{E_{Au(111)}}} \qquad \textit{Eqn. 5.1}$$

Using this procedure the lattice parameters obtain from the LEED measurements are $\boldsymbol{a}$ = (2.0 ± 0.1) nm; $\boldsymbol{b}$ = (1.3 ± 0.1) nm; θ = 90° for the HB phase. The S-phase with two molecules per unit cell only occurs in small domains on the surface and thus, is not observed in LEED images [12]. The lattice parameters obtained from LEED and STM values are comparable.

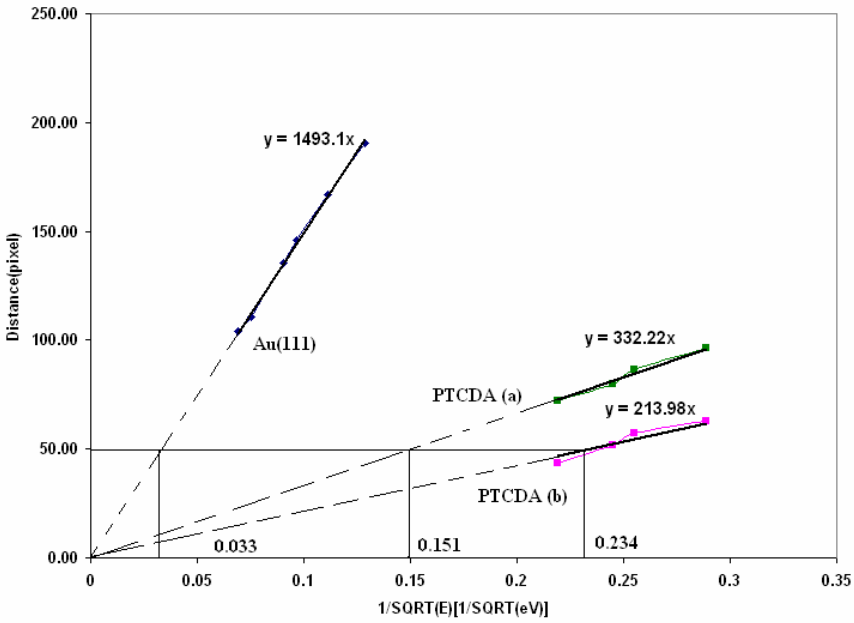

Fig. 5.6 Calibration curve for Au(111) and PTCDA.

5.2.3. Synchrotron Based X-ray Photoelectron Spectroscopy (XPS) of PTCDA on Reconstructed Au(111).

Fig. 5.7 shows the (a) C 1s and (b) O 1s XPS spectra of PTCDA on the Au(111) surface. The carbon atoms in PTCDA can be classified into four categories as indicated by the chemical structure in Fig. 5.1: carbonyl group, -C=O (C1), -C-CO (C2), –C=C- (C3) and -CH (C4). The positions of these peaks as determined by fitting Voigt profiles

to the XPS spectra are at binding energies of 288.5, 285.3, 284.8 and 284.5 eV for C1, C2, C3 and C4 respectively [18-20]. All binding energies are determined to an accuracy of ± 50 meV. In addition, satellite peaks of C 1s are also observed in the spectra shown in Fig. 5.7. These are attributed to shake-up processes that are caused by excitations of the valence electrons upon the sudden creation of a core hole and are described by two-hole-one-particle states (*2hp*). Two satellite peaks of C 1s were identified: the first satellite peak (Sat 1), at a binding energy of 290.1 eV, corresponds to excitation on the carbonyl group (C1); the second satellite peak (Sat 2) at a binding energy of 286.8 eV, is attributed to the carbon atoms in the aromatic rings C3. The carbonyl group, C1, produces a more intense shake-up intensity in comparison to the shake up intensity from the main aromatic peak, C3.

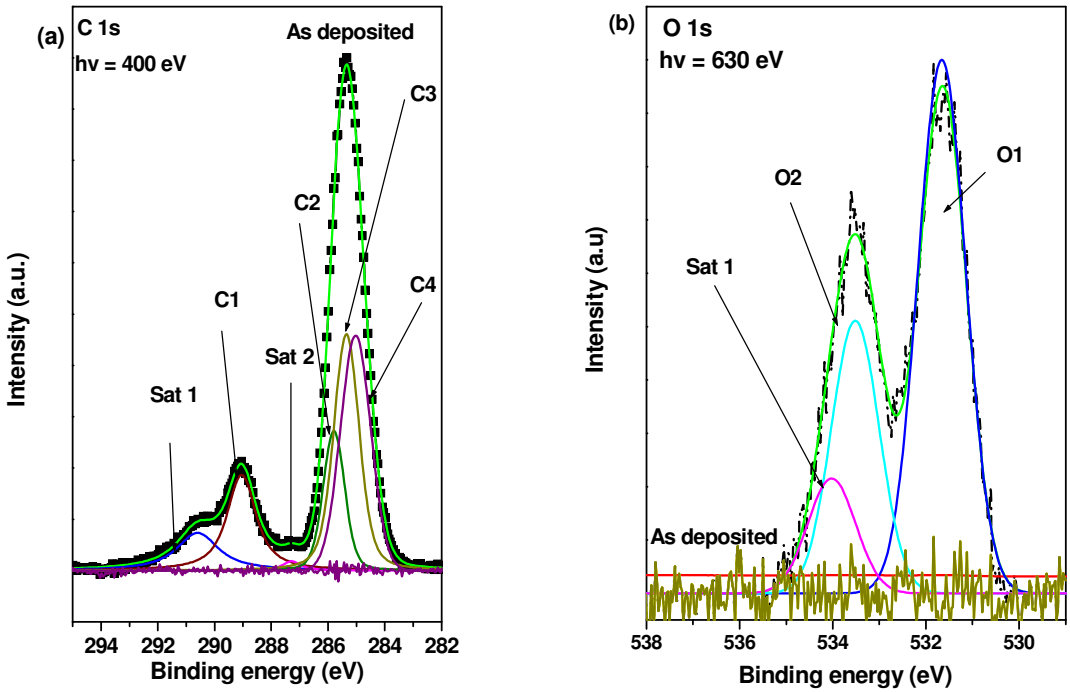

Fig. 5.7 XPS spectra for (a) C 1s and (b) O 1s core levels PTCDA on reconstructed Au(111) at 1 ML coverage.

In the O 1s XPS spectrum, there are two peaks which are attributed to the different chemical environments of the oxygen atoms in the anhydride and carbonyl functional groups [20]. The peaks can be assigned by their relative intensity between the anhydride and the carbonyl groups which is 2:1. The O 1s binding energies corresponding to the –C=O and –C-O-C- oxygen atoms are 531.7 eV and 533.6 eV, respectively, giving an energy separation of 1.90 eV. One significant satellite peak from O1 was observed at a binding energy of 534.0 eV. Based on the calculation by Schőll *et al.* [20], two satellites peaks for O1 and one satellite peak for O2 are predicted. However, only the satellite

peaks from the O1 atom is observed with any significant intensity and hence, fitted in the current work. A summary of the results obtained from fitting the C and O 1s core level XPS spectra are tabulated in Table 5.1.

Table 5.1 Results of the fitting procedure for the binding energy positions and relative intensities of C 1s and O 1s of the PTCDA. The percentage is the fraction of the component area over the whole core level area. ΔE is the position of the component energy with respect to the main peak.

Experimental Analysis				
Core level	**Component**	**eV**	**ΔE**	**%**
C 1s	**Sat 1**	290.1	+5.57	9.7
	C1 -C=O	288.5	+4.02	16.3
	Sat 2	286.8	+2.26	1.1
	C2 -C-CO	285.3	+0.76	13.8
	C3 -C-H	284.8	+0.32	29.0
	C4 –C=C-	284.5	0	30.1
O 1s	**O1** C=O	531.7	0	55.6
	O2 -C-O-C-	533.6	+1.90	31.9
	Sat 1	534.0	+2.39	12.5

A shake up is a process where the photoelectron looses energy by exciting an electron transition around the Fermi level. In an organic semiconductor system, the lowest energy shake up possible is from the HOMO into the LUMO. Hence, the ΔE of the satellite peaks in Table 5.1 could represent the bandgap (HOMO-LUMO) of the PTCDA molecule. According to Hirose *et al.* [21], the bandgap of PTCDA is 2.2 eV, which is in agreement with the ΔE value obtained from Sat. 2 at 2.26 eV.

5.2.4. X-ray Absorption Spectroscopy (XAS) of PTCDA on Reconstructed Au(111).

Fig. 5.8 shows the (a) C 1s and (b) O 1s XAS spectra recorded at normal incidence (NI), normal emission (NE) and grazing incidence (GI, 70^{o}) from 1 ML of PTCDA on the Au(111) surface. The positions of the peaks in the XAS spectra are determined to an accuracy of 50 meV. The sharp intense peaks below 290 eV are due to electron transitions from the C 1s levels of the different C species into unoccupied final states. The first two peaks of the spectrum at 283.7 eV and 285.1 eV, labelled A and B respectively in Fig. 5.8a, are assigned to transitions from the carbon atoms in the aromatic perylene core into LUMO, LUMO+1 and LUMO+3 orbitals, respectively [19]. The third structure, peak C, at around 287.0 – 288.0 eV is dominated by two transitions within the functional anhydride group. The two transitions of the anhydride group are assigned to the peaks at 287.2 eV (peak C1) and 288.8 eV (peak C2) respectively. A comparison of the spectra recorded at different angles, especially the normal incidence

(NI), in C 1s and O 1s XAS as shown in Fig. 5.8, suggest that the geometry of PTCDA molecules are orientated parallel to the Au(111) surface.

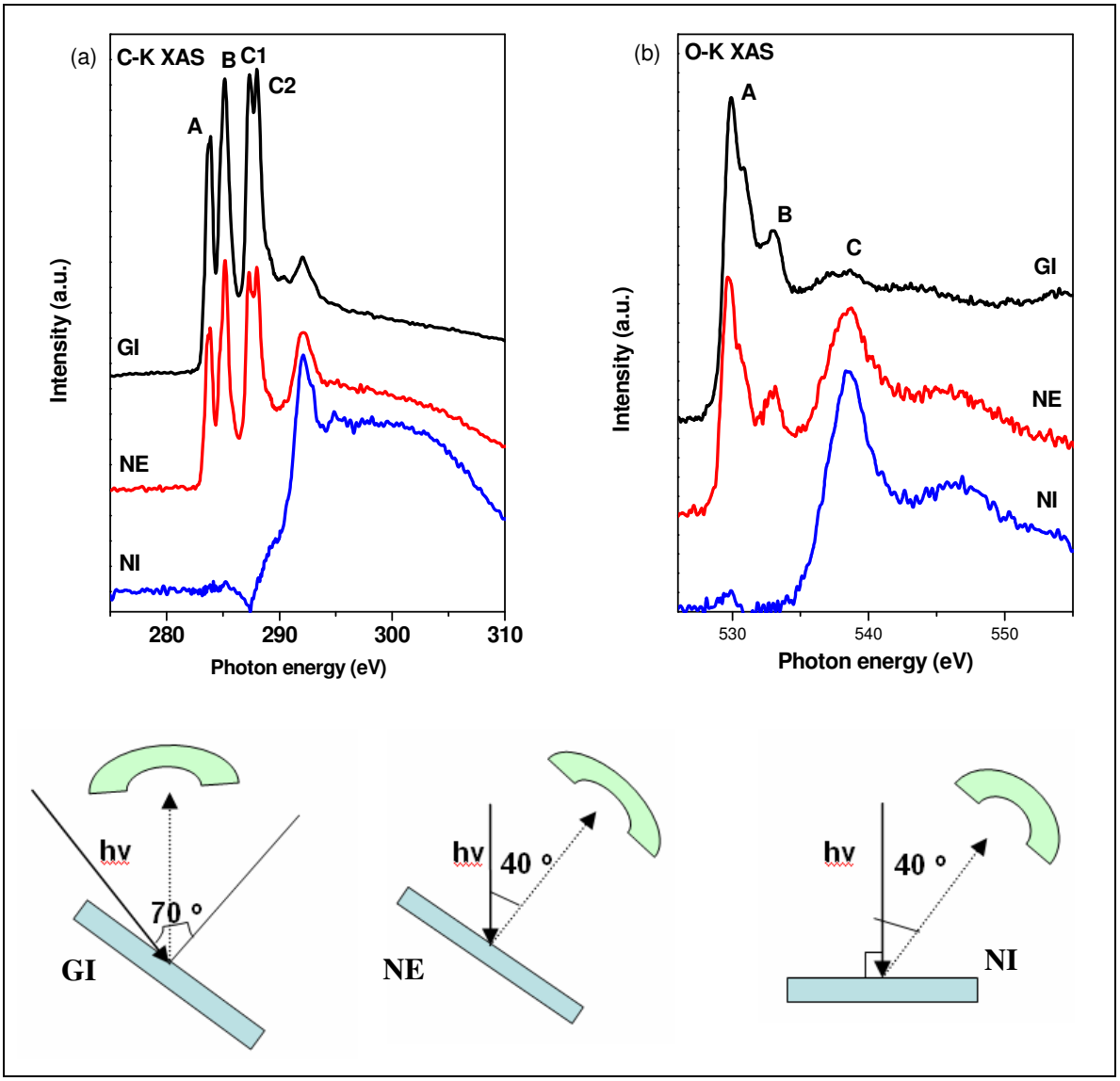

Fig. 5.8(a) C-K XAS and (b) O-K XAS data of PTCDA a monolayer on Au(111), recorded at normal, incidence (NI), normal emission(NE) and grazing incidence (GI,70°) .

The O 1s XAS spectra (Fig. 5.8b) show one strong peak at 529.9 eV which, in higher resolution, comprises at least two large contributions with peak B at 533.1 eV and a weaker peak at 535.1 eV (peak C) [22]. The main structure (peak A) originates from the excitation of 1s core level of the oxygen atom in the carbonyl group (-C=O) while the peak at 538.6 eV is attributed to excitation of the bridging O atom in the anhydride group(-C-O-C-). Peak A is associated with the excitation of the terminal O atom, that corresponds with the XPS binding energy of 531.7 eV, into the LUMO [22]. Peak B is assigned to a transition from the same atom into LUMO +1. However, transitions into

higher orbitals such as the LUMO+2 and LUMO+3 cannot be ruled out [22]. Peak C is attributed to the transitions from the bridging O atom into LUMO and LUMO+1. The resonance assignments are presented in Table 5.2.

Table 5.2 Assignments and energy positions of the C- K XAS and O- K XAS resonances for PTCDA.

PTCDA	Peak	Resonance Positions (eV)	Assignments
C- ***1s XAS***	**A**	283.7	Aromatic perylene into LUMO, LUMO +1 & LUMO+3
	B	285.1	
	C1	287.2	Anhydride group
	C2	288.0	
O- ***1s*** **XAS**	**A**	529.9	Carbonyl group, C=O
	B	533.1	
	C	538.6	-C-O-C-

In summary, an analysis using STM, XPS, LEED and XAS of PTCDA on Au(111)-(22 x $\sqrt{3}$) has been carried out. STM images show two different domains, the herringbone (HB) and square (S) phases. The XPS spectra of the C 1s and O 1s peaks were deconvolved and are in good agreement with previous work reported above. In LEED, the diffraction pattern from the HB phase can be distinguished. The unit cell parameter was determined and compared with STM values of 2.0 nm × 1.3 nm. Finally, the XAS results show that the PTCDA molecules are orientated parallel to the Au(111) surface.

5.2.5. Scanning Tunnelling Microscopy (STM) of the Bimolecular TAPP-PTCDA System on the Reconstructed Au(111).

TAPP and PTCDA molecules were deposited sequentially, each to a coverage of approximately 0.5 ML, on the clean Au(111) surface held at room temperature. A phase separation between TAPP and PTCDA molecules was observed in the STM images (see Fig. 5.9a). The sample was then annealed at 360 ^{o}C for 60 minutes in order to initiate a polymerisation reaction. The excess TAPP and un-reacted PTCDA are desorbed from the gold surface during the annealing process. Bare areas of Au(111) are observed in the STM images after annealing Fig. 5.9(b). The covalent bonded nano-networks are stable at room temperature and are imaged for a range of sample biases. Other annealing temperatures of 220 ^{o}C and 290 ^{o}C to initiate the polymerisation process between PTCDA and TAPB were used during the preliminary studies and resulted in phase separations of these molecules.

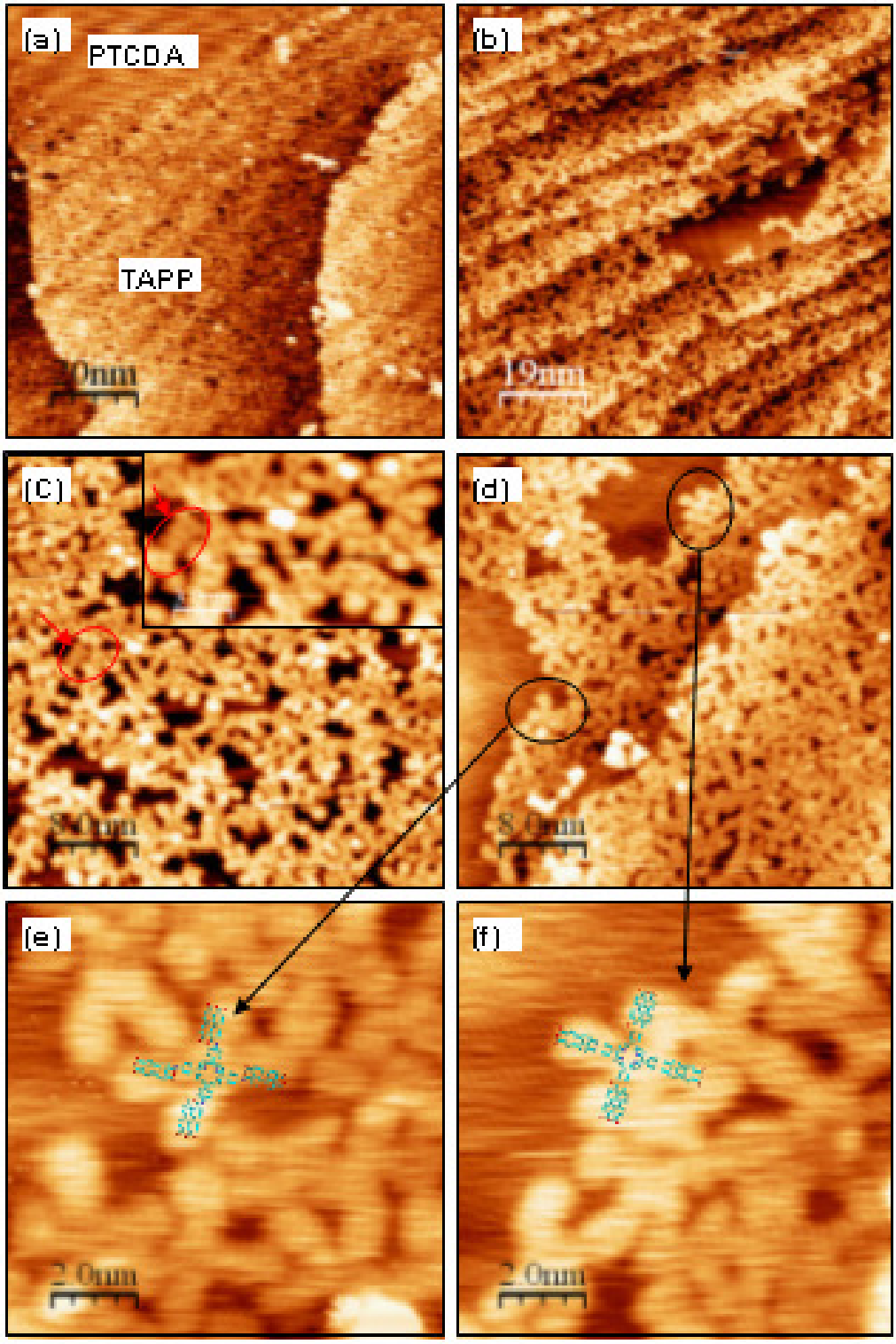

Fig. 5.9 (a) STM image (100 nm ×100 nm, V_s = -1.3 V_s,I = 0.5 nA) of mixed TAPP & PTCDA (before annealing); (b) STM image (100 nm ×100 nm, V_s STM image (40 nm ×40 nm, V_s = -1.5 V, I = 0.5 nA)= 1.5 V, I = 1.3 nA) after 350 °C annealing;(c) STM image (40 nm ×40 nm, V_s =+2.2V, I = 0.2 nA) ;(d) (e) &(f) enlargement of image (d); image (e) shows the formation iso-imides, image (f) shows the formation of imides.

Both imides and iso-imides are formed from the reaction of the TAPP with the PTCDA as shown in Fig. 5.9(d - f). The majority of covalently bonded molecules are found on

the Au(111) surfaces. However, not all of the TAPP molecules react with the four PTCDA molecules. The STM images show that molecules of TAPP have reacted with one, two, three or four units of PTCDA. A covalent reaction between TAPP molecules is also found on the surface as indicated by the red arrows in the enlarged region shown in Figs. 5.9(c). This process hinders the formation of a nano-network between TAPP and PTCDA.

5.2.6. Synchrotron based X-ray Photoemission Spectroscopy (XPS) of the Bimolecular TAPP-PTCDA System on the Reconstructed Au(111).

Fig. 5.10 shows the XPS spectra of the C 1s and O 1s core levels taken from approximately one monolayer of TAPP/PTCDA as deposited on Au(111) (Fig. 5.10 lower) and after annealing to 360 ^{o}C for 30 minutes (Fig. 5.10 upper). When TAPP and PTCDA are deposited sequentially, the fingerprint spectrum of the PTCDA is observed in the 288 – 292 eV energy regions (Fig. 5.10a). This peak corresponds to the carbonyl group and the satellite peak from the carbonyl group of the C 1s core level in the XPS spectrum. After annealing to 360 ^{o}C, the C 1s peak is attenuated in this region. The ratio of area under the curve of C 1s after annealing when compared to pre-annealed surface is 0.68. This is attributed to the loss of excess and un-reacted PTCDA molecules from the surface. The PTCDA molecules which have reacted with the TAPP molecule to form imides or iso-imides remain on the Au(111) surface. Our preliminary study shows that when PTCDA is deposited by itself on Au(111), it is not stable when heated beyond 300 ^{o}C. This is confirmed by XPS measurements of the C 1s core level of PTCDA which shows that most PTCDA molecules have desorbed from Au(111) surfaces after annealing at 300 °C. Therefore, the C 1s XPS signal recorded in this experiment is a measure of the PTCDA molecules that have remained on the surface and reacted covalently with the TAPP molecules to form a disordered covalently bonded nano-network.

No significant change is observed in the O 1s core level spectra before or after annealing at 360^{o}C. The ratio of O 1s before and after annealing is calculated to be 0.37, suggesting that reactions between the oxygen species from PTCDA and amino groups from TAPP has taken place and some of the un-reacted PTCDA molecules have desorbed from the surfaces. This is attributed to the fact that both imides and iso-imides reactions can occur and therefore both oxygen species are involved in reactions. Therefore, there is a very slight change in the peak intensity for both the carbonyl and

the anhydride peaks. The measured change in the relative intensity of these peaks is approximately 10 %. However, it is not possible to determine the absolute change in the intensities of both peaks.

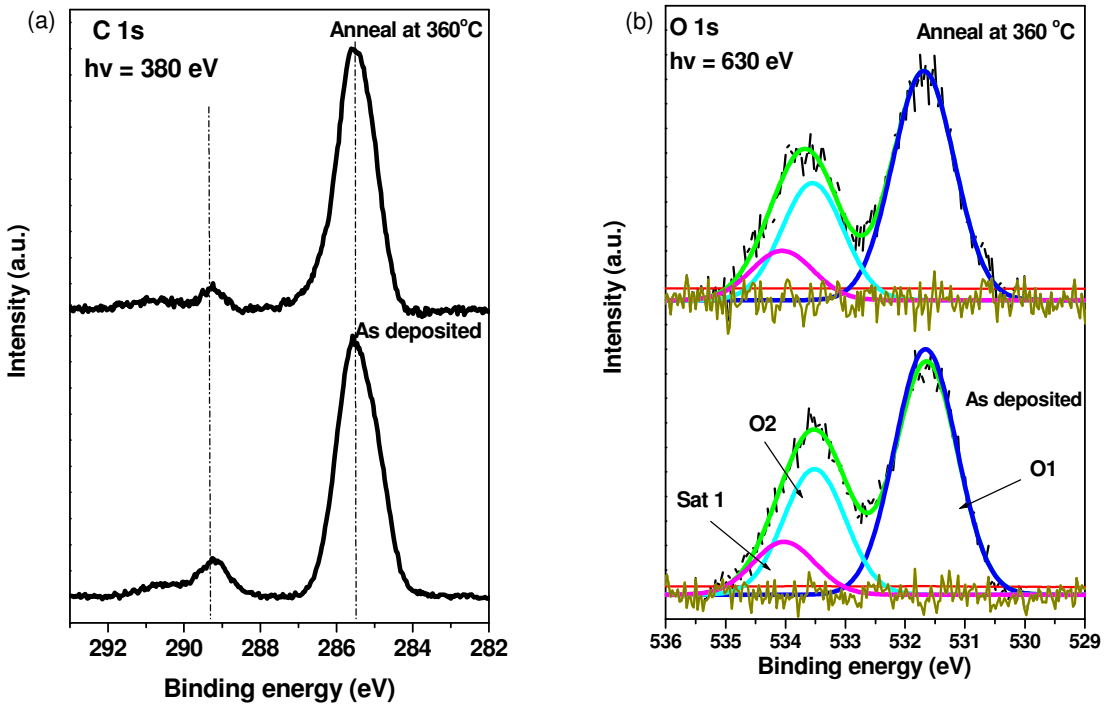

Fig. 5.10 XPS spectra from (a) C 1s and (b) O 1s core level for ~1-ML of TAPP/PTCDA on the reconstructed Au(111) surface as deposited and after annealing at 360 ℃.

5.2.7. X-ray Absorption Spectroscopy (XAS) of the Bimolecular TAPP-PTCDA System on the Reconstructed Au(111).

Fig. 5.11 shows the (a) C- 1s and (b) O- 1s XAS spectra recorded at grazing incidence (70^{o}) from the TAPP/PTCDA overlayer on the Au(111) surface, before and after polymerisation process. The grazing incidence C- 1s XAS spectrum of TAPP recorded after annealing at 150 ^{o}C is selected as a reference in this experiment as it shows the peaks A, B and C which were discussed in Section 3.2.1. It is observed that peak B in the TAPP/PTCDA sample has decreased significantly when a comparison is made to the pure TAPP C- 1s XAS spectrum. This is further evidence that a reaction between the amino group on the TAPP and the anhydride group on the PTCDA molecule has taken place.

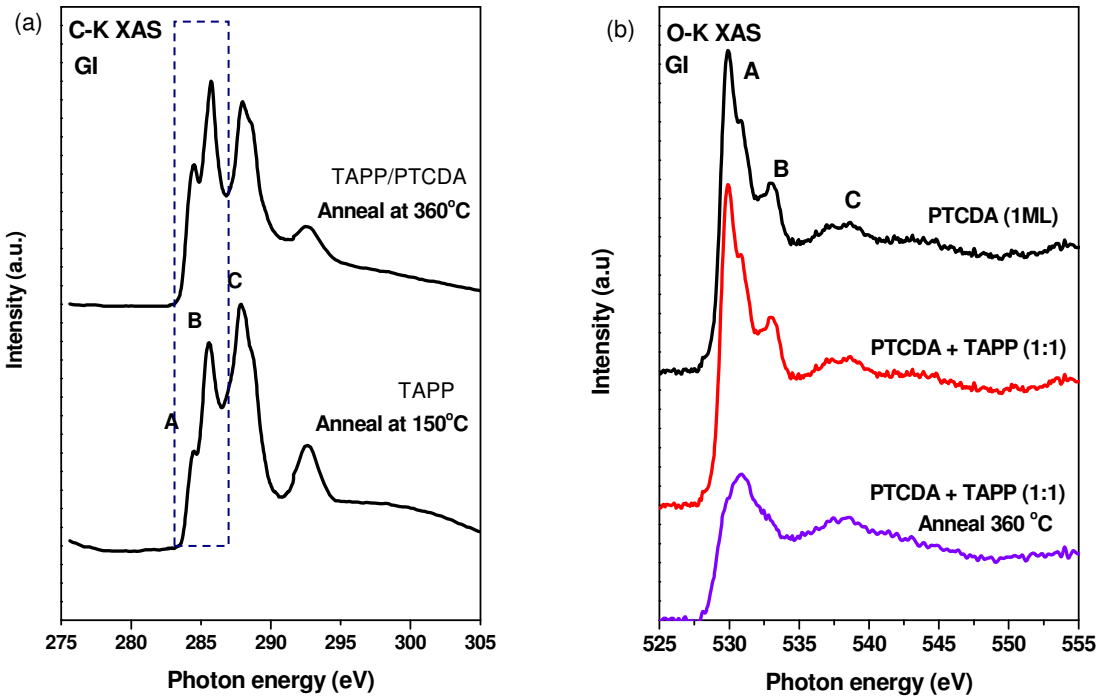

Fig. 5.11 (a) C- 1s XAS spectra of TAPP annealed at 150°C and TAPP/PTCDA annealed at 360 °C on Au(111); (b) O- 1s XAS spectra of PTCDA and TAPP/PTCDA (1 ML) on Au(111) as deposited and after annealed at 360 °C, all spectra are recorded at grazing incidence (GI).

Fig. 5.11(b) shows the O - 1s XAS spectra recorded from the PTCDA alone, TAPP/PTCDA interface as deposited and after annealing at 360 °C. The O- 1s XAS spectrum from the as deposited layer shows the three peaks which correspond to the carbonyl group (peak A + peak B) and the anhydride group (peak C) in the PTCDA molecule. The peak assignments were also discussed in Section 3.2.1(d). When the sample is annealed to 360 °C, a significant broadening of the peaks is observed. This indicates that a reaction has taken place between the TAPP and PTCDA molecules. The reactions between the amino groups and anhydride groups have occurred. However, the type of covalent bonding such as HN-NH or –N=N- cannot be clearly distinguished with any certainty. Hence, this broadening could be associated with delocalisation of the electrons on the molecules formed by covalent bonding or changes in the molecular structure of the PTCDA. Assignment of broadened peaks could not be carried out due to the fact that many peaks correspond to atoms in different chemical environments and hence, they are not distinguished clearly in the spectra. However, the strongest peak (peak A) is still observed at approximately (530.8 eV) although it appears slightly shifted to higher photon energy by 1 eV.

5.3 Summary.

The growth and ordering of 3,4,9,10-perylene tetracarboxylic dianhydride (PTCDA) and the reaction between TAPP and PTCDA via polyimidisation on Au(111) was investigated in detail using STM, XPS and XAS. A well-ordered molecular layer of PTCDA was obtained in which the plane of the molecules was orientated parallel to the Au(111) surface. The molecule formed a close-packed structure with both rectangular herringbone, (HB) phase and square (S) phase. The HB phase is the dominant phase and has a rectangular unit cell with dimensions (1.89 ± 0.1) nm × (1.37 ± 0.1) nm as measured from STM images. The S-phase is comprised of PTCDA molecules aligned in a square pattern and has dimensions of (1.80 ± 0.1) nm × (1.80 ± 0.1) nm. The values calculated from STM are in agreement with values obtained from the LEED measurements.

Preparation of a covalently bonded nano-network between TAPP and PTCDA was subsequently studied in detail. The polyimidisation reaction between TAPP and PTCDA was successfully carried out and formed a mixture of imides and iso-imides which caused disordered and disconnected networks. However, not all of the amine sites on the TAPP molecules are involved in the reaction with PTCDA molecules. Some TAPP molecules have reacted with one, two, three or four units of PTCDA. This is the underlying reason which prohibits the formation of a more ordered nano-network. In addition, a reaction between individual TAPP molecules also occurs after annealing at 350 ^{o}C. This situation hinders a complete reaction with PTCDA when an equal proportion of TAPP and PTCDA were deposited on the Au(111) surface. Similarly, PTCDA molecules desorbed when the temperature exceeds 300 ^{o}C. Hence, a different sample preparation approach, such as deposition on the substrate held at elevated temperature, may be required in order to obtain a wider coverage of molecules and a more ordered covalently bonded network on the Au(111) surface.

References:

[1] S.A. Krasnikov, C.M. Doyle, N.N. Sergeeva, A.B. Preobrajenski, N.A. Vinogradov, Y.N. Sergeeva, A.A. Zakharov, M.O. Senge, A.A. Cafolla. *Formation of extended covalently bonded Ni porphyrin networks on the Au (111) surface,* Nano Res. (2011) 1.

[2] L. Grill, M. Dyer, L. Lafferentz, M. Persson, M.V. Peters, S. Hecht. *Nano-architectures by covalent assembly of molecular building blocks,* Nat. **2** (2007) 687.

[3] M.I. Veld, P. Iavicoli, S. Haq, D.B. Amabilino, R. Raval. *Unique intermolecular reaction of simple porphyrins at a metal surface gives covalent nanostructures,* Chem. Commun. **2008** (2008) 1536.

[4] N. Zwaneveld, R. Pawlak, M. Abel, D. Catalin, D. Gigmes, D. Bertin, L. Porte. *Organized formation of 2D extended covalent organic frameworks at surfaces.* J. Am. Chem. Soc. **130** (2008) 6678.

[5] S. Weigelt, C. Busse, C. Bombis, M.M. Knudsen, K.V. Gothelf, T. Strunskus, C. Woll, M. Dahlbom, B. Hammer, E. Laegsgaard, F. Besenbacher, T.R. Linderoth. *Covalent interlinking of an aldehyde and an amine on a Au(111) surface in ultrahigh vacuum,* Angew. Chem. Int. Ed. Engl. **46** (2007) 9227.

[6] N. Nicoara, E. Román, J.M. Gómez-Rodríguez, J.A. Martín-Gago, J. Méndez. *Scanning tunneling and photoemission spectroscopies at the PTCDA/Au(1 1 1) interface,* Org. Electron. **7** (2006) 287.

[7] E. Kawabe, H. Yamane, R. Sumii, K. Koizumi, Y. Ouchi, K. Seki, K. Kanai. *A role of metal d-band in the interfacial electronic structure at organic/metal interface: PTCDA on Au, Ag and Cu,* Org. Electron. **9** (2008) 783.

[8] F. Tautz, S. Sloboshanin, J. Schaefer, R. Scholz, V. Shklover, M. Sokolowski, E. Umbach. *Vibrational properties of ultrathin PTCDA films on Ag (110),* Phys. Rev. B. **61** (2000) 16933.

[9] V. Shklover, F.S. Tautz, R. Scholz, S. Sloboshanin, M. Sokolowski, J.A. Schaefer, E. Umbach. *Differences in vibronic and electronic excitations of PTCDA on Ag(111) and Ag(110),* Surf. Sci. **454-456** (2000) 60.

[10] S. Duhm, A. Gerlach, I. Salzmann, B. Bröker, R.L. Johnson, F. Schreiber, N. Koch. *PTCDA on Au (111), Ag (111) and Cu (111): Correlation of interface charge transfer to bonding distance,* Org. Electron. **9** (2008) 111.

[11] M. Toerker, T. Fritz, H. Proehl, F. Sellam, K. Leo. *Tunneling spectroscopy study of 3,4,9,10-perylenetetracarboxylic dianhydride on Au(1 0 0),* Surf. Sci. **491** (2001) 255.

[12] S. Mannsfeld, M. Toerker, T. Schmitz-Hübsch, F. Sellam, T. Fritz, K. Leo. *Combined LEED and STM study of PTCDA growth on reconstructed Au (111) and Au (100) single crystals,* Org. Electron. **2** (2001) 121.

[13] www.isa.au.dk.

[14] www.maxlab.lu.se.

[15] I. Chizhov, A. Kahn, G. Scoles. *Initial growth of 3, 4, 9, 10-perylenetetracarboxylic-dianhydride (PTCDA) on Au (111): a scanning tunneling microscopy study,* J. Cryst. Growth. **208** (2000) 449.

[16] T. Schmitz-Hübsch, T. Fritz, F. Sellam, R. Staub, K. Leo. *Epitaxial growth of 3, 4, 9, 10-perylene-tetracarboxylic-dianhydride on Au (111): A STM and RHEED study,* Phys. Rev. B: Condens. Matter. **55** (1997) 7972.

[17] P. Fenter, F. Schreiber, L. Zhou, P. Eisenberger, S.R. Forrest. *In situ studies of morphology, strain, and growth modes of a molecular organic thin film,* Phys. Rev. B. **56** (1997) 3046.

[18] S.K.M. Henze, O. Bauer, T.L. Lee, M. Sokolowski, F.S. Tautz. *Vertical bonding distances of PTCDA on Au (111) and Ag (111): Relation to the bonding type,* Surf. Sci. **601** (2007) 1566.

[19] Y. Zou, L. Kilian, A. Schöll, T. Schmidt, R. Fink, E. Umbach. *Chemical bonding of PTCDA on Ag surfaces and the formation of interface states,* Surf. Sci. **600** (2006) 1240.

[20] A. Schöll, Y. Zou, M. Jung, T. Schmidt, R. Fink, E. Umbach. *Line shapes and satellites in high-resolution x-ray photoelectron spectra of large π-conjugated organic molecules,* J. Chem. Phys. **121** (2004) 10260.

[21] Y. Hirose, A. Kahn, V. Aristov, P. Soukiassian, V. Bulovic, S. Forrest. *Chemistry and electronic properties of metal-organic semiconductor interfaces: Al, Ti, In, Sn, Ag, and Au on PTCDA,* Phys. Rev. B. **54** (1996) 13748.

[22] J. Taborski, P. Väterlein, H. Dietz, U. Zimmermann, E. Umbach. *NEXAFS investigations on ordered adsorbate layers of large aromatic molecules,* J. Electron. Spectrosc. Relat. Phenom. **75** (1995) 129.

Chapter 6:

Scanning Tunnelling Microscopy (STM) Studies of 1,3,5-tris(4-aminophenyl)benzene (TAPB) Molecules on Noble Metal Surfaces and Covalent Bonding of TAPB with PTCDA on Ag(111) Surface.

6.0 Introduction.

Recent publications on covalent polymerisation on metal surfaces have demonstrated some progress; some promise and some interesting systems [1-6]. However, while it is relatively easy to initiate inter-molecular covalent bonding on metal surfaces, forming ordered and extended polymeric networks is still a challenge due to the irreversible nature of most covalent bonding schemes under UHV conditions. To date, Tanoue *et al.* [7] and Dienstmaier *et al.* [8] have demonstrated reversible reactions in solution to form covalent organic frameworks (COF). Tanoue *et al.* reacted 5,10,15,20-tetrakis(4-aminophenyl)porphyrin (TAPP) with isophthalaldehyde (IPA) in aqueous solution on Au(111) surfaces to form small patches of highly ordered networks. However, Dienstmaier *et al.* was able to use similar methods to react 1,4-benzenediboronic acid (BDBA) on HOPG surfaces to form long-range ordered, covalent organic frameworks (COF).

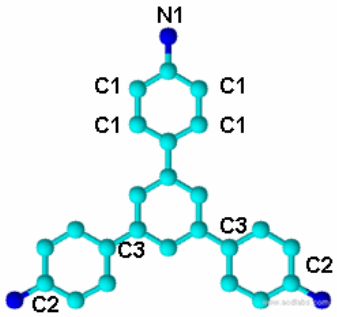

Fig. 6.1 Chemical structural of TAPB. In the molecular representation, light blue balls are carbon atom and dark blue balls are nitrogen. The numbering in the structure is to indicate carbon and nitrogen components.

This study is divided into two parts; the first describes the deposition and ordering of 1,3,5-tris(4-aminophenyl)benzene (TAPB) on the Au(111) and Ag(111) surfaces studied by STM and XPS. TAPB is a three fold symmetric molecule with amino groups attached in the *para* position on the phenyl rings (Fig. 6.1). The ability of three fold symmetric molecules to form symmetric networks of covalent organic frameworks with varying pore sizes have been studied recently [5,9] . The different pore sizes are due to various polygonal cells formed in the networks. The objective of studying TAPB molecules is to form covalent networks as proposed in Scheme 6.1 below. The molecules can form three to six membered rings depending on the substrate temperatures and type of substrate used [9].

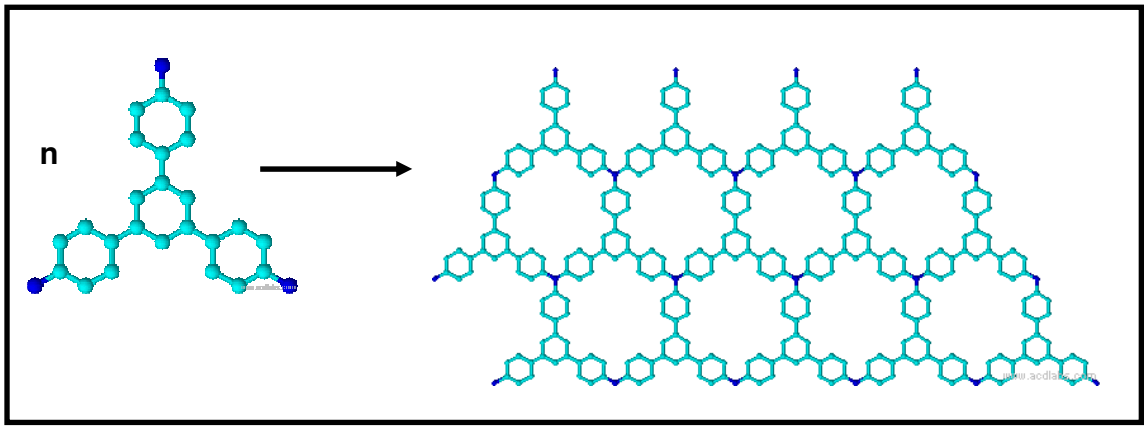

Scheme 6.1 Diagram to show the formation of TAPB honeycomb networks.

The second part of this study describes an STM/XPS study of the structures obtained when TAPB is co-deposited with PTCDA on the Ag(111) surface. This study complements the results presented in Chapter 5, where a similar study was carried out on Au(111) using TAPP and PTCDA molecules. The results show that the reaction between PTCDA and TAPP formed disordered covalently bonded networks. In this case, TAPB is a simpler molecule where only one nitrogen species (amino group, NH_2) is present in contrast to TAPP molecule which has three nitrogen species. The resulting networks are influenced by the symmetry of the molecules, hence, the TAPB molecules should result in different structures to those observed with the TAPP molecules. Additionally, there was no phase separation observed in the mixture of TAPB and PTCDA during our preliminary study.

A brief investigation of PTCDA on Ag(111) was performed using STM and LEED before the experiments involving co-deposition of TAPB and PTCDA were carried out.

Co-depositing differently shaped molecules is expected to lead to the formation of complicated supramolecular structures [6]. In previous studies by other groups, two dimensional (2D) hydrogen bonded networks were investigated by mixing PTCDA with 4, 4" diamino-*p*-terphenyl (DATP), 2, 4, 6-tris(4-aminophenyl)1, 3, 5-triazine (TAPT) [10] and pentacene [11]. Studies have also been conducted by Sun *et al.*[6] involving PTCDA and melamine, whereby different PTCDA/melamine ratios resulted in different structures. The initial assumption underpinning the work presented in this chapter is that the PTCDA and TAPB should form O--HN hydrogen bonds on Ag(111). Thermal annealing is usually used to influence and modify 2D structures based on single [12] and multi molecular building blocks [13,14]. Hence, the evolution of the PTCDA/TAPB system under different thermal treatments was monitored using STM and XPS.

6.1. Experimental.

All measurements were carried out in an ultra-high vacuum (UHV) chamber. The TAPB molecules (Tokyo Chemical Industry) were degassed at 200 ^{o}C for 24 hours. The molecules were then deposited onto either Au(111) or Ag(111) crystals from a Mo crucible which was heated to 210 ^{o}C by a tungsten coil. The deposition pressure in the preparation chamber was 3×10^{-10} mbar. Deposition of the TAPB on the clean crystals was performed at both room temperature and on surfaces held at elevated temperatures (200 ^{o}C, 250 ^{o}C and 300 ^{o}C). Details of the PTCDA deposition parameters were presented in Chapter 5.

Measurements to investigate the covalent bonding were performed at room temperature on surfaces prepared with different TAPB to PTCDA ratios and at different annealing temperatures. Details of the experimental techniques used, STM and XPS, are presented in Section 2.2 and 2.3; respectively of Chapter 2. All binding energies in XPS are determined to an accuracy of $\pm$ 100 meV. The STM images were acquired with the Omicron Scala electronics recorded at room temperature. The coverage in this chapter was determined by calculating the C 1s to metal ratio from the XPS measurements. Processing of the STM data was done using the WSxM software [15]. The core level analysis of the data was performed using a Voigt lineshape deconvolution in the Fityk peak fitting software [16] .

6.2. Results and Discussion.

6.2.1. Scanning Tunnelling Microscopy (STM) of TAPB on Au(111) at Room Temperature (RT).

Fig. 6.2 shows a series of STM images of TAPB molecules after deposition on Au(111) at room temperature. Fig. 6.2(a) was recorded after coverage of 0.4 ML of TAPB was deposited. The Au(111) ($22 \times \sqrt{3}$) reconstruction is clearly visible indicating that there is very little interaction between the molecules and the Au surface. After a second deposition of 1.5 ML, at a higher molecular flux, thick layers of TAPB were obtained as shown in Fig, 6.2(b). Here, the step shows an unusual zigzag pattern. While it is hard to find an explanation for this unusual behaviour, it was also observed on the Ag surface (Section 6.2.5). Subsequently, the thick layer sample was annealed at 150 ^{o}C in an attempt to induce ordering of the molecules on the surface. However, this resulted in 75 % desorption of TAPB molecules (Fig. 6.2c). A further anneal at 200 ^{o}C (Figure 6.2d) resulted in no appreciable change in either the XPS C 1s intensities or STM images. From this sequence experiments, it is concluded that the TAPB molecules do not form self assembled monolayers on the Au(111) surface. Desorption of the molecules was observed at temperatures of 100 ^{o}C (STM image not shown). This suggests a repulsive intermolecular interaction or a weak interaction between the TAPB molecules and Au(111) surface. The STM observations presented in Fig 6.2 is further confirmed by the XPS results discussed below.

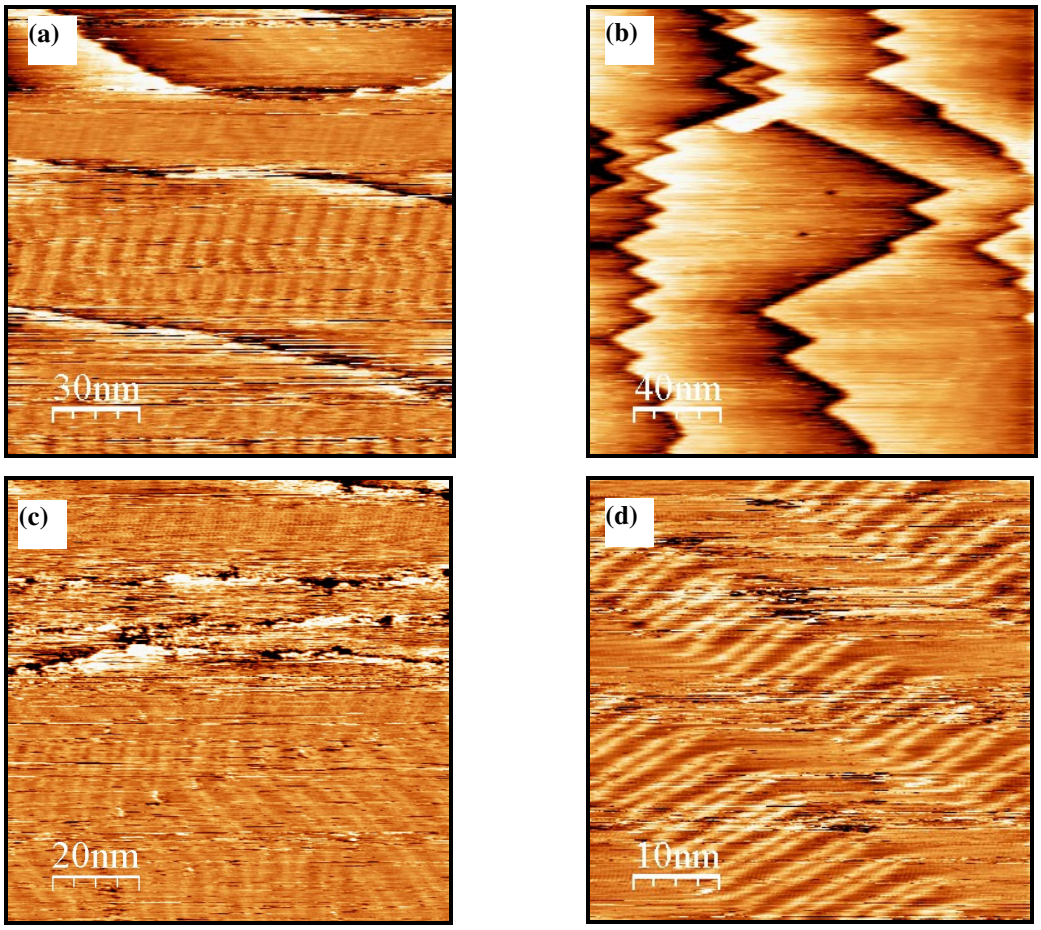

Fig. 6.2 (a) STM image (89 nm × 89 nm, Vs = +1.0 V, I =0.2 nA) of TAPB on Au(111) after 0.4 ML TAPB deposition; (b) STM image (200 nm × 200 nm, Vs = +0.5 V, I =0.3 nA) after 1.5 ML of deposition; (c) STM image (200 nm × 200 nm, Vs = +1.4 V, I =0.2 nA) after150 ^{o}C anneal; (d) STM image (50 nm × 50 nm, Vs = +1.2 V, I =0.4 nA) after 200 ^{o}C anneal.

6.2.2. X-ray Photoelectron Spectroscopy of TAPB molecules on Au(111) at Room Temperature.

The C 1s and N 1s XPS spectra are presented in Fig. 6.3. There are three components expected on the C 1s core level associated with -C=C- (C1) from the phenyl rings, -C-NH_2 (C2) and Ph-C- (C3) bonds as shown in Fig. 6.1. However, the energy resolution is not sufficient to resolve these spectral components expected for this molecule and therefore, the C 1s spectrum is fitted with a single peak centred at 284.4 eV which corresponds to the carbon peak associated with the phenyl rings in the TAPB molecule. The amino group (NH_2) is the only nitrogen component expected from TAPB molecules. When the sample is annealed to 150 ^{o}C, the intensity of the C 1s peak decreases by a factor of ~3 in agreement with the coverage observed in the STM images shown in Fig. 6.2. Similarly, since all of the nitrogen atoms are in the same chemical environment (–NH_2), a single component is measured at a binding energy of 399.4 eV in the N 1s spectra. The N 1s peak decreases by a factor of 3.6 after annealing at 150

^{o}C. No sign of covalently bonded networks are observed as there is no shift in the binding energy of N 1s to confirm any chemical reaction.

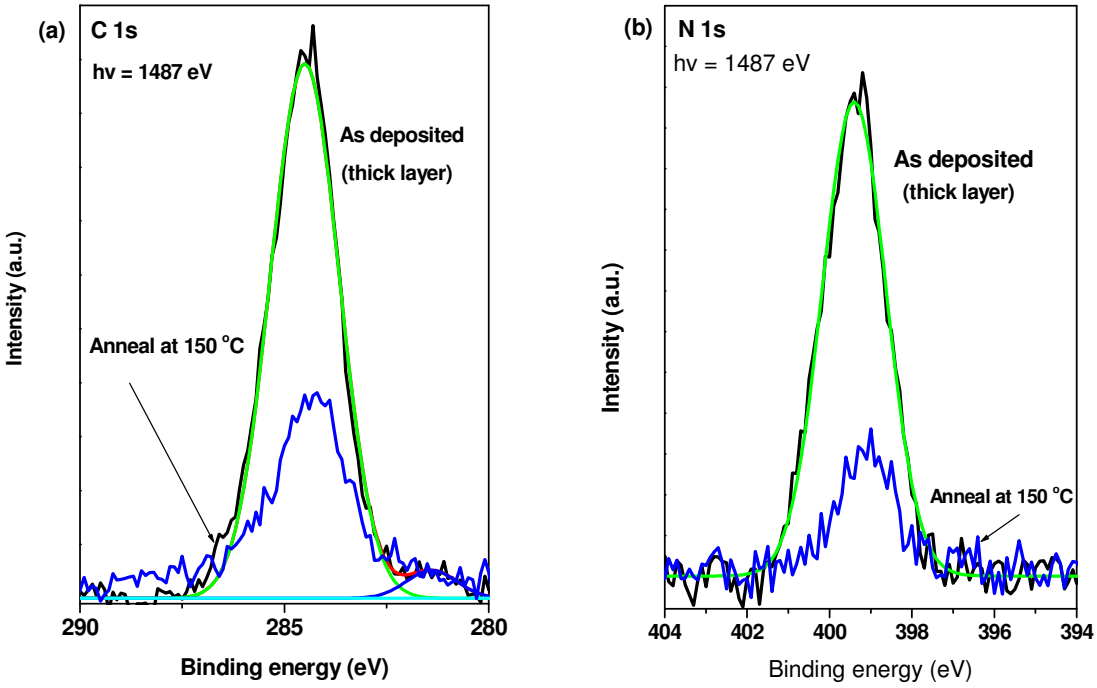

Fig. 6.3 Comparison of XPS (a) C 1s and (b) N 1s spectra of as deposited of TAPB on Au(111) and after annealing at 150 ^{o}C.

6.2.3. Scanning Tunnelling Microscopy (STM) of TAPB on Au(111) at Elevated Temperatures.

In order to initiate a reaction between the individual TAPB molecules, three experiments were performed in which the molecules were deposited on the Au(111) surfaces which were held at 200 ^{o}C, 250 ^{o}C and 300 ^{o}C respectively. The TAPB effusion cell was held at 210 ^{o}C and the deposition was carried out for 15 minutes in each of the experiments. These cell parameters are chosen since they correspond to a coverage equivalent to one ML on the room temperature substrate.

For the 200 ^{o}C deposition the STM images showed the presence of TAPB molecules at the Au(111) as shown in Fig. 6.4(a - c) molecules are the step edges. The coverage is estimated to be 0.33 ML (based on the XPS measurements). The STM images also appeared unresolved while scanning which indicates loose molecules being dragged by the STM tip, while the (22 x $\sqrt{3}$) reconstruction of Au(111) could be observed clearly. This shows that this temperature is not suitable for this approach where substrate is held

at elevated temperature. The sticking coefficient between the surface and the molecules was low at this temperature where only approximately 0.23 ML was deposited on the surface. Small areas of network are observed on the terraces, however, the networks that formed are observed to be disordered and mainly located at the step-edges.

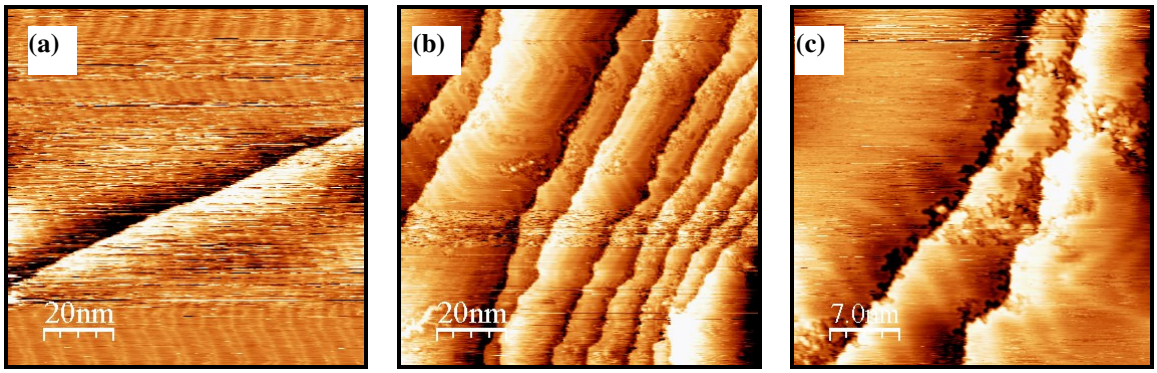

Fig. 6.4 (a) STM image (100 nm × 100 nm, Vs = +0.6 V, I =0.2 nA) of TAPB; (b) STM image (100 nm × 100 nm, Vs = +2.0 V, I =0.2 nA) after annealing at 280 °C; (c) STM image (35 nm × 35 nm, Vs = +2.0 V, I =0.2 nA) after annealing at 280 °C when the substrate is held at 200 °C.

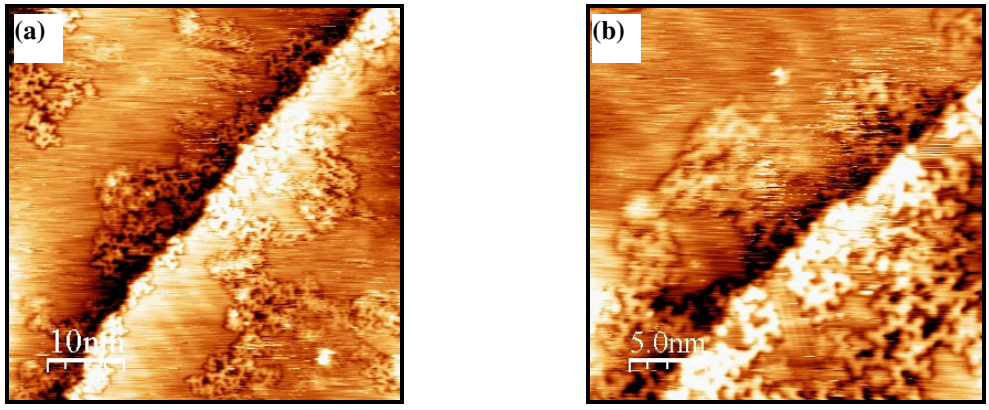

Fig. 6.5 (a) STM image (50 nm × 50 nm, Vs = -0.3 V, I =0.1 nA) of TAPB; (b) STM image (25 nm × 25 nm, Vs = -0.2 V, I =0.1 nA) when the substrate is held at 250 °C.

For deposition on at the Au(111) surface at 250 °C, a network is formed on the crystal as shown in Fig. 6.5. The networks formed are disordered and the growth appears to nucleate at the step edges. This temperature has proven to be the most suitable to grow networks although the networks formed are not ordered. The estimated coverage formed at this temperature is 0.3 ML.

The results of two separate experiments carried out at 300 °C are presented in Fig. 6.6. Here a TAPB deposition time of 15 minutes resulted in coverage of about 0.3 - 0.4 ML based on the coverage measured in the STM images. The networks are disordered and grow over the entire Au(111) surface. The networks mainly consist of oligomers and no

hexagonal cells are observed. This experiment was repeated with a 30 minute deposition time, resulting in a more densely packed network with relatively little uncovered Au surface remaining (Fig.6.6c and d). At this deposition, the estimated coverage is 1 ML.

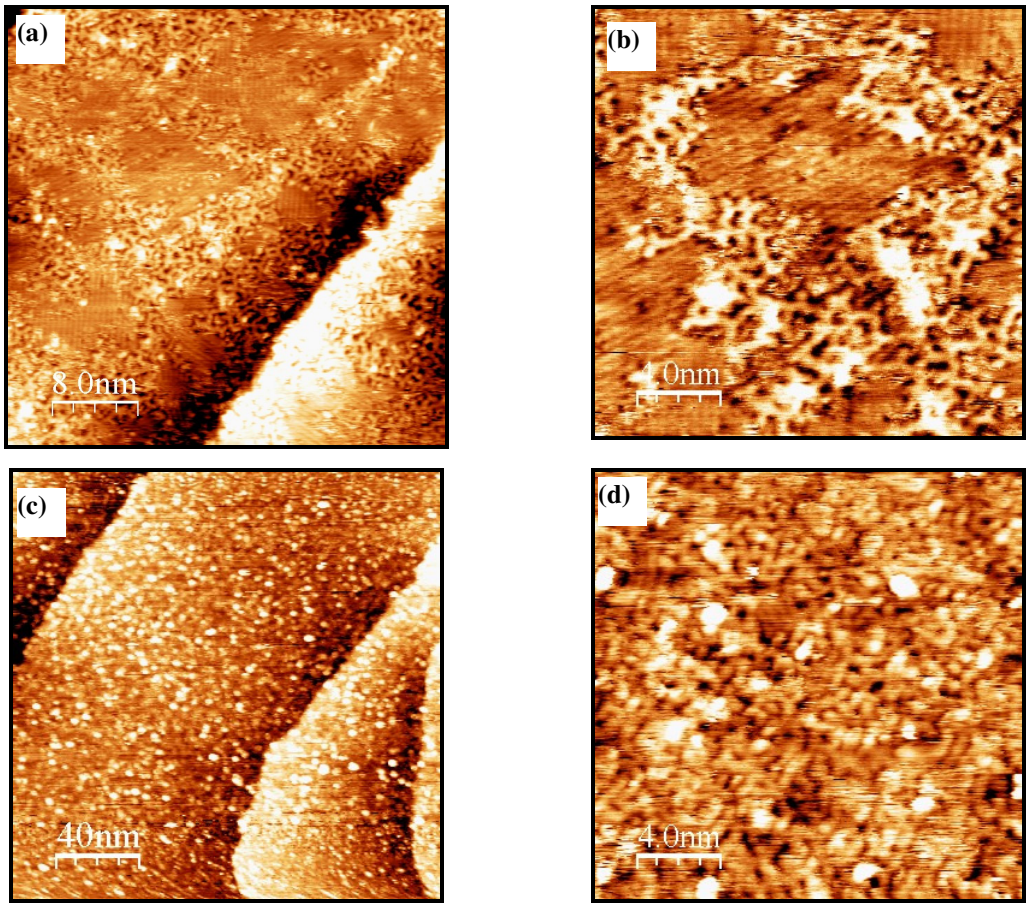

Fig. 6.6 (a) STM image (40 nm × 40 nm, Vs = +0.2 V, I =0.2 nA) of TAPB at 0.3 ML; (b) STM image (20 nm × 20 nm, Vs = -0.7 V, I =0.3 nA) at 0.3 ML; (c) STM image (200 nm × 200 nm, Vs = -1.0 V, I = 1.0 nA) at 1 ML; (d) STM image (20 nm × 20 nm, Vs = +0.5 V, I =0.1 nA) at 1 ML when the substrate is held at 300 °C.

In Fig. 6.6(b), a reconstruction of the Au surface consisting of a series of parallel rows in the empty regions of the network is observed. Analysis of the image shows that there are three different orientations of this structure rotated at 120 ° relative to each other which indicates that the observed structure is related to the underlying Au surface. To confirm this hypothesis, a series of images were analysed using the WSxM software. Line profiles of the structures, shown in Fig. 6.7(b), gives the average distance between rows of (0.4 ± 0.03) nm. This is further confirmed by a Fast Fourier Transform (FFT) of these regions (Fig. 6.7c), which is subsequently plotted as a k-vector graph in Fig. 6.7(d). The FFT measured line is (0.5 ± 0.02) nm and corresponds to twice the spacing of the atomic rows in the $[\bar{1}10]$ direction of the Au(111) surface. Hence, this finding

shows that the TAPB has modified the surface structure from a $(22 \times \sqrt{3})$ to a (2×1) reconstruction.

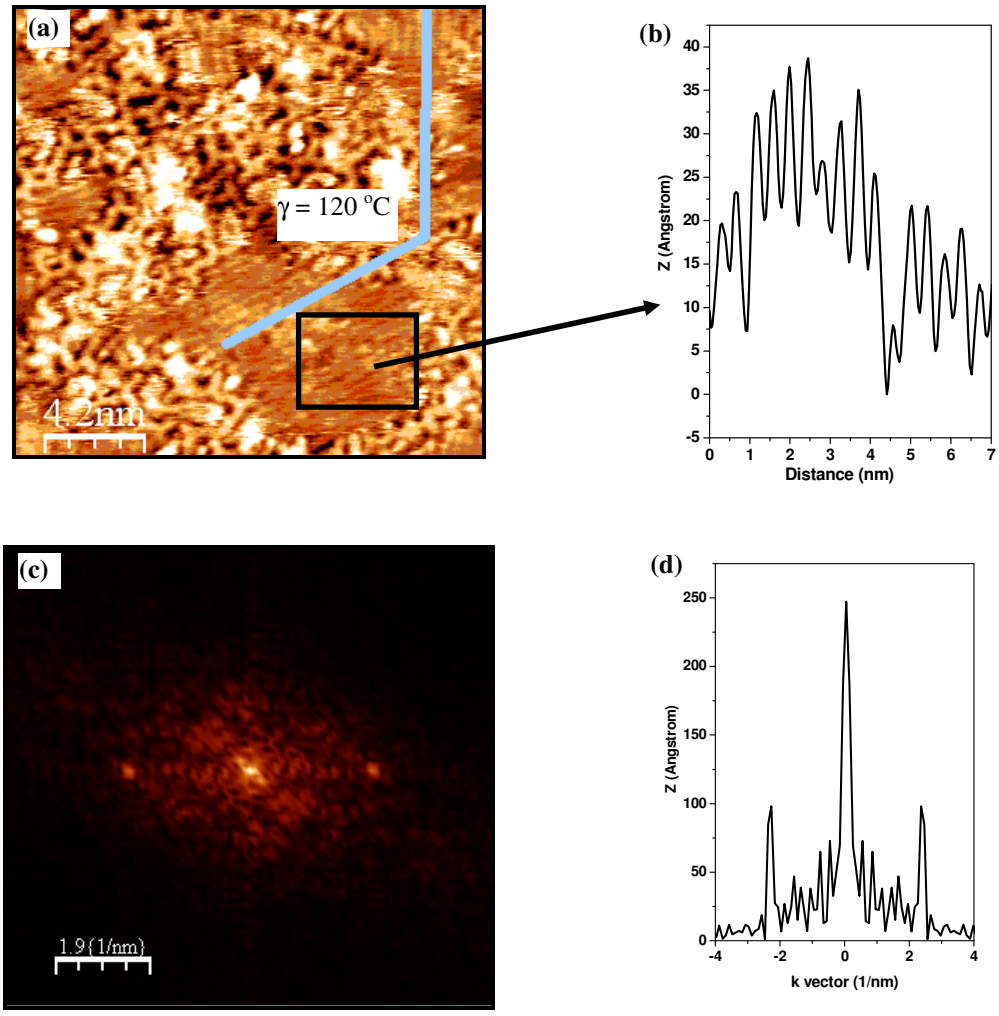

Fig. 6.7 Image analysis to determine the lattice constant of the waves observed in the STM image obtained in (a).

6.2.4. X-ray Photoelectron Spectroscopy (XPS) of TAPB on Au(111) at Elevated Temperatures.

Fig. 6.8 shows a comparison between the N 1s spectra after a room temperature deposition with that of a film deposited on a series of substrates held at different elevated temperatures. No binding energy shift is observed in the N 1s peak as a function of substrate temperature. The qualitative observation from these spectra is that the N 1s peak at substrate temperatures held at 200 °C and 250 °C are similar to those observed in the room temperature measurements. The N 1s peak measured from the 300 °C surface is broader. There is a significant broadening of the peak on the lower binding energy side which indicates a new chemical environment for the nitrogen at this substrate temperature. It is noted that the STM images confirm networking among

TAPB molecules in these substrate held at 300 °C, although the exact nature of the covalently bond formed is not known. The possible reactions that can occur are described in Section 3.2.1, Chapter 3.

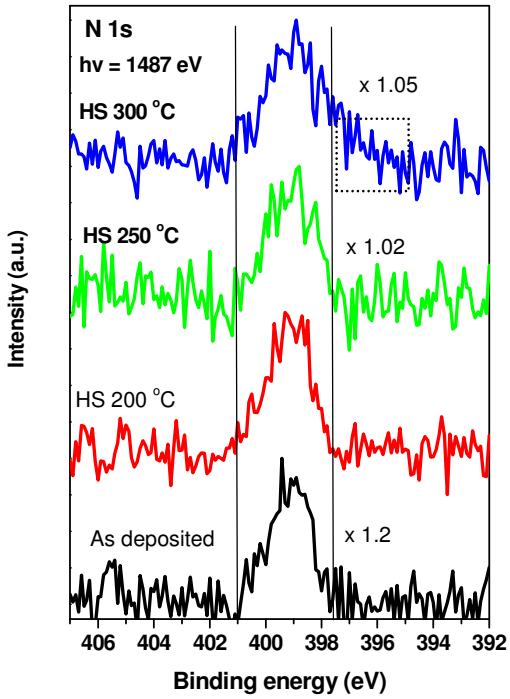

Fig. 6.8 Comparison of XPS of N 1s spectra of as deposited of TAPB on Au(111) and at different annealing temperatures at 200 °C, 250 °C and 300 °C .

From the experiments conducted on Au(111) the TAPB molecules do not form self-assembled layers on Au(111) surfaces when deposited at room temperature. While the substrate held at elevated temperature does initiate covalently bonding of the TAPB molecules, the networks obtained are disordered and are formed mainly of oligomers. Among the three studied substrate temperatures, 250 °C or 300 °C are found to give similar results when deposited for 15 minutes and produce networks at a good growth rate in contrast with substrate temperature at 200 °C where few networks are formed. In the experiment at 300 °C, a (2 × 1) reconstruction of the Au surface is observed in the regions not covered by the network, the (2 × 1) spacing is measured to be (0.5 ± 0.02) nm.

6.2.5. Scanning Tunnelling Microscopy (STM) of TAPB on the Ag(111) Surface at Room Temperature (RT) .

The ordering of TAPB molecules was also studied on the Ag(111) surface. Fig. 6.9 shows STM images taken at different coverages. The observed behaviour is similar to that observed on Au(111), suggesting a repulsive force between molecules. The hexagonal structure of the Ag(111) surface appeared to be better resolved in these images as compared to the images obtained from the clean Ag(111) surface (Section 2.7.2, Chapter 2). The atomic resolution from Fig. 6.9(b) is from the underlying Ag surfaces and is not of the molecules. This could be due to a TAPB molecule attached to the STM tip which makes the tip atomically sharper. Hence, it greatly improves the resolution of the surface image. This behaviour is observed until a thick layer is formed, which is sufficient to inhibit the imaging of the underlying silver in Fig. 6.9(c). Here, the unusual zigzag pattern observed on the Ag(111) is also reported seen on the Au(111) surfaces (refer to Section 6.2.1).

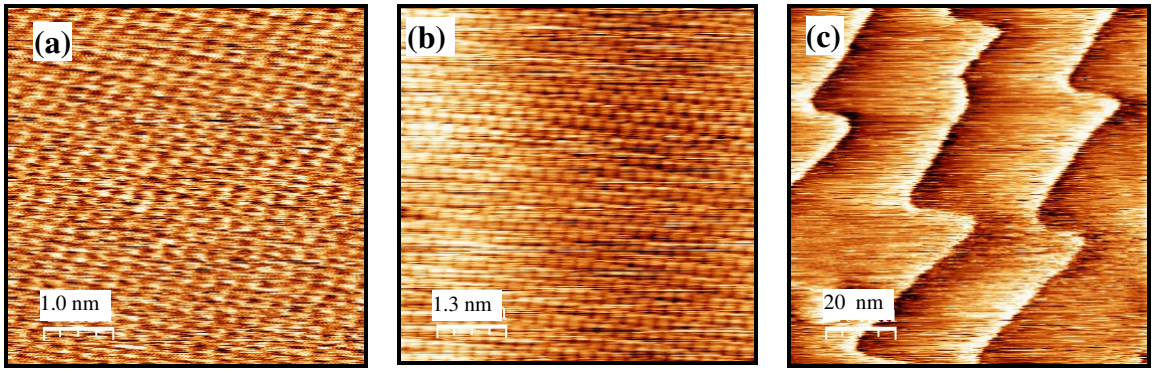

Fig. 6.9 Room temperature deposition of TAPB on Ag(111) (a) STM image (5 nm × 5 nm, Vs = +0.3 V, I =0.1 nA) at 0.4 ML; (b) STM image (5.5 nm × 5.5nm, Vs = +0.5 V, I =0.05 nA) after 5 ML; (c) STM image (100 nm × 100 nm, Vs = +0.5 V, I =0.05 nA) after 5ML.

6.2.6. X-ray Photoelectron Spectroscopy (XPS) on the Ag(111) Surface at Room Temperature (RT) .

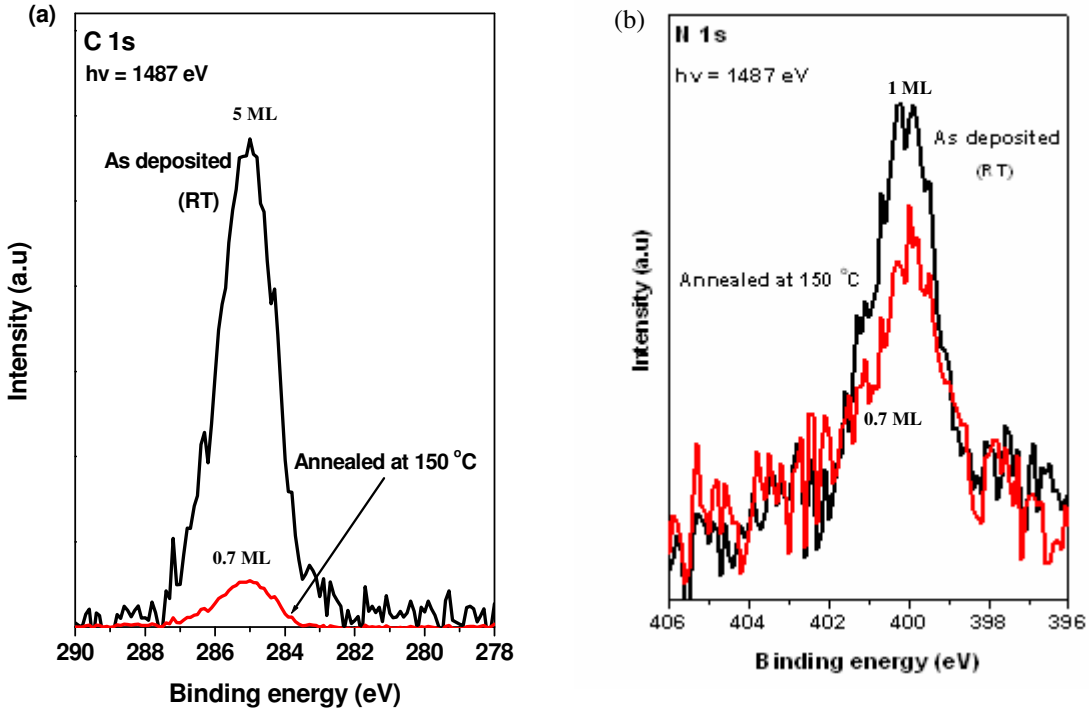

Fig. 6.10 XPS spectra for (a) C 1s and (b) N 1s spectra of substrate deposited at room temperature and after annealing to 150 °C.

Fig. 6.10 shows the XPS spectra of C1s and N1s before and after annealing at 150 °C. The C 1s is decreased more than five fold from 5 ML to 0.7 ML when it was annealed to 150 °C. TAPB molecules have desorbed from the Ag(111) surface. This suggests that the intermolecular interactions are repulsive.

The N 1s baseline subtraction was performed according to procedures described in Section 3.3.5. The N 1s was not measured at 5 ML. Hence, the coverage at 1 ML is taken as an example to illustrate the decreased of the N 1s intensity after annealing. The N 1s intensity decreased one third from 1.0 ML to 0.7 ML after annealing at 150 °C. No binding energy shift is observed to suggest any reaction occurs among TAPB molecules.

6.2.7. Scanning Tunnelling Microscopy (STM) of TAPB on Ag(111) Surface at Elevated Temperatures.

TAPB molecules were deposited on the Ag(111) surface at three different substrate temperatures. When the molecules were deposited on an Ag(111) at a substrate temperature of 200 ^{o}C, the same phenomena as observed with room temperature substrate deposition took place, that is, no TAPB molecules or networks were observed (Fig. 6.11), although XPS results indicate that 1.3 ML of TAPB is deposited on the surface. In this case, STM imaging suggests that 200 ^{o}C substrate temperature on Ag(111) is not hot enough to initiate any reactions among amino groups on TAPB molecules to form covalent bonded networks. Instead, it is suggested that a TAPB molecule has attached onto the STM tip and makes the tip atomically sharp. Hence, the scanning from STM showed the hexagonal structure of the Ag(111) surface. Similar result were reported and described on Au(111) where TAPB molecules were deposited on substrate hold at room temperature in Section 6.2.5.

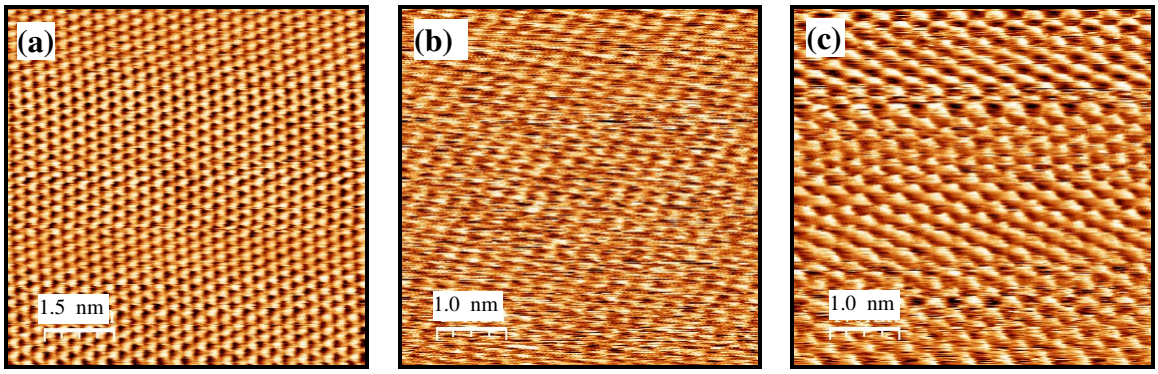

Fig. 6.11 (a) STM image (7.5 nm × 7.5 nm, Vs = -0.3 V, I =0.1 nA) of TAPB; (b) STM image (7.5 nm × 7.5 nm, Vs = -0.03 V, I =0.3 nA); (c) STM image (5 nm × 5 nm, Vs = -0.03 V, I =0.3 nA. All surfaces were prepared by depositing 1.3 ML of TAPP on a Ag(111) substrate held at 200 ^{o}C.

In the case of TAPB deposition on the Ag(111) surface at 250 ^{o}C there are two important observations. (i) At this substrate temperature, the self-assembly of TAPB molecules is observed; the arrows in Fig. 6.12(a) show two small patches that consist of 10 - 20 molecules of TAPB which are arranged in an ordered manner and (ii) disordered covalently bonded networks are observed.

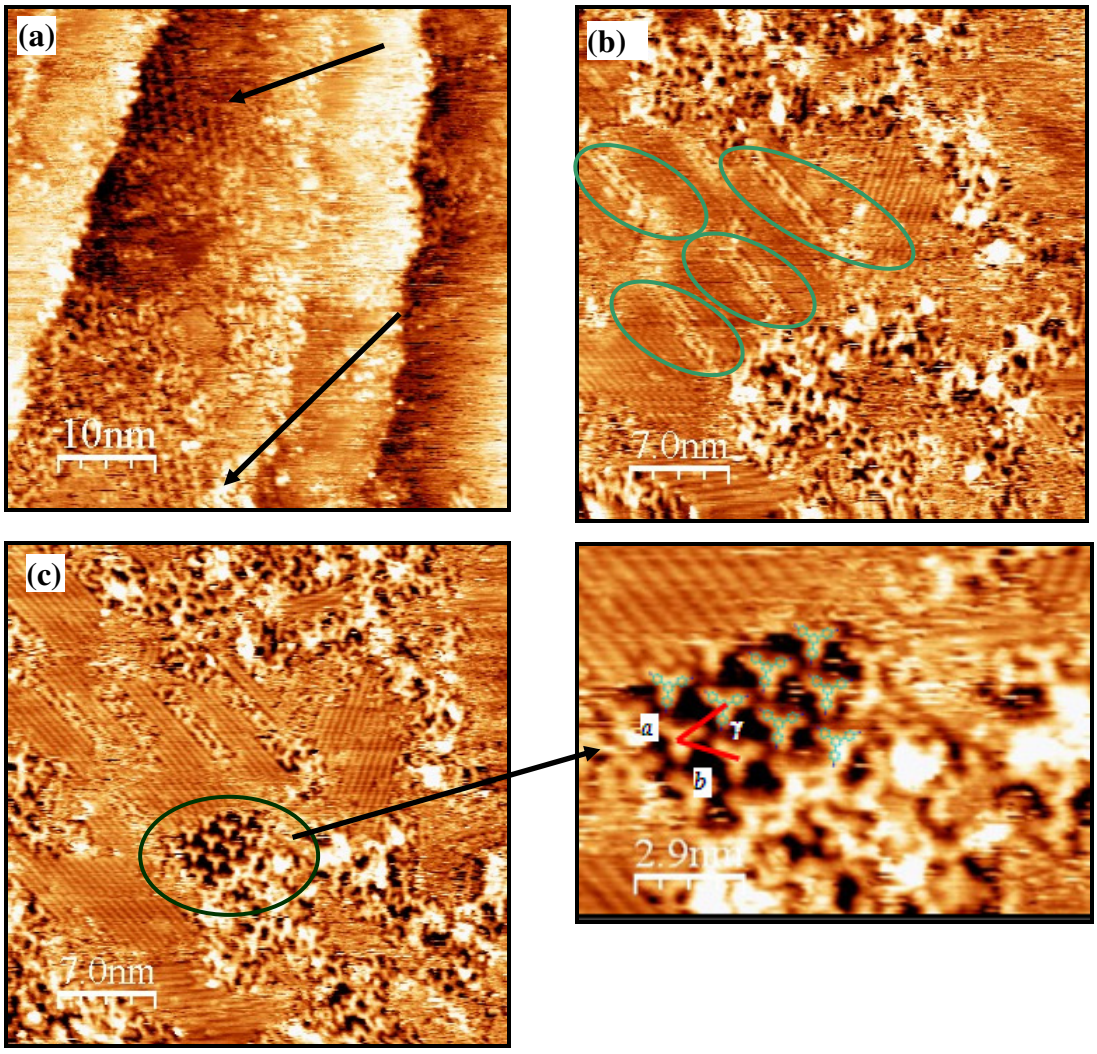

Fig. 6.12 (a) STM image (50 nm × 50 nm, Vs = +0.4 V, I =0.1 nA) of TAPB; (b) STM image (3 5nm × 35 nm, Vs = +0.08 V, I =0.05 nA); (c) STM image (50 nm ×50 nm, Vs = +0.08 V, I =0.05 nA. All surfaces were prepared by depositing 0.6 ML of TAPP on a Ag(111) substrate held at 250 °C.

The appearance of self-assembled TAPB patches could be due to the fact that 250 °C substrate temperature allows for better interaction of TAPB molecules with Ag(111) substrate, which overcomes the molecule-molecule repulsion observed in the deposition on substrate held at room temperature. The unit cell of the ordered TAPB regions is oblique, with lattice parameters: $\boldsymbol{a}$ = 1.0 ± 0.1 nm and $\boldsymbol{b}$ = 1.0 ± 0.1 nm with an angle of 60 ± 5° (Fig. 6.12c). Moreover, there are a numbers of TAPB molecules arranged in rows alternatively rotated by 180 ° and parallel to the (2 × 1) reconstruction as shown in Fig. 6.12(b) in green ovals. In addition, covalently bonded molecules are also observed at this temperature. The lines observed in Fig. 6.12(b & c) correspond to a (2 × 1) reconstruction of the Ag(111) surface and are similar to the reconstruction observed when TAPB molecules are deposited on the Au(111) surface mentioned in Section 6.2.3. The measured spacing of the lines is (0.5 ± 0.03) nm. Domains rotated at 60°

relative to each other suggest that this reconstruction is associated with the Ag surface. An explanation for this phenomenon was presented in Section 6.2.1. This scenario on Ag is also observed in the substrate held at 250 ^{o}C. Disordered covalently bonded networks mainly oligomers are found throughout the surface.

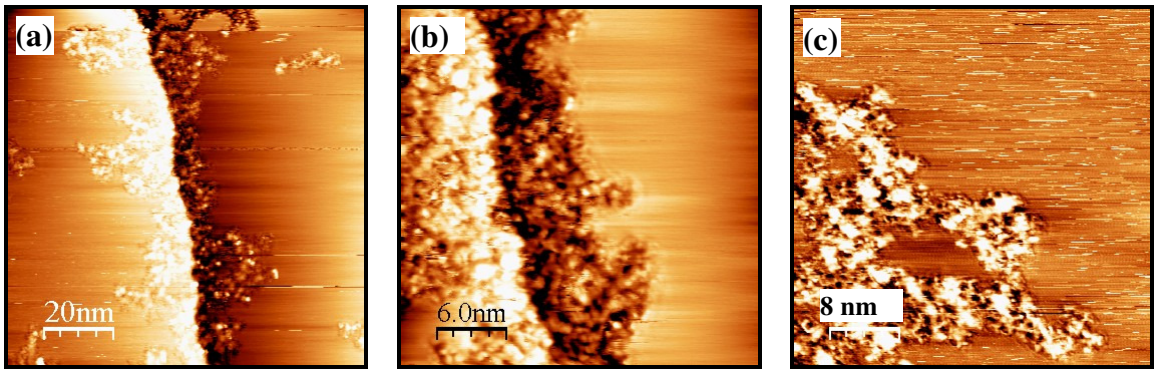

Fig. 6.13 (a) STM image (100 nm × 100 nm, Vs = -0.9 V, I =0.08 nA) of TAPB; (b) STM image (30 nm × 30 nm, Vs =- 0.9 V, I =0.08 nA); (c) STM image (40 nm × 40 nm, Vs = -1.0 V, I =0.1 nA. All surfaces were prepared by depositing 0.5 ML of TAPP on a Ag(111) substrate held at 300 ^{o}C.

The substrate temperature was elevated to 300 ^{o}C. This temperature causes partial decomposition of TAPB networks which can be observed as brighter spots on the surfaces and the networks are not clearly distinguished (Fig. 6.13). The networks formed are mainly concentrated on the step-edges of the Ag(111) crystal. The coverage obtained is approximately 0.5 ML based on the XPS measurements of C 1s /Ag 3*d* ratio.

6.2.8. X-ray Photoelectron Spectroscopy (XPS) of TAPB on Ag(111) Surface at Elevated Temperatures.

Fig. 6.14 shows the C 1s and N 1s XPS spectra for TAPB deposition on an Ag(111) substrate held at 200 ^{o}C, 250 ^{o}C and 300 ^{o}C. The coverage on the surface is estimated using C 1s/Ag 3*d* ratio. The deposition at a substrate temperature of 200 ^{o}C results in a large coverage estimated at 1.3 ML and is larger than the sample deposited on a substrate held at 250 ^{o}C estimated at 0.6 ML, whereas the TAPB coverage on a substrate held at 300 ^{o}C is 0.7 ML. Based on the STM measurements , a substrate temperature of 250 ^{o}C is the most suitable for covalent bonding to occur without decomposition of the molecules as the self-assembly of TAPB molecules and TAPB networks are found on Ag(111) surfaces held at 300 ^{o}C as discussed in Section 6.2.7.

The full width at half maximum (FWHM) of the XPS C 1s peaks measured on the substrate held at elevated temperatures is greater than that observed for the room temperature deposition and annealing performed on the same sample at 150 ^{o}C. The peak positions, intensities and values of FWHM are tabulated in Table 5.1. The broadening of the C 1s peak was initially interpreted as a sign of decomposition. However, on closer examination, it appears that this is not the case as the C 1s spectra for substrate temperatures of 200 ^{o}C and 250 ^{o}C have the same FWHM value as the peak at 300 ^{o}C deposition. Therefore, it is proposed that the broadening of the C 1s peak is due to a new chemical environment present at the lower binding energy which could be attributed to the interaction of TAPB with the Ag surface. However, this statement is still speculative as there is no other further analysis which can confirm this hypothesis.

Table 6.1 The summary of FWHM values of substrate held at room temperature and substrate held at elevated temperature.

Experiments	**Peak (± 0.1 eV)**	**Intensities (Area)**	**FWHM (eV)**
Room temperature deposition	285.1	28.35	1.6 ± 0.02
Annealing at 150 ^{o}C	285.1	2.62	1.6 ± 0.03
Hot surface at 200 ^{o}C	285.0	2.36	2.0 ± 0.01
Hot surface at 250 ^{o}C	285.0	0.89	1.9 ± 0.03
Hot surface at 300 ^{o}C	284.9	1.08	1.9 ± 0.02

The N 1s baseline subtraction was carried out according to procedures mentioned in Section 3.3.5(b) in Chapter 3. The N 1s XPS peak intensity recorded from 250 ^{o}C and 300 ^{o}C substrates decreased completely as shown in Fig. 6.14(b). The signal to noise ratio is very low and hence, no conclusive finding can be determined. Despite the low signal to noise ratio, it appears that there is no nitrogen present. One possible explanation for this is the reaction of amino groups on the TAPB molecules has resulted in complete disassociation of the nitrogen on a substrate held at elevated temperature and the –(C-C)- bond is formed instead of –NH-NH- or -N=N- bonds that are formed in the other experiments with TAPP molecules on all surfaces (Chapter 3) or in the experiments with TAPB molecules on Au(111) discussed above. If this were indeed the case, this would be very interesting and unusual behaviour. Further work such as synchrotron measurements could be employed to confirm this hypothesis.

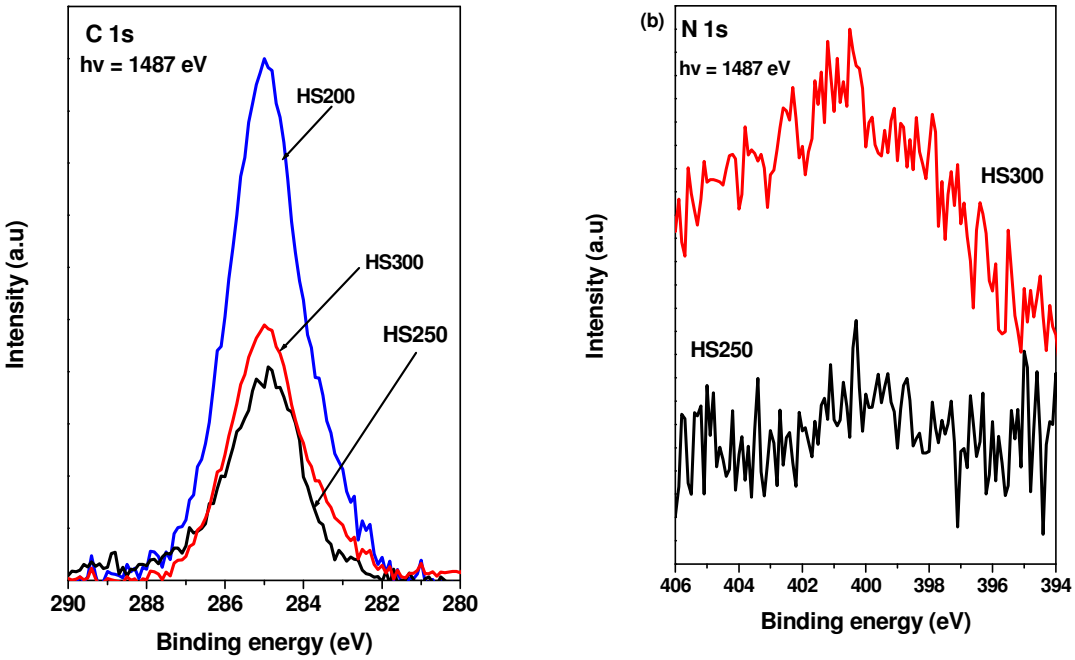

Fig. 6.14 Comparison of XPS (a) C 1s and (b) N 1s spectra of substrate deposited at 200 °C, 250 °C and 300 °C.

Deposition of TAPB molecules on the Ag(111) surface results in some unexpected results. Areas of self-assembled TAPB were found when the molecules were deposited on Ag(111) at 250 °C. The molecules do not self-assembled on Ag(111) at room temperature and mostly desorb from surface at a low annealing temperature. Evidence from the XPS measurements suggest that the bonding between the TAPB molecules is -C-C- instead of the HN-NH or –N=N- bonding which was a more likely mechanism for the amino group reactions in the substrate held at elevated temperature. However, this conclusion is not final due to low signal to noise ratio. Deposition of TAPB on an Ag(111) substrate held at 250 °C changed the reconstruction of Ag(111) from (1×1) to (2 × 1).

6.2.9. Scanning Tunnelling Microscopy (STM) and Low Energy Diffraction (LEED) Studies of PTCDA on Ag(111) .

Fig. 6.15 (a and b) shows STM images of PTCDA deposited on Ag(111) at room temperature. The two molecules are rotated by an angle of (80 ± 3)° with respect to each other. This structure is identified as a herringbone (HB) structure (Fig. 6.15a). It is a typical HB structure which has been reported, in Chapter 3 on Au(111) and by Glockler *et al*. [17] specifically for Ag(111) and Ag(110) surfaces. This structure has dimensions of (1.3 ± 0.1) nm × (2.0 ± 0.1) nm. The other structure shown in Fig. 6.15(b) is closer to a square unit cell with dimensions of (1.4 ± 0.1) nm × (1.4 ± 0.1) nm. The molecules in the unit cell are rotated by (90 ± 2)^{o} relative to each other. To our knowledge, this structure has not been reported in the literature.

Fig. 6.15(c) shows a LEED pattern from the PTCDA on Ag(111) surface recorded at a primary beam energy of 24.0 eV. It shows a large number of sharp and well-resolved superstructure spots, which indicate that a long-range ordered superstructure with a large unit cell, has formed. In this case, the LEED pattern confirmed the presence of the HB pattern on the surface which is in agreement with the STM images above. The unit vectors of the reciprocal lattice are illustrated in Fig. 6.15(d) [17]. The commensurability of this structure can be determined from LEED. Since the overlayer is of lower symmetry than that of the underlying substrate, there are six-symmetry equivalent domains of the adsorbate on the (111) surface which result in the sixfold symmetry of the resulting pattern (three 120 ^{o}-rotations × two reflections).

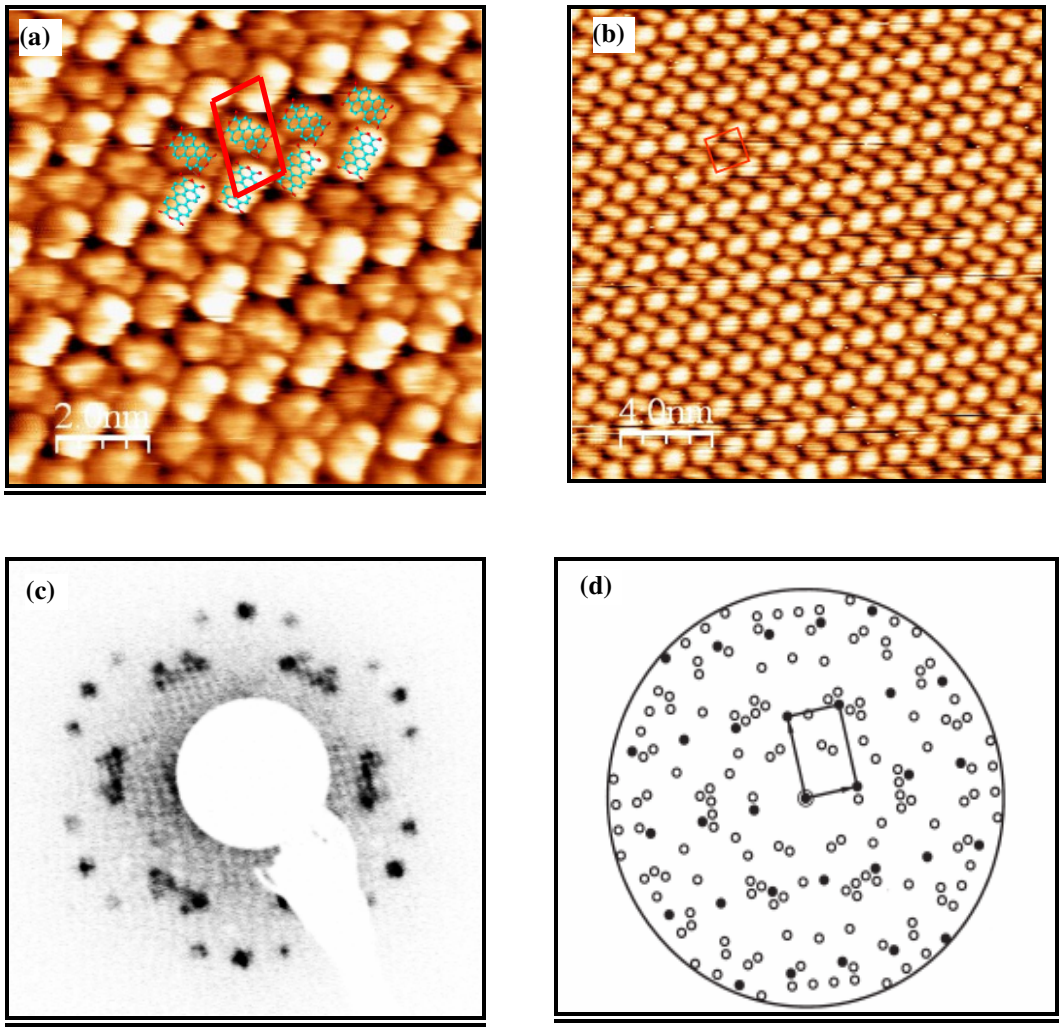

Fig. 6.15 STM images of PTCDA on Ag(111) at 1 ML (a) STM image (20 nm × 20 nm, Vs = +1.4 V, I =0.4 nA); (b) STM image (10 nm × 10 nm, Vs = - 1.7 V, I =0.03 nA); (c)LEED pattern of PTCDA on Ag(111) at 20.0 eV; (d) Kinematic construction of the LEED pattern. For one of the six symmetry-equivalent domains, filled symbols are used [17].

6.2.10. X-ray Photoelectron Spectroscopy (XPS) of PTCDA on Ag(111) .

Fig. 6.16 shows the O 1s XPS spectra from 1 ML of PTCDA on the Ag(111) surface. There are two oxygen species in the PTCDA molecule, and hence, two distinct contributions to the XPS spectra. The peak labelled O1 at a binding energy of 531.0 eV corresponds to the carbonyl group (-C=O), while the peak labelled O2 at a binding energy of 533.5 eV, is associated with anhydride groups (-C-O-C). The peak labelled Sat1, at a binding energy of 534.7 eV, is due to shake-up process in the oxygen. The shake up process is due to the initial photoionisation producing an ion in an excited state as opposed to its ground state. As a result, the photoelectrons emitted will have a slightly lower kinetic energy than the majority which were emitted from a ground state ion. The same spectral region was also recorded on a clean Ag(111) crystal and used for background subtraction. In this energy region, a peak is observed at a binding energy

of 533 eV which is produced by the β-satellite of the Ag $3p_{1/2}$ peak. The background is removed by dividing the O 1s spectra by the background recorded from the clean Ag(111) surface to give the contribution of the O 1s signal from the PTCDA. Subsequently, a Shirley background is subtracted and the O 1s peaks are fitted with a Gaussian lineshape using the Fityk software. The intensity ratio of the O 1s components, O2/O1, is not 0.5 as expected from the stochiometry of the molecule, and as is observed in the case of PTCDA on the Au(111) surface. The value of O2/O1 is 0.95. This is due to a strong the interaction of the PTCDA with the Ag(111) surface which was previously reported by Zou *et al.*[18]. Additionally, a study of PTCDA on Ag(111) using normal incidence x-ray standing wave (NIXSW) by Hauschild *et al.* [19] has demonstrated that the carbonyl groups interact with the Ag surfaces moving closer to the surface than the anhydride oxygen, further confirming PTCDA has interaction with Ag surface.

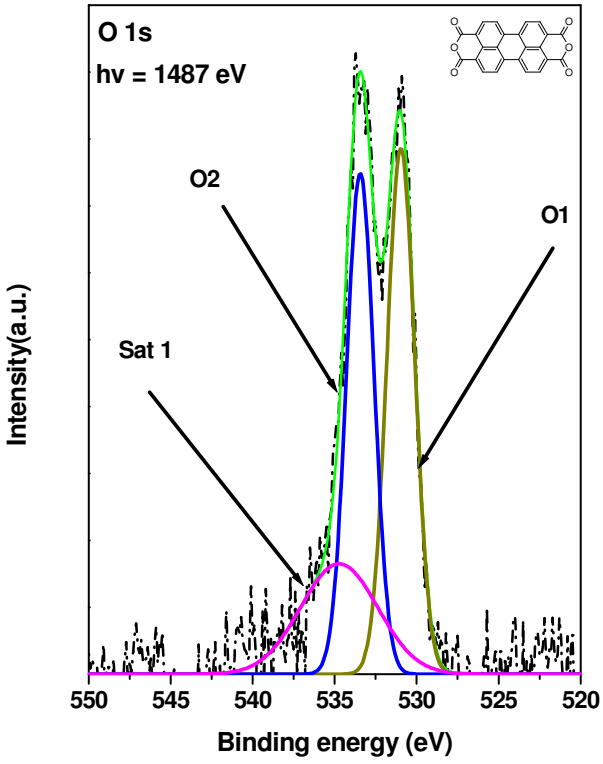

Fig. 6.16 O 1s XPS core level spectrum of PTCDA on Ag(111) at 1 ML coverage.

6.2.11. Scanning Tunnelling Microscopy (STM) of Co-deposited TAPB and PTCDA on Ag(111).

PTCDA and TAPB were deposited on an Ag(111) surface in a 1:1 ratio at a total estimated coverage of between 0.8 ML and 1 ML. PTCDA molecules were observed to have stronger intermolecular interaction among each other in the previous experiments whereas TAPB molecules haves stronger repulsion interaction between themselves. Hence, TAPB molecules were deposited initially followed by deposition of PTCDA molecules with the intention for TAPB to interact with PTCDA immediately after the deposition. However, the reverse sequence where PTCDA deposition is performed first, followed by TAPB depositions was never carried out in this work. Therefore, the result of this reverse sequence is not known. After the initial deposition at room temperature, a self assembled structure is observed in the STM images. This system was then annealed to different temperatures (130 ^{o}C, 150 ^{o}C, 170 ^{o}C, 200 ^{o}C and 240 ^{o}C) which ultimately resulted in covalent bonding between the PTCDA and TAPB molecules. Based on this preliminary study, the covalent bonding occurs at a temperature of between 200 ^{o}C and 240 ^{o}C depending on the initial coverage, with the reaction occurring at a higher temperature for the higher coverage. This is likely due to the TAPB and PTCDA molecules having more space to react if the surface is less densely packed.

Fig. 6.17(a) and (b) show a large area of self-assembled molecules after the deposition of TAPB and PTCDA at room temperature. The PTCDA molecules are arranged in parallel rows separated by the TAPB molecules with alternate molecules orientated at 180^{o} with respect to each other as shown in Fig. 6.17(c and d). Within the PTCDA rows the molecules usually occur in pairs with a periodicity of (2.4 ± 0.1) nm and a gap between adjacent pairs. In addition, Fig. 6.17(d) shows an area which has the same structure as Fig. 6.16(c), (red circle) adjacent to areas where the PTCDA rows have periodic gaps. This arrangement with periodic gaps will be assigned as '*Structure A*'. In this sample, '*Structure A*' is predominantly formed after deposition of the molecules. The measured unit cell is oblique with dimensions of (2.8 ± 0.1) nm × (2.5 ± 0.1) nm and an angle of (75 ± 2)^{o} as depicted in Fig. 6.17(f).

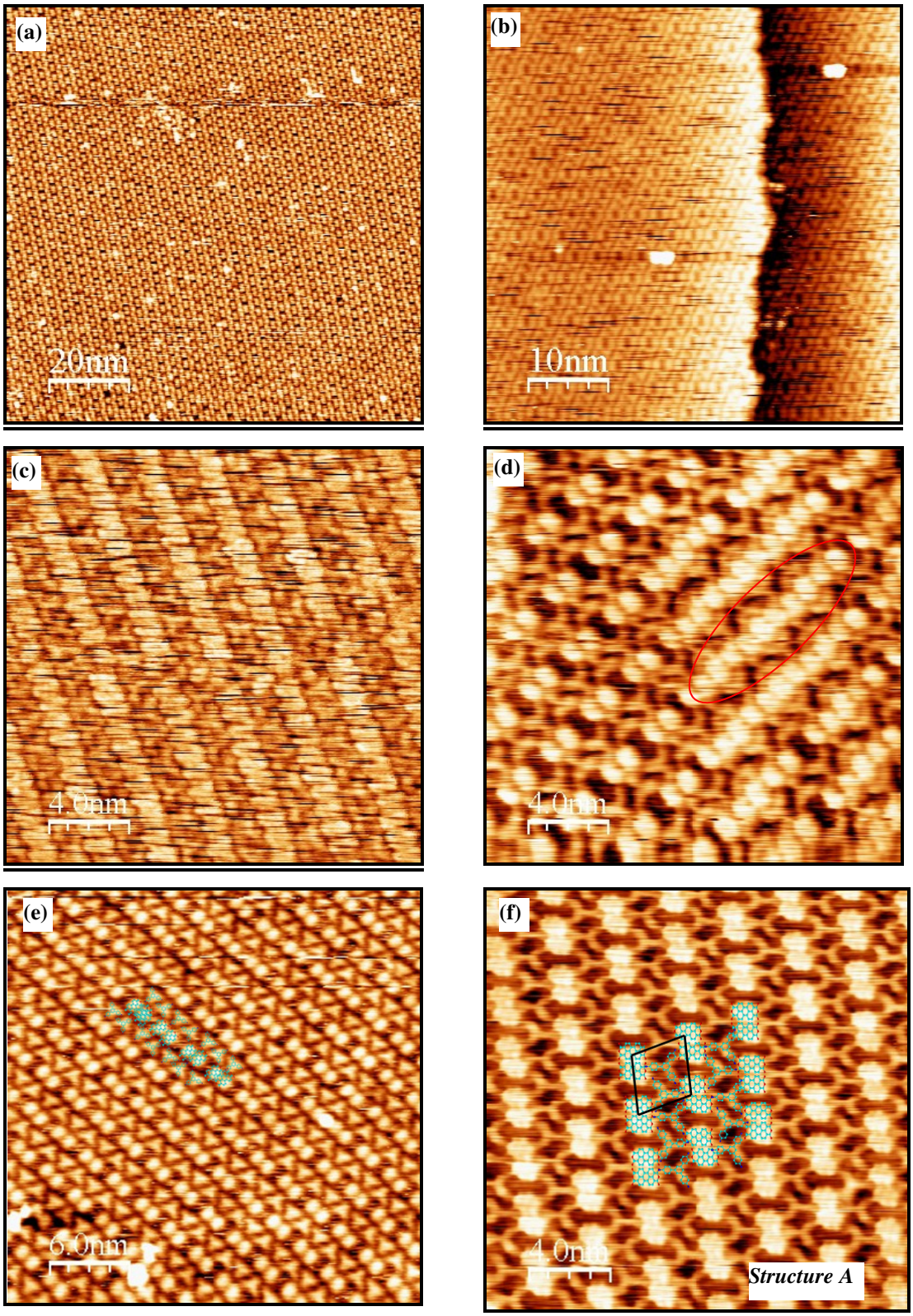

Fig. 6.17 Self-assembled of PTCDA-TAPB(1:1) as deposited (a) STM image (100 nm × 100 nm, Vs = -0.08 V, I =0.1 nA) ; (b) STM image (80 nm × 80 nm, Vs = +0.5 V, I =0.1 nA); (c) STM image (20 nm× 20 nm, Vs = -0.1V, I =0.5 nA); (d) STM image (20 nm × 20 nm, Vs = +0.5 V, I =0.1 nA); (e) STM image (30 nm × 30 nm, Vs =+0.5V, I =0.1 nA); (f) STM image (20 nm× 20 nm, Vs = -0.8 V, I =0.2 nA).

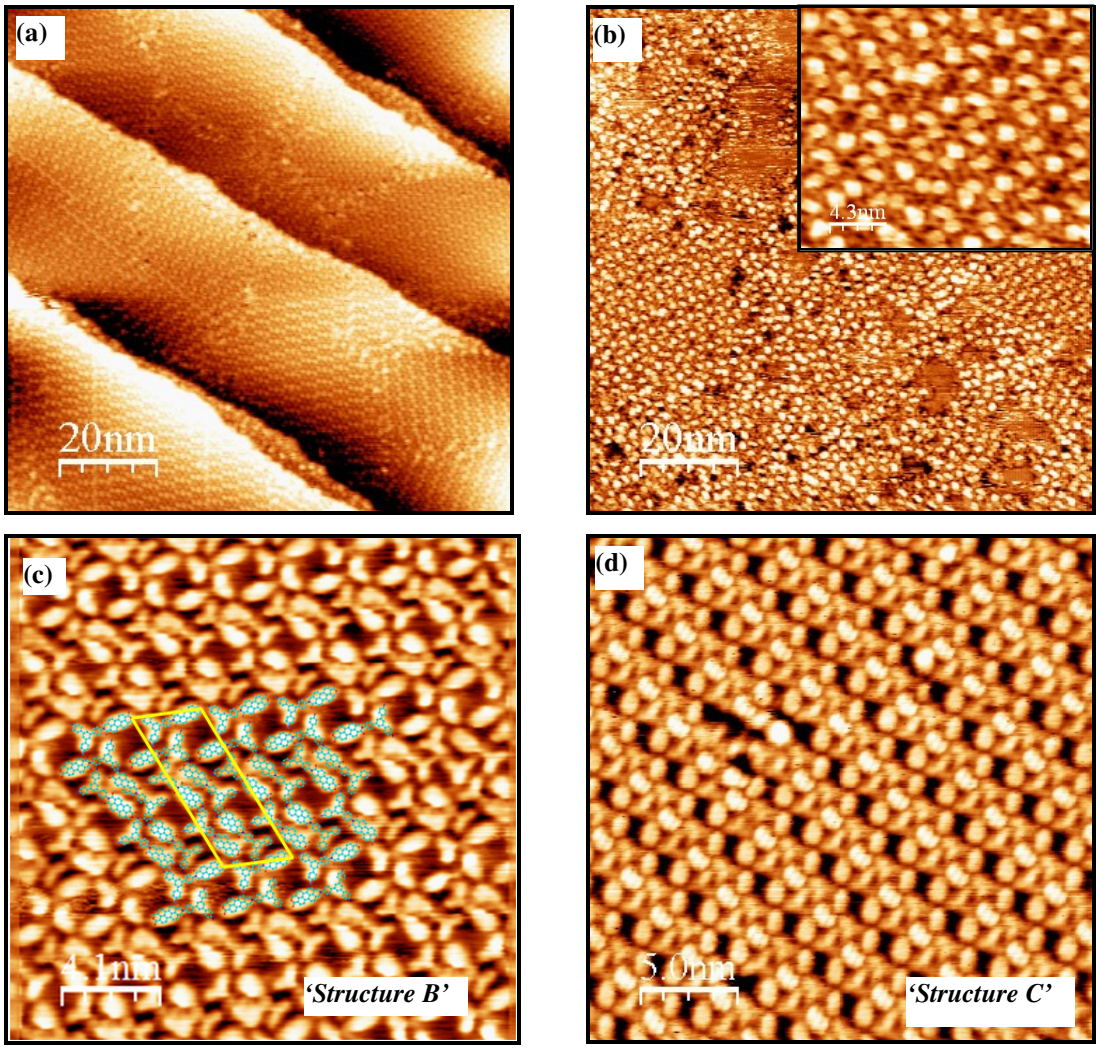

Fig. 6.18 Self-assembled of PTCDA-TAPB(1:1) after annealing at 130 °C (a) STM image (100 nm × 100 nm, Vs = -0.18 V, I =0.5 nA) ; (b) STM image (100 nm × 100 nm, Vs = -0.5 V, I =0.1 nA); (c) STM image (20 nm × 20 nm, Vs =+0.7V, I =0.1 nA); (d) STM image (25 nm × 25 nm, Vs = -0.03 V, I =0.1 nA).

When the sample is annealed at 130 °C, at least three new molecular arrangements are observed, typical images of which are shown in Figure 6.18. Fig. 6.18(a) shows a large area of the surface, and demonstrates that all the molecules are still in ordered arrangements. There is one new pattern which is rarely seen on the surface (Fig. 6.18b). This arrangement consists of a core of three TAPB molecules surrounded by six H-bonded PTCDA molecules. Rows of these units run parallel to each other with a border region consisting of blocks containing two PTCDA molecules and four TAPB molecules. Fig. 6.18(c) shows a structure in which a TAPB molecule has covalently bonded to a single PTCDA molecule. An amino group of the TAPB molecule is reacted with the anhydride group on one side of PTCDA. This structure is labelled *'Structure B'*. The unit cell is oblique with dimensions (2.8 ± 0.1) nm × (7.1 ± 0.1) nm and an angle of (60 ± 2)° between unit cell vectors. The majority of the surface shows pattern

designated as '*Structure C*' where the PTCDA molecules are arranged in groups of three with the middle molecule of the three rotated by 45 degrees relative to the other two molecules. TAPB is arranged 180 ^{o} alternately with each other in rows above and below the PTCDA molecules as depicted in Fig. 6.18(d). The unit cell of '*Structure C*' measured from Fig. 6.18(c) is (2.9 ± 0.1) nm × (2.4 ± 0.1) nm with an angle of (75 ± 2)^{o} between unit cell vectors.

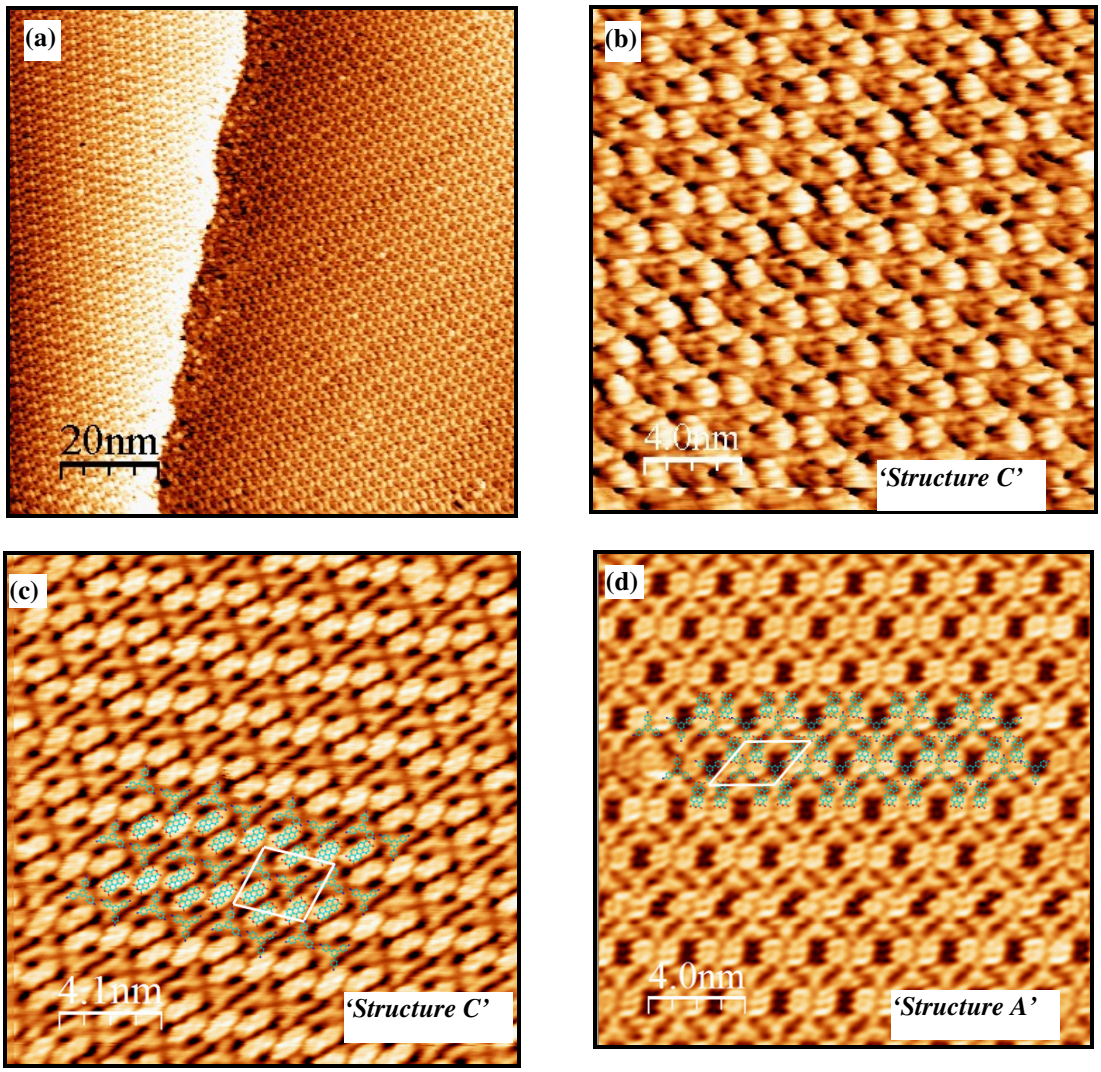

Fig. 6.19 Self-assembled of PTCDA-TAPB(1:1) after annealed at 150 ^{o}C (a) STM image (100 nm × 100 nm, Vs = -0.5 V, I =0.1 nA) ; (b) STM image (100 nm × 100 nm, Vs = -0.5 V, I =0.1 nA) (c) STM image (20 nm × 20 nm, Vs = -0.5 V, I =0.1 nA); (d) STM image (20 nm × 20 nm, Vs = -0.5 V, I =0.1 nA).

Fig. 6.19 shows a series of STM images recorded after the sample was annealed to 150 ^{o}C. No new patterns are observed. Both '*Structure A*' and '*Structure C*' are observed.

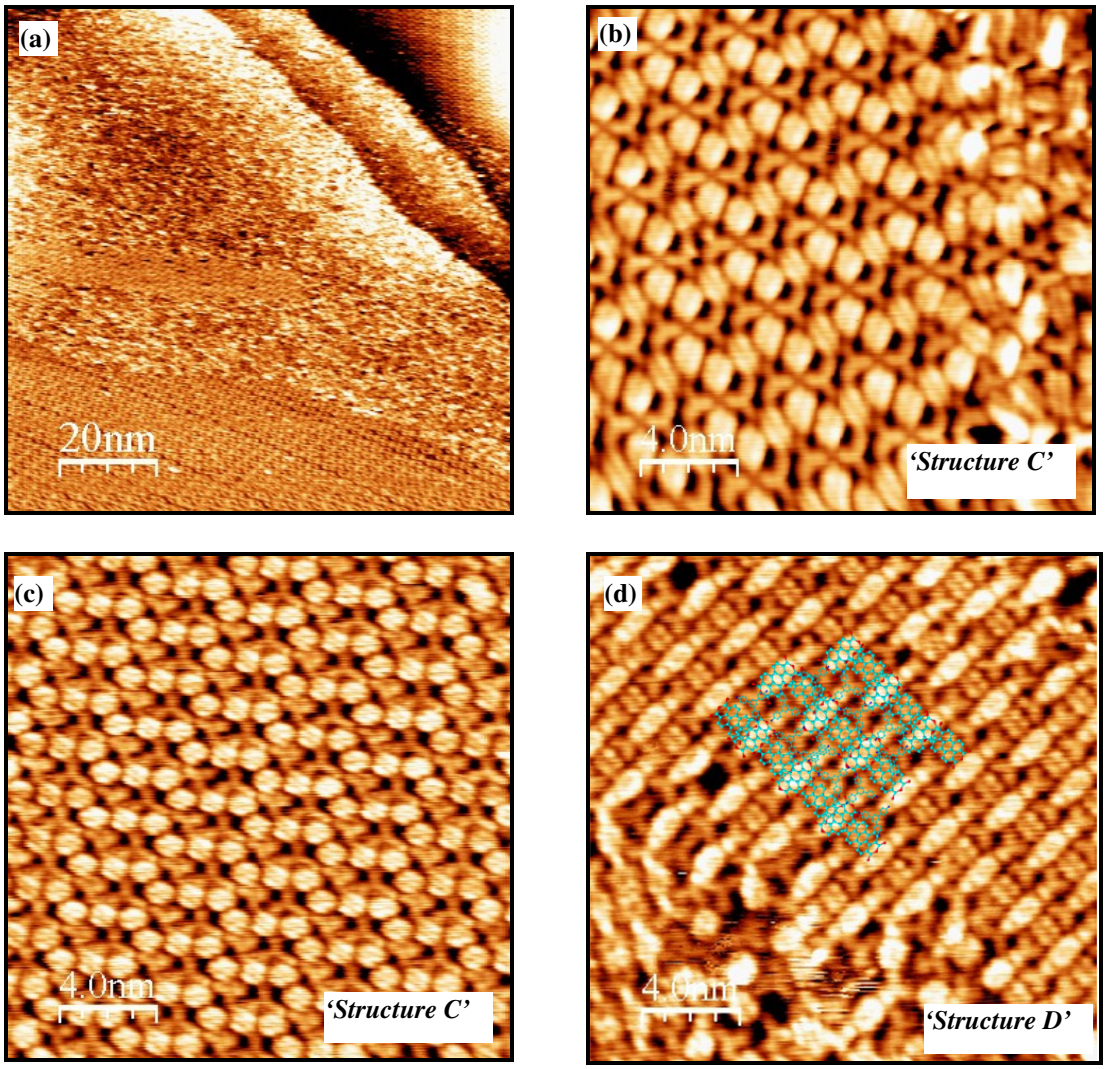

Fig. 6.20 Self-assembled/Networks of PTCDA-TAPB(1:1) after annealed at 170 °C (a) STM image (100 nm × 100 nm, Vs =+0.5 V, I =0.1 nA) ; (b) STM image (20 nm × 20 nm, Vs = -1.0 V, I =0.1 nA); (c) STM image (20 nm × 20 nm, Vs =-0.7V, I =0.1 nA); (d) STM image (20 nm × 20 nm, Vs = -0.7 V, I =0.1 nA).

When the annealing temperature is increased to 170 °C, some disordered areas start to form as shown in Fig. 6.20(a) although large areas remain ordered. The surface is now primarily composed of '*Structure C*'. However, another new pattern consisting of an arrangement of two TAPB molecules covalently bonded to the anhydride groups each end of a single PTCDA molecule (Scheme 6.2) is also observed on this surface ('*Structure D'*). The unit cell of '*Structure D*' from Fig. 6.20(d) is rectangular and was measured at (4.8 ± 0.1) nm × (2.3 ± 0.1) nm. Within the rows of PTCDA and TAPB in '*Structure D*', the PTCDA molecules are arranged alternatively to TAPB with a periodicity of (2.2 ± 0.1) nm.

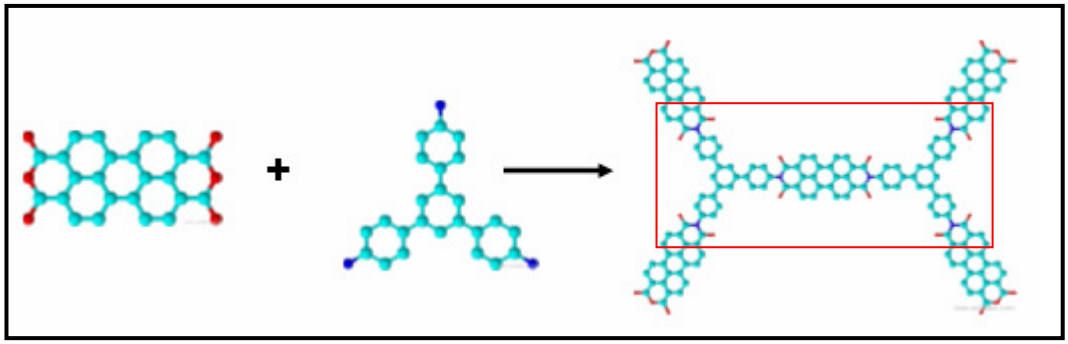

Scheme 6.2 Reactions from PTCDA and TAPB to form covalently bonded networks.

More disordered networks are observed when the annealing temperature is increased to 200 ^{o}C. '*Structure C*' is observed but not as much as on the lower temperature surfaces. Some areas show more disordered networks as depicted in Fig. 6.21(a). A new structure ('*Structure E'*) is found where the unit cell is (2.8 ± 0.1) nm × (2.3 ± 0.1) nm with an angle of (50 ± 2)^{o} between unit cell vectors as shown in Fig. 6.21(b).'*Structure D'* is still observed but in a very small area (Fig. 6.21c and d). In the disordered networks (Fig. 6.21e and f), small ordered structures are still observed. They appear as 'herringbone' structures where the rows are filled alternately with PTCDA and TAPB molecules as depicted in Fig. 6.21(f). This arrangement was not widely seen.

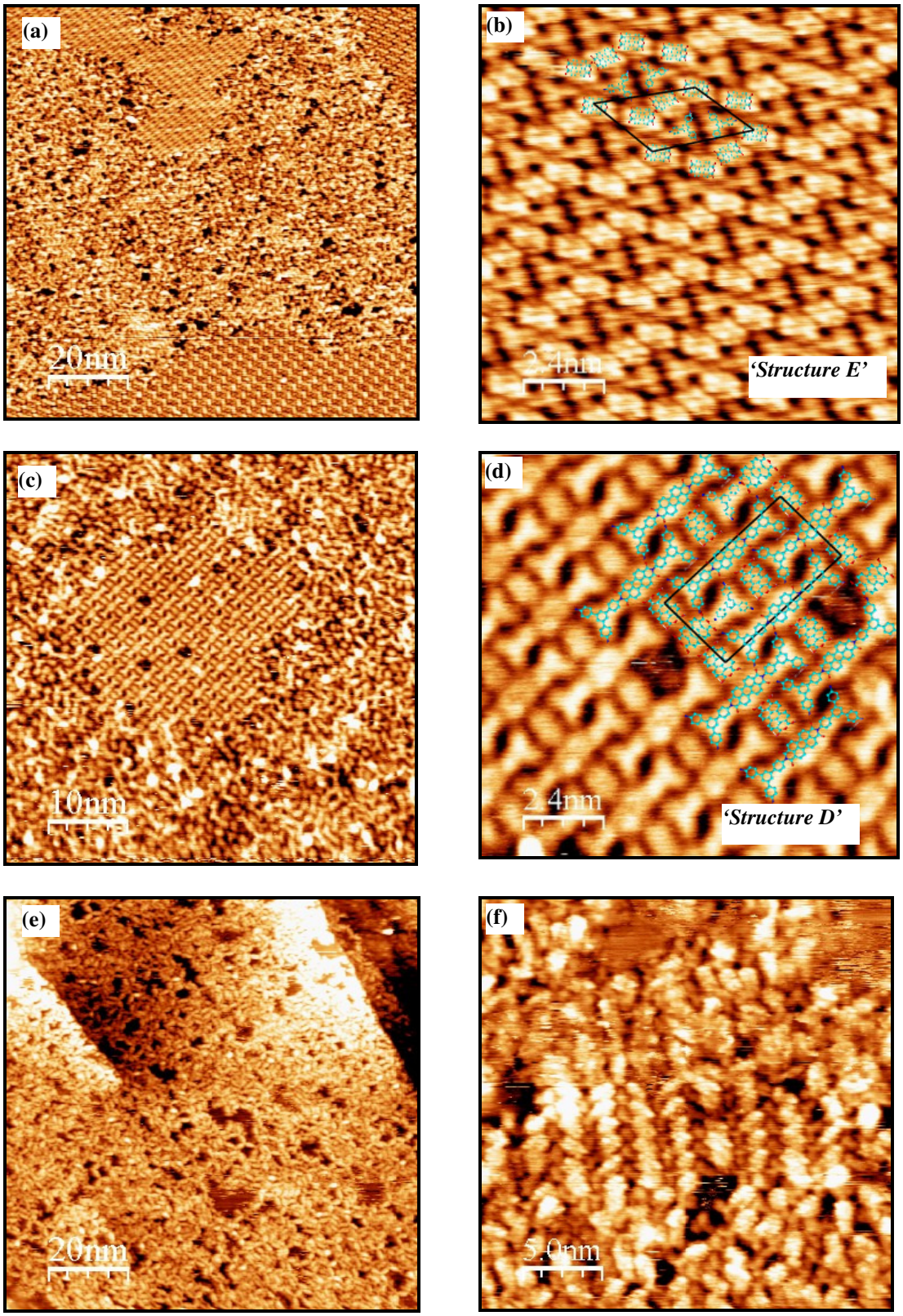

Fig. 6.21 Self-assembled/Networks of PTCDA-TAPB(1:1)after annealed at 200 °C (a) STM image (100 nm × 100 nm, Vs = -1.2 V, I =0.1 nA) ; (b) STM image (12 nm × 12 nm, Vs = -1.2 V, I =0.1 nA); (c) STM image (50 nm × 50 nm, Vs = +0.5 V, I =0.5 nA); (d) STM image (12 nm × 12 nm, Vs = +0.5 V, I =0.1 nA); (e) STM image (100 nm × 100 nm, Vs =-0.4V, I =0.1 nA); (f) STM image (25 nm × 25 nm, Vs = -0.4 V, I =0.1 nA).

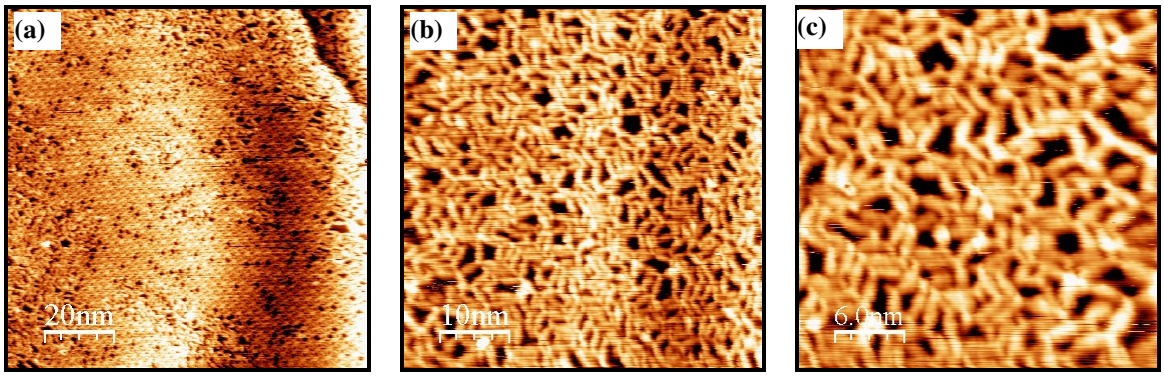

Fig. 6.22 Networks of PTCDA-TAPB(1:1) after annealed at 240 °C (a) STM image (100 nm × 100 nm, Vs = +0.3 V, I =0.1 nA) ; (b) STM image (50 nm × 50 nm, Vs = +1.3 V, I =0.1 nA); (c) STM image (30 nm × 30 nm, Vs = +1.3 V, I =0.1 nA).

When the surface is further annealed to 240 °C, almost the entire surface is covered with covalently bonded disordered networks as shown in Fig. 6.22 (b) and (c). The networks appeared to be long-range, connected, covalently bonded networks which were not observed in the systems described in the previous chapters. There are just small patches of ordered network as seen in Fig. 6.22(a).

6.2.12. X-ray Photoelectron Spectroscopy (XPS) of Co-deposited TAPB and PTCDA on Ag(111).

Fig. 6.23(a) shows the O 1s XPS spectra of a TAPB-PTCDA film as it is annealed at various temperatures up to 240° C. These spectra have been smoothed for the sake of clarity. The baselines of the spectra have been subtracted and the areas of the O1 and O2 peaks extracted using Fityk (Fits are not shown in the spectra). The evolution of O2/O1 ratio for this system is plotted in Fig. 6.23(b).

On the mixed PTCDA-TAPB sample, the O 1s XPS spectrum is different from the corresponding O 1s spectrum for 1 ML of PTCDA on Ag(111). It appears that the interaction of the PTCDA molecules with the Ag(111) substrate is different in the mixed PTCDA/TAPB film to than of PTCDA with Ag(111), as the ratio of O2/O1 from the latter is 0.95 which is not close to the expected ratio 0.5 for the PTCDA molecule in the absence of interaction with the surface. Hence, the introduction of the TAPB molecules affects the interactions of PTCDA with the Ag(111) surface.

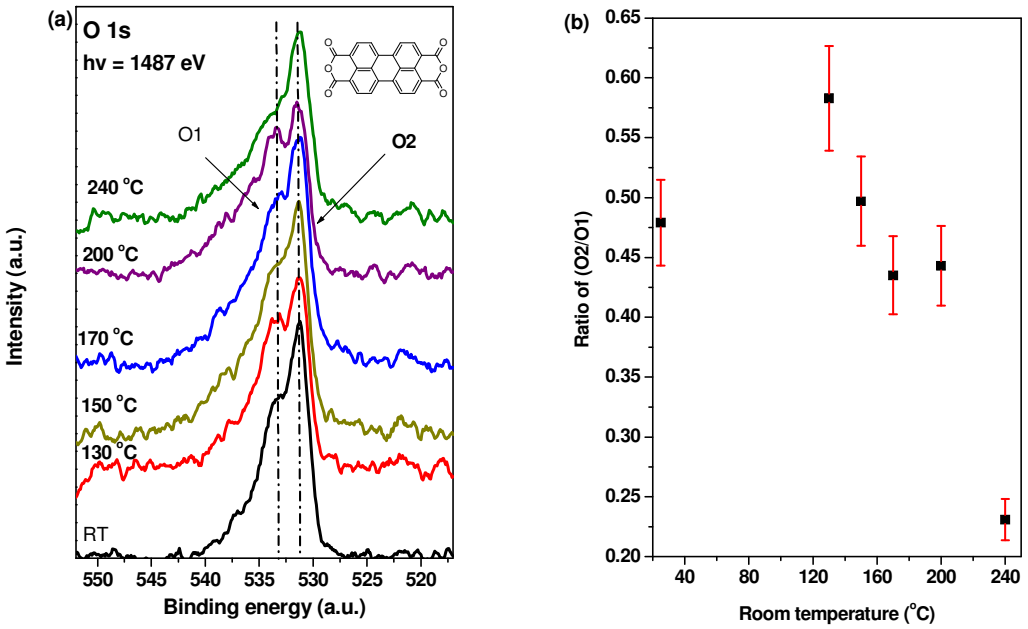

Fig. 6.23 (a) XPS spectra of O 1s from different annealing temperature of TAPB-PTCDA (1:1) experiments; (b) The scattered plot of (O2/O1) ratios from different annealing temperature.

When the sample is annealed to 130 °C, the ratio of O2/O1 increases to 0.58 ± 0.04. At this stage, the STM images show at least four different TAPB/PTCDA structures that all involve H-bonding between the molecules and there is no evidence of covalently bonded structures except for '*Structure B'*. When the substrate is annealed the molecules diffuse to achieve the lowest energy configuration on the surface and hence, the annealing induces the re-arrangement of molecules to form new structures. On further annealing to temperatures between 150° C and 200° C, the O2/O1 ratio returns to ~0.5. At this stage, STM images show little change in the molecular ordering. While some patches of disorder are observed in the STM images, this does not appear to affect the ratio of O2/O1 significantly in the XPS spectra except for an overall decrease in the O 1s intensity after annealing at 200 °C due to some PTCDA molecules having desorbed from the surface. When the annealing temperature is increased to 240 °C, the O2 peak which is associated with the anhydride bonding (–C-O-C-) decreases significantly and the O2/O1 ratio has decreased to 0.23, indicating that a chemical reaction has taken place between the amino groups from the TAPB and the anhydride groups of the PTCDA to form covalent bonded networks (refer to reaction Scheme 6.2). The STM images show that the self-assembled layer has been disrupted and only covalently bonded networks are observed on the surface which is in agreement with the results obtained from XPS measurements above. Based on the STM images, covalent reaction favours the formation of the imide structure instead of the iso-imide structure.

This result agrees with the XPS measurements, which indicate that the covalent bonded structures react on the anhydride group instead of the carbonyl groups on PTCDA.

The experiments involving PTCDA and TAPB molecules have shown the formation of covalently-bonded networks. Nonetheless, some work, including deposition on other noble metals, tuning the ratio of PTCDA and TAPB molecules and the annealing temperature are crucial to control the reaction process and form more ordered networks.

6.3. Summary.

The ordering and reaction of 1, 3, 5-tris(4-aminophenyl) benzene (TAPB) molecules was investigated by STM and XPS on the Au(111) and Ag(111) surfaces. Two approaches, namely deposition on a substrate held at room temperature and deposition on a substrate held at elevated temperature were conducted to compare the formation of networks on these surfaces.

TAPB molecules do not self-assemble on Au(111) and Ag(111). They desorbed easily from the surfaces at temperatures as low as 100 ^{o}C. With the substrate held at elevated temperatures, networks are formed which are disordered and consist of mainly short-range oligomers. During the course of the annealing experiments (250 ^{o}C), TAPB molecules caused uncovered areas of the Au(111) and Ag(111) substrates to reconstruct into a (2×1) ordering.

PTCDA molecules on Ag(111) self-assembled two type of herringbone (HB) structures. The unit cell for a typical reported HB is rectangular and has a unit cell of (1.3 ± 0.1) nm $\times$ (2.0 ± 0.1) nm. The other structure which has never been reported (to the best of our knowledge) is closer to a square unit cell with dimensions of (1.4 ± 0.1) nm $\times$ (1.4 ± 0.1) nm. A strong interaction of the PTCDA with the Ag(111) surface results in a O2(carbonyl)/O1(anhydride) intensity ratio of 0.95, which is much higher than the expected stoichiometric ratio of 0.5.

TAPB molecules were co-deposited with PTCDA molecules on Ag(111) surfaces in a one to one ratio. At least seven ordered structures are observed throughout the annealing process from room temperature until networks are formed at 200 ^{o}C to 240 ^{o}C. H-bonding between the amino groups and the anhydride groups plays a very

important role in determining the observed structures before the covalently bonded networks are formed. Five structures are fully analysed and their unit cells are tabulated in the Table 6.2.

Table 6.2: Summary of different structures obtained from the mixture of PTCDA and TAPB (1:1) at different temperatures.

Structure	**Unit cell (nm × nm ± 0.1)**	**Angle ($a \times b \pm 2$) ^{o}**	**Temperature (^{o}C)**
A	2.8 × 2.5	75	As deposited
B	2.7 × 7.1	60	130
C	2.9 × 2.4	75	130
D	4.8 × 2.3	90	170
E	2.8 × 2.3	50	200

The results show that long-range, connected networks are formed in this bimolecular system. There is still plenty of scope for further exploration of this system which includes variation of the PTCDA to TAPB ratio and the types of surfaces used with the objective of forming more ordered networks.

References:

[1] L. Grill, M. Dyer, L. Lafferentz, M. Persson, M.V. Peters, S. Hecht. *Nano-architectures by covalent assembly of molecular building blocks,* Nat. **2** (2007) 687.

[2] M. Treier, N.V. Richardson, R. Fasel. *Fabrication of surface-supported low-dimensional polyimide networks,* J. Am. Chem. Soc. **130** (2008) 14054.

[3] S. Weigelt, C. Busse, C. Bombis, M.M. Knudsen, K.V. Gothelf, T. Strunskus, C. Woll, M. Dahlbom, B. Hammer, E. Laegsgaard, F. Besenbacher, T.R. Linderoth. *Covalent interlinking of an aldehyde and an amine on a Au(111) surface in ultrahigh vacuum,* Angew. Chem. Int. Ed. Engl. **46** (2007) 9227.

[4] S. Weigelt, C. Busse, C. Bombis, M.M. Knudsen, K.V. Gothelf, E. Lægsgaard, F. Besenbacher, T.R. Linderoth. *Surface synthesis of 2D branched polymer nanostructures,* Angew. Chem. Int. Ed. **47** (2008) 4406.

[5] N. Zwaneveld, R. Pawlak, M. Abel, D. Catalin, D. Gigmes, D. Bertin, L. Porte. *Organized formation of 2D extended covalent organic frameworks at surfaces.* J. Am. Chem. Soc. **130** (2008) 6678.

[6] X. Sun, H.T. Jonkman, F. Silly. *Tailoring two-dimensional PTCDA–melamine self-assembled architectures at room temperature by tuning molecular ratio,* Nanotechnol. **21** (2010) 165602.

[7] R. Tanoue, R. Higuchi, N. Enoki, Y. Miyasato, S. Uemura, N. Kimizuka, A.Z. Stieg, J.K. Gimzewski, M. Kunitake. *Thermodynamically controlled self-assembly of covalent nanoarchitectures in aqueous solution,* ACS Nano. (2011).

[8] J.F. Dienstmaier, A.M. Gigler, A.J. Goetz, P. Knochel, T. Bein, A. Lyapin, S. Reichlmaier, W.M. Heckl, M. Lackinger. *Synthesis of well-ordered COF monolayers: surface growth of nanocrystalline precursors vs. direct on-surface polycondensation,* ACS Nano. (2011).

[9] O. Ourdjini, R. Pawlak, M. Abel, S. Clair, L. Chen, N. Bergeon, M. Sassi, V. Oison, J.M. Debierre, R. Coratger. *Substrate-mediated ordering and defect analysis of a surface covalent organic framework,* Phys.l Rev. B. **84** (2011) 125421.

[10] M. Treier, M.T. Nguyen, N.V. Richardson, C. Pignedoli, D. Passerone, R. Fasel. *Tailoring low-dimensional organic semiconductor nanostructures,* Nano Lett. **9** (2009) 126.

[11] W. Chen, H. Li, H. Huang, Y. Fu, H.L. Zhang, J. Ma, A.T.S. Wee. *Two-dimensional pentacene: 3, 4, 9, 10-perylenetetracarboxylic dianhydride supramolecular chiral networks on Ag (111),* J. Am. Chem. Soc. **130** (2008) 12285.

[12] C.J. Li, Q.D. Zeng, Y.H. Liu, L.J. Wan, C. Wang, C.R. Wang, C.L. Bai. *Evidence of a thermal annealing effect on organic molecular assembly,* Chem. Phys. Chem. **4** (2003) 857.

[13] S. Jensen, H. Früchtl, C.J. Baddeley. *Coupling of triamines with diisocyanates on Au (111) leads to the formation of polyurea networks,* J. Am. Chem. Soc. **131** (2009) 16706.

[14] M. Di Marino, F. Sedona, M. Sambi, T. Carofiglio, E. Lubian, M. Casarin, E. Tondello. *STM Investigation of temperature-dependent two-dimensional supramolecular architectures of C60 and amino-tetraphenylporphyrin on Ag (110),* Langmuir. **26** (2010) 2081.

[15] I. Horcas, R. Fernández, J.M. Gómez-Rodríguez, J. Colchero, J. Gómez-Herrero, A.M. Baro. *WSXM: A software for scanning probe microscopy and a tool for nanotechnology,* Rev. Sci. Instrum. **78** (2007) 013705.

[16] M. Wojdyr. *Fityk: a general-purpose peak fitting program,* J. Appl. Cryst. **43** (2010) 1126.

[17] K. Glockler, C. Seidel, A. Soukopp, M. Sokolowski, E. Umbach, M. Bohringer, R. Berndt, W.D. Schneider. *Highly ordered structures and submolecular scanning tunnelling microscopy contrast of PTCDA and DM-PBDCI monolayers on Ag (111) and Ag (110),* Surf. Sci. **405** (1998) 1.

[18] Y. Zou, L. Kilian, A. Schöll, T. Schmidt, R. Fink, E. Umbach. *Chemical bonding of PTCDA on Ag surfaces and the formation of interface states,* Surf. Sci. **600** (2006) 1240.

[19] A. Hauschild, R. Temirov, S. Soubatch, O. Bauer, A. Schöll, B. Cowie, T.L. Lee, F. Tautz, M. Sokolowski. *Normal-incidence x-ray standing-wave determination of the adsorption geometry of PTCDA on Ag (111): Comparison of the ordered room-temperature and disordered low-temperature phases,* Phys. Rev. B. **81** (2010) 125432.

Chapter 7:

Conclusions and Future Work.

7.1. Conclusions.

The aim of this research was to develop strategies for the formation of covalently bonded nano-networks on noble metal surfaces through amine reactions. Two molecules with amino groups were studied; namely 5,10,15,20- tetrakis(4-aminophenyl) porphyrin (TAPP) and 1,3,5-tris(4-aminophenyl) benzene (TAPB). TAPP was selected due to the large number of potential uses of porphyrin functionalized surfaces, while TAPB was selected to investigate the effect of different symmetry on network formation. The systems were investigated using scanning tunnelling microscopy (STM) and X-ray photoelectron spectroscopy (XPS). Ultraviolet photoelectron spectroscopy (UPS), low energy electron diffraction (LEED), synchrotron based techniques were also employed to complement the STM experiments. Two main approaches to network formation were employed; in the first method the molecules were deposited on a substrate held at room temperature and subsequently annealed to initiate the polymerisation process; in the second method the molecules were deposited onto a substrate at elevated temperatures, with the intention of polymerising during the deposition process. These two approaches however, gave similar outcomes where the networks formed were disordered and contained mostly oligomers especially for the TAPP systems.

TAPP molecules were deposited on Au(111), Ag(111) and Cu(111) surfaces. In this study, four possible reactions of the amino groups were proposed to form covalently bonded networks (refer to Scheme 3.1). The first three reactions are two-step coupling oxidation reactions accompanied by the elimination of N_2. The fourth reaction is assumed to proceed in a manner analogous to aniline polymerisation and involves oxidative coupling [1]. From the XPS N 1s spectra, HN-NH or –N=N- bonding was considered to be more likely to occur than –C-C- bonding because the XPS spectra showed the presence of nitrogen. However, it was not possible to distinguish between HN-NH and –N=N- bonding due to the small binding energy difference between these two species in the XPS spectra. The Ag(111) surface was found to have the weakest interaction with the TAPP molecules since the molecules desorbed from the surface at a low annealing temperature. A T-stacking arrangement was identified when these

molecules were self-assembled on Au(111) and Ag(111) surfaces. When the substrate was held at room temperature during the deposition, and the surface was then subsequently annealed, covalently bonded networks were only formed on the Au(111) and Cu(111) surfaces. The structures formed were short ranged and consisted of disordered oligomers. Nonetheless, TAPP formed covalently bonded networks on all substrates that were held at elevated temperatures although these networks were not well-ordered. In addition to the polymerisation processes observed on noble metals after annealing, metalation of the porphyrin molecule with Cu atoms from the surface or Cu adatoms was observed for the Cu(111) system.

The electronic structure of TAPP molecules deposited on Au(111) and Cu(111) surfaces was explored from sub-monolayer(ML) to thick film by ultraviolet photoelectron spectroscopy (UPS). The π and σ states were monitored during the polymerization process on these two surfaces. Three kinds of interactions were found in the Au(111) growth study: (i) a single peak was found at low binding energy (BE) in the UPS spectra due to the molecule-substrate interaction at sub-ML coverage, probably due to a conformational adaptation of the phenyl rings to optimize the molecule-substrate interaction; (ii) two peaks were found at low-BE in the UPS spectra and the interaction is relaxed when the first densely packed ML coverage is obtained, (iii) the molecules interact with each other through van der Waals forces after more than a ML is achieved. On the other hand, there was a stronger interaction between the TAPP molecules and the Cu(111) surface. A single peak (HOMO) is monitored from sub-ML to a thick layer. Similar to the Au(111), van der Waals interactions were the dominant force when the coverage was more than a ML. The polymerization reaction on Au(111) and Cu(111) surfaces causes modification of the MOs which is observed as a strong modifications of electronic structure both above and below the substrate *d* bands. An overall broadening and shifting of several features was observed due to this polymerisation process. A decrease in the work function with increasing coverage was observed on both Au(111) and Cu(111). This result was attributed to the pillow-effect [2].

The interaction of TAPP with 3,4,9,10-perylene tetracarboxylic dianhydride (PTCDA) was investigated to study reactions that can occur between the PTCDA anhydride (–C-O-C-) and carbonyl groups (–C=O) and the amino (NH_2) groups on the TAPP molecules. The PTCDA molecules formed herringbone (HB) and square (S) phases on Au(111). Phase separation of TAPP and PTCDA molecules was observed when they

were co-deposited onto Au(111) surfaces. A polyimidisation reaction between TAPP and PTCDA was observed when this interface was annealed. However, a mixture of imides (NH_2 group with –C-O-C-group) and iso-imides (NH_2 group with –C=O group) was formed, which induced disordering of the resulting networks. In addition, there were reactions occurring between the TAPP molecules during the polymerisation process. Hence, the number of polyimidisation reactions between TAPP and PTCDA molecules have further reduced due to the competition from the polymerisation reactions between TAPP and TAPP molecules. This resulted in the formation of more disordered networks on the Au(111).

1,3,5-tris(4-aminophenyl) benzene (TAPB) molecules were investigated on the Au(111) and Ag(111) surfaces. TAPB molecules do not self-assemble on the Au(111) and Ag(111) surfaces and they desorbed from the surfaces at 150 ^{o}C for Au(111) and 100 ^{o}C on Ag(111) surfaces. With the substrate held at elevated temperatures, the covalently bonded structures formed are disordered oligomers. During the course of the annealing experiments, it was observed that the TAPB molecules caused uncovered areas of the Au(111) and Ag(111) substrate to reconstruct into a (2 × 1) ordering. Before the co-deposition of TAPB and PTCDA molecules was investigated, a short study of the ordering and electronic structure of PTCDA molecules on Ag(111) was carried out. Two structures were observed with a square unit cell and a herringbone structure. To our knowledge the square reconstruction has not been reported previously in the literature. When TAPB molecules were co-deposited with PTCDA molecules on Ag(111) surfaces in a one to one ratio, at least seven ordered structures were observed throughout the annealing process from room temperature until covalently bonded networks were formed at temperatures of between 200 to 240 ^{o}C. Hydrogen bonding between the amino groups and the anhydride groups played a crucial role in determining the geometry of these structures. At the end of the experiment, long-range and covalently bonded networks were successfully formed via polyimidisation reaction of the anhydride groups from PTCDA and amino groups from TAPB molecules.

From the results obtained, it was concluded that the reactions among TAPP molecules or TAPP with PTCDA molecules were not successful in forming long range nano-networks. The structures obtained consist of mainly oligomers. However, the TAPB and PTCDA system were shown to improve the formation of networks although the

ordering of the networks could still be further explored and improved by manipulating the ratio of TAPB and PTCDA deposited.

7.2. Future Work.

Suggestions for future work are proposed and described below.

7.2.1. Research work with 1,3,5-tris(4-aminophenyl)benzene (TAPB).

The experimental results presented in Chapter 6 showed that there is still much to discover in the TAPB and PTCDA system. Different hydrogen bonded ordering of the binary PTCDA and TAPB system can be controlled through the manipulation of the TAPB to PTCDA ratio. Further work with other molecules that also contain anhydride groups such as 3, 4, 9,10-tetra-carboxylic-diimide (PTCDI) and 1, 4, 5, 8-naphthalene-tetracarboxylic-dianhydride (NTCDA) as illustrated in Fig.7.1 could be studied on different metal surfaces. Long-range and connected networks were already demonstrated in this thesis; these studies would be carried out with the objective of obtaining better ordered networks.

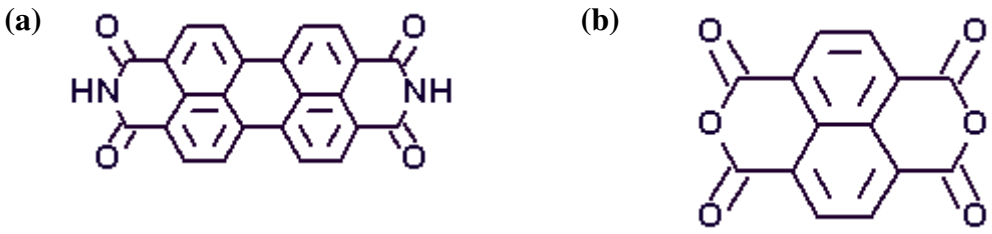

Fig. 7.1 Chemical structure of (a) PTCDI and (b) NTCDA.

7.2.2. Self- assembly and Covalent Reaction of 5,15-bis(4-phenyl)-10,20-bis(4-carboxyphenyl) porphyrin (BCPP) and TAPP on Au(111).

Investigation on the formation of covalently bonded networks of aromatic amides through a polycondensation reaction is proposed. Aromatic polyamides are considered to be a high performance material (HPM) due to their superior thermal and mechanical properties, which make them practical for advanced technologies such as asbestos substitutes, electrical insulation, bullet-proof body armour, industrial filters, and protective and sport clothing [3].

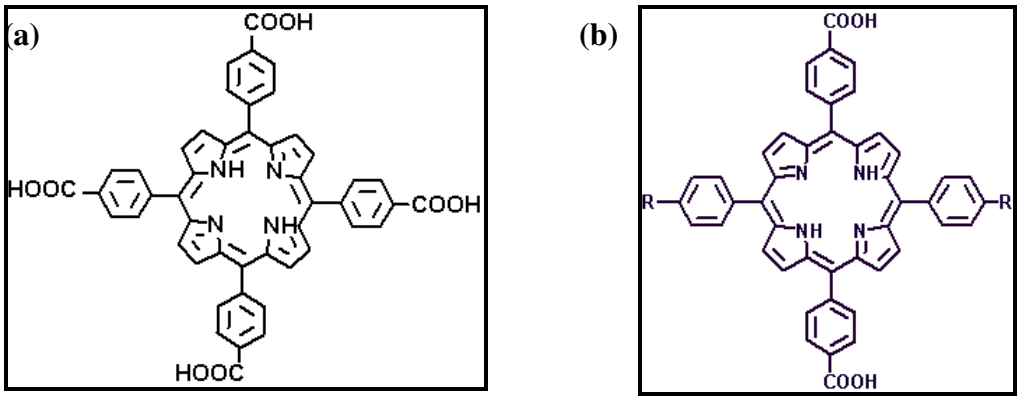

Fig. 7.2 Chemical structure of (a) TCPP and (b) BCPP, R= OH or aliphatic chains.

At the early stage of this PhD project, much effort was spent on attempting to deposit 5,10,15,20-tetrakis(4-carboxyphenyl)porphyrin (TCPP) (Fig.7.2a) on Au(111). However, no significant flux of molecules was detected, leading to the assumption that the material polymerised in the crucible before deposition could occur. A literature review showed that it is possible to deposit the substituted bis(carboxyphenyl)porphyrin, Fig 7.2 (b) [4-8]. Hence, in future work, studies of 5, 15-bis(4-**R-**phenyl)-10,20-bis(4-carboxyphenyl) (BCPP), **R** = OH, tetratertbutyl, or aliphatic chains (see Fig.7.2b) porphyrin is proposed. 5,10,15,20-tetrakis(4-aminophenyl)porphyrin (TAPP) and BCPP are selected for this reaction because BCPP has carboxylic groups which contain two chemically different oxygen species (hydroxyl, -OH and carbonyl, -C=O groups). However, the –OH group is more reactive and hence, the reaction with –OH group will be the dominant pathway as compared to the –C=O group. In addition, BCPP has almost the same size as TAPP and therefore, more uniform and ordered nanomeshes are expected to form.

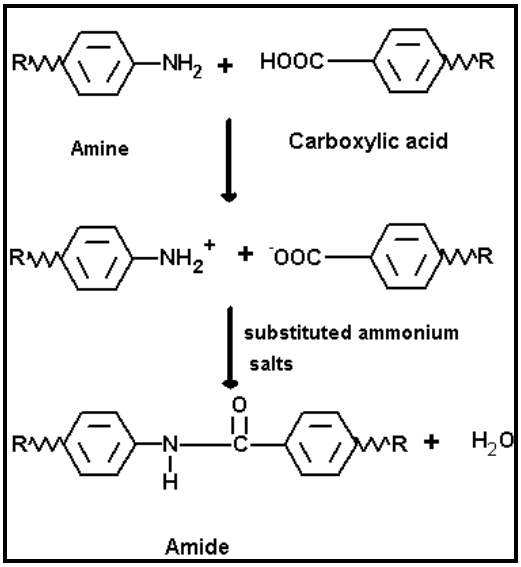

Scheme 7.1 Basic reaction for amide synthesis.

The TAPP and BCPP would be deposited and self-assembled on the Au(111) or Ag(111) surfaces via H-bonding. The reaction between the amino group and hydroxyl group shown in Scheme 7.1 would form covalent bonds to produce a nanomesh after annealing.

7.2.3. Synchrotron Radiation Technique on TAPB Molecules.

The work carried out on the TAPB and PTCDA systems (Chapter 6) could be extended to include synchrotron radiation techniques such as photoelectron spectroscopy (PES) and X-ray absorption spectroscopy (XAS) to gain more insight into the reaction mechanisms of the system.

7.2.4. Density Functional Theory (DFT) Calculations.

A collaboration with Dr. Corinne Dufaure from ENSIACET/CIRIMAT, Toulouse, France has been initiated to perform DFT calculations of TAPP molecules on Au(111) and Cu(111) substrates. This project was started in December, 2011 and is expected to take at least one year to produce results since it involves large and complicated systems.

7.2.5. Fullerene (C_{60}) and 5,10,15,20-tetrakis(4-aminophenyl)porphyrin (TAPP) Studies on Au(111).

C_{60} is an electron acceptor (A) and molecules such as porphyrins act as electron donors (D). These donor-acceptor interactions, particularly between porphyrin based materials and C_{60} has shown many promising results which have been reviewed by Bonifazi *et. al* [9] although direct charge transfer from/to the substrate might complicate systems. This organic nanomaterials research has shown potential applications in different fields such as sensing, catalysis, photovoltaics and nano-electronics [10,11].

C_{60} and the self-assembled organic molecules on metal surfaces or semiconductor single crystal surfaces to form supramolecular bi-dimensional (2D) ordering were investigated by a few research groups previously [9,12,13]. This state-of-art research, however, is still very much focused on the fundamental issues. Sedona *et al.* [12,14] performed experiments on 5,15-bis(4-aminophenyl)-10,20-diphenylporphyrin ($TPP(NH_2)_2$) with fullerene (C_{60}) molecules. They successfully formed extended, ordered, and covalently linked bi-components of C_{60} and $TPP(NH_2)_2$ by using annealing technique. Thus, the possible strategy to obtain large 2D long-range ordered, covalently bonded nanostructures (between TAPP and C_{60}) requires two steps:

(i) a large 2D supramolecular structure with long-range ordered is produced by exploiting the weak interactions between the organic molecules.

(ii) this structure is stabilised by covalent bonds initiated by thermal activation of a specific reaction between the units that does not occur spontaneously during the self-assembly process [12].

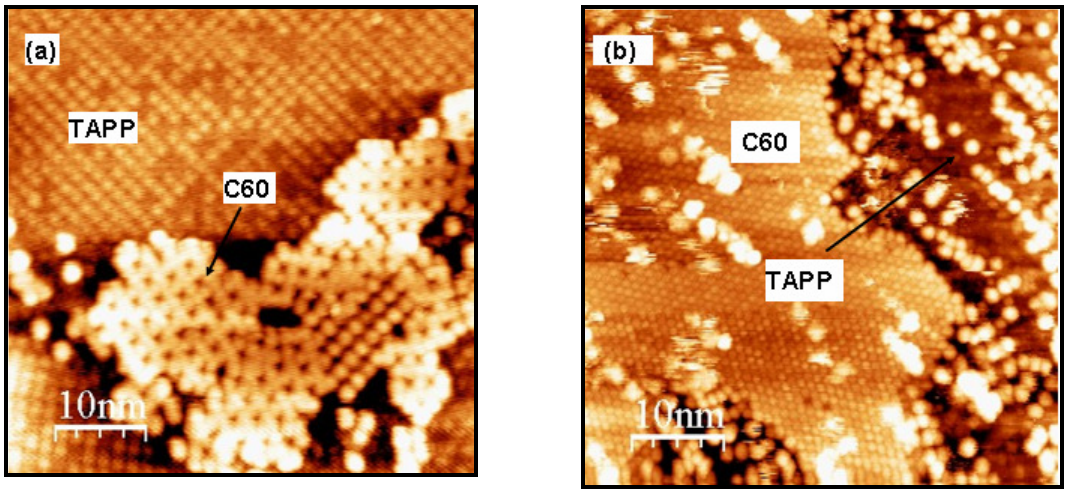

Fig. 7.3(a) STM image (50 nm ×50 nm, Vs = +1.5 V, I = 0.1 nA) when C_{60} molecules are on top of TAPP after 150 ^{o}C annealing; (b) STM image (50 nm ×50 nm, Vs = +2.5 V, I =0.3 nA); (c) STM image (50 nm ×50 nm, Vs = -1.0 V, I =0.1 nA) when TAPP is deposited on top of a ML of C_{60} after annealing at 250 ^{o}C on Au(111).

Some early work was carried out in this research where C_{60} was deposited onto a ML of TAPP on Au(111) and also, *vice-versa* Some of the results obtained are depicted in Fig. 7.3. Observation showed promising results for the formation of covalently bonded nano-structures especially when the TAPP molecules were deposited on top of a ML of C_{60}. After annealing at 250 ^{o}C, the XPS showed a shift in N1s spectrum which indicates reaction occurring between TAPP and C_{60}. On the other hand, C_{60} molecules desorbed after annealing at 350 ^{o}C when C_{60} atoms were deposited on top of a ML of TAPP, suggesting no reactions have occurred. These results are interesting and hence, the effort to further explore this project is encouraged.

With the future work proposed above, it indicates that there is still much work to be explored with both TAPP and TAPB systems. The challenge is to control the ordering of the networks formed. However, the results obtained to date have shown a very positive direction. The current work has definitely opened a new path in the organic nanomaterials field especially work that deals with amine reactions.

References:

[1] M.G. Walter, C.C. Wamser. *Synthesis and characterization of electropolymerized nanostructured aminophenylporphyrin films,* J. Phys. Chem. **114** (2010) 7574.

[2] G. Witte, S. Lukas, P.S. Bagus, C. Woll. *Vacuum level alignment at organic/metal junctions:"Cushion" effect and the interface dipole,* Appl. Phys. Lett. **87** (2005) 263502.

[3] http://www.chemguide.co.uk/organicprops/amides/polyamides.html.

[4] O. Ivasenko, D.F. Perepichka. *Mastering fundamentals of supramolecular design with carboxylic acids. Common lessons from X-ray crystallography and scanning tunneling microscopy,* Chem. Soc. Rev. **40** (2010) 191.

[5] M. Vinodu, I. Goldberg. *Synthesis and versatile supramolecular self-assembly of the 5, 15-bis (4-hydroxyphenyl)-10, 20-bis (4-carboxyphenyl) porphyrin scaffold,* Cryst. Eng. Comm. **6** (2004) 215.

[6] F. Nishiyama, T. Yokoyama, T. Kamikado, S. Yokoyama, S. Mashiko, K. Sakaguchi, K. Kikuchi. *Interstitial accommodation of C60 in a surface‐Supported supramolecular network,* Adv. Mater. **19** (2007) 117.

[7] F. Nishiyama, T. Yokoyama, T. Kamikado, S. Yokoyama, S. Mashiko. *Layer-by-layer growth of porphyrin supramolecular thin films,* Appl. Phys. Lett. **88** (2006) 253113.

[8] T. Yokoyama, T. Kamikado, S. Yokoyama, S. Mashiko. *Conformation selective assembly of carboxyphenyl substituted porphyrins on Au (111),* J. Chem. Phys. **121** (2004) 11993.

[9] D. Bonifazi, A. Kiebele, M. Stöhr, F. Cheng, T. Jung, F. Diederich, H. Spillmann. *Supramolecular Nanostructuring of Silver surfaces via self-assembly of [60]fullerene and porphyrin modules,* Adv. Funct. Mater. **17** (2007) 1051.

[10] A. Credi. *Artificial molecular motors powered by light,* Aust. J. Chem. **59** (2006) 157.

[11] R. Garcia, R.V. Martinez, J. Martinez. *Nano-chemistry and scanning probe nanolithographies,* Chem. Soc. Rev. **35** (2006) 29.

[12] F. Sedona, M. Di Marino, M. Sambi, T. Carofiglio, E. Lubian, M. Casarin, E. Tondello. *Fullerene/porphyrin multicomponent nanostructures on Ag (110): From supramolecular self-assembly to extended copolymers,* ACS Nano. (2010).

[13] D. Bonifazi, G. Accorsi, N. Armaroli, F. Song, A. Palkar, L. Echegoyen, M. Scholl, P. Seiler, B. Jaun, F. Diederich. *Oligoporphyrin arrays conjugated to [60]fullerene: Preparation, NMR analysis, and photophysical and electrochemical properties,* Helv. Chim. Acta. **88** (2005) 1839.

[14] M. Di Marino, F. Sedona, M. Sambi, T. Carofiglio, E. Lubian, M. Casarin, E. Tondello. *STM investigation of temperature-dependent two-dimensional supramolecular architectures of C60 and amino-tetraphenylporphyrin on Ag (110),* Langmuir. **26** (2010) 2081.

Appendix A.

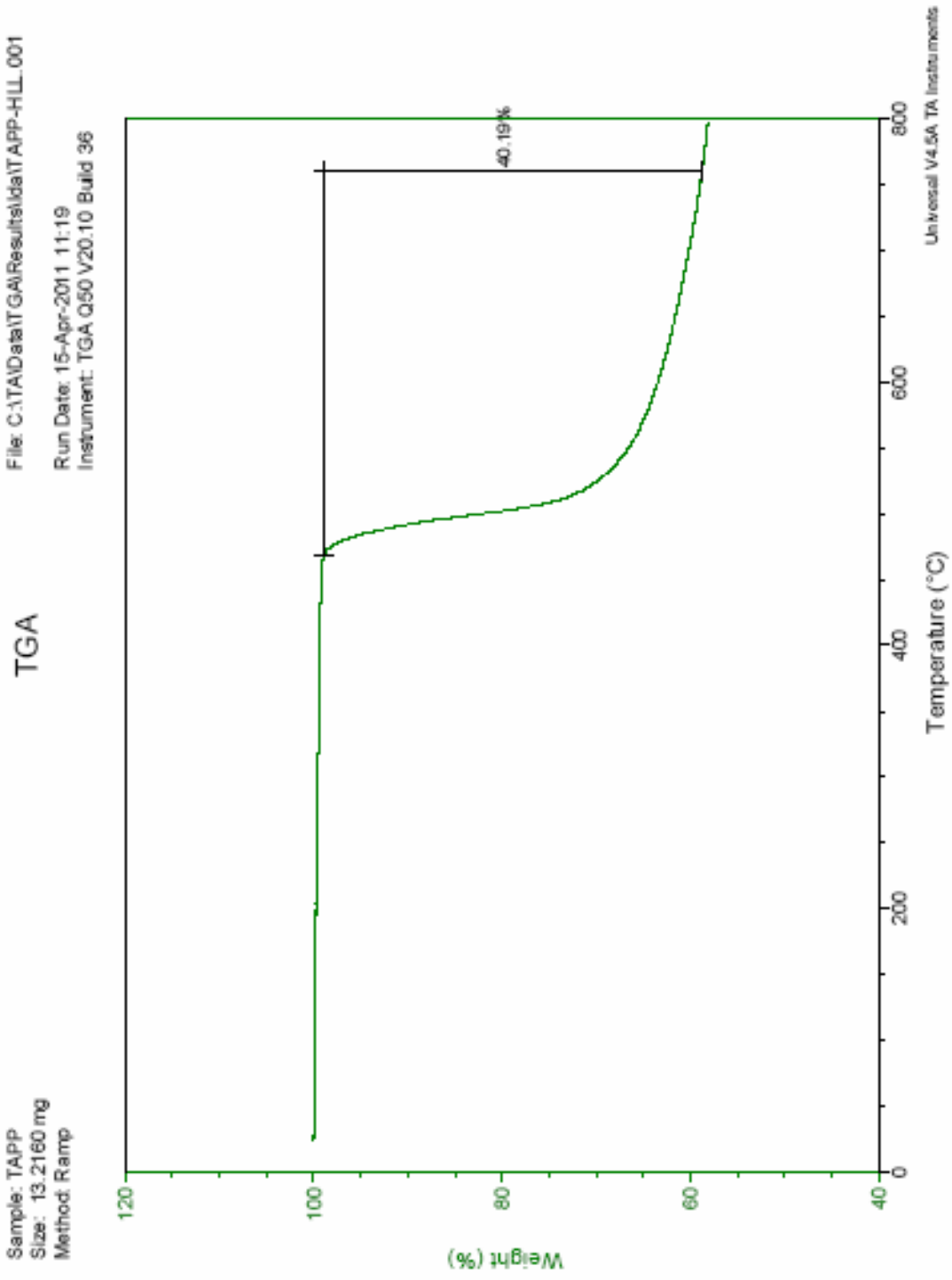
TGA
File: C:\TA\Data\TGA\Results\Data\TAPP-HLL.001
Run Date: 15-Apr-2011 11:19
Instrument: TGA Q50 V20.10 Build 36
Sample: TAPP
Size: 13.2160 mg
Method: Ramp
40.19%
Weight (%)
Temperature (°C)
Universal V4.5A TA Instruments

Appendix B.

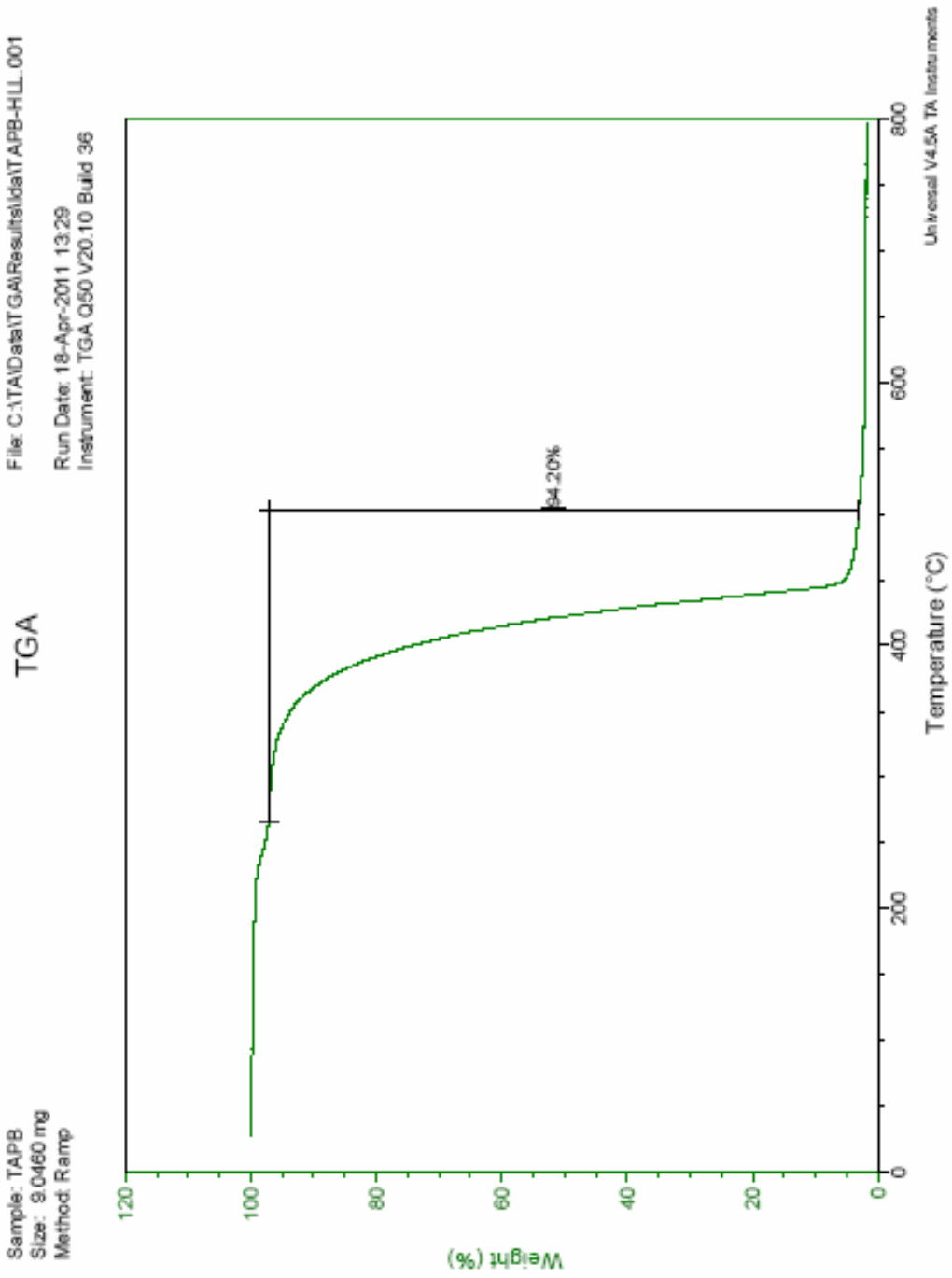
File: C:\TA\Data\TGA\Results\da\TAPB-HILL.001
Run Date: 18-Apr-2011 13:29
Instrument: TGA Q50 V20.10 Build 36
TGA
Sample: TAPB
Size: 9.0460 mg
Method: Ramp
84.20%
Weight (%)
Temperature (°C)
Universal V4.5A TA Instruments